THESE de DOCTORAT DE L'INSA LYON,
membre de l'UNIVERSITE DE LYON

délivré en partenariat international avec
CHONGQING UNIVERSITY

Ecole Doctorale N° 162
(Mécanique, Energétique, Génie civil, Acoustique)

Spécialité / discipline de doctorat :
Génie Mécanique

Soutenue publiquement/à huis clos le 20/10/2023, par :
Zongze Li

Study on Creep Fatigue Mechanical Characteristics and Constitutive Model of Salt Rock

Devant le jury composé de :

Christophe PETIT   Professor University of Limoges   Président.e

Yang JU   Professor China University of Mining and Technology, Beijing   Rapporteur.e
Daniel DIAS   Professor Université Grenoble Alpes   Rapporteur.e

Daniel NELIAS   Professor INSA Lyon   Directeur.rice de thèse
Deyi JIANG   Professor Chongqing University   Co-directeur.rice de thèse
Marion FOURMEAU   Assistant Professor INSA Lyon   Co-encadrant.e de thèse

Département FEDORA – INSA Lyon - Ecoles Doctorales

SIGLE	ECOLE DOCTORALE	NOM ET COORDONNEES DU RESPONSABLE
CHIMIE	**CHIMIE DE LYON** https://www.edchimie-lyon.fr Sec. : Renée EL MELHEM Bât. Blaise PASCAL, 3e étage secretariat@edchimie-lyon.fr	**M. Stéphane DANIELE** C2P2-CPE LYON-UMR 5265 Bâtiment F308, BP 2077 43 Boulevard du 11 novembre 1918 69616 Villeurbanne **directeur@edchimie-lyon.fr**
E.E.A.	**ÉLECTRONIQUE, ÉLECTROTECHNIQUE, AUTOMATIQUE** https://edeea.universite-lyon.fr Sec. : Stéphanie CAUVIN Bâtiment Direction INSA Lyon Tél : 04.72.43.71.70 secretariat.edeea@insa-lyon.fr	**M. Philippe DELACHARTRE** INSA LYON Laboratoire CREATIS Bâtiment Blaise Pascal, 7 avenue Jean Capelle 69621 Villeurbanne CEDEX Tél : 04.72.43.88.63 **philippe.delachartre@insa-lyon.fr**
E2M2	**ÉVOLUTION, ÉCOSYSTÈME, MICROBIOLOGIE, MODÉLISATION** http://e2m2.universite-lyon.fr Sec. : Bénédicte LANZA Bât. Atrium, UCB Lyon 1 Tél : 04.72.44.83.62 secretariat.e2m2@univ-lyon1.fr	**Mme Sandrine CHARLES** Université Claude Bernard Lyon 1 UFR Biosciences Bâtiment Mendel 43, boulevard du 11 Novembre 1918 69622 Villeurbanne CEDEX **sandrine.charles@univ-lyon1.fr**
EDISS	**INTERDISCIPLINAIRE SCIENCES-SANTÉ** http://ediss.universite-lyon.fr Sec. : Bénédicte LANZA Bât. Atrium, UCB Lyon 1 Tél : 04.72.44.83.62 secretariat.ediss@univ-lyon1.fr	**Mme Sylvie RICARD-BLUM** Institut de Chimie et Biochimie Moléculaires et Supramoléculaires (ICBMS) - UMR 5246 CNRS - Université Lyon 1 Bâtiment Raulin - 2ème étage Nord 43 Boulevard du 11 novembre 1918 69622 Villeurbanne Cedex Tél : +33(0)4 72 44 82 32 **sylvie.ricard-blum@univ-lyon1.fr**
INFOMATHS	**INFORMATIQUE ET MATHÉMATIQUES** http://edinfomaths.universite-lyon.fr Sec. : Renée EL MELHEM Bât. Blaise PASCAL, 3e étage Tél : 04.72.43.80.46 infomaths@univ-lyon1.fr	**M. Hamamache KHEDDOUCI** Université Claude Bernard Lyon 1 Bât. Nautibus 43, Boulevard du 11 novembre 1918 69 622 Villeurbanne Cedex France Tél : 04.72.44.83.69 **hamamache.kheddouci@univ-lyon1.fr**
Matériaux	**MATÉRIAUX DE LYON** http://ed34.universite-lyon.fr Sec. : Yann DE ORDENANA Tél : 04.72.18.62.44 yann.de-ordenana@ec-lyon.fr	**M. Stéphane BENAYOUN** Ecole Centrale de Lyon Laboratoire LTDS 36 avenue Guy de Collongue 69134 Ecully CEDEX Tél : 04.72.18.64.37 **stephane.benayoun@ec-lyon.fr**
MEGA	**MÉCANIQUE, ÉNERGÉTIQUE, GÉNIE CIVIL, ACOUSTIQUE** http://edmega.universite-lyon.fr Sec. : Stéphanie CAUVIN Tél : 04.72.43.71.70 Bâtiment Direction INSA Lyon mega@insa-lyon.fr	**M. Jocelyn BONJOUR** INSA Lyon Laboratoire CETHIL Bâtiment Sadi-Carnot 9, rue de la Physique 69621 Villeurbanne CEDEX **jocelyn.bonjour@insa-lyon.fr**
ScSo	**ScSo*** https://edsciencessociales.universite-lyon.fr Sec. : Mélina FAVETON INSA : J.Y. TOUSSAINT Tél : 04.78.69.77.79 melina.faveton@univ-lyon2.fr	**M. Bruno MILLY** Université Lumière Lyon 2 86 Rue Pasteur 69365 Lyon CEDEX 07 **bruno.milly@univ-lyon2.fr**

*ScSo : Histoire, Géographie, Aménagement, Urbanisme, Archéologie, Science politique, Sociologie, Anthropologie

Acknowledgements

As the completion of my doctoral thesis marks its conclusion, my doctoral academic journey in France is drawing to a close. I would like to take this opportunity to express my heartfelt gratitude to all those who have supported and guided me throughout my doctoral journey. Completing this thesis would not have been possible without your unwavering assistance, encouragement, and expertise.

First and foremost, I am deeply thankful to my thesis supervisor, Prof. Daniel Nelias and Deyi Jiang. Your dedication to research, your invaluable insights, and your patient guidance have been instrumental in shaping this work. Your mentorship has not only contributed to the academic development of this thesis but has also played a pivotal role in my personal growth as a researcher.

I would also like to extend my appreciation to my thesis co-supervisor, Dr. Marion Fourmeau. Your constructive feedback, probing questions, and expert perspectives have added immense value to this research. Your commitment to academic excellence has inspired me to strive for the highest standards in my work.

My gratitude extends to my colleagues and fellow graduate students, Bo, Chunhui, Ruochen, Baptiste, Aude, Fupeng and so on. They have provided a stimulating intellectual environment throughout my doctoral journey. The insightful discussions, collaborations, and shared experiences have been invaluable.

I am also thankful to China Scholarship Council for their financial support, which made this research possible. Your belief in the potential of this work has been a significant motivator.

Lastly, my family and friends have been a constant source of encouragement and support. I am grateful for their patience, understanding, and unwavering belief in me.

In closing, I want to express my profound appreciation to everyone who has contributed to this doctoral journey. Your support has been the wind beneath my wings, propelling me to reach this significant milestone. I am humbled by your faith in me and the belief that my research can contribute to our collective knowledge.

Sincerely,

Zongze LI

05/09/2023

Résumé

Le 12 décembre 2015, la 21e Conférence des Parties (COP21) s'est réunie à Paris, où les représentants de 195 pays membres des Nations Unies ont approuvé l'Accord de Paris. L'accord visait à limiter l'augmentation de la température mondiale à moins de 2°C ce siècle, avec des efforts pour la restreindre davantage à 1,5°C. Atteindre le pic des émissions de carbone et la neutralité carbone est essentiel pour atteindre ces objectifs. Les énergies renouvelables sont une initiative cruciale pour les nations du monde entier afin d'atteindre le pic des émissions de carbone et la neutralité carbone comme prévu. Le sel gemme, caractérisé par de bonnes propriétés rhéologiques, une faible porosité, une faible perméabilité et des propriétés d'auto-guérison, offre une voie efficace pour le stockage d'énergie par air comprimé, améliorant ainsi l'efficacité de l'utilisation des énergies renouvelables. Compte tenu des conditions opérationnelles des centrales de stockage d'énergie par air comprimé, les réservoirs de cavernes de sel doivent supporter des charges cycliques discontinues de fréquences variables d'injection et d'extraction de gaz, ainsi que des pressions de fonctionnement, ce qui signifie une interaction de fluage-fatigue alternée. Dans le contexte de la construction et de l'exploitation de centrales de stockage d'énergie par air comprimé en cavités de sel dans le monde entier, cette étude examine systématiquement les caractéristiques mécaniques de fluage-fatigue de la roche réservoir de la cavité de sel sous l'influence de multiples facteurs. En utilisant une combinaison d'analyse de recherche, d'étude expérimentale et de dérivation théorique, les principaux contenus de la recherche et les conclusions sont les suivants:

(1) Des essais de fluage-fatigue à charge uniaxiale ont été réalisés pour étudier l'interaction entre le fluage et la fatigue de la roche saline en variant le temps d'intervalle de haute tension. Les résultats indiquent que la courbe caractéristique mécanique de fluage-fatigue de la roche saline ressemble à celle des essais de fatigue traditionnels. L'introduction de charges cycliques favorise la déformation par fluage, mais cette amélioration diminue avec l'augmentation du temps d'intervalle de haute tension. La présence d'intervalles de haute tension conduit à des déformations résiduelles plus importantes avant les intervalles qu'après. À mesure que la période d'intervalle de haute tension s'allonge, la durée de vie en fatigue des échantillons de roche saline diminue, tandis que la durée de vie en fluage augmente. L'interaction entre le fluage et la fatigue

est due aux réponses distinctes de la structure interne de la roche saline à la fatigue et au fluage.

(2) Des essais de fluage-fatigue à différentes pressions de confinement ont été réalisés pour explorer l'influence de la pression de confinement sur les caractéristiques mécaniques de fluage-fatigue de la roche saline. L'étude révèle qu'une pression de confinement plus élevée renforce la résistance et la déformation ultime de la roche saline. Avec l'augmentation de la pression de confinement, la déformation de la roche saline présente finalement un seul stade, similaire à l'essai de fluage-fatigue uniaxial. La fatigue favorise également le fluage, et le modèle de déformation résiduelle reste cohérent, bien que cette différence diminue avec une pression de confinement plus élevée. La transition fragile-ductile de la roche saline sous différentes pressions de confinement est la cause de la variation de ses caractéristiques mécaniques de fluage-fatigue. Lors de la conception des niveaux de pression de gaz de fonctionnement pour les centrales de stockage d'énergie par air comprimé en cavités de sel, il faut tenir compte de l'influence de la profondeur sur l'état de contrainte de la roche environnante.

(3) En utilisant des dispositifs d'émission acoustique, l'impact de différentes niveaux de contrainte sur les caractéristiques mécaniques de fluage-fatigue de la roche saline dans des conditions uniaxiales et triaxiales a été surveillé. La recherche montre que la déformation par fluage augmente avec des niveaux de contrainte plus élevés. Cependant, au sein de chaque cycle, la déformation par fluage présente une tendance à la baisse avec l'augmentation du nombre de cycles. Ce n'est qu'à la dernière étape des cycles que la déformation par fluage montre une augmentation finale. À des niveaux de contrainte plus faibles, les intervalles de haute tension continuent d'influencer les cycles de fatigue. Avec l'augmentation des niveaux de contrainte, les valeurs de déformation résiduelle avant et après l'intervalle augmentent. La présence de la pression de confinement atténue cette tendance à la hausse. Les signaux d'émission acoustique reflètent des modèles distincts de rupture de la roche, avec une rupture par cisaillement étant plus sévère dans les essais de fluage-fatigue triaxiaux gradués. Les paramètres d'émission acoustique et les données mécaniques illustrent que, avec l'augmentation des niveaux de contrainte, la déformation plastique et les dommages dominent la phase de fluage.

(4) Des essais de fluage-fatigue à long terme de la roche saline ont été réalisés en concevant différentes périodes de chargement et de déchargement, ainsi que des limites de contrainte, explorant les caractéristiques mécaniques de fluage-fatigue de la roche saline sur des durées prolongées. La recherche a montré que, dans les essais de fluage-

fatigue à long terme, plus le taux de chargement en contrainte est faible, plus grande est la déformation générée dans la roche saline. La variation du niveau de contrainte a un impact plus important sur le fluage que sur les cycles de chargement et de déchargement en fatigue (taux de chargement en contrainte). Le changement d'état de contrainte affecte considérablement le taux de déformation de la roche saline.

(5) En définissant des variables d'état et en introduisant des facteurs de déchargement et de fissure, un nouveau modèle constitutif de fluage-fatigue pour la roche saline a été établi en tenant compte de l'interaction entre le fluage et la fatigue. La recherche indique que dans les essais de fluage-fatigue à longue durée de la roche saline, plus le taux de chargement en contrainte est faible, plus grande est la déformation produite. L'influence des changements de limite de contrainte sur le fluage l'emporte sur celle des cycles de chargement et de déchargement en fatigue. Les changements d'état de contrainte affectent le taux de déformation de la roche saline. Sur la base des résultats expérimentaux, un nouveau modèle constitutif de fluage-fatigue pour la roche saline, prenant en compte l'interaction entre le fluage et la fatigue, a été établi en incorporant une variable d'état caractérisant le niveau de durcissement de la roche sur la base du modèle de fluage de Norton. Le modèle décrit de manière précise l'impact des trajets historiques de chargement-déchargement sur les propriétés mécaniques viscoplastiques de la roche saline. Quatre ensembles de données d'essais mécaniques de roche saline différents avec des trajets de contrainte variables ont été utilisés pour valider ce modèle constitutif de fluage-fatigue. Les courbes d'ajustement et les courbes d'essai des quatre trajets de contrainte présentent une bonne cohérence, ce qui indique que le modèle prend en compte de manière exhaustive les effets du temps, de la charge et de l'état sur le fluage-fatigue de la roche saline, décrivant efficacement les caractéristiques de déformation plastique du fluage-fatigue de la roche saline sous différents trajets de contrainte..

Mots-clés: roche saline, Fluage-fatigue, Pression de confinement, Émission acoustique, Variables d'état, Modèle constitutif.

Abstract

In December 12, 2015, the 21st Conference of the Parties (COP21) was convened in Paris, where representatives from 195 United Nations member countries approved the Paris Agreement. The accord aimed to limit the global temperature rise to within 2°C this century, with efforts to further restrict it to 1.5°C. Achieving carbon peak and carbon neutrality is pivotal to attaining these goals. Renewable energy stands as a crucial initiative for nations worldwide to achieve carbon peak and carbon neutrality as scheduled. Salt rock, characterized by good rheological properties, low porosity, low permeability, and self-healing properties, offers an effective avenue for compressed air energy storage, enhancing the efficiency of renewable energy utilization. Given the operational conditions of compressed air energy storage plants, salt cavern reservoirs must endure discontinuous cyclic loads of varying injection and extraction gas frequencies and operating pressures, signifying alternating creep-fatigue interaction. Against the backdrop of constructing and operating salt cavern compressed air energy storage plants all over the world, this study systematically investigates the creep-fatigue mechanical characteristics of salt cavern reservoir rock under the influence of multiple factors. By employing a combination of research analysis, experimental study, and theoretical derivation, the primary research content and conclusions are as follows:

(1) Uniaxial stress-driven creep-fatigue tests were conducted to study the interaction between salt rock creep and fatigue by varying the high stress interval time. Results indicate that the creep-fatigue mechanical characteristic curve of salt rock resembles that of traditional fatigue tests. The introduction of cyclic loads promotes creep deformation, but this enhancement weakens with increased high stress interval times. The presence of high stress intervals leads to larger residual strains before intervals than after. As high stress interval period extends, the fatigue life of salt rock samples decreases, while the creep life increases. The interaction between creep and fatigue is due to the distinct responses of salt rock's internal structure to fatigue and creep.

(2) Creep-fatigue tests under different confining pressures were conducted to explore the influence of confining pressure on salt rock's creep-fatigue mechanical characteristics. The study reveals that increasing confining pressure enhances salt rock's strength and ultimate deformation. With elevated confining pressure, salt rock deformation ultimately displays a single stage, similar to the uniaxial creep-fatigue test.

Fatigue also promotes creep, and the pattern of residual strain remains consistent, though this difference diminishes with higher confining pressure. The brittle-ductile transition of salt rock under different confining pressures is the cause of variation in its creep-fatigue mechanical features. When designing the operating gas pressure levels for salt cavern compressed air energy storage plants, the influence of depth on the surrounding rock's stress state must be considered.

(3) Using acoustic emission devices, the impact of different stress levels on salt rock's creep-fatigue mechanical characteristics under uniaxial and triaxial conditions was monitored. Research demonstrates that creep strain increases with higher stress levels. However, within each cycle, creep strain exhibits a declining trend with an increase in cycle number. Only in the final stage of cycles does creep strain show a final increase. At lower stress levels, high stress intervals continue to influence fatigue cycles. With rising stress levels, both pre- and post-interval residual strain values increase. The presence of confining pressure mitigates this upward trend. Acoustic emission signals reflect distinct rock failure patterns, with shear failure being more severe in graded triaxial creep-fatigue tests. Both acoustic emission parameters and mechanical data illustrate that with increasing stress levels, plastic deformation and damage dominate the creep stage.

(4) Long-time creep-fatigue tests of salt rock were conducted by designing different loading and unloading periods and stress limits, exploring salt rock's creep-fatigue mechanical characteristics over extended time spans. The research showed that in the long-term creep-fatigue tests, the smaller the loading stress rate, the greater the deformation generated in salt rock. The variation in stress level has a greater impact on creep than fatigue loading cycles (stress loading rate). The change in stress state significantly affects the deformation rate of salt rock.

(5) By defining state variables and introducing unloading and crack factors, a novel creep-fatigue constitutive model for salt rock was established that considers creep-fatigue interaction. Research indicates that in long-duration creep-fatigue tests of salt rock, the smaller the loading stress rate, the greater the deformation produced. The influence of stress limit changes on creep outweighs that of fatigue loading and unloading. Changes in stress state impact salt rock's deformation rate. Based on the experimental results, a new creep-fatigue constitutive model for salt rock that considers creep-fatigue interaction was established by incorporating a state variable that characterizes rock hardening level on the basis of the Norton creep model. The model

accurately describes the impact of historical loading-unloading paths on salt rock's viscoplastic mechanical properties. Four different salt rock mechanical test data sets with varying stress paths were used to validate this creep-fatigue constitutive model. The fit curves and test curves of the four stress paths demonstrate good consistency, indicating that the model comprehensively considers the effects of time, load, and state on salt rock's creep-fatigue, effectively describing the creep-fatigue plastic deformation features of salt rock under different stress paths.

Keywords：Salt rock, Creep-fatigue, Confining pressure, Acoustic emission, State variables, Constitutive model.

Content

Les Résumé de Thèse en Français

1 Introduction

Le 2 décembre 2015, 195 États membres des Nations Unies se sont réunis à Paris, en France, lors de la 21e Conférence des Nations Unies sur les changements climatiques. La Chine, les États-Unis, la France, le Royaume-Uni, la Russie et d'autres pays majeurs du monde ont signé l'Accord de Paris sur le climat lors de cette conférence. Cet accord appelle les pays du monde entier à limiter l'augmentation de la température moyenne mondiale à moins de 2°C par rapport aux niveaux préindustriels et à travailler pour limiter cette augmentation à 1,5°C au-dessus des niveaux préindustriels. Le récent sommet sur le climat de Glasgow a renforcé l'appel au respect des objectifs de l'Accord de Paris et a exhorté les États membres à éliminer l'utilisation du charbon et à avancer vers la neutralité carbone mondiale, c'est-à-dire la compensation des émissions et la séquestration du dioxyde de carbone à l'échelle mondiale, entre 2050 et 2100. Le gouvernement chinois a décidé d'atteindre le pic des émissions de carbone d'ici 2030 et la neutralité carbone d'ici 2060. Le gouvernement français souhaite atteindre le même objectif dix ans plus tôt que prévu.

Il existe deux moyens d'atteindre la neutralité carbone : (1) L'utilisation de mécanismes de compensation carbone pour réduire la quantité totale d'émissions de carbone générées. Par exemple, la reforestation et l'achat de bons d'énergie renouvelable. (2) L'utilisation de technologies à faibles émissions de carbone, voire nulles. Par exemple, on utilise des sources d'énergie renouvelable (telles que l'éolien et le solaire) pour éviter les émissions de dioxyde de carbone dans l'atmosphère résultant de la combustion de combustibles fossiles. Cependant, en raison de la nature intermittente et fluctuante de l'énergie renouvelable, il est difficile de la connecter directement au réseau en raison de ses caractéristiques de production d'énergie instable et continue. L'un des moyens efficaces de résoudre ce problème est d'utiliser des dispositifs de stockage d'énergie pour stocker l'énergie renouvelable pendant les périodes de faible consommation d'énergie et la libérer de manière régulière pendant les périodes de forte consommation d'énergie dans le but d'assurer une alimentation électrique continue et stable. Étant donné que la roche saline présente une bonne rhéologie, une faible porosité, une faible perméabilité et des caractéristiques d'auto-guérison des dommages, l'utilisation de cavernes salines abandonnées pour construire

des centrales de stockage d'air comprimé (CAES) peut répondre aux besoins de stockage de l'énergie éolienne, solaire et d'autres énergies renouvelables, ainsi qu'aux besoins du développement minier durable (Fig. 1). La base de l'utilisation des cavernes salines comme centrales CAES est de garantir la stabilité de la roche environnante du réservoir de stockage de la caverne saline.
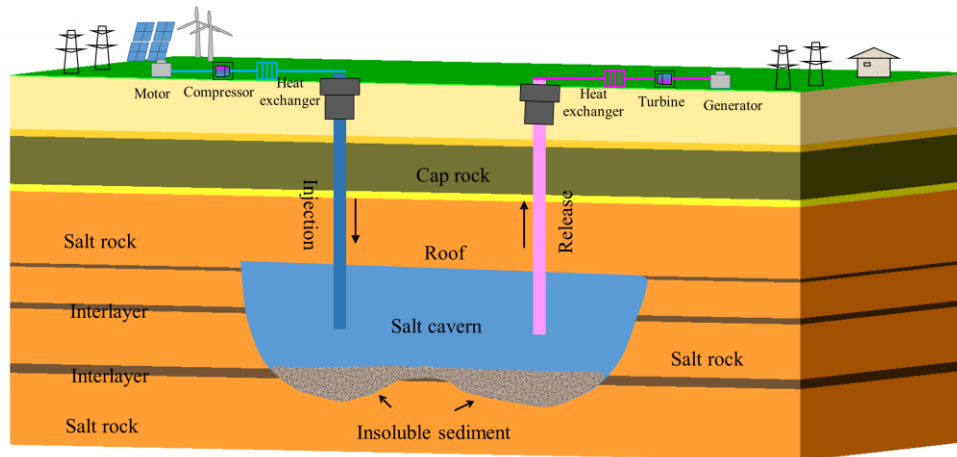
Fig. 1.1 Schéma de la centrale électrique à stockage de gaz sous pression de Salt Cave

Dans la recherche sur la mécanique de base de la roche saline, des chercheurs du monde entier ont mené de nombreuses études fondamentales. Les chercheurs ont également mené des études approfondies sur les propriétés mécaniques de fluage et de fatigue des roches, produisant de nombreux résultats de recherche.

L'étude des matériaux soumis à des plateaux de contrainte élevée, c'est-à-dire les effets de fluage-fatigue, a été largement étudiée par des chercheurs du monde entier dans le domaine des métaux. Les propriétés de fluage-fatigue d'autres matériaux tels que l'asphalte, les panneaux de bois, etc., ont également été partiellement étudiées. Les études sur les propriétés mécaniques de fluage-fatigue des roches sont rarement rapportées, et il n'y a que quelques articles pertinents qui enquêtent sur les propriétés mécaniques de fluage-fatigue des roches. Compte tenu des résultats des essais de fatigue réalisés sous de faibles intervalles de contrainte, nous devrions accorder plus d'attention aux caractéristiques de fatigue de la roche saline sous un plateau de contrainte élevée pendant le fonctionnement d'un réservoir de stockage d'air. Par conséquent, dans cette thèse, nous avons conçu des essais de fluage sous différentes contraintes pour la roche saline, des essais de fluage-fatigue avec différents intervalles de contrainte élevée, des essais de fluage-fatigue sous différentes pressions de confinement et des essais de fluage-fatigue à long terme. À l'aide d'équipements d'observation tels que l'émission acoustique, nous avons analysé en détail la distribution

macroscopique des fissures et l'évolution microscopique des dommages de la roche saline sous l'alternance de fluage-fatigue, et nous avons établi un modèle constitutif mécanique de fluage-fatigue de la roche saline qui prend en compte l'interaction entre le fluage et la fatigue. Les résultats de la recherche ont une importance de référence importante pour le fonctionnement sûr des réservoirs de stockage de cavernes salines CAES dans des projets concrets.

2 Caractérisation mécanique par fluage-fatigue de roches salines soumises à des contraintes uniaxiales

Pendant le fonctionnement d'une centrale électrique CAES, il existe une différence spatiale et temporelle dans l'utilisation de l'énergie entre le côté demande (foyers, usines, etc.) et le côté approvisionnement (éolien, solaire, etc.). Autrement dit, lorsqu'une source d'énergie durable génère de l'électricité et la stocke dans une cavité de sel à l'aide d'air comprimé, le gaz n'est pas immédiatement libéré pour produire de l'électricité, il y a donc une certaine période de stabilisation à haute pression. De même, il y aura une période de stabilisation à basse pression pour la pression interne du gaz une fois que la centrale CAES aura terminé son pic de demande. L'étude des propriétés mécaniques de fatigue simples des roches salines ne reflète pas pleinement l'état mécanique réel de la roche environnante du réservoir CAES. Par conséquent, il est nécessaire de mener des recherches pertinentes sur les caractéristiques mécaniques du fluage-fatigue de la roche saline.
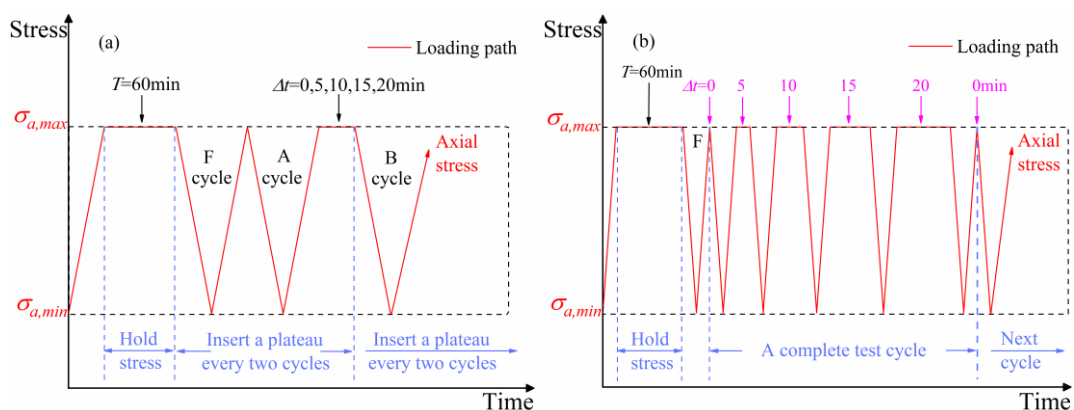
Fig. 2.1 Loading paths for the creep-fatigue tests: (a) CCFs and (b) VCF.

Dans ce chapitre, nous avons mis en place un essai de mécanique de fluage-fatigue des roches salines avec différentes durées de plateau de contrainte élevée, et le schéma de l'essai est illustré dans la figure 2.1 ci-dessous. Les résultats expérimentaux montrent que le plateau anglais élevé affecte de manière significative la déformation résiduelle de fatigue, ce qui fait que la déformation résiduelle du cycle post-plateau est inférieure à celle du cycle pré-plateau. L'ajout de la fatigue accélère la vitesse de déformation du fluage. Il existe une interaction entre la fatigue et le fluage.

3 Caractérisation mécanique par fluage-fatigue de roches salines soumises à des contraintes triaxiales

Les réservoirs de cavernes salines utilisés dans les centrales électriques CAES sont souvent situés en profondeur, et la roche environnante du réservoir est dans un état de contrainte triaxiale. Lorsque la cavité est formée par une exploitation minière soluble dans l'eau, l'équilibre original des contraintes de la roche environnante du réservoir est modifié, et la contrainte différentielle dans le champ de contrainte provoquera une déformation continue de la roche environnante. Pour tous les matériaux rocheux, l'existence d'une pression de confinement augmente d'une part la résistance ultime de la roche et améliore la capacité portante de la roche ; d'autre part, elle augmente la ténacité de la roche, de sorte que certaines des roches dans la partie peu profonde de la performance des roches dures ordinaires, dans la partie profonde de la performance de la grande déformation des caractéristiques des roches tendres. Par conséquent, afin de se rapprocher de la réalité technique et de révéler les propriétés mécaniques de fluage-fatigue et la loi d'évolution des dommages de la roche environnante des cavernes de sel souterraines, il est nécessaire d'effectuer des essais triaxiaux de fluage-fatigue des roches salines sous différentes pressions de confinement.
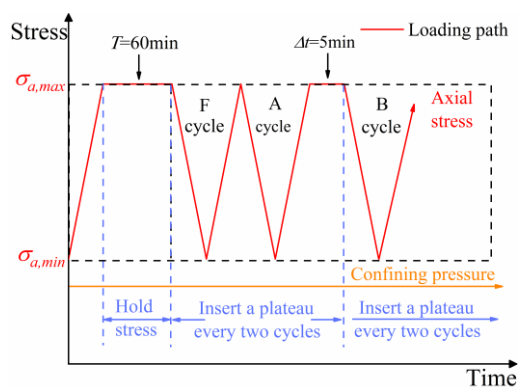
Fig. 3.1 Loading paths during the triaxial creep–fatigue (TCF) tests.

Il a été constaté que l'interaction entre le fluage et la fatigue existe toujours. L'effet de la pression de confinement inhibe cette interaction. La transformation fragile-ductile de la roche saline à différentes pressions de confinement est responsable de la variation des caractéristiques mécaniques de fluage-fatigue de la roche saline. L'effet de la profondeur sur l'état de contrainte de la roche environnante doit être pris en compte lors de la conception du niveau de pression de gaz d'exploitation d'une centrale de stockage de gaz sous pression en caverne de sel. Ceci est particulièrement important pour les cavernes de dissolution verticales.

4 Caractérisation mécanique du fluage-fatigue à plusieurs niveaux d'amplitude des roches salines à l'aide d'une analyse des signaux d'émission acoustique

Au cours de l'exploitation d'une centrale électrique CAES en cavité saline, la variation de la pression d'injection de gaz affecte également l'évolution de l'endommagement des roches environnantes du réservoir. La technique d'émission acoustique (AE) est un outil efficace pour étudier les modèles d'évolution des dommages des matériaux. Les chercheurs du monde entier ont mené de nombreuses études sur les propriétés mécaniques des roches en se basant sur la surveillance de la fatigue, de la compression, de la tension et du fluage par la technique d'émission acoustique. L'évaluation de la stabilité structurelle des matériaux rocheux à l'aide des paramètres des signaux d'EA (nombres, énergie, fréquence de crête, durée, etc.) est une méthode largement utilisée, rapide et intuitive. Dans ce chapitre, nous nous concentrerons sur l'évolution de l'endommagement des roches salines sous l'influence de différentes pressions de confinement et de niveaux de contrainte à l'aide des techniques d'EA.
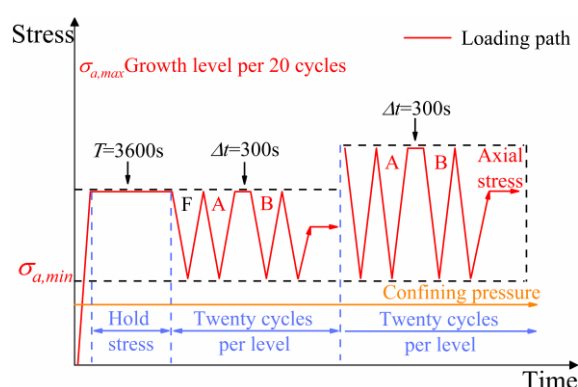
Fig. 4.1 Loading paths for the uniaxial and triaxial stepwise creep–fatigue tests.

À des niveaux de contrainte inférieurs, l'effet d'intervalles de contrainte plus élevés sur la fatigue de la roche commence à se manifester. Au fur et à mesure que le niveau de contrainte augmente, les valeurs de déformation résiduelle avant et après l'intervalle augmentent. La présence d'une pression périmétrique réduit cette tendance à l'augmentation. Les paramètres d'émission acoustique et les données mécaniques montrent que la déformation plastique et l'endommagement pendant la phase de fluage dominent progressivement à mesure que le niveau de contrainte augmente. Dans la phase finale, les contraintes subies pendant le fluage sont transformées en forces qui entraînent l'expansion des fissures.

5 Propriétés mécaniques de fluage-fatigue à long terme de la roche saline

Dans les trois chapitres précédents, les influences de multiples facteurs tels que la durée des intervalles de contraintes élevées (fluage), la pression de confinement, les niveaux de contrainte, etc. sur les caractéristiques mécaniques du fluage-fatigue des roches salines ont été systématiquement étudiées.

Cependant, en raison de la conception expérimentale, les essais susmentionnés ont été réalisés en une seule journée de travail. Étant donné que la fréquence d'écrêtage des centrales de stockage d'énergie à air comprimé est souvent de l'ordre de plusieurs jours [278], la réalisation d'essais de fluage-fatigue de longue durée sur des roches salines devient cruciale pour une compréhension précise de l'évolution des dommages dans les réservoirs de cavernes salines. C'est pourquoi, dans ce chapitre, avec des fréquences d'écrêtement des pointes et des pressions de stockage de gaz variables, trois séries d'essais de fluage-fatigue de longue durée sur des roches salines ont été conçues. Ces essais visent à explorer les caractéristiques mécaniques de fluage-fatigue des roches salines à l'échelle opérationnelle des installations de stockage de gaz.
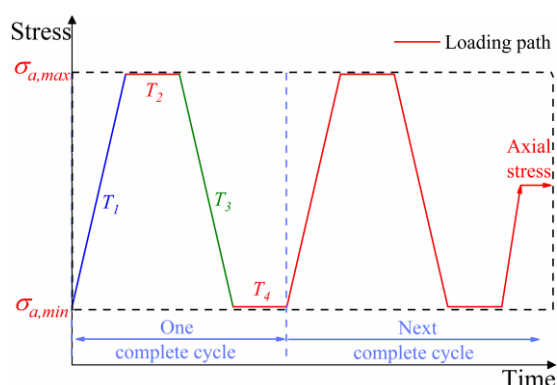
Fig.5.1 Loading path for long-time creep-fatigue (LTCF) tests on salt rocks.

Dans les essais de fluage-fatigue de longue durée sur les roches salines, plus la vitesse de chargement est faible, moins la déformation générée pendant la phase de chargement est importante. L'influence des changements de la limite supérieure de contrainte sur le fluage des roches salines est plus importante que celle du cycle de chargement de la fatigue. Cependant, dans la phase de déchargement et dans la phase d'intervalle de faible contrainte, des schémas différents sont observés. Les expériences démontrent que l'état de contrainte modifie de manière significative le taux de déformation de la roche, mais que son impact varie en fonction des différentes conditions de chargement/déchargement.

6 Nouvelle modélisation constitutive du fluage-fatigue des roches salines basée sur des variables d'état

Les études menées dans les chapitres précédents ont permis de tirer les principales conclusions suivantes : avec l'augmentation de la vitesse de contrainte, la déformation plastique des roches salines par cycle diminue, et la déformation des roches salines se distingue en déformation de chargement qui est affectée par la vitesse de contrainte, et en déformation de fluage qui n'est pas affectée pour l'essentiel. La recherche sur le fluage et la fatigue des roches salines montre qu'il existe une interaction entre le fluage et la fatigue. La fatigue peut accélérer la déformation par fluage et, à son tour, l'effet de durcissement de la phase de fluage réduira la déformation résiduelle des roches salines, la destruction finale de la roche saline dans la charge de fluage-fatigue est le résultat de la double action du fluage et de la fatigue, lorsque les fissures de perforation de grain induites par le fluage et les fissures induites par la fatigue le long des limites de grain de la fracture ou des fractures de perforation de grain se rencontrent et convergent, ce qui aboutit à la destruction de la roche saline. Les modifications de la limite supérieure de contrainte ont également un effet significatif sur l'endommagement des spécimens de roches salines. L'étude ci-dessus montre que les caractéristiques spéciales du modèle ontologique mécanique de fluage-fatigue pour les roches salines et d'autres modèles ontologiques de fluage et de fatigue devraient prendre en compte les effets du fluage et de l'extension de la fracture sur la fatigue ainsi que les effets de l'historique de chargement et de déchargement sur le fluage. Dans ce qui suit, le modèle constitutif de fluage-fatigue pour les roches salines sera dérivé et validé pour cette caractéristique sur la base de certaines des lois obtenues lors des essais.
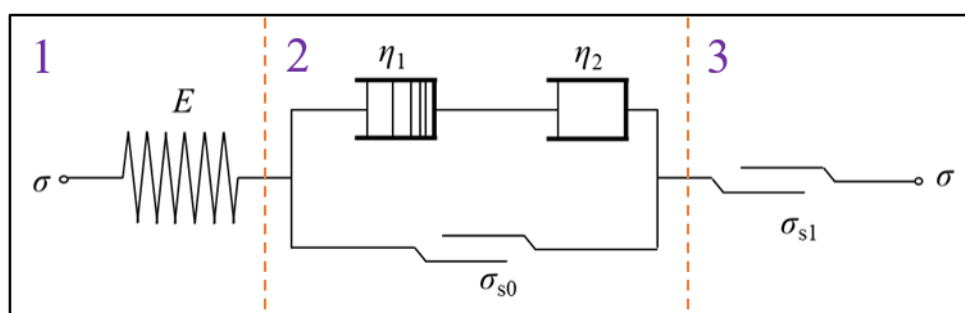
Fig. 6.1 Creep-fatigue rheological model.

Un nouveau modèle intrinsèque de fluage-fatigue des roches salines prenant en compte l'interaction fluage-fatigue est établi en introduisant la variable d'état caractérisant le degré de durcissement de la roche sur la base du modèle de fluage de

Norton. Sur la base du modèle ontologique de fluage-fatigue proposé, la déformation des roches salines est divisée en deux parties : la déformation de fluage (déformation dépendante du temps) et la déformation de chargement (déformation indépendante du temps).

Quatre voies de chargement différentes, à savoir l'essai de fluage à contrainte constante, l'essai de fatigue cyclique avec chargement et déchargement, l'essai de fluage-fatigue uni/triaxial et l'essai de fluage-fatigue à long terme, sont utilisées pour vérifier le modèle de fluage-fatigue. La comparaison entre les courbes ajustées des quatre chemins de contrainte inutilisés et les courbes expérimentales montre que l'accord entre les deux est meilleur, ce qui signifie que le modèle peut bien décrire le modèle de fluage-fatigue sous différents chemins de contrainte en prenant en compte les effets du temps, de la charge et de l'état sur le fluage et la fatigue de la roche saline. caractériser la déformation plastique de fluage-fatigue de la roche saline sous différents chemins de contrainte.

1 Introduction

1.1 Background and significance

1.1.1 *The necessity of renewable energy usage*

On November 6, 2022, the World Meteorological Organization (WMO) of the United Nations published the report 'Interim Global Climate 2022' (WMO,2022). According to the study, the past eight years have been the hottest on record, with rising greenhouse gas concentrations and accumulated heat contributing to the phenomenon [1]. In addition, 2022 extreme heat waves, droughts and devastating floods have affected millions of lives and caused billions of dollars in damages [2].

The signs and impacts of climate change are also becoming more pronounced. The rate of sea level rise has doubled since 1993. It has risen by nearly 10 mm since January 2020, accounting for 10 percent of the overall sea level rise [3]. To add insult to injury, the rate of warming is likewise accelerating, with the 10-year average temperature for the period 2013-2022 estimated to be 1.14°C above the pre-industrial baseline of 1850-1900. This exceeds the Intergovernmental Panel on Climate Change's (IPCC) Sixth Assessment Report estimate of 1.09°C [4]. This sequence of extreme weather events suggests that global warming caused by carbon dioxide from the world's industrial activities is already having a severe impact on the climate. Carbon dioxide-induced global warming is already having a serious impact on our living environment. This is despite the fact that at the 21st United Nations Climate Conference in 2015, 195 countries from around the world signed the *Paris Agreement*, which aims to reduce carbon dioxide emissions and minimize the effects of greenhouse gases [5,6]. However, the climate and environmental disasters show that human beings have not significantly recognized the harm caused by climate change.

In fact, as early as 1980, the world's three major environmental protection organizations, The International Union for Conservation of Nature (IUCN), the United Nations Environment Programme (UNEP) and the World Wildlife Fund (WWF), jointly published the *World Conservation Strategy 1980* for the protection of the world's environment [8]. The concept of sustainable development was clearly put forward. One of the core requirements of sustainable development is to reduce the use of non-renewable energy sources (fossil energy), accelerate the development of renewable (green) energy sources, and gradually increase their share in energy use [9]. The *Paris*

Agreement, for its part, specifies targets for countries to increase the use of renewable energy to reduce greenhouse gas emissions, to limit the increase in global average temperature to less than 2°C above pre-industrial levels and to work towards limiting the temperature increase to 1.5°C above pre-industrial levels, and calls on member States to phase out the use of coal by 2050 to 2100 and to achieve offsets for global carbon dioxide releases and sequestration [10].

Although since the beginning of the 20th century, countries around the world have gradually recognized the need for renewable energy use, especially after 2015, the proportion of renewable energy in primary energy consumption has been increasing from less than 1% in 1995 to 5.7% in 2020, as required by the *Paris Agreement*. However, compared to the primary energy consumption ratios of 31.2% for oil, 27.2% for coal, and 24.7% for natural gas (Figure 1.1), the use of renewable energy is still far from adequate [11].
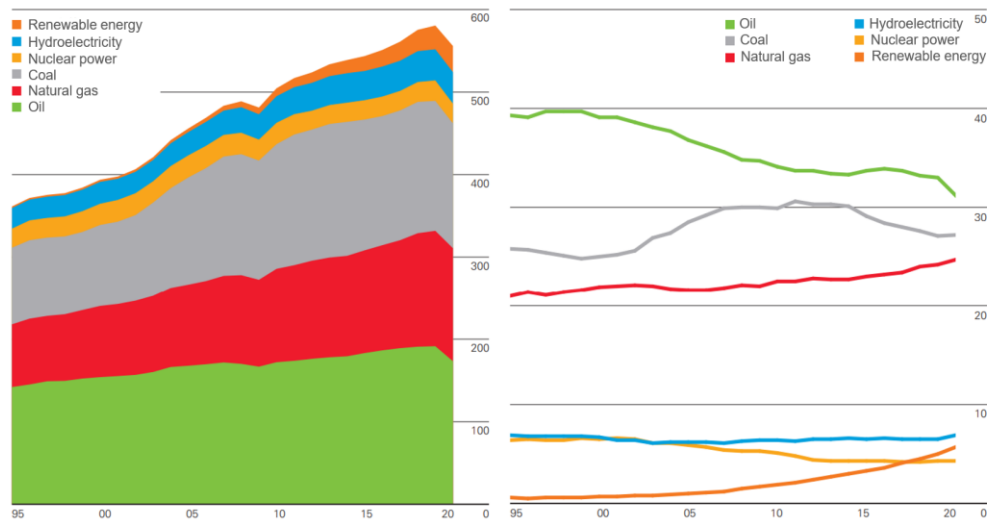
Fig. 1.1 Global energy consumption and share of primary energy consumption.

In the Global Energy Transition 2050 report by the International Renewable Energy Agency (IRENA), it is pointed out that government plans still fall far short of meeting emission reduction requirements. Under current and proposed policies, there is only a possibility of less than 70% (66%) to achieve the global target of limiting temperature rise to below 2°C [12,13]. This calls for us to increase the scale of renewable energy deployment by at least six times. This is particularly important for China, as it currently ranks only seventh among the top 10 countries in terms of the share of renewable energy in primary energy consumption (Figure 1.2), and has not yet reached the global average

for sustainable energy use [14].
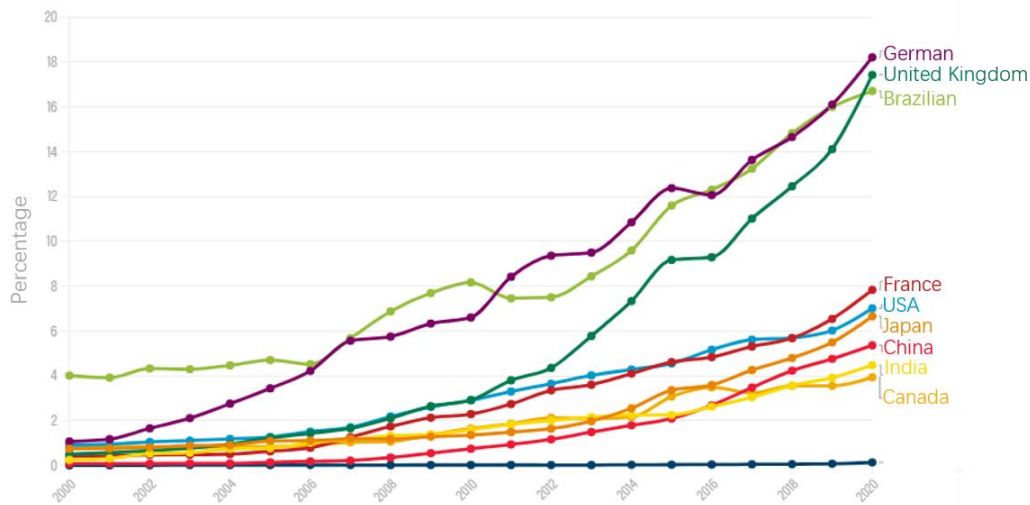
Fig. 1.2 Share of non-water renewable energy in major 10 countries all over the word.

There are two main ways to accelerate the achievement of carbon peaking and carbon neutrality: (1) using carbon offset mechanisms to reduce the total amount of carbon emissions generated. Examples include decreasing the total production, afforestation or the purchase of renewable energy vouchers; (2) increase the use of renewable energy, with the ultimate goal of using only low-carbon energy sources instead of fossil fuels, so that the amount of carbon released and absorbed back into the Earth does not increase to reach equilibrium [15]. However, due to the intermittent, random and unstable nature of renewable energy (such as wind, solar, etc.), direct integration into the grid will have many adverse effects [16,17]. As a result, renewable energy sources face difficulties in grid integration and consumption. The phenomenon of large-scale wind and light abandonment has appeared. According to statistics between 2011 and 2016, China's average annual wind abandonment rate was around 13%, which is equivalent to the energy generated by 10 million tons of standard coal (Figure 1.3). By 2018 China's renewable energy wasted due to grid integration and consumption problems still exceeded 50 billion kWh [18,19]. How to effectively solve the grid-connected consumption of renewable energy has become an important task to ensure the future energy security and development of the world.
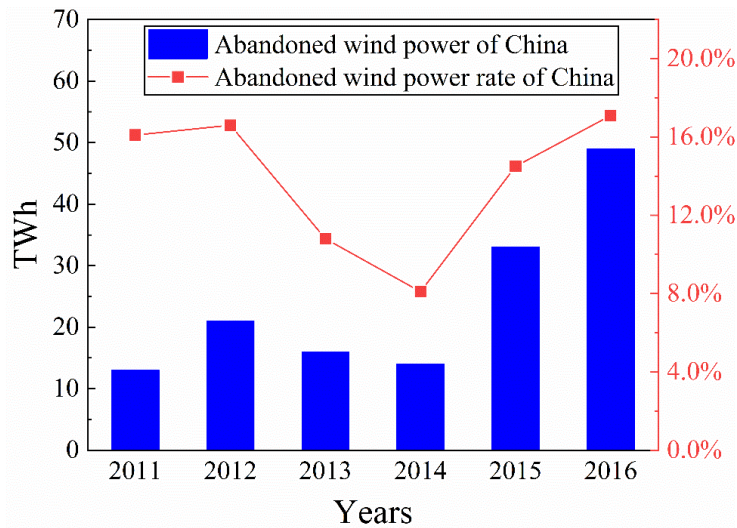
Fig. 1.3 Abandoned wind power and rate of China between 2011 and 2016.

In addition to constructing cross-regional power transmission channels and researching cross-regional renewable energy power scheduling technologies to improve the efficiency of renewable energy consumption [20-22], another effective approach is to use energy storage technology for "peak shaving and valley filling", proper to renewable energy [23-26]. This approach not only addresses the large-scale utilization of renewable energy and improves its efficiency but also gradually promotes its replacement of fossil fuels as the new primary energy source. Moreover, it enhances the peak-shifting capability of the power system, making it an indispensable technological means to facilitate the global power system's comprehensive transition towards low-carbon transformation. Therefore, it is urgent to intensify the development and accelerate the construction of electricity storage projects [27,28].

1.1.2 *Current Status of Global Energy Storage Technology Development*

Electricity storage technology refers to the electricity generated by excess or intermittent renewable energy sources in the trough of electricity consumption storage, in the peak of electricity consumption stable release, to meet a continuous and stable power supply technology [29-31]. Energy storage technology can separate power generation and power consumption in time and space in two dimensions, to make up for the power system cannot be 'storage and release' shortcomings, so that the rigid power supply system becomes more flexible. This can calm the volatility of large-scale clean energy generation access to the grid, improve the security of grid operation, economy and flexibility. Energy storage is the key to guarantee the large-scale

development of clean energy and the safe and economic operation of the power system [32].

Energy storage technologies can be divided into two main categories based on their storage methods: direct energy storage [33] and indirect energy storage[34]. Direct energy storage refers to the process of charging and discharging electrical energy directly through the conversion of magnetic and electric fields. It mainly includes superconducting magnetic energy storage [35] and supercapacitor energy storage[36]. These energy storage devices typically have short storage times, allowing for rapid energy release. While they have a relatively small storage capacity, they boast high energy utilization efficiency, making them suitable for short-duration and high-frequency energy storage. They are commonly used to control voltage fluctuations in power transmission networks, ensuring the safe operation of the electrical grid. Indirect energy storage differs from direct energy storage in that it involves converting surplus electrical energy before storing it. This category includes chemical energy storage [37,38] (such as flow batteries [39], lithium/lead batteries[40]) and mechanical energy storage[41] (like flywheels[42], compressed air[43], and pumped hydro storage[44]). Among these, lithium/lead batteries and flywheel energy storage also fall under short-duration and high-frequency energy storage. Considering the characteristics of clean energy generation, such as wind and solar power, long-duration and large-scale energy storage represented by flow batteries, compressed air energy storage, and pumped hydro storage, can leverage their long cycles and high capacity to regulate the fluctuations in renewable energy generation over extended periods. This ensures stable power supply, reduces overall electricity costs, and meets the demands of the electricity grid over longer timeframes. Table 1.1 provides an overview of the main energy storage solutions, with main characteristics and pros and cons.

Table 1.1 Efficiency, cost of generation, lifetime, advantages and disadvantages of various energy storage solutions (reference).

Categorization	Type of Energy storage	Efficiency /%	Power generation cost/$ Kwh	Life/ year	Advantages	Dis Advantages
Mechanical	Compressed Air	50-70	0.45-0.5	60	Environmentally friendly and non-	Difficulty in site selection

Energy Storage	Energy Storage				polluting, high efficiency	
	Pumped Hydro Storage	70-75	0.2-0.26	40-50	High energy storage, long duration of energy release, mature and reliable technology	Geological conditions Demanding
	Gravitational Energy Storage	＞85	0.5	30	Simple principle, low technical threshold	Low energy density. Excessive construction scale
	Flywheel Energy Storage	＞90	0.8	20	High efficiency, high instantaneous power, fast response time	Low energy density. Short release time
Electrochemical energy storage	Lithium Ion Battery	85-98	0.62-0.82	＞5000	High energy density, long cycle life, good power characteristics, fast response time	High prices. There are security risks
	Sodium-Ion Battery	＞80	0.65-0.85	＞50000	As above	As above
	Lead-Acid Battery	70-90	0.61-0.83	3000	Higher specific power, better safety, lower cost	Have a shorter lifespan. Pollution of the environment
	Vanadium Flow Battery	75-85	0.7-0.95	10000	Long battery life; power and capacity independent design; good safety	Low energy density. Low reliability

Chemical energy storage	Hydrogen Energy Storage	30-50	>1	1~2	Adequate supply, non-toxic and non-polluting	Expensive. Low efficiency
Thermal energy storage	Molten Salt Energy Storage	<60	0.9	25	High energy storage density, good stability, inexpensive and easy to obtain	Low thermal conductivity, Corrosive, with Certain safety hazards

As of 2021, the global installed capacity of energy storage has exceeded 209 GW. Among this, the United States accounts for 34%, China accounts for 24%, and Europe accounts for 22%, collectively representing over 90% of the total[45-47]. Pumped hydro storage, being the most mature energy storage technology, constitutes nearly 90% of the share. However, despite its prominence, pumped hydro storage faces strict limitations due to geographical potential constraints. It suffers from slow start-up, long construction periods, limited resource endowment, and relatively high costs. Although compressed air energy storage exhibits relatively lower efficiency, it offers significant advantages such as shorter construction periods, fewer storage site limitations, longer lifespan, environmental cleanliness without pollution, and unrestricted energy storage cycles. As a result, it is considered the primary direction for future energy storage technology development [48].

Existing compressed air energy storage (CAES) plants can be categorized into two types: the supplementary combustion CAES [49] and the non-supplementary combustion CAES [50], based on whether additional fossil energy is required. Both types of CAES utilize electrical energy to compress air into high-pressure gas for storage. The main difference lies in the release of high-pressure gas for power generation. The supplementary combustion CAES involves heating the compressed air during expansion to generate greater thrust and maintain system circulation. This process requires the burning of coal or natural gas to heat the air, which is known as "supplementary combustion," as shown in Fig 1.4. As a result, traditional supplementary combustion CAES faces technological constraints, including the reliance on fossil fuels like natural gas to provide heat, leading to lower system efficiency. Typically, the overall efficiency is only around 40% to 55%[51].
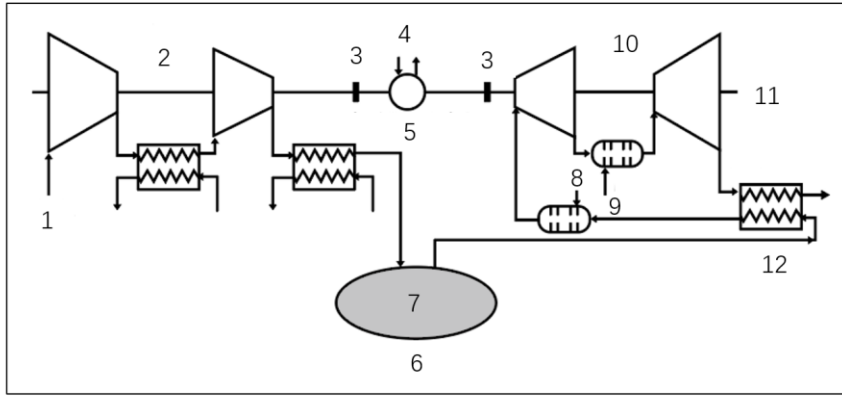
1.Air , 2.Compactors, 3.Clutches, 4. electronic, 5.electric motor/ generator, 6.Air storage
7.Compressed air, 8.Fuel, 9.Combustion chamber, 10.Turbin, 11. Exhaust gas, 12. Heat exchange

Fig. 1.4 Schematic diagram of a supplementary combustion compressed air energy storage plant.

Another type of non-supplementary combustion CAES aligns better with clean and environmentally friendly characteristics, offering promising prospects, as illustrated in Fig. 1.5. The non-supplementary combustion CAES utilizes its "internal circulation" to store the energy generated during the compression of air through heat exchange. This stored thermal energy is released during power generation, serving as a natural "propellant." The entire process involves no combustion or emissions, making it highly suitable for carbon neutrality requirements and achieving zero emissions. Moreover, it boasts higher efficiency, with electrical energy conversion rates exceeding 65% [52].
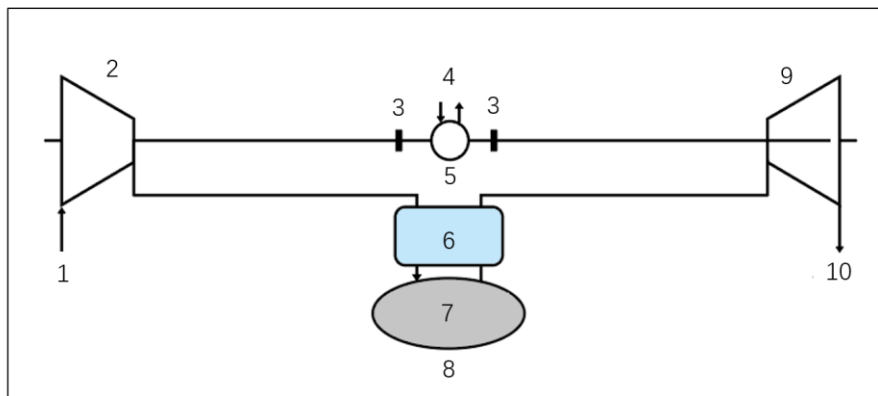
1.Air , 2.Compactors, 3.Clutches, 4. electronic, 5.electric motor/ generator, 6. Thermal storage
7.Compressed air, 8.Air storage, 9.Turbin, 10. Exhaust gas

Fig. 1.5 Schematic diagram of a non-supplementary combustion compressed air energy storage
plant.

Salt rock possesses several excellent properties, including low porosity, low

permeability, self-healing of damage, good rheological behavior, solubility in water for easy extraction, and chemical stability. Salt rock formations are also the most structurally dense and tightly sealed geological bodies in nature [53-56]. This makes the salt caverns formed after water dissolution have excellent sealing and stability, making them ideal places for storing various types of energy resources [57].

In the 1950s, the United Kingdom made its first attempt to use salt caverns for oil storage. As of 2018, the United States has established over 60 salt cavern oil storage facilities, with its strategic petroleum reserves (720 million barrels) stored entirely in salt cavities. Germany, France, Russia, Canada, and other countries have also built salt rock oil storage facilities [58-61]. In terms of natural gas storage, countries utilizing salt caverns for this purpose include the United States, Canada, Germany, France, and Italy. Currently, there are more than 70 salt cavern gas storage facilities worldwide, with a total working gas capacity exceeding 25 billion cubic meters. The United States alone has 31 salt rock gas storage facilities with a total working gas capacity of 1.78 billion cubic meters [62-64]. For compressed air energy storage, Germany built its first 290 MW salt cavern air-compressed energy storage power station in Huntorf in 1978, as shown in Fig. 1.6. It has been operating steadily for nearly 40 years [65].
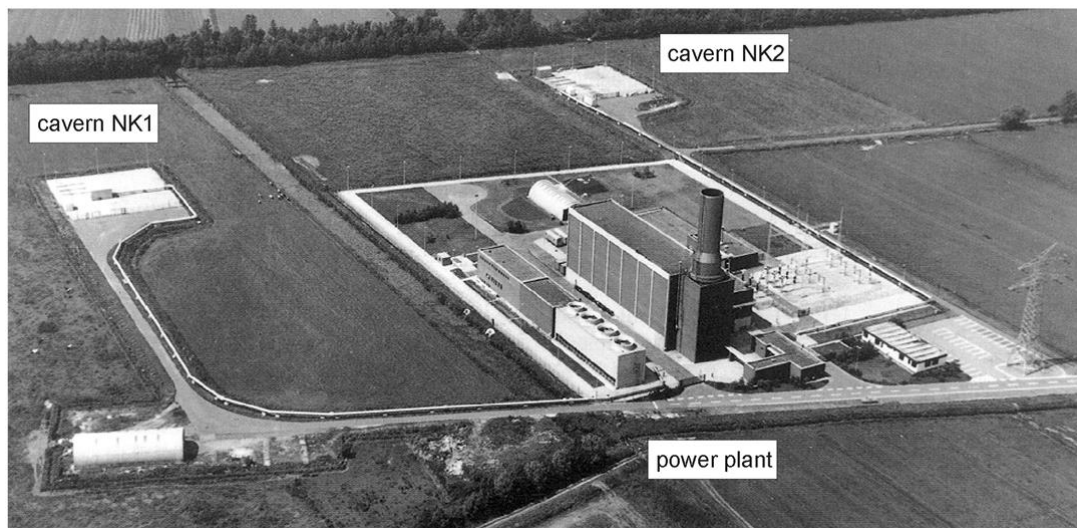
Fig. 1.6 View of the Huntorf CAES plant in Germany.

In 1991, the United States established the world's second commercial salt cavern compressed air energy storage (CAES) power station in McIntosh, Alabama, with a capacity of 110 MW[66]. China's evaluation and utilization of salt cavern storage began in the 1990s. In 2004, PetroChina started construction of China's first salt cavern gas

storage facility, the Jintan Salt Cavern Gas Storage, as part of the West-East Gas Pipeline project. Currently, three storage facilities have been completed, with a commercial gas supply capacity of 600 million cubic meters. During the 13th Five-Year Plan period, China also planned multiple salt cavern gas storage facilities in Jintan, Huaian, Pingdingshan, Yunying, and Zhangshu, with a total working gas capacity exceeding 8 billion cubic meters once completed. In terms of salt cavern oil storage, China has conducted extensive preliminary research, forming pre-feasibility reports, and has currently planned six salt cavern oil storage facilities [67-69]. China's first salt cavern CAES power station, the Jintan Salt Cavern Compressed Air Energy Storage National Pilot Demonstration Project, began construction in 2017 and successfully connected to the grid for power generation on September 30, 2021[70]. The initial phase of the power station has a generating capacity of 60 MW and a storage capacity of 300 MW/h, with a future planned capacity of 1000 MW.

France is also one of the earliest countries to establish energy reserves [71,72]. With extensive experience in the construction, use, and management of salt caverns, it stands out with its diverse range of stored products, including not only crude oil but also various refined petroleum products. This valuable experience can provide substantial support for global strategic underground energy storage in salt caverns. France has completed over 10 operational salt cavern storage facilities, as shown in Fig. 1.7, accounting for 40% of the country's national strategic reserves. The strategic petroleum reserves in France include crude oil, gasoline for vehicles, aviation kerosene, diesel, household fuel, lighting kerosene, jet engine fuel, heavy oil, liquefied petroleum gas, and more. Notably, the Lisieux region stores 1.2 million cubic meters of refined petroleum products, the Marolles region stores 14 million cubic meters of light oil, the Noeux-les-Mines region stores 3 million cubic meters of refined petroleum products, and the Etrez region stores 120,000 cubic meters of refined petroleum products, among others. France's first salt cavern gas storage facility was established in Tersanne in 1968. Subsequently, Etrez, Manosque, and Hauteriver salt cavern gas storage facilities were also built, with a total gas storage capacity of 3 billion cubic meters and a working gas capacity of 1.155 billion cubic meters.
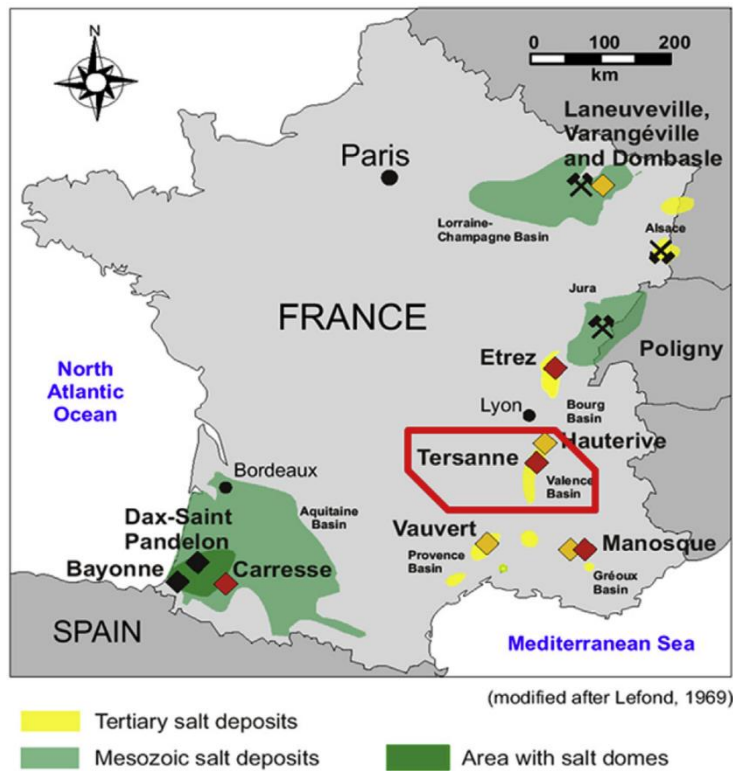
Fig. 1.7 Distribution map of salt mines in France=.

In conclusion, the construction of compressed air energy storage (CAES) power stations using salt caverns offers multiple advantages. It not only enhances the efficiency of clean energy utilization, facilitates peak shaving and load balancing to address the supply-demand disparity in the power grid but also enables the resourceful utilization of abandoned salt mine cavities, meeting the requirements for sustainable green mining development. Furthermore, it contributes to achieving global goals of carbon peaking and carbon neutrality. One of the key factors in ensuring the stable operation of salt cavern CAES power stations is to guarantee the long-term stability of the salt caverns that store high-pressure air [73].

1.1.3 Significance of the study of creep and fatigue mechanical properties of salt rocks

Salt caverns are subjected to very different stress states in the surrounding rock of the cavity due to their different uses. When used as storage for wastes such as alkali slag and nuclear waste, there is little need to consider the effect of pumping on the stress fluctuations in the surrounding rock of salt cavern reservoirs [74-76]. Considering the chemical corrosion properties of alkali slag and the continuous exothermic properties of nuclear waste, more research efforts have been focused on the mechanical properties

of salt rocks subjected to chemical-stress coupling (e.g., alkali slag) [77,78] and temperature-stress coupling (e.g., nuclear waste) [79-81]. When used to store oil and natural gas, the salt cavern storage enclosure is more subjected to the creep action of constant stress as the peaking cycle may often be measured in quarters or even years [82,83]. However, CAES operate differently from all of the above, operating more frequently, even peaking as often as twice a day. Frequent gas injection and exhaust of CAES leads to the salt cavern storage surrounding rock under cyclic loading, which is prone to fatigue. Figure 1.8 shows a typical pressure change cycle of the salt cavern of the Huntorf CAES plant in Germany, and one cycle is about several hours or one day [84].
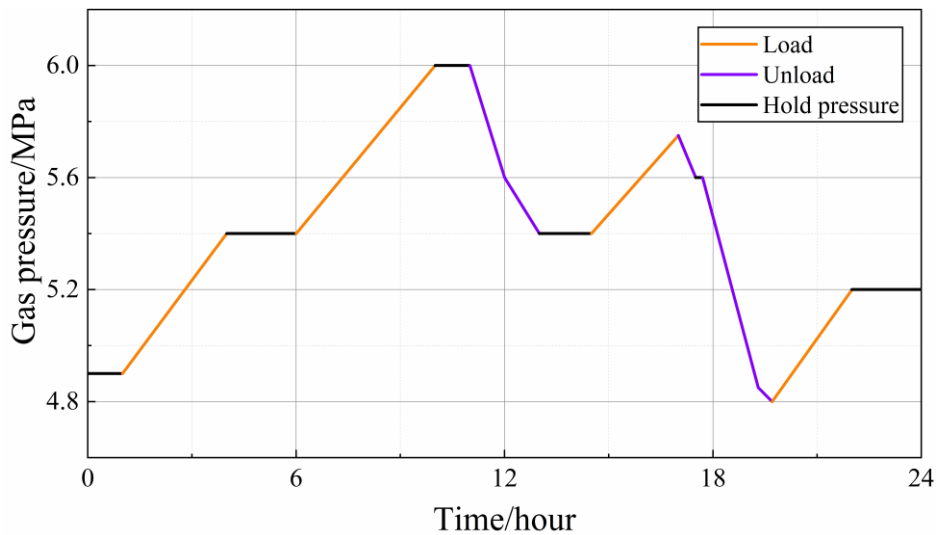
Fig. 1.8 Schematic diagram of the operating gas pressure of the Huntorf CAES plant within 24 hours.

Simultaneously, during the charging and discharging process, due to the need for load balancing, the salt rock remains in a constant pressure state for a certain period. Additionally, salt rock exhibits good rheological properties, leading to continuous creep deformation during the constant loading period. Consequently, during the operation of a compressed air energy storage (CAES) salt cavern, the surrounding rock is subjected to a dual effect of creep and fatigue. Both creep and fatigue induce irreversible deformation (plastic deformation) [85,86]. Under the alternating effects of creep and fatigue, the surrounding rock of the salt cavern undergoes processes such as dislocation slip, cumulative damage, and crack propagation, affecting the stability of the salt cavern and potentially leading to instability and failure.

Therefore, studying the interaction between creep and fatigue in salt rock, revealing the evolutionary behavior of creep and fatigue damage, and establishing a constitutive model for creep and fatigue in salt rock are of paramount importance. Investigating the damage, failure, and instability behavior of the CAES salt cavern under different working load conditions can provide scientific recommendations for the global construction of compressed air energy storage power stations utilizing salt caverns. Moreover, this research is of significant reference and guidance for optimizing the operational schemes and improving the economic efficiency of compressed air energy storage power stations.

1.2 State-of-the-art

Underground salt deposits can be mined by water-soluble mining (e.g., oil cushioning and air cushioning) to form large closed cavities. The extremely low permeability and good rheology of salt rocks are the basis for their ability to serve as underground reservoirs for energy. Numerous studies have been carried out on the stability of salt caverns for the storage of oil and gas [87]. This has laid a good foundation for us to study the mechanical properties of the surrounding rock of salt cavern CAES, but considering the special characteristics of the operation mode of CAES plants, which have more frequent peak shifting and a certain length of stabilization period, the fatigue properties of salt rock under cyclic loading, especially the creep-fatigue mechanical properties, are more worthy of our attention. Due to the needs of mining, construction and other industries, researchers have conducted a lot of tests and studies on the fatigue and creep mechanical properties of rocks under cyclic and constant loads [88-92], and achieved good research results. This provides a reference for our further research on the creep-fatigue properties of salt rocks.

1.2.1 *Fatigue mechanical properties of rocks under cyclic loading*

In various geological processes and rock engineering constructions, rocks are often subjected to cyclic loading. For example, geological tectonic processes may lead to crustal deformations influenced by solid tidal forces [93], cyclic seismic impacts forming rock bedding planes [94], and cyclic loading from overlying strata in underground coal mining causing roof subsidence [95]. Due to the cyclic loading, rocks experience fatigue damage, which can significantly impact the stability of underground engineering

projects. Therefore, understanding the deformation and failure mechanisms, as well as constitutive models, of rocks under cyclic loading is crucial for accurately assessing the long-term stability of underground rock structures. Researchers studying the fatigue mechanics of rocks have primarily focused on the following aspects:

The deterioration of the mechanical properties of rocks under cyclic loading is referred to as rock fatigue, and the maximum stress level that rocks can withstand without failure under infinite cycles is called rock fatigue strength [96]. The number of cycles causing rock failure under specific loading conditions is known as rock fatigue life. In rock fatigue mechanical testing, researchers mainly study the fatigue characteristics of rocks under different loading conditions such as frequency, waveform, and amplitude, as well as the stress states such as uniaxial, triaxial, tension, compression, and shear, and the environments including dry-wet cycling and freeze-thaw cycling.

Ge et al [97], concluded that the fatigue deformation of rocks is mainly divided into three stages, namely the initial stage, the isotropic stage and the accelerated stage, and found that the upper limit stress ratio and amplitude are the main factors affecting the fatigue life of rocks by varying the stress ratio cyclic loading and unloading experiments. Guo et al [98], carried out uniaxial cyclic loading and unloading fatigue experiments on salt rock and found that the axial strain, deformation modulus and fatigue damage process of salt rock can be divided into the same three stages. Ma et al[99], studied the denaturation, strength and damage characteristics of salt rock under cyclic unloading in triaxial state through different loading waveform parameters and different peripheral pressure experiments of salt rock, and inferred that the upper threshold of deformation damage of salt rock in triaxial cyclic unloading is 80%~89%. Zhao et al [100], carried out dry and wet cyclic tests on mudstone from Sifenshan, Chongqing, and found that dry and wet cycling damaged the pore structure of the mudstone, increased the porosity. With the increase of porosity, the uniaxial compressive strength of the mudstone decreased, and an exponential function between the uniaxial compressive strength and the number of cycles was established. It was also found that the compressive strength of mudstone was related to the number of wet and dry cycles and the initial porosity. Zhu et al [101], used acoustic emission to study the fatigue characteristics of gypsum plagioclase under cyclic loading, and pointed out that the stress level of cyclic loading has a large influence on the fatigue characteristics. Wang et al [102], investigated the elastic modulus law of fractured sandstone under cyclic loading by using a combination of laboratory tests and numerical simulation, and obtained that the elastic modulus of

most specimens showed the phenomenon of strengthening with the cyclic loading cycles increase. Lu et al [103], investigated the effect of circumferential pressure on the fatigue characteristics of yellow sandstone, and proposed that the deformation is more suitable than the strength as a criterion for rock damage in the fatigue damage process. Han et al [104], investigated the creep model of salt rock under cyclic loading, proposed a deformation factor based on the test results, and modified the Burgess creep model. Fan et al [105,106], carried out a study on the fatigue characteristics of salt rock under discontinuous loads, and found that interval fatigue accelerated the damage accumulation and the fatigue characteristics of the salt rock under discontinuous loads. They found that interval fatigue accelerates damage accumulation and shortens the fatigue life of salt rocks, Jiang et al [107], analyzed the Bauschinger effect and residual stresses as the main causes of this phenomenon from the theoretical point of view. Chen et al [108], studied the stress state and volume change rule of salt cavity under different gas extraction rates by numerical simulation. Zhou et al [109], found through the salt rock permeability experiment and Computed Tomography (CT) scanning that the permeability of salt rock changes greatly under the action of seepage and peripheral pressure, and it is consistent with the change of porosity.

In terms of fatigue damage models describing the nonlinear mechanical properties of rocks under cyclic loading, researchers have mainly proposed the following types of constitutive models: classical elastic-plastic constitutive models, constitutive models based on internal variables and fatigue damage models based on energy dissipation [110,111].

By comparing the generalized Kelvin-Voigt creep constitutive model under low-frequency cyclic/static loading, Huang et al [112], found that the trends of the two models over time are consistent. The deceleration and stabilization phases of the cyclic loading model are smaller than those of the static loading under the condition of equal upper limit stresses. Drawing on the theory of rock creep, Guo et al[113],. Defined three fatigue constitutive model elements of elasticity, viscosity, and plasticity, gave the accelerated fatigue parameter n, and established a nonlinear viscoelastic-plastic fatigue constitutive model considering the decelerating, stabilizing, and accelerating phases. The fatigue acceleration parameter n was found to be inversely related to the uniaxial compressive strength of the rock. Cerfontaine et al [114], proposed an intrinsic model suitable for describing the fatigue damage of brittle rocks based on the theory of cumulative plastic strain and the assumption of reducing the cohesion of the rock material by cyclic

loading. And the model was validated using three kinds of rocks: marble, sandstone and granite. The results show that the model can reproduce the change trend of fatigue test and can effectively predict the fatigue life. Zhang et al [115], investigated the microstructural changes of salt rock under cyclic loading, and pointed out that the fracture extension inside the salt rock was mainly dominated by inter-crystal fractures, and the number of fractures was positively correlated with the upper limit stress, and the macro porosity inside the salt rock showed a trend of increase in the total porosity with the development of fatigue test. An empirical fatigue model was obtained by solving the S-shaped inverse function and verified. Yang et al [116], investigated the strength change and fatigue deformation characteristics of coal rock under cyclic loading, and the results showed that the stress threshold for fatigue damage occurred in coal rock was lower compared with hard rock. The damage of coal rock can be predicted based on the change of unloaded elastic modulus of radial deformation of coal rock, and the development of coal rock damage variables with cyclic loading was fitted according to the theory of continuum damage mechanics. Dai et al [117], based on the assumption of Lemaitre's strain equivalence, combined with Weibull's statistical damage model of microscopic defects and the fracture mechanics model of macroscopic joints, described the deformation of jointed rock under cyclic loading and the degradation behavior of strength properties of nodular rock under cyclic loading. An intrinsic fatigue damage model based on residual strain is also proposed. By defining new fatigue damage variables, Li et al [118], based on the high circumferential fatigue damage model, the hardening parameter, which has a power law relationship with the stress amplitude and the number of cycles, was introduced to derive the evolution equation of low circumferential fatigue damage in rocks, and the model was verified using the measured fatigue data of sandstone. The model is found to be able to fit the evolution curve of the low-cycle fatigue damage of rocks better.

The aforementioned research on the fatigue mechanics and damage evolution of rocks has laid the groundwork for further accurately assessing the stability of the surrounding rock of salt cavern storage under gas injection and production conditions.

1.2.2 *Creep mechanical properties of rocks under constant loads*

The deformation of rock under constant load increases with time, called creep, is one of the most important characteristics of rock [119]. In the process of underground

geotechnical engineering, especially deep geotechnical engineering, construction and operation, the deformation of surrounding rock due to creep and the destabilization of the structure is one of the main reasons affecting the safety of underground engineering, and the study of the creep mechanical properties of rock is of great significance to ensure the long-term stability of underground building structures. Since the 1920s, researchers have carried out a large number of creep tests different conditions, summarized in many creep deformation laws [120-124].

Li et al [125], carried out long-time graded creep tests on serpentine marble and found that the steady-state creep rate and creep strain showed an increasing trend with the increase of stress level and time. By comparing the inflection points of isochronous stress-strain curves, the long-term creep strength of serpentine marble was determined to be around 35 MPa. Hu et al [126], simulated the uniaxial creep mechanical properties of non-homogeneous granite by using PFC^{2D} particle flow numerical simulation software, by setting different grain diameters, and combining the equivalent crystalline model and stress corrosion model. The results show that the homogeneity of the rock shows a positive correlation with the uniaxial compressive strength and long-term creep strength, and the non-homogeneous factor shows a negative correlation with the damage time of creep failure under a given stress level, and the microstructure of the rock controls the damage form of rock creep. Zhou et al [127], studied the creep deformation law of gas coal under high-temperature triaxial stress, pointing out that when the temperature is low (200°C), during the 100-hour creep experiment, the gas coal only shows the two-stage characteristics of creep. While at higher temperature (400°C), the gas coal entered the accelerated creep stage after only 6 hours. It is confirmed that the increase of temperature determines the creep process of gas-coal, and combined with the change rule of porosity, it is judged that 300°C is the critical temperature at which the creep state of gas-coal is changed. Zhang et al [128], gave the creep damage characteristics of mudstone subjected to dynamic/static load, and found that the larger the axial static load, the greater the influence of disturbance amplitude and frequency on the creep damage of mudstone, and the creep time is negatively correlated with the amplitude and frequency. The addition of dynamic loading led to a decrease in the strength of the particles within the rock, weakened the bonding effect between particles, and accelerated the expansion of intergranular and intragranular cracks. Zafar et al [129], used Barre granite containing double defects to investigate the creep and relaxation experiments of brittle rocks at multiple stress levels, and the results

showed that when the stress level exceeded the crack damage threshold, the failure time of the creep is much smaller than that of the loosely failure time. Creep produces higher cumulative acoustic emission events and event rates than relaxation. The *b*-value of AE derived by the maximum likelihood method can be used as a precursor to macroscopic damage in rock specimens. The above studies are an important contribution to the understanding of the creep properties of rocks, but are mainly aimed at brittle rocks with high hardness.

Salt rock, as a typical soft rock, has strong rheological properties and can produce large deformation at low stress [130]. Researchers have also carried out a large number of salt-rock creep tests. Yang et al [131], used digital image correlation (DIC) to study the microstructural changes and damage evolution in the creep process of salt-rock. Ma et al [132], investigated the effect of gypsum content on the creep rate of salt-gypsum strata, and found that the steady-state creep rate of high gypsum salt-rock strata was lower than that of high salt-salt-salt-rock strata under the same temperature and stress conditions. Lance et al [133], investigated the effect of cyclic loading and unloading on the spreading characteristics and creep response of the salt rock of Avery Island, U.S.A., and found that cyclic loading and unloading did not have much impact on the creep. Li et al [134], investigated the effect of temperature on the creep damage evolution process of salt rocks using the discrete element method. Luangthip et al [135], investigated the content of carnallite in the Maha Sarakham salt rock, Thailand, and its correlation with creep properties. Hamami et al [136], investigated the strain hardening properties of the salt rock during the creep process by using triaxial multi-stage creep tests.

Establishing a model that can accurately predict the long-term creep of rock has been key to evaluate whether the underground geotechnical engineering can operate stably for a long time. Existing rock creep models are mainly categorized into the following three types: (1) creep empirical models [137], (2) component combination models [138], (3) fracture damage models [139].

Empirical rock creep models are fitted based on measured data from rock creep tests to construct correlation functions of stress, strain and time. Common types of functions for empirical modeling of creep include power law, logarithmic, exponential, and hybrid equations of the three. The empirical equation for rock creep can generally be expressed in the following three-stage form,

$$\varepsilon(t) = \varepsilon_e + \varepsilon_1(t) + Vt + \varepsilon_3(t) \tag{1.1}$$

where $\varepsilon(t)$ is the total creep strain, ε_e is the instantaneous elastic strain produced by the instantaneous loading of stress, $\varepsilon_1(t)$ is the creep strain in the decelerated creep stage, Vt is the creep strain in the stable deformation stage, where V is the steady-state creep rate, and $\varepsilon_3(t)$ is the creep strain in the accelerated creep stage. For different rocks or different experimental conditions, the corresponding empirical creep model can be obtained directly by fitting experimental data. Wu et al [140], found that the creep of coal rock conforms to the logarithmic empirical formula by studying the creep test of coal rock, and obtained the parameters of the empirical formula for the creep of coal rock under different stress conditions. Ding et al [141], established the creep equation of soft and weak interlayer by studying the creep characteristics of soft and weak interlayer in open slope. Zhang et al [142], carried out triaxial creep test on mudstone, and obtained the nonlinear creep equation of mudstone through the creep empirical model. The model is easy to understand, has high fitting accuracy, and can guide the relative rock engineering. However, the empirical model can only reflect the deformation law of rock creep under loading paths corresponding to the test conditions. Taking the deceleration creep as an example, the typical deceleration creep equation is

$$\varepsilon_1(t) = At^n, 0 < n < 1 \tag{1.2}$$

$$\varepsilon_1(t) = A \ln t \tag{1.3}$$

$$\varepsilon_1(t) = A \ln(1 + at) \tag{1.4}$$

$$\varepsilon_1(t) = A[(1 + at)^n - 1] \tag{1.5}$$

Where A, n and a are constants with appropriate dimensions. These functions can usually fit the strain data in some limited time period, but not in the entire test time, and the physical significance of the parameters in the model is usually not clear. It is therefore difficult to reflect the intrinsic mechanism of the rock creep damage, and cannot be promoted and applied in other geotechnical engineering, adaptability is poor.

Element combination model is the elastic unit (Hooker's body), viscous unit (Newton's body), plastic unit (St. Vernand's body) through the series-parallel combination of creep model. Currently more common element combination model is given by Maxwell model,

$$\varepsilon = \left(\frac{\sigma_o}{k}\right) + \left(\frac{\sigma_o t}{\eta}\right) \tag{1.6}$$

Or Kelvin model

$$\varepsilon = \left(\sigma_o / k\right)\left[1 - e^{-kt/\eta}\right] \tag{1.7}$$

where k is the stiffness factor, η is the viscosity factor, and σ_o is the instantaneous loading stress.

Models such as Burgers, viscoplastic and Nishihara: some generalized creep models consisting of several identical models in series or parallel (e.g., generalized Maxwell model and generalized Kelvin model) are also used when needed. Classical component combination models are widely used in the mechanical analysis of rock underground engineering due to the clear physical meaning of their parameters and the ability to visually characterize the complex mechanical properties of rocks [143-146]. Compared with the empirical model, the unit combination model can more accurately respond to the elastic, viscous and plastic characteristics of rock-like materials. Moreover, the combination can be closer to the actual situation of rock creep by adjusting the number of units. Researchers have carried out a lot of research. Jiang et al [147], by connecting the strain-triggered inertial element in series with the classical Nishihara model, proposed an extended Nishihara model, which can fit the triaxial creep test curve of sandstone very well. The results show that the smaller the value of inertia mass, the faster the axial strain increases in the creep acceleration stage, the shorter the time to failure, and the failure time of sandstone creep is highly dependent on the applied stress level. Li et al [148], with the help of the Burgers creep model, through the introduction of fractional-order Abel viscous unit and aging factor, established a new three-dimensional creep model that can respond to the deformation of soft rock under the water-rock interaction with time, and achieved good results. A new three-dimensional creep model was developed by introducing a fractional order Abel viscous unit and a time-dependent factor that can reflect the deformation of soft rock with time under water-rock interaction, and good fitting results were achieved as well. A viscoplastic model that reproduces the creep behavior and inelastic deformation of rock during the loading-unloading cycle was developed by Haghighat et al [149], Maximization of dissipated energy during plastic flow using Perzyna type of viscous deformation was combined with an improved Cam-clay plastic deformation model. This plastic flow

model is of the correlation type, where the viscous deformation is proportional to the ratio of the driving stress to the material viscosity. However, in the models, the constitutive parameters of the unit cells, such as elastic modulus, viscosity coefficient, and yield strength, are often treated as constants. Even with the presence of time variables, deformation remains linear under given time conditions. As a result, it can only reflect the linear changes in the rock creep process. However, most rocks in the natural environment are heterogeneous materials, and their changes are not linear. Especially in the accelerated creep stage, the nonlinear characteristics of rocks become more pronounced, leading to poor consistency between the theoretical curves of traditional component combination models and experimental data [150-152]. In order to reflect the nonlinear relationship between stress and strain in the creep process, many scholars began to study the nonlinear creep model of rocks, and new creep models were proposed by considering the creep parameters of rocks as time-dependent variables. Hou et al[153]. proposed a four-component model reflecting the creep behaviors of rocks with different initial damage value on the basis of the results of the creep tests of sandstones. Cheng et al [154], considered the viscoelastic-plastic characteristics and damage evolution of rocks. Building upon the improved Nishihara model, they proposed a nonlinear rock creep model that incorporates damage evolution to predict rock creep behavior. This model introduces damping elements and nonlinear viscoplastic bodies into the classical Nishihara model to simulate the accelerated creep stage of soft rocks. Zhou et al [155], proposed a fractional-order creep model for salt rock by replacing the viscous unit in the Nishihara model with a variable-order Abel damper based on the theory of damage mechanics of continuous media and the theory of fractional-order derivatives. Wang et al [156], considered the strength and elastic modulus of the rock as a function of the creep time, and proposed a nonlinear, non-smooth, plastic-viscous eigen-model to reflect the nonlinear creep behavior.

In recent years, with the continuous development of rock damage mechanics and fracture mechanics, many scholars try to introduce new theories of damage mechanics and fracture mechanics to establish a rock creep model based on fracture damage theory [157,158]. Zhou et al [159], proposed a nonlinear creep model considering damage on the

basis of improved Nishihara model, Chen et al [160], based on the relationship between damage mechanics and elastic modulus, established an intrinsic model of damage creep that accurately reflects the creep characteristics of rock under acid corrosion and true triaxial stress, and found that the model not only accurately describes the creep properties of rock in the transient elastic strain stage and isokinetic creep stage, but also describe the nonlinear characteristics of the creep curves in the decay creep stage and accelerated creep stage. Hoxhaet al [161], analyzed the effect of relative humidity on the creep of gypsum, and introduced damage variables to establish a damage model for gypsum creep, which better describes the accelerated creep stage.

By applying damage theory to establish damage models, it is possible to provide a more comprehensive reflection of the creep and damage behavior of rocks. In the analysis of rock creep, rock damage can lead to inelastic flow and creep. Damage theory can be applied to stage-wise damage accumulation, ultimately leading to accelerated creep failure. Fracture mechanics is a discipline that studies material crack strength and crack propagation. Due to the discontinuity and heterogeneity of rocks, using fracture mechanics methods to study the rheological mechanisms of rocks is of significant importance. The fracture creep models of rocks have also been extensively studied and have achieved numerous achievements [162,163].

1.2.3 *Advancements in Rock Creep-Fatigue Mechanics Research*

The research on rock creep and fatigue, as described above, has played a crucial role in accurately assessing the damage evolution of the surrounding rock in salt caverns used for compressed air energy storage (CAES) power plants. However, considering the actual operational mode of CAES power plants during gas injection and withdrawal cycles, as shown in Figure 1.9, there are time intervals where the surrounding rock is subjected to creep-fatigue alternating actions. Therefore, studying the interaction between rock creep and fatigue, and establishing a creep-fatigue constitutive model for rock under loading and unloading, can provide a more precise evaluation of the stability of the salt caverns used as storage reservoirs. This research holds significant importance in ensuring the safe operation of compressed air energy storage power plants [164].

The concept of creep-fatigue interaction was originally proposed by researchers studying the fatigue mechanics of metals at high temperatures. It was found that metals used at high temperatures often experience an interaction between creep and fatigue

under low-frequency cyclic loading conditions, leading to premature failure compared to the theoretically calculated fatigue life. In recent years, several researchers have investigated the mechanical properties of various alloys under the interaction of fatigue and creep-fatigue. Their studies have indicated that stress levels, dwell times, temperature variations, and test environments directly influence the effects of the interaction between fatigue and creep in metals [165-170]. For instance, Asada et al [171], developed a model based on damage mechanics to describe the creep-fatigue interaction behavior of 9Cr-1Mo-V-Nb steel under constant dwell time conditions. They pointed out that fatigue and creep are comprised of component damage during each cycle, and are given by the product of the number and size of components. The creep-fatigue interaction behavior is considered to be caused by the early growth of creep component damage size due to fatigue loading during each cycle, resulting in early failure. Wang et al [172], systematically studied the creep-fatigue interaction behavior of a nickel-based single crystal superalloy under various strain (tensile) dwell conditions at 900 °C using an in-situ SEM platform. They found that the initial cyclic life rapidly decreases with increasing dwell time, followed by a slight increase in cyclic life for dwell times exceeding 60 seconds. This phenomenon was attributed to the accumulation of non-elastic strains under different dwell conditions. Non-elastic strain accumulates more under dwell fatigue conditions than pure fatigue loading, and increases with dwell time. However, after a dwell time of 60 seconds, it decreases again due to the formation of a more stable network structure at longer dwell times. Goyal et al [173], developed a model to represent the creep-fatigue damage mechanism resulting from the combined effects of fatigue, creep, oxidation, and corrosion, which depends on various loading conditions. They pointed out that under creep and oxidation conditions, cracks mainly propagate along grain boundaries starting from the notch surface, while under fatigue-oxidation conditions, cracks propagate trans granularly. Numerous studies have indicated that as stress dwell time and level increase, the fatigue life of materials significantly decreases, demonstrating the significant interaction between creep and fatigue. Therefore, it is necessary to study the mechanical properties of other materials under creep-fatigue loading conditions.

As some materials will often be affected by creep-fatigue loading, some researchers have also carried out experimental studies on the mechanical properties of these materials under creep-fatigue interaction, Zhu et al [174], studied the fatigue damage characteristics of asphalt mixtures under cyclic loading, and proposed a

damage evolution equation for asphalt considering the creep-fatigue damage effect. The study shows that the fatigue damage of asphalt materials is due to the joint damage effect of creep and fatigue. Qi et al [175], analyzed the creep mechanical properties of saturated soft clay under cyclic loading, established an empirical equation of cumulative plastic strain that can be applied in practical engineering and imported into Abaqus finite element numerical simulation software for secondary development. It was found that the deformation of saturated soft clay increased greatly after considering the creep effect. Zhou et al [176], carried out the creep fatigue test of plastic wood composite flooring, and the study showed that the strain curve of creep-fatigue of plastic wood flooring is similar to the pure creep curve, which is divided into three stages. With the increase of creep load percentage, the life of plastic wood flooring decreases, creep, fatigue interaction will reduce the strength of plastic wood flooring. Sain et al [177], investigated the fatigue creep behavior of thermoplastic wood fiber composites, both unmodified and functionally modified. For PVC, PE, and PP-based composite materials, creep is largely influenced by the load level, time, and temperature. Slight elevations in temperature above ambient conditions significantly enhance creep in PVC-wood fiber composites.

In the field of rocks, researchers also found that fatigue and creep are similar in time dimension, that is, the deformation curve can be divided into three stages: decelerated deformation-steady deformation-accelerated deformation [178], and the creep eigen-structure model can also be used to describe the damage evolution process of fatigue in rocks. Wang et al [179], investigated the mechanical properties of the creep of salt rock under the action of long-term cyclic loading, and pointed out that the upper limit of the stress determined the development trend of the stress-strain curve of the salt rock. It is pointed out that the upper stress limit determines the development trend of the stress-strain curve of salt rock, and the average maximum creep rate in the stable creep stage decreases with the increase of the cycle and increases with the increase of the upper stress limit. Based on Kachanov creep damage theory, Miao et al [180], established a fatigue rheological damage model of rock under cyclic loading by combining with Burgers model. By substituting the sinusoidal stress function into the constant stress in the rheological differential eigenstructure equation, the one-dimensional and three-dimensional differential-type damage eigenstructure equations of rocks under cyclic loading were derived. The model can accurately describe the fatigue rheological damage development trend of siltstone under cyclic loading. Xu et al [181], modified the

Poyhting-Thomson rheological fatigue model according to the real fatigue process under cyclic loading of salt rock, using the time-dependent power function to describe the strain increment caused by fatigue damage, and the results showed that the model can better describe the strain time curve of salt rock. Through the above studies, it can be found that researchers tend to transform the time function of creep into a function related to the number of load actions to characterize the damage of the material, for rocky materials, especially salt rock, scholars have investigated the creep properties of salt rock under cyclic loading, which is regarded as a function related to time. However, the above-mentioned studies mainly involve deriving constitutive equations and fitting data to illustrate the interaction between creep and fatigue. There are relatively few experiments that directly demonstrate the mutual influence between creep and fatigue in rocks [182,183]. For the rock low-stress creep-fatigue test, researchers have conducted some studies, Cui et al [184], studied the interval fatigue characteristics of salt rock under uniaxial conditions using acoustic emission, and found that the time interval accelerates the accumulation of damage in salt rock, and this phenomenon becomes more pronounced with longer time intervals. Jiang et al [185], investigated the interval fatigue characteristics of concrete and proposed that residual stresses generated from non-coherent deformation in concrete can promote the damage of concrete specimens during the interval duration. In comparison, high-stress creep-fatigue tests on rocks are rarely reported, with only a few studies focused on sandstone, salt rock, and other rock types. Wang et al [186], conducted creep-fatigue loading tests on prefabricated angle-cracked sandstone and found that after creep loading, the deformation modulus and secant modulus of the sandstone significantly decreased, increasing the energy dissipation of the rock and accelerating sample damage. Shi et al [187], used acoustic emission to study the influence of creep on the fatigue mechanics of red sandstone specimens with prefabricated cracks under different stress levels. They found that applying short-term, low-stress creep loads can reduce the increase of fatigue deformation parameters, slow down the decay of elastic parameters, and delay the occurrence of Felicity effect (The Felicity effect in Physics, is an effect observed during acoustic emission in a structure undergoing repeated mechanical loading.) in the rock mass, with a slower Felicity decay. Ma et al [188], investigated the creep-fatigue mechanics of salt rock under acoustic emission monitoring and found that under the combined action of creep and fatigue loads, the cyclic life of salt rock significantly decreased compared to what is observed in pure fatigue or pure creep tests, indicating a clear interaction between fatigue damage

accumulation and creep damage accumulation. With the increase of creep loading time, the creep life of salt rock showed a linear increase, while the fatigue life exhibited an exponential decrease. Some researchers also used equipment such as computer tomography (CT) and low-field nuclear magnetic resonance (NMR) to study the internal micro-damage evolution of rocks under creep-fatigue loading [189]. The above-mentioned research on material creep-fatigue mechanics can provide references for analyzing the creep-fatigue mechanics characteristics of salt rock.

1.3 Research Content

Against the backdrop of carbon peak and carbon neutrality, global sustainable energy development has ushered in new opportunities. This paper takes the construction and operation of salt cavern compressed air energy storage (CAES) power plants as the background and considers the unique peaking demand of salt cavern CAES power plants. The surrounding rock of salt cavern storage will be subjected to the dual effects of creep and fatigue. Through laboratory experiments, theoretical analysis, and model studies, we designed creep tests under different stress levels for salt rock, creep-fatigue tests with different high-stress interval times, creep-fatigue tests under different confining pressures, and long-term creep-fatigue tests. With the help of observation equipment such as acoustic emission, we analyzed in detail the macroscopic crack distribution and microscopic damage evolution of salt rock under creep-fatigue alternation and established a salt rock creep-fatigue mechanical constitutive model that considers the interaction between creep and fatigue. The specific research contents are as follows:

(1) Creep-fatigue mechanical characterization of salt rock under unidirectional stresses

Uniaxial creep-fatigue tests of salt rock with different high stress plateaus were carried out to analyze the damage evolution of salt rock creep-fatigue under different high stress intervals, and to explain the effect of salt rock creep-fatigue interaction on the residual strain and creep strain of salt rock from a microscopic point of view.

(2) Creep-fatigue mechanical characterization of salt rock under three-way stresses

The triaxial creep-fatigue test of salt rock under different peripheral pressures was carried out to study the influence of different peripheral pressures on the creep-fatigue

stress-strain curves of salt rock, analyze the influence of peripheral pressure densification effect on the creep-fatigue interactions of salt rock, and reveal the influence of the construction depth of the pressurized-gas storage plant on the peripheral rock of the salt cavern storage.

(3) Multilevel amplitude creep-fatigue mechanical characterization of salt rock under acoustic emission monitoring

Uniaxial/triaxial creep-fatigue tests of salt rock under different stress levels were carried out to study the effects of different stress levels on the creep-fatigue mechanical properties of salt rock. With the help of acoustic emission monitoring equipment, the effect of multi-level amplitude creep/fatigue loading on the damage evolution of salt rock was analyzed.

(4) Long-time creep-fatigue mechanical characterization of salt rock

Based on the real peaking frequency of the compressed air energy storage (CAES) power plant, long-term creep-fatigue tests on salt rock were conducted. On a relatively long-time scale, the influence of different operating pressure upper limits and cycles on the creep-fatigue mechanical properties of salt rock was studied, and the effect of stress state variations on salt rock creep-fatigue deformation was analyzed in detail.

(5) Creep-fatigue constitutive modeling of salt rock considering creep-fatigue interaction

Based on the existing research data, a new creep-fatigue constitutive model for salt rock was developed by incorporating a state variable that characterizes the degree of rock hardening into the Norton creep model. This model takes into account the interaction between creep and fatigue in salt rock. The model was validated using test data from salt rock creep-fatigue mechanical experiments.

2 Creep-fatigue mechanical characterization of salt rock under uniaxial stresses

2.1 Introduction

During the operation of a CAES power plant, there is a spatial and temporal difference in the use of energy between the demand side (households, factories, etc.) and the supply side (wind, solar, etc.). That is, when a sustainable energy source generates electricity and stores it in a salt cavern by means of compressed air, the gas is not immediately released to generate electricity, so there is a certain period of high-pressure stabilization. Similarly, there will be a lower pressure stabilization period for the internal gas pressure after the CAES plant has completed its peaking [193]. The study of simple salt rock fatigue mechanical properties does not fully reflect the real mechanical state of the surrounding rock of the CAES reservoir [194]. On the one hand, the effect of low stress on the fatigue behavior of rocks has been well investigated by scholars around the world. On the other hand, the effect of high stress plateaus, i.e. fatigue behavior under creep-fatigue alternation, has been studied for metals [195-197], asphalt, plastic wood flooring or saturated soft clay [198-201], but is rarely reported on rock materials. Therefore, there is a need to carry out relevant research on the mechanical characteristics of creep-fatigue of salt rock.

2.2 Experimental materials and methods

2.2.1 *Salt rock material and specimens*

Salt rock is a sedimentary rock composed mainly of NaCl, with metallic glossy on fresh surfaces, easily absorbed by water via deliquescence, and with a cubic crystal form. Salt deposits are chemically deposited by the evaporation and concentration of water under arid climatic conditions and specific geological conditions. Usually, sedimentary deposits are stratified and in some cases contain impurities and inclusions, such as mudstone. Due to tectonic movement, a buried salt rock layer will flow upward and intrude into the overlying rock layer or make the overlying rock layer arch up, forming salt mounds. Salt rocks are widely distributed in the Earth's crust, and the largest salt mines worldwide are located mainly in North America and Asia, where they are hundreds to thousands of meters thick [190]. The salt rock samples used in this paper are extracted from the Khewra salt rock mine located in Pakistan in the northern

Himalayas, excavated within the base of a thick layer of highly folded, faulted, and stretched Ediacaran to early Cambrian evaporites of the Salt Range Formation. Figure 2.1 shows the geological distribution map of salt rocks in northern Pakistan [191].
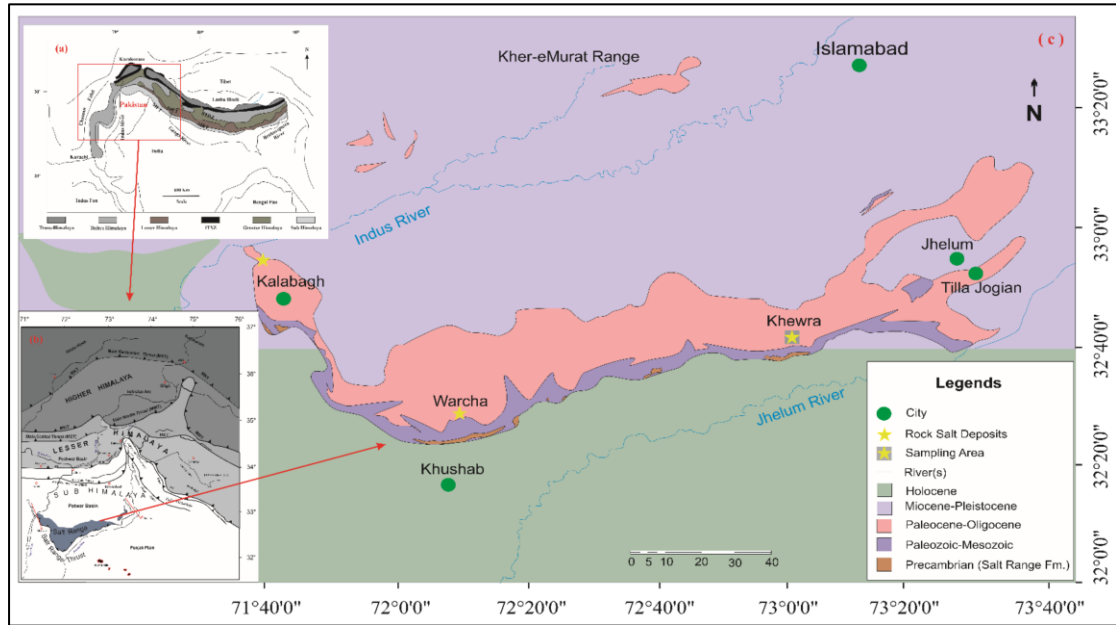
Fig. 2.1 Geological distribution map of salt rocks in northern Pakistan

This salt is translucent, pink, reddish to beef-colored red, while some exhibits alternating bands of red and white. The composition of the salt rock was observed using X-ray diffraction (XRD), and it was found to have a high NaCl content of more than 96% (Fig. 2.2). The remaining components are small amounts of insoluble impurities, such as Na_2SO_4, K_2SO_4 and mudstone.
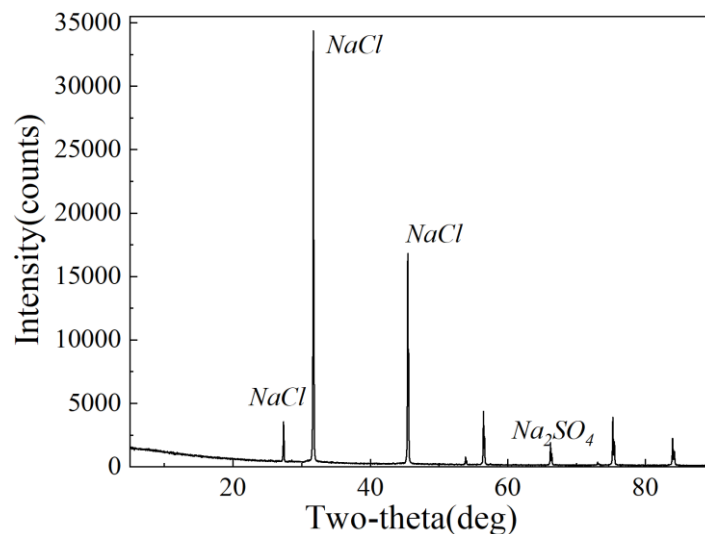
Fig. 2.2 XRD results of the tested salt rock.

The salt rocks selected for processing were derived from large rocks buried at the same horizon and without significant differences or fractures. According to the "Rock Mechanics Test Procedure" developed by the Laboratory and Field Test Standardization Committee of the International Society for Rock Mechanics (ISRM) [192], samples were taken in the same direction and processed into standard cylindrical specimens 100 mm in height and 50 mm in diameter, with flatness errors of the upper and lower end surfaces of less than ±0.05 mm by using a dry corer. Specimens with uniform impurity distributions, similar colors and no directly visible cracks were selected for the test. The salt rock specimens are shown in Fig. 2.3.

Fig. 2.3 Salt rock specimens.

To mitigate the impact of moisture on the test results, the salt rock specimens were subjected to a 24-hour low-temperature (60°C) drying process in a drying oven (Fig. 2.4) prior to mechanical testing. To reduce the end effects during mechanical testing, a lubricant was applied between two Teflon shims positioned at both specimen extremities in contact with the indenter.

Fig. 2.4 Constant temperature drying oven.

2.2.2 *Testing equipment*

The tests were conducted at the State Key Laboratory of Coal Mine Disaster Dynamics and Control, Chongqing University, using the MTS815 Rock Mechanics Test System (Fig. 2.5), manufactured by MTS, USA.

Fig. 2.5 The MTS 815 rock mechanics test system used in this experiment

The main technical specifications of the testing aparatus are given here:

1）Axial Load ≤4600kN

2）Confining Pressure ≤140MPa

3）Pore Water Pressure ≤70MPa

4）Permeability Delta P $\leqslant$2MPa

5）Stiffness of Load Frame   10.5$\times$10N/m

6）Hydraulic source flow   31.8L/min

7）Servo Valve sensitivity   290Hz

8）Channels of Data Acquisition   10 Chans

9）Minimum Sampling time   50μs

10）Output waveforms: straight line, sine, half-sine, triangle, square, random

11）Specimens

Maximum diameter of triaxial test   100mm

Maximum height   200mm

Maximum diameter of uniaxial test   300mm

Maximum height   600mm

The testing machine can realize automatic data acquisition, and is equipped with three sets of independent servo system controlling the shaft pressure, confining pressure and pore (permeability) pressure, servo valve response agile (290HZ), high test precision; and direct contact with the specimen of the elongation instrument is also by the U.S. MTS company, can be in the high temperature (200 ° C), high-pressure (140MPa) oil in the work of the precise, can be the most accurate measurements of rock before and after the destruction of the stress-strain.

The tester can carry out uniaxial compression tests as well as triaxial tests on a variety of rocks. Stresses are defined positive in compression here. Triaxial compression tests can be realized under various level of confining pressure, giving two possible testing conditions:

$$\left.\begin{array}{l} \sigma_1 > \sigma_2 = \sigma_3 \\ \sigma_1 = \sigma_2 > \sigma_3 \end{array}\right\} \qquad (2.1)$$

Monotonic loading, fatigue and creep tests can be performed in a load- or displacement-controlled manner.

2.2.3 *Uniaxial compressive strength*

As a first step, the uniaxial compressive strength, UCS, of the salt rock needs to be characterized. This value will later be useful to design the creep and fatigue testing, in particular the stress amplitude that are applied. Three uniaxial monotonic tests were

conducted in a room with a temperature of 23-26° and relative humidity 55%-65%. The stress-strain curves of salt rock specimens No.2 are shown in Fig. 2.6. The axial strain ε_a and radial strain ε_r are computed from axial and radial elongation measurements respectively, while the volumic strain ε_v is computed through the equation:

$$\varepsilon_v = \varepsilon_a + 2*\varepsilon_r \qquad (2.2)$$
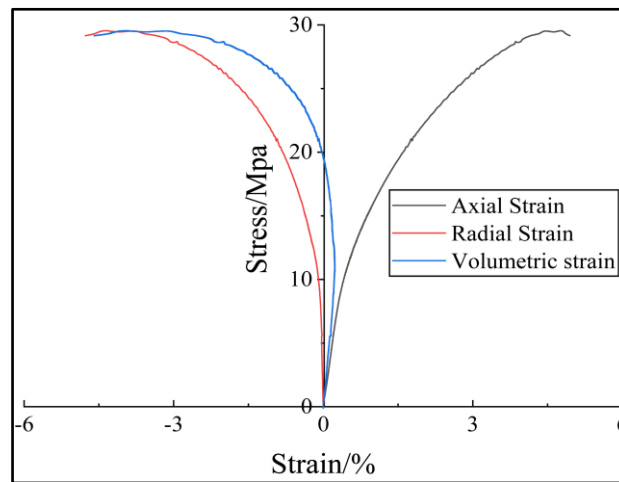
Fig. 2.6 Uniaxial stress–strain curves of the salt rock specimen from test No.2.

The uniaxial compressive strength of the specimens was computed as the maximum stress reached (Table 2.1) and the average value of three specimens is UCS=30.1 MPa.

Table 2.1 Uniaxial compressive strength of three tested specimens.

	Test No.1	Test No.2	Test No.3	Average UCS/MPa
Salt rock	29.5	30.2	30.6	30.1

2.2.4 *Creep-fatigue testing procedure*

The loading scheme for the creep-fatigue test of the salt rock was as follows: first, the upper stress limit is applied and the load was stabilized for one hour defined as *T* stage before releazed. The purpose of this "first one hour high stress plateau i.e. *T*-stage" is to simulate the rheological state of the salt cavern surrounding rock due to the long-term high-pressure environment when the salt cavern is first injected with air. Subsequently, a high stress plateau is applied and held for a given duration during every other stress cycle. The purpose of this setup (alternating cycle with and without plateaus) was to allow a comparative analysis of the effects of two different stress cycles, on the same specimen, therefore avoiding the dispersion caused by specimen variability.

Six experiments were carried out. Five conventional creep-fatigue (CCF)tests, and

one validation creep-fatigue (VCF) test. The five CCF tests were performed with high stress plateaus lasting 0 min, 5 min, 10 min, 15 min, and 20 min. Note that the 0 min test is the control group to observe the difference with and without creep. The pre-plateau cycle is defined as the A cycle, and the post-plateau cycle is defined as the B cycle. The first cycle (F cycle) is neither a pre-plateau nor a post-plateau and is called the first cycle. The loading path for CCF tests is illustrated in Fig. 2.7(a). During the VCF test, high stress plateaus lasting 0, 5, 10, 15, and 20 min were applied to the same specimen, as shown in Fig. 2.7(b). This test was used for validation first, to verify the accuracy of the other five tests and, second, to avoid the influence of testing specimen.
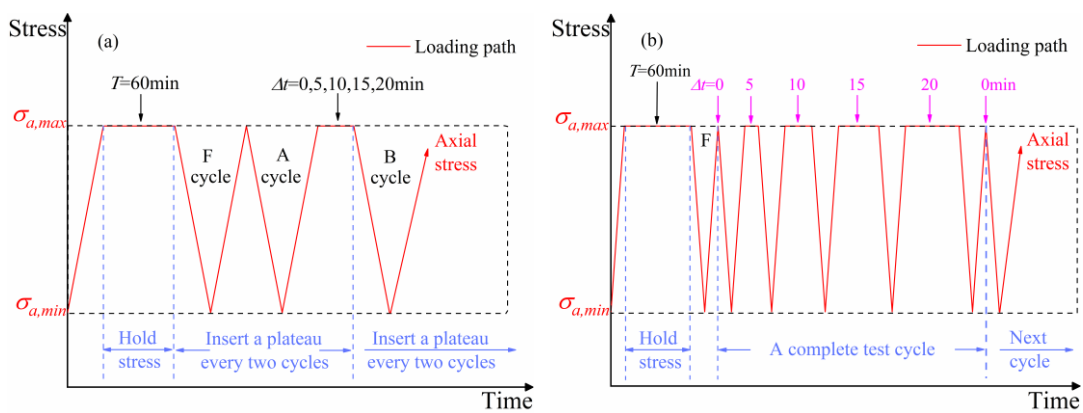
Fig. 2.7 Loading paths for the creep-fatigue tests: (a) CCFs and (b) VCF

The specific test procedure is as follows. First, place the selected specimen between the two indenters, and close the protection window to ensure the safety of the testing machine. Turn on the power to the test machine and the control computer. Secondly, set the loading program, and apply a certain preload force to the specimen to ensure the fit between the specimen and the indenter. After the preload force is applied, start the program according to Fig 2.7 procedures. Third, after the specimen is destroyed and the tests stops automatically, remove the specimen and store it in a sealed plastic bag.

The loading and unloading levels and rates of the test were as follows: A computer-controlled program was used to load up to 85% of the uniaxial compressive strength (25 MPa) at a rate of 2 kN/s as the upper limit pressure, held for one hour, and then unloaded down to 3% of the uniaxial compressive strength (1 MPa) at the same rate as the loading rate. Compared to the conditions in a real CAES plant, the upper limit pressure selected for the laboratory test was higher, the lower limit pressure was lower, and the unloading pressure was faster, to be able to complete the test in one working

day (12-24 hours). Therefore, this experiment is focused on determining the effect of creep on fatigue at the laboratory scale. Each loading path was carried out one time. The main results of the creep-fatigue tests are shown in Table 2.2. The fatigue life is defined as the number of cycles of loading that the specimen undergoes before complete failure, and the creep life is defined as the total time spent under high stress plateau during the test (including the first one-hour high stress period).

Table 2.2 Test results of the CCF tests.

Plateau times/min	Fatigue life/cycle	Creep life/min
0	201	60
5	112	275
10	88	430
15	68	495
20	60	580

2.2.4 *Test procedure*

(1) Open the test machine and place the selected salt rock samples in the center of the indenter. Apply preload to compress the specimen.

(2) Close the protective cover of the tester and turn on the tester. Set the computer program and start the test.

(3) When the samples is broken, the machine stops automatically; the power of the test system is turned off, and the specimen is removed and stored in a sealed plastic bag.

2.3 Test results and analysis

2.3.1 *Stress–strain curve in the uniaxial creep-fatigue tests*

The fatigue stress–strain curves for the 0, 5 and 10 min CCF tests and VCF test are shown in Fig. 2.8. The common feature of the four curves is that the salt rock undergoes a large deformation after the first loading. After the one-hour first high stress plateau, for the CCF test at 5 min, as an example, the specimen enters the creep-fatigue cyclic loading stage, and the fatigue curve shows a comb-dense-comb development pattern on the whole. This is similar to conventional fatigue [202], indicating that the high stress plateau does not change the essential characteristics of the fatigue curve. However, its first stage (deceleration deformation stage, I) is indeed greatly shortened. Previous

studies [182] have found that we can roughly consider the first 20% of cycles of fatigue damage of salt rock as the deceleration deformation stage, but in this test, the deceleration deformation stage accounts for only approximately 10% of the whole cycle. At the same time, the distinction between the deceleration deformation and the stabilization deformation (the second stage, Ⅱ) stages of the specimen is not obvious because after the loading stage, the specimen undergoes another hour of high stress, the internal cracks of the specimen are compacted and compressed, and the integrity of the specimen is improved. When entering the third stage (accelerated deformation stage, Ⅲ) near the damage, the curve becomes sparse again, and not only the deformation in the high stress plateau but also the residual strain generated by the cyclic loading increases (the law of residual strain will be described in section 2.3.2). The specimens from the 5 min CCFT eventually broke down during the last high stress plateau. A similar pattern of development was observed for the remaining five sets of tests; the 0 min CCF test (i.e., conventional fatigue) specimens were damaged in the loading stageof the last cyclic load, and the damage stress was slightly less than the upper limit stress, which is consistent with the majority of the test phenomena, indicating that even though the test was designed for an initial one-hour high stress plateau, it did not change the nature of the fatigue test.
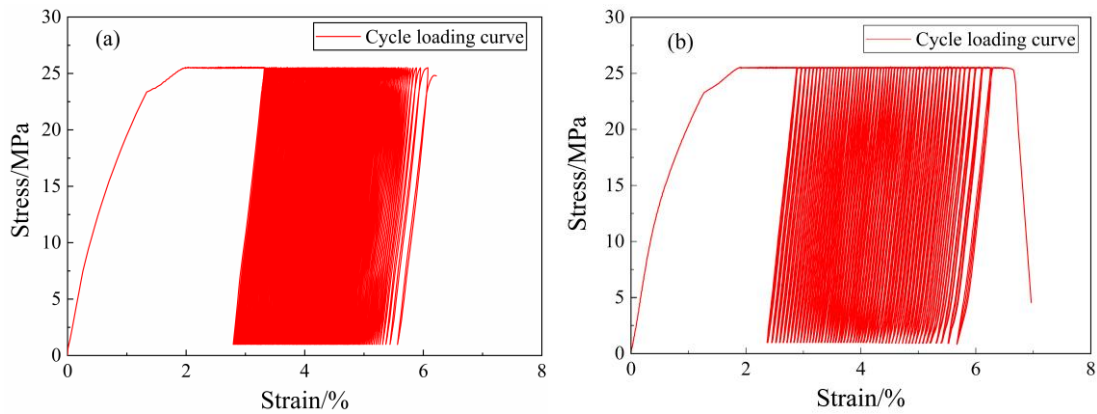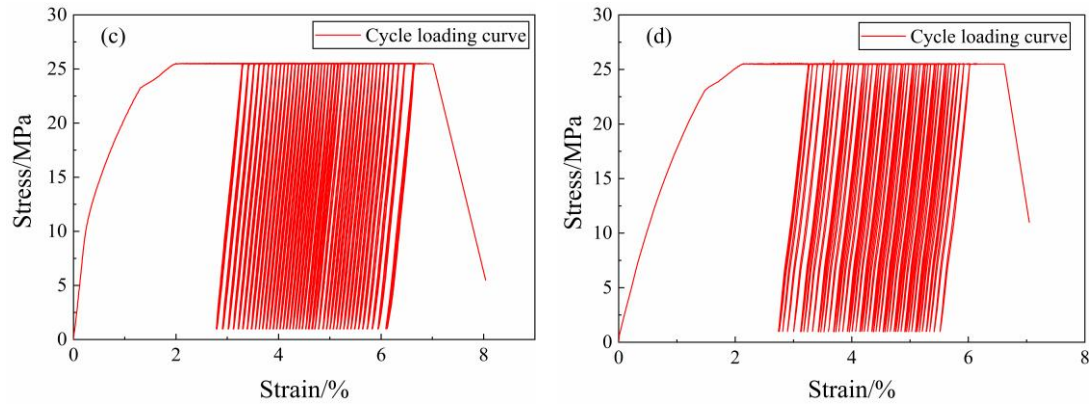
Fig. 2.8 The stress–strain curves of the (a) 0 min plateau time CCF test, (b) 5 min plateau time CCF test, (c) 10 min plateau time CCF test, and (d) is the VCF test.

For the four CCF tests, the total test time is different for two reasons: the number of cycles before failure is different (larger for shorter plateau duration), and the plateau duration varies between tests (5 to 20min). Therefore, it is not really straight forward to interpret the experimental results in term of total duration. Instead, taking the time when the 5 min CCF test enters the third stage as the calculation limit, calculate the difference between the strain of the specimens in the four CCF tests at the same test time and the strain when they first entered the creep-fatigue alternating stage, as shown in Fig 2.9 below:
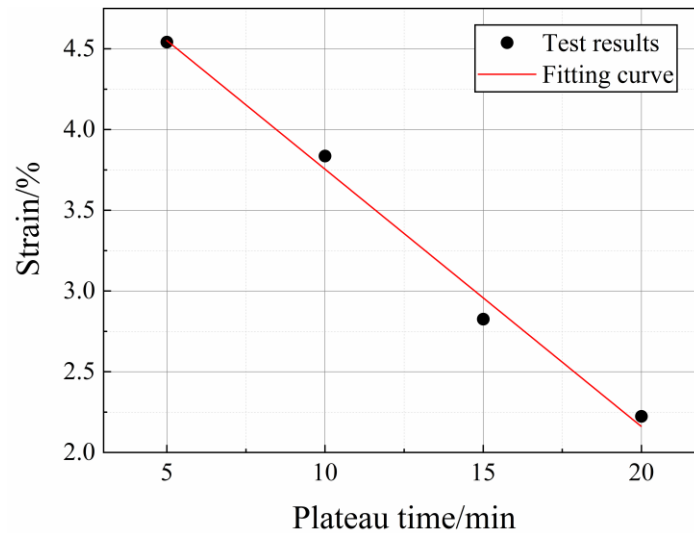
Fig. 2.9 The strain difference at the same test time for salt rock inthe 5, 10, 15 and 20 min CCF test.

From the Fig. 2.9, it can be observed that under the same test duration of 5, 10, 15, and 20min for the CCF tests, the corresponding strain differences of the salt rock

specimens exhibit a decreasing trend and show a nearly linear relationship. This phenomenon can be attributed to the fact that under the same test duration, shorter high-stress plateau durations result in more cyclic loads applied to the specimens. In the early stage of the tests, the cracks generated by cyclic loading are compacted during the high-stress interval. As the tests progress, these cracks gradually evolve from small cracks to large ones, and the high-stress interval transforms from promoting crack closure to driving crack propagation and sliding of fracture surfaces. This leads to an accelerated deformation rate of the specimens, and they quickly enter the third stage, ultimately leading to failure.

2.3.2 *Creep-fatigue strain rate in salt rock*

In addition, the deformation rate for the high stress creep period for each test were calculated to observe the pattern of variation in creep rate (v_c) at a given plateau time with the following equation:

$$v_{ci} = \frac{\varepsilon_{ci}}{t_i} \tag{2.2}$$

where i is the number of high-stress cycles excluding the initial one hour high stress period (for this one hour high-stress period, v_c is calculated by dividing it into 4 equal parts), ε_{ci} is the creep strain difference at the high stress plateau and t_i is the plateau time (for the initial one hour high stress period, the high stress period is divided into four time points bounded by 200 s, 1000 s, 1800 s, 2600 s, and 3400 s). For the high stress plateau during creep-fatigue, v_c is calculated by removing 10% of the creep time before and after. The purpose is to eliminate errors in the alternating periods of acceleration/unloading and creep. The v_c values for the 5 min CCF test are shown in Fig. 2.10.
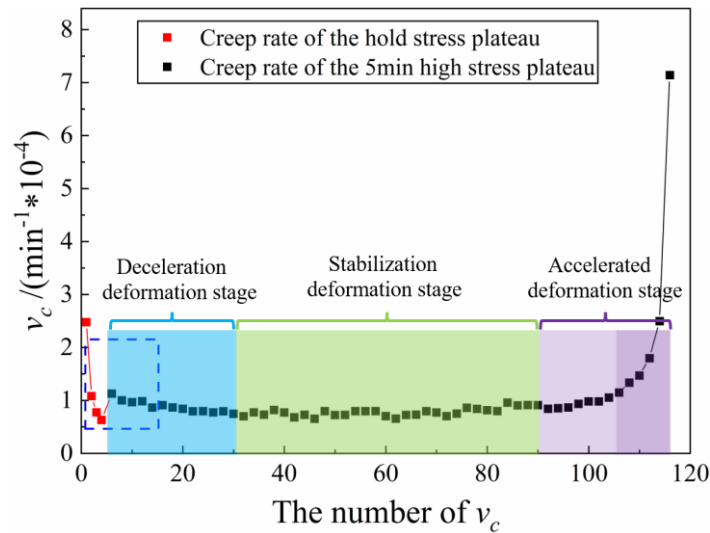
Fig. 2.10 Creep rate during the 5 min plateau time CCFT.

The figure shows that the v_c of the salt rock specimens shows a decreasing trend during the first hour-long high stress plateau, but the decreasing trend slows, which is consistent with the known results of rock creep tests. This indicates that a salt rock specimen is in the first stage of creep, i.e., deceleration creep, reflecting the rapid closure of internal microfractures/pores, when subjected to external loading, leading to an increased integrity of the specimen. After the first cyclic loading (i.e., fatigue action), we observed an increase in v_c during the first alternating creep-fatigue action (as shown in the blue box of Fig. 2.10). This indicates that fatigue has a positive effect on creep because after the withdrawal of pressure and reloading, some of the fractures and structural surfaces inside the rock specimen that had been stabilized were opened again, resulting in a jump in v_c (i.e., the salt rock specimen is considered to have restarted the creep process with a larger creep rate, similar to the process in the red part). Describe what is in blue, green and purple stages before the last 20%. Entering the last 20% of the cycle, the v_c of the salt rock increases again, and the salt rock specimen enters the third stage of creep, commonly called accelerated creep stage. At this time, the microfractures inside the salt rock develop rapidly, and the fracture surface gradually penetrates to form a macrofracture surface. During the last 5% of the cycle, v_c shows an exponentially rising trend. Finally, in the last creep period, the salt rock specimen is structurally destabilized and damaged. The v_c exceeded 7×10^{-4} min^{-1}, far exceeding

the initial v_c of $2,5 \times 10^{-4} min^{-1}$.

To investigate the effect of fatigue on creep for different high stress plateau times (5 to 20min), we calculated the average creep rate ($\bar{v}_c$) and average creep strain ($\bar{\varepsilon}_c$) during the second stage by using Eqs. (2.3) and (2.4):

$$\bar{v}_c = \frac{\sum_n^m v_{ci}}{m-n} \tag{2.3}$$

$$\bar{\varepsilon}_c = \frac{\sum_n^m \varepsilon_{ci}}{m-n} \tag{2.4}$$

where n and m are the beginning and end loading cycle numbers of the second stage in every CCF test. The results are shown in Fig. 2.11.
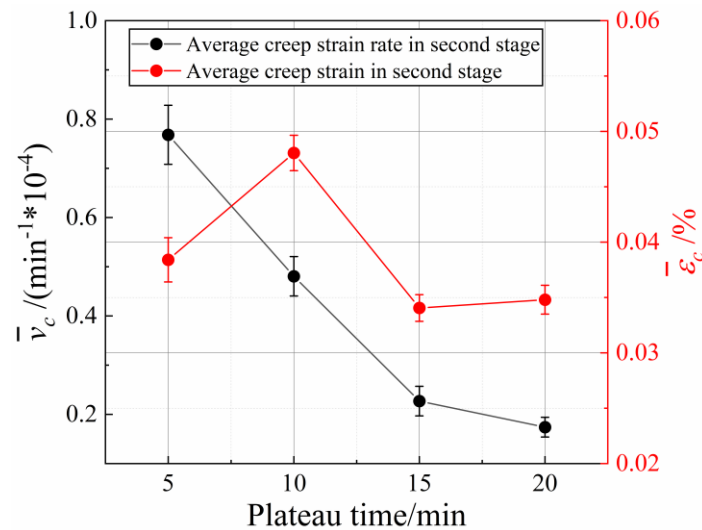
Fig. 2.11. Average creep rate and strain during the stabilization deformation (the second stage, Ⅱ) under different plateau times.

We found that as the duration of the high stress plateau increases, the average creep rate decreases, indicating that the effect of fatigue on creep gradually weakens. However, there is a threshold value for this phenomenon, i.e., the creep rate for 5, 10, and 15 min shows a linear decrease, but the creep rate for 15 and 20 min, decreasesless, indicating that the effect of fatigue on creep stabilizes when the plateau duration is longer than 15 min. It increases during 5min and 10min plateau, decreases between 10min and 15min, and increases slightly again between 15min and 20min CCF test. In a first analysis, this would suggest that the 15min plateau time would be an optimum for salt rock samples in the CCF test. However, for guiding recommendations regarding

salt cavern storage, it is necessary to provide them based on tests conducted at the engineering scale., so we prefer not to draw any strong conclusions here. The creep deformation and strain rate for the VCF test was calculated with the same method, showing the same trend as in the CCF test, i.e. the average creep rate and average creep strain at each cycle (0 to 20min duration) correspond to the values obtain for the corresponding CCF test.

2.3.3 *Creep-fatigue residual strain in salt rock*

Rocks are deformed when subjected to external loads, and the deformation includes reversible elastic deformation and irreversible plastic deformation (i.e., residual strain). When a rock is subjected to cyclic loading, plastic deformation will occur with each cycle. In a creep-fatigue test, creep deformation and fatigue deformation together lead to plastic deformation of the salt rock, and when the plastic deformation accumulates to a critical state, the rock will become damaged.

The residual strain (ε_r) per cycle for the creep-fatigue test is calculated by the following equation:

$$\varepsilon_{ri} = \varepsilon_{ai} - \varepsilon_{bi} \qquad (2.5)$$

where i is the number of cycles (excluding the first cycle), ε_{ai} is the axial strain at the start of the current cycle (start of the unloading of a cycle), and ε_{bi} is the axial strain at the end of the same cycle (end of the loading of the cycle).

The residual strain ε_r patterns for the control group (i.e., the specimens tested during the 0 min) and 5 min CCF tests, are shown in Fig. 2.12. We found that, compared with conventional fatigue, the ε_r of the control and high stress plateau groups do not have obvious boundaries between the first and second stages and enter the second stage faster, which is similar to the law of fatigue curve development, for reasons analysed in the previous section (not be repeated here). Another obvious difference is that the ε_r of A and B cycles of the control test (no stress plateau) are not significantly different, while the ε_r of A and B cycles of the specimens undergoing fatigue combined with high stress plateaus are significantly different, with ε_r of A cycles significantly larger than those of B cycles. This difference was observed throughout the two first stages of the test process, while this difference is less clear during the third stage of the test. This pattern was found for the other three fatigue test groups with 10, 15, and 20 min plateaus.
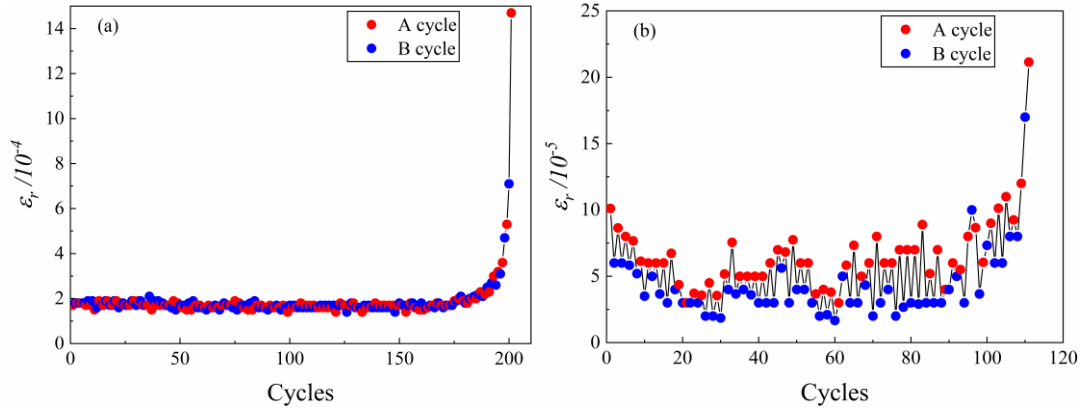
Fig. 2.12. Calculated axial residual strain from the (a) 0 min plateau time CCF test and (b) 5 min plateau time CCF test.

Considering that A cycle and B cycle of the creep-fatigue test are always in different positions (the A cycle is always in the even position, and the B cycle is always in the odd position, including the first cycle), the ε_r of the A and B cycles at the corresponding positions were solved by using the arithmetic mean method, as shown in the following equations:

$$\varepsilon_{r,Ai}=\begin{Bmatrix} \varepsilon_{r,Ai}, i=even\ 2 \leq i < N \\ \frac{\varepsilon_{r,A(i-1)}+\varepsilon_{r,As(i+1)}}{2}, i=odd, 3 \leq i < N \end{Bmatrix} \tag{2.6}$$

$$\varepsilon_{r,Bi}=\begin{Bmatrix} \frac{3\varepsilon_{r,B3}-\varepsilon_{r,B5}}{2},\ i=2 \\ \varepsilon_{r,Bi}, i=odd\ 3 \leq i < N \\ \frac{\varepsilon_{r,B(i-1)}+\varepsilon_{r,B(i+1)}}{2}, i=even, 4 \leq i < N \end{Bmatrix} \tag{2.7}$$

where $\varepsilon_{r,Ai}$ and $\varepsilon_{r,Bi}$ are the ε_r results of the A and B cycles in the *i*th cycle, respectively, and *N* is the number of loading cycles.

Four different plateaus were set up for the tests, and each set of tests showed that ε_r of A cycle were greater than the ε_r of B cycle. However, the effect of different plateaus on the development of ε_r varies. We calculated the average value of the difference between the ε_r of A cycle and B cycle during the second stage (stable deformation stage) for the various plateau durations, using Eq. (2.8):

$$\Delta\bar{\varepsilon}_r=\frac{\sum_n^m(\varepsilon_{r,An}-\varepsilon_{r,Bn})}{m-n} \tag{2.8}$$

where $\Delta\bar{\varepsilon}_r$ is the average value of the difference between the ε_r values of A cycle and B cycle from Eqs. (2.6) and (2.7), and *n* and *m* are the beginning and end loading cycle numbers of the second stage. The calculation results are shown in Fig. 2.13.

61
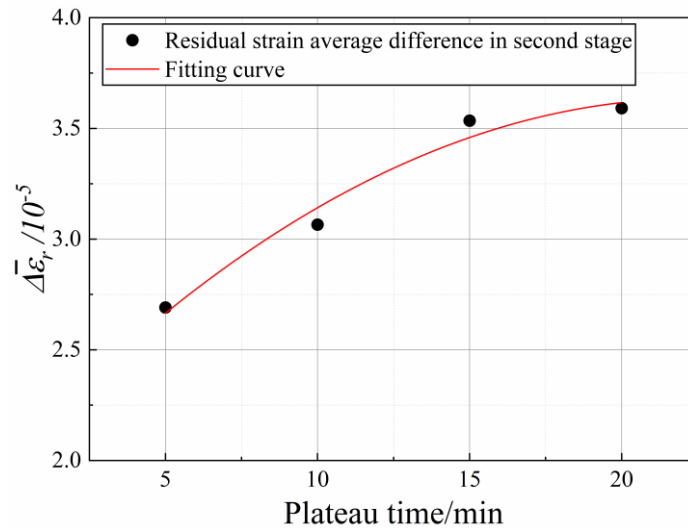
Fig. 2.13. Average values of the residual strain difference between A and B cycles under different plateau times.

We found that the average value of the residual strain difference increases gradually with increasing high stress plateau time. This shows that the effect of creep on fatigue increases with increasing plateau time. Additionally, there seem to be a threshold in this increase, consistent with the conclusions obtained in section 2.3.2 indicating that the effect of creep on fatigue is also stabilizing. The interaction between creep and fatigue is a positive interaction. We discuss the specific reasons for this pattern below.

2.3.4 *Relation between fatigue life and creep life in the creep-fatigue test of salt rock*

In the process of salt rock creep-fatigue testing, the damage sustained by salt rock is constituted by both fatigue damage and creep damage. Regarding fatigue damage, the initiation and propagation of rock fatigue cracks are influenced by its micro-fissure forms. Rock fatigue failure fractures include transgranular fractures, intergranular fractures, and a combination of transgranular and intergranular fractures. Different mineral crystals within the rock exhibit distinct fracture patterns [203]. For instance, in granite, where feldspar, quartz, and mica crystals coexist, transgranular fractures primarily occur in feldspar crystals under fatigue loading. Quartz crystals experience a limited amount of both transgranular and intergranular fractures, while mica crystals mainly undergo intergranular fractures. The loading pattern for fatigue involves cyclic loading and unloading, where the dynamic effects and energy changes resulting from loading and unloading promote transgranular fractures. Moreover, due to the presence

of grain boundary defects, cracks can nucleate at weak points along the grain boundaries, leading to intergranular fractures. When transgranular crack initiation is close to intergranular crack nucleation, coupled transgranular-intergranular fractures may occur. Among these three types of micro-cracks, intergranular fractures exhibit the fastest growth rate, followed by transgranular fractures [204]. Intergranular cracks tend to develop in the direction of loading, whereas the growth direction of transgranular cracks is more random. During reverse unloading, stress concentration occurs at the crack tip area, inducing significant residual tensile stress and promoting crack extension [205]. Scanning electron microscope observations of failure surfaces reveal that the primary micro-mechanism for salt rock fatigue testing is cleavage failure, with shear failure as a secondary factor. Intergranular and transgranular cracks coexist within the fracture surface [206]. Under cyclic loading and unloading, the microstructure of the rock repeatedly undergoes deformation, with more movement occurring along grain boundaries, resulting in intergranular fractures. The cohesion between particles at grain boundaries consequently decreases, leading to particle detachment. Detached particles intensify this frictional movement, causing further particle detachment and generating visible macroscopic debris [207]. The initiation and development of fatigue cracks are also influenced by the presence of primary cracks, which, under stress concentration, serve as starting points for rock failure crack formation [208]. With an increase in the number of fatigue cycles, more tip cracks are formed, and internal cracks transition from straight to curved as deformation progresses [209].

The mechanism of creep damage is somewhat different. The process of rock creep deformation failure involves crack initiation, growth, bifurcation, and coalescence, ultimately leading to rock rupture [210]. Cracks originate from the formation of creep micropores and the diffusion of micro-defects [211]. In the vicinity of rock grain boundaries, stress concentration often occurs due to the discordant movement of grains and the presence of impurities, leading to pore formation. Pores continue to grow under constant loading, eventually connecting with surrounding pores to form intergranular micro-cracks. These micro-cracks then further connect and converge to form main cracks. Secondary cracks develop around the main crack, and creep fractures mainly develop along the direction of the principal stress (or a smaller angle) [212]. In the case of crystalline minerals like salt rock, there are internal defects such as grain vacancies [213], dislocations, and grain boundaries, which, under constant loads, temperature, and

humidity, undergo diffusion and subsequently initiate cracks [214]. The entire process of creep crack initiation, development, and coalescence is influenced by the microstructural heterogeneity of the rock. The unevenness of the rock causes differences in the location of crack initiation and the rate of crack propagation and widening. The presence of impurity particles within the rock, the variation in grain size, and the orientation of grains all directly affect crack initiation. Different deformation moduli and Poisson's ratios of various grains and impurities result in the need for the microstructure of the rock to adjust its motion over time under load, and the initiation and development of cracks are outcomes of the mutual adjustment and coordination of the rock's microstructural motion [215].

Few experimental studies on creep-fatigue of rocks have been conducted, but research on creep fatigue of metals has been ongoing for nearly 60 years [216-219]. Here, drawing on the statistical method of metal creep-fatigue life, the fatigue life is defined as the number of cycles of loading that the specimen undergoes before complete failure, and the creep life is defined as the total time spent under high stress plateau during the test (including the first one-hour high stress period). the fatigue life for various plateau time is shown in Fig. 2.14.
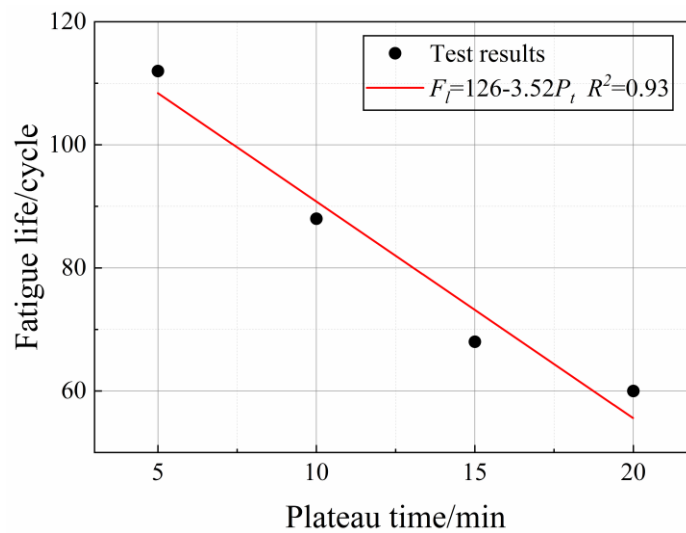
Fig. 2.14. Fatigue life for different plateau times.

We found that with the increase in plateau time, the fatigue life decreases and satisfies a linear equation:

$$F_l = 126 - 3.52P_t, \ R^2 = 0.93 \tag{2.9}$$

The creep life for various plateau time is shown in Fig. 2.15.
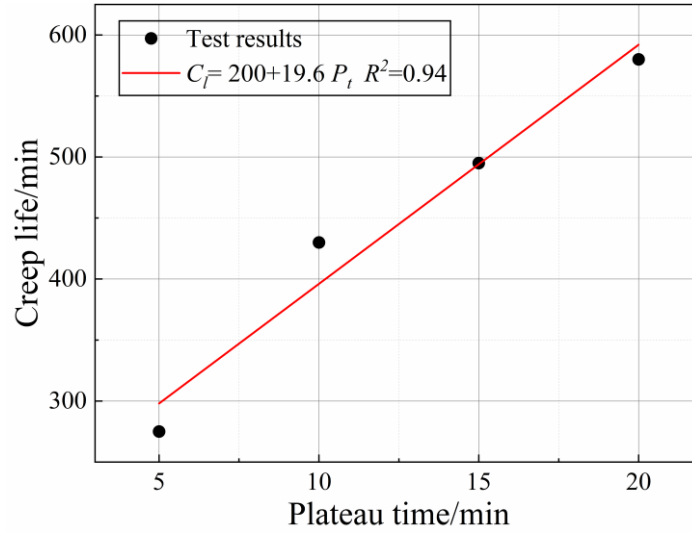
Fig. 2.15. Creep life for different plateau times.

With the increase in plateau time, creep life increases and satisfies the following linear equation:

$$C_l = 200 + 19.6P_t, R^2 = 0.94 \qquad (2.10)$$

This is close to the conclusion reached by the creep-fatigue testing of metals. According to a study by Joseph Oldham et al [220], the damage equation of metallic materials during creep-fatigue damage can be defined as follows:

$$\text{Fatigue damage: } \Sigma_\alpha \left(\frac{N}{N_d} \right) \qquad (2.11)$$

$$\text{Creep damage: } \Sigma_\beta \left(\frac{T}{T_c} \right) \qquad (2.12)$$

For materials damaged during creep-fatigue experiments, fatigue and creep damage are cumulative processes. If fatigue and creep separately affect the material during the test, the damage equation can be written as:

$$\Sigma_\alpha \left(\frac{N}{N_d} \right) + \Sigma_\beta \left(\frac{T}{T_c} \right) = 1 \qquad (2.13)$$

However, in the American Society of Mechanical Engineers (ASME) code [221], there is a positive interaction assumed between creep and fatigue in metallic materials during the creep-fatigue test. Therefore, Eq. (2.13) is modified as follows:

$$\Sigma_\alpha \left(\frac{N}{N_d} \right) + \Sigma_\beta \left(\frac{T}{T_c} \right) < 1 \qquad (2.14)$$

Further analysis revealed that a correlation term could be used to represent the interaction of creep and fatigue.

$$\sum \alpha \left(\frac{N}{N_d} \right) + \gamma \left[\mu \left(\frac{N}{N_d} \right) + \theta \left(\frac{T}{T_c} \right) \right]^{\delta} \sum \beta \left(\frac{T}{T_c} \right) = 1 \qquad (2.15)$$

where N is the number of cycles, N_d is the total number of cycles in the test under the α type, T is the creep time, T_c is the total creep time in the test under the β type, and γ, μ, θ, and δ are the coefficients related to creep-fatigue interactions.

For a given test, the test conditions and environment were determined. Therefore, some scholars [222,223] have simplified Eq. (2.15) by simplifying the creep-fatigue correlation term to $B \left(\frac{N}{N_d} \times \frac{T}{T_c} \right)^{\frac{1}{2}}$. A new equation is proposed:

$$\frac{N}{N_d} + B \left(\frac{N}{N_d} \times \frac{T}{T_c} \right)^{\frac{1}{2}} + \frac{T}{T_c} = 1 \qquad (2.16)$$

where B is the correlation coefficient, and a larger value indicates that the creep-fatigue interaction is stronger. Fig 2.16 show the normalized fatigue life and creep life for the 4 different tests (5, 10, 15, 20min CCF test). For salt rock, a B value of 1.01 is obtained. This indicates the existence of creep-fatigue interactions, which is consistent with the experimental phenomenon. There are many uncertain structures within our rock, as a natural material, that are difficult to observe and resulting in a relatively dispersed mechanical property. Moreover, the tests reflect that the interactions between creep and fatigue are not consistent. A more accurate equation is given as follows:

$$\frac{N}{N_d} + A \left(\frac{N}{N_d} \right)^{\varphi} \left(\frac{T}{T_c} \right)^{\omega} + \frac{T}{T_c} = 1 \qquad (2.17)$$

where A is the interaction coefficient and φ and ω are the fatigue and creep damage indices, respectively, which reflect the degree of fatigue damage and creep damage on the creep-fatigue interaction damage. We speculated that for this experiment, A can be adopted as the hardening factor of creep on the fatigue residual strain, and B can be adopted as the catalytic factor of fatigue on creep rate. We will complete more tests to finalize the values of these coefficients.
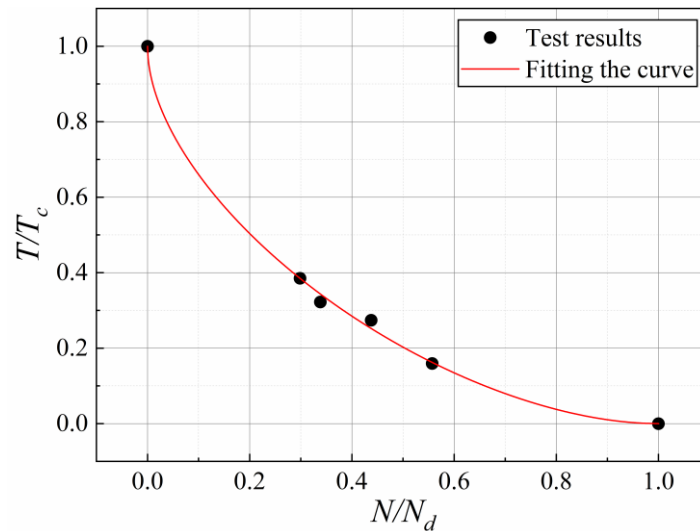
Fig. 2.16 Normalized creep life and fatigue life for creep-fatigue tests (5, 10, 15, 20min CCF test) on salt rocks, with fitting curve.

2.4 Mechanisms of creep-fatigue interactions in salt rocks

In pure fatigue testing of salt rock, there is no significant difference in the development of residual strain per cycle except for the traditional three stages [224]. In the low-stress-interval fatigue test, the residual strain in the post-interval cycle is greater than the residual strain before the interval [225]. The residual stresses during the low stress interval were considered to be the cause of this phenomenon. In the creep-fatigue experiments completed by the authors, however, the opposite phenomenon occurred, with the residual strain before the high stress plateau being greater than the residual strain after the plateau. The fatigue cycles can also affect the creep rate and strain of the salt rock. We think that the following reasons are responsible for this phenomenon.

Factors affecting the deformation mechanism of the material include the internal structure and the external environment. The internal structure includes the grain size and impurity distribution, and the external environment includes the temperature, stress state, and hydrogeological environment. It has been pointed out that the creep of salt rocks can be divided into dislocation creep (Fig. 2.17(b)) and pressure solution creep (Fig. 2.17(c)) [226,227]. Dislocation creep mainly occurs inside the salt rock crystals, while pressure dissolution creep mainly occurs at the grain boundaries of the salt rock.
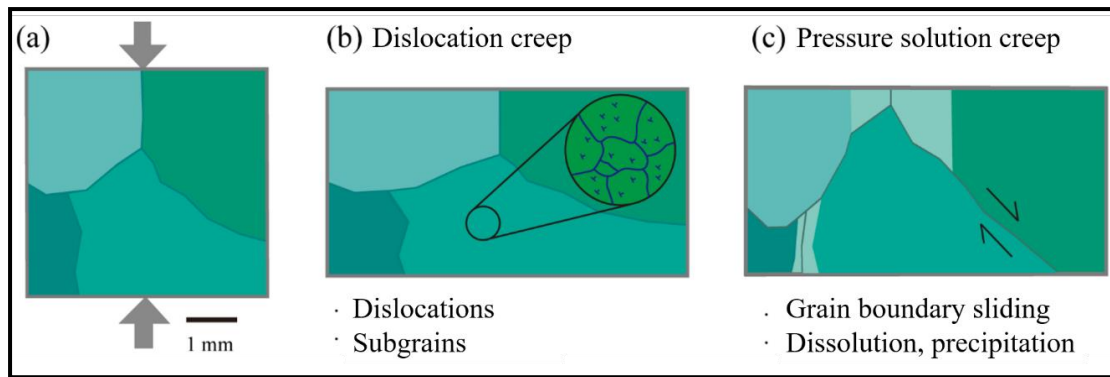
Fig. 2.17 Schematic diagram of salt rock dislocation creep and pressure dissolution creep.

The main influence of pressure dissolution creep, in addition to the fundamental factor of stress, is mainly related to the moisture conditions between the salt rock grain boundaries and to the temperature. In the presence of moisture at the salt rock grain boundaries, the salt rock crystals in a high-stress region dissolve, are transported through the fluid, and finally deposit in a low-stress region [228]. Pressure dissolution creep [229-231] is accompanied by the relative dissolution, sliding and rotation of the grains, which gradually eliminates the pores. The temperature level also determines the rate of pressure dissolution creep.

When the temperature is very high, the stress is very low when the creep rate is proportional to the stress, this creep and dislocation relationship is not large, the deformation is mainly caused by the directional flow of the material under the action of stress, this creep is called diffusion creep.
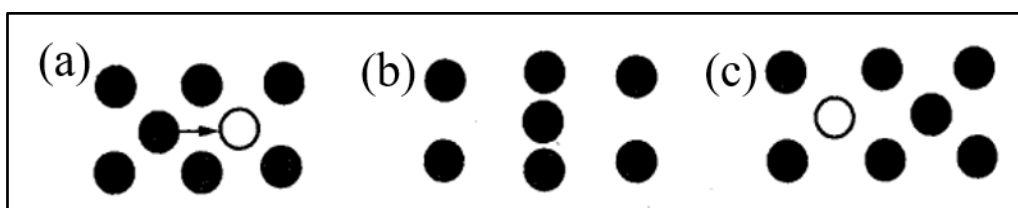
Fig.2.18 Diffusion caused by hole

If there are no atoms at a certain equilibrium position in the atomic arrangement, such as the hollow circle shown in Fig. 2.18 (a), the place is called a hole. The atom on the left, under the action of thermal perturbation, crosses the energy barrier state shown in Fig. 2.18 (b) and results in the configuration shown in Fig. 2.18 (c), where the atoms move one equilibrium position to the right. When a large number of atoms make this movement, it becomes diffusion. When diffusion is directional, it causes macroscopic

deformation.

In polycrystalline materials, according to the preferential path of atoms, diffusion can be categorized into grain boundary diffusion or bulk diffusion. Grain boundary diffusion refers to the diffusion of atoms moving along the grain boundaries, grain boundary diffusion dominated creep is called Coble creep. Bulk diffusion is the movement within the grain, also known as Nabarro-Herring creep. Under the action of external forces, diffusion is directional. Since at relatively low temperatures, the energy barriers are generally smaller at grain boundaries than within the lattice, grain boundary diffusion is the main causative agent. Whereas at higher temperatures, more atoms within the grain bulk diffuse and its induced strain dominates. The strain rate induced by grain boundary diffusion can be modelled as:

$$\frac{d\varepsilon}{dt} = k_1 \frac{\sigma V}{KT} \frac{D_{gb}\delta}{d^2} \tag{2.18}$$

where, k_1 is the coefficient related to the shape of the grain boundary, V is the volume occupied by a single atom, D_{gb} is the grain boundary diffusion coefficient, δ is the thickness of the diffusion layer at the grain boundary, and d is the average diameter of the grain. The strain rate due to bulk diffusion can be modeled as:

$$\frac{d\varepsilon}{dt} = k_2 \frac{\sigma V}{KT} \frac{D_v}{d^2} \tag{2.19}$$

where, k_2 is a coefficient related to grain shape and D_v is the bulk diffusion coefficient.

From Eqs (2.18) and (2.19), it can be seen that the strain rate of creep caused by diffusion is linearly related to the stress. It can be inferred that the main mechanism of viscous creep is diffusion. Therefore, viscous creep is also often called diffusion creep. On the other hand, it can be seen from Eqs. (2.18) and (2.19) that if the grain is refined, i.e., if d is reduced, the increase in creep rate due to grain-boundary diffusion is greater than that due to body diffusion, and thus will dominate.

Heard et al [232]. found experimentally that the conditions under which diffusion creep occurs in salt rock are: (1) the stress is lower than 0.45 MPa, which makes the dislocation density in the crystal very low, and the dislocation motion contributes very little to the total deformation; (2) the temperature is sufficiently high to make the atomic diffusion rate very fast, and the deformation is mainly generated by the directional flow of the atoms.

Since the factors affecting the pressure dissolution creep are well controlled (the test salt rock specimens were dried at a low temperature of 60°C for 24 hours before the

test, and the temperature and humidity of the test environment were kept relatively constant during the experiment), the pressure dissolution creep has less influence on the test variables. However, we still observed pressure dissolution creep at some of the grain boundaries, as shown in Fig. 2.19.
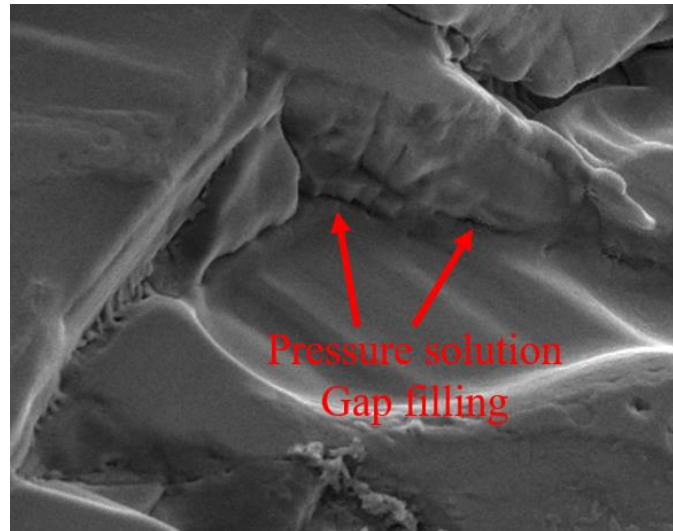
Fig. 2.19 Salt rock pressure dissolution boundary traces (as shown by the red arrow)

Dislocation creep [233,234] is a more complex form of creep associated with innate crystalline defects within the salt rock, including point defects, line defects, and surface defects.

Here is a brief description of point defects as an example. Point defects are lattice defects of atomic scale magnitude, also known as zero-dimensional defects. During the crystal formation process or under certain physico-mechanical conditions, such as high-energy radiation or thermal activation, point defects are easily formed within the crystal. As shown in Fig 2.20 there are three types of point defects: Schottky defects (denoted as S defects), Frenkle defects (denoted as F defects), and heterogeneous replacement atoms.
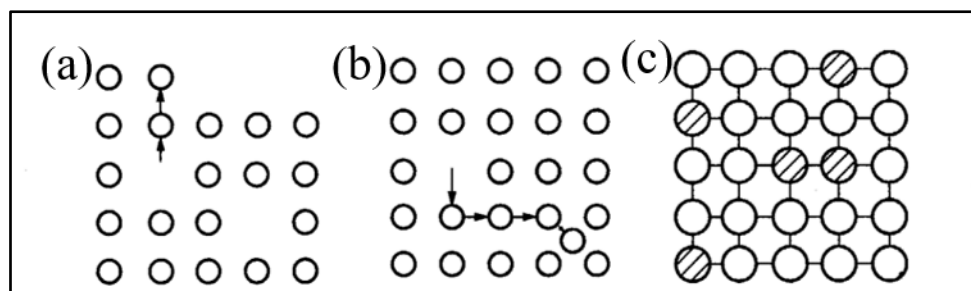
Fig. 2.20 S defect (a), F defect (b) and heterogeneous replacement atom (c).

In previous studies [235], researchers have found large discrepancies between the theoretical strengths of crystalline materials and their experimentally measured values, a contradiction that led to the discovery of dislocations in crystals and the development of related theories. When a crystal is subjected to the crystallizing effects of impurities, temperature changes, or vibrational stresses, the arrangement of its internal plasmas is distorted, and the atomic arrangements slide against each other, no longer conforming to the regular arrangement of an ideal crystal, leading to defects called dislocations. More specifically, a dislocation is the demarcation point between the slipped and unslipped areas. The surface on which the relative slip occurs is called the slip surface, the direction in which the slip occurs is called the slip direction, and the boundary between the slipped and unslipped regions is called the slip line. The simplest dislocations can be categorized into two types: edge dislocations and helical dislocations, and the difference is linked to the direction of the dislocation line and the direction of the dislocation movement under the action of external forces. As shown in Fig. 2.21 (a), assuming that the crystal undergoes a relative slip in the interatomic distance in the upper and lower parts of the region ABCD, the dividing line between the slipped and unslipped regions is AD, which is the so-called dislocation line that forms an irregular arrangement of atoms. When the direction of slip is perpendicular to the dislocation line called edge-type dislocation; when the direction of slip is parallel to the dislocation line, such as Figure 2.21 (b), then the spiral dislocation. If the boundary of the slip region is a curve AC, as in Fig. 2.21 (c), then in different parts of the curve, there are spiral dislocations parallel to the curve, perpendicular to the curve edge-type dislocations as well as a mixture of both parallel and perpendicular components of the motion, called mixed dislocations.

(a) (b) (c)
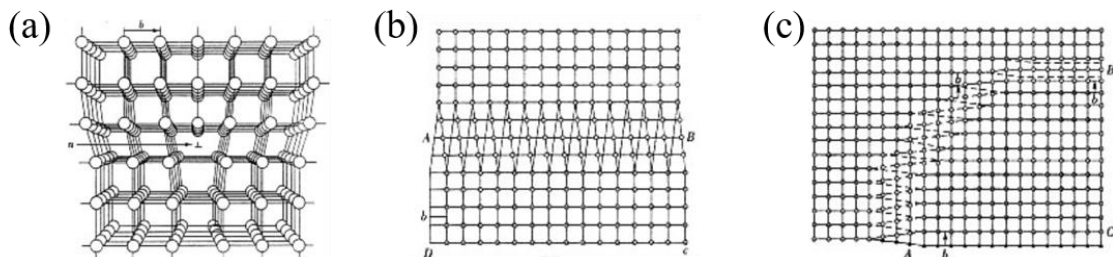
Fig. 2.21 Edge dislocation (a), Spiral dislocation (b) and Fixed dislocation (c)

Motion is an important aspect of the nature of dislocations; without motion of dislocations, there would not be plastic deformation of crystals, and the ease of dislocation motion is directly related to the strength of crystals. In salt rock, as a typical homogeneous crystalline material, dislocations are commonly used to explain its creep deformation. For inelastic deformation, dislocations are the most important crystal defects in salt rocks [236].
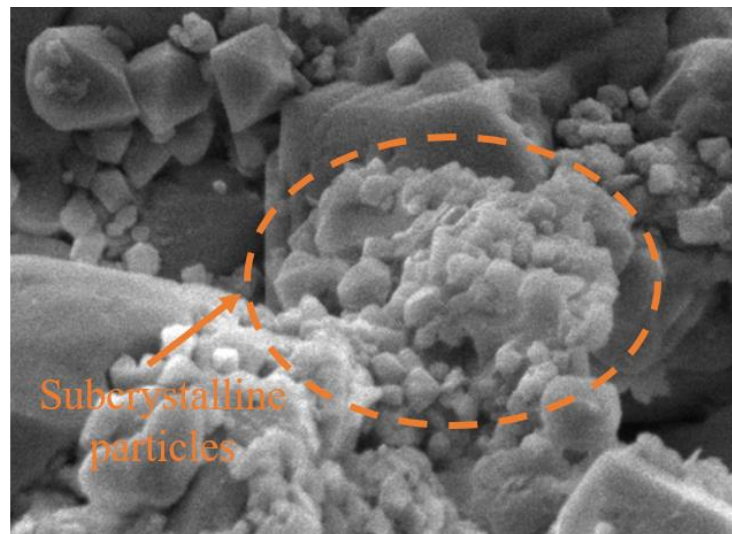
Fig. 2.22 Large number of subcrystalline particles produced by dislocation creep (orange dashed oval).

When subjected to external loading, the dislocations within the crystal will slip or climb to achieve creep deformation [237]. During this process, the crystals of salt rocks will gradually subcrystallize, and the diameter of the subcrystals shows a negative correlation with the deviator stresses applied to the crystals. The crystal changes are shown in Fig. 2.22. Adjacent grains may have different dislocations, and their intersections are called grain boundaries. Smaller crystals with different dislocations within the grains are subcrystals, and the interface between the grains is called the subcrystal boundary. The deformation of salt rock crystals includes the deformation of the grains themselves, as well as the deformation caused by the slip of the grain boundaries. Neighboring grains may have different dislocations and their intersections are called grain boundaries. A grain boundary is a natural facet defect. Saltstone is a polycrystalline composite medium consisting of many grains, each of which is a small

single crystal. Neighboring grains have different orientations and their intersections are called grain boundaries. The interior of the crystal grains often consists of many crystal blocks with small differences in orientation, and the interfaces between the blocks are called subgranular boundaries. The structure of the crystal surface is different from that of the crystal interior. Since the surface is the termination surface of atomic arrangement, there is no bonding of atoms in the solid on one side, and its coordination number is less than that of the crystal interior, which leads to the deviation of surface atoms from their normal positions and affects the neighboring layers of atoms, resulting in a point distortion that is higher than that in the crystal interior in terms of energy. The deformation of salt rock crystals includes the deformation of the grains themselves, as well as the deformation caused by grain boundary slip.

The results of related tests show that the greater the difference in orientation between two crystals, the greater the amount of slip; in this case, the creep rate increases. While primary slip occurs at the grain boundary, secondary slip may also occur in the grain boundary affected zone (GBAZ) [238] due to stress concentration, and both temperature and stress can affect the size of GBAZ [239]. At the same time, if the difference in orientation between the two crystalline surfaces is smaller, the amount of slip is smaller, which means that the creep rate decreases. During the creep-fatigue experiments [240], the unloading and reloading of stress changes the inherent arrangement between the salt rock crystals in the high stress plateau, leading to crystal disorder (Fig. 2.23). As the difference in orientation between the crystals increases [241], the rate of salt rock creep increases in our analysis of the fatigue-accelerated creep rate. At the same time, as dislocation creep proceeds, dislocation interception and plugging will prevent the dislocation from continuing to slip[242]; to make the dislocation move again or continue to deform, a greater external force will be required or the environmental factors will be changed to make the dislocation overcome these obstacles. This is also the reason why the residual strain after the high stress plateau is smaller than before the plateau, which can be seen as equivalent to a slight increase in the strength of the salt rock after the high plateau and thus an increased ability to resist deformation.
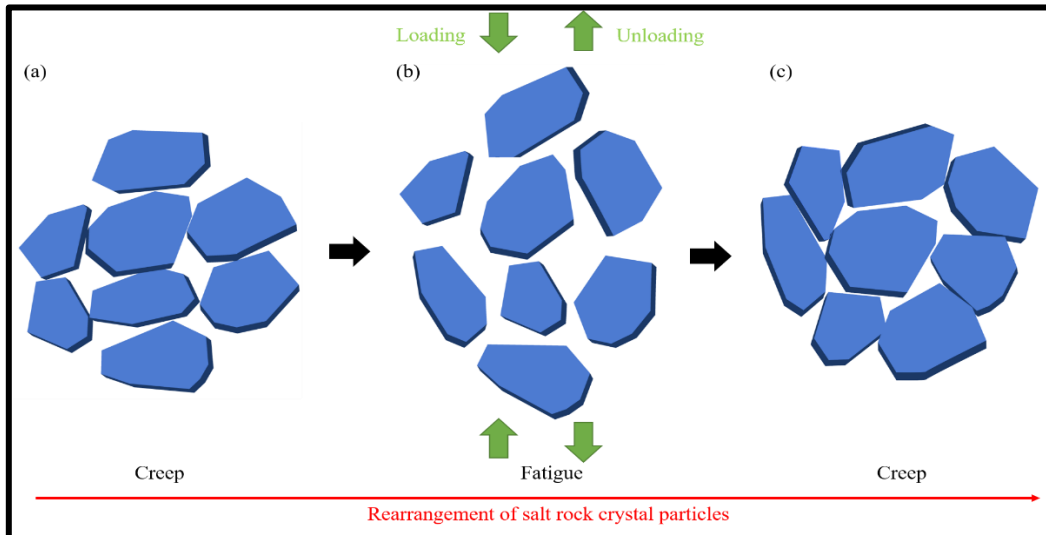
Fig. 2.23. Schematic diagram of the macroscopic level of the salt rock: (a) the last creep stage, (b) the cyclic loading stage after creep stage, and (c) the creep stage after cyclic loading.

Under a constant load, the creep-generated microhole defects gradually develop and continue to grow and then link with surrounding holes to form microcracks, which further link and converge to form the main crack through the crystal. In the later stage of the creep-fatigue test, when the creep-induced grain-piercing cracks meet the fatigue-induced cracks along the grain fractures or grain-piercing fracture cracks and converge, an interactive effect arises that accelerates the damage of the specimen (Fig. 2.24). Therefore, the effect of creep-fatigue loading on the surrounding rock must be considered when evaluating the safety factor of CAES plants using salt caverns.
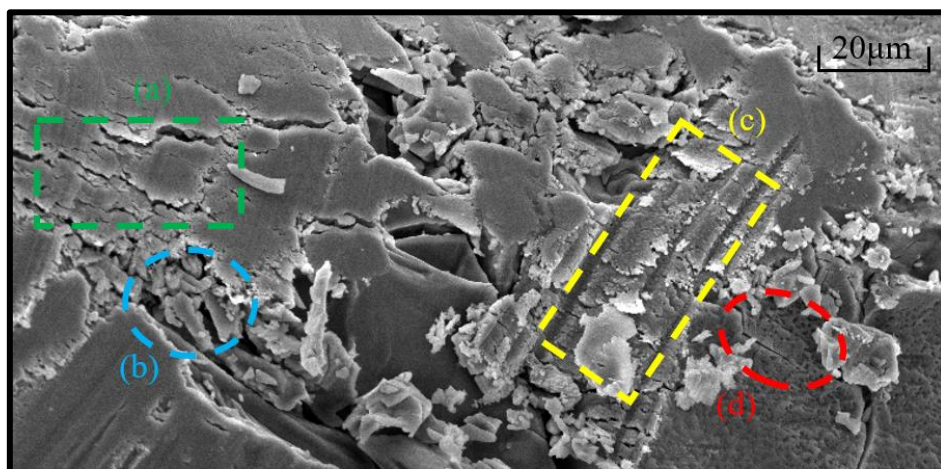
Fig. 2.24 The scanning electron microscopy image of a salt rock specimen: (a) The green box shows fatigue microcracks and throughgoing cracks, (b) the blue circle shows the grains

produced by the crushing of salt rock crystals, (c) the yellow box shows the traces of crystal slippage during cyclic loading, (d) and the red circle shows the crystal-piercing cracks produced during creep.

2.5 Conclusions

Due to the need for peak demand CAES power station in the change of gas pressure will exist in a certain time interval, that is, salt cavern reservoir surrounding rock is subjected to creep - fatigue alternating action. Therefore, when evaluating the stability of the salt cavern reservoir, the creep-fatigue mechanical properties of the salt rock need to be specifically studied. In this chapter, the creep-fatigue interaction of salt rock is investigated by setting different high stress plateaus durations (0, 5, 10, 15 and 20 min), and the reasons for the interaction are explained from a microscopic point of view. The main conclusions are as follows:

(1) The development law of creep-fatigue stress-strain curves is similar to that of conventional fatigue tests, and is also divided into three stages of combing-intensive-combining. The cyclic load has a promoting effect on creep deformation, but this promoting effect is gradually weakened with the increase of the high stress plateau time, and the creep deformation seems minimal when the high stress plateau is 15min.

(2) The residual strain before the high stress plateau of the creep-fatigue test is greater than that after the high stress plateau, which is different from the results of the conventional salt rock fatigue test. With the increase of the time of the high stress plateau period, the difference of residual strain before and after the plateau increased, but this increase seems to saturate.

(3) The fatigue life of the salt-rock specimens decreases and the creep life increases with the increase of high-stress plateau duration. According to the creep-fatigue damage equation, it can be obtained that there is an interaction between creep and fatigue during the salt rock creep-fatigue test.

(4) During cyclic loading, the rearrangement of salt rock crystals accelerates the creep rate of salt rock during high stress plateaus. The cross-cutting and plugging of dislocations within the salt rock prevented the dislocations from continuing to slip, which in turn hardened the salt rock, resulting in a larger residual strain in the cycle before the high-stress plateau than in the cycle after the plateau.

3 Creep-fatigue mechanical characterization of salt rock under triaxial stresses

3.1 Introduction

Salt cavern reservoirs used in CAES power plants are often located deep underground, and the surrounding rock of the reservoir is in a triaxial stress state [243]. When the cavity is formed by water-soluble mining, the original stress balance of the reservoir surrounding rock is changed, and the differential stress in the stress field will cause continuous deformation of the surrounding rock. For all rock materials, the existence of confining pressure on the one hand increases the ultimate strength of the rock and improves the bearing capacity of the rock; on the other hand, it increases the toughness of the rock, so that some of the rocks in the shallow part of the performance of ordinary hard rocks, in the deep part of the performance of the large deformation of the soft rock characteristics. With the increase of the confining pressure, the rock will be transformed from brittle response to full ductile response, which is especially important for salt rocks, and the temperature and confining pressure ranges in which the transformation occurs are much smaller than those of other types of rock materials [244]. The effect of the confining pressure on the ductility of salt rock is quite significant. Therefore, in order to be closer to the engineering reality and to reveal the creep-fatigue mechanical properties and damage evolution law of underground salt cavern surrounding rock, it is necessary to carry out triaxial salt rock creep-fatigue tests under different confining pressures on the same basis as creep-fatigue tests reported in Chapter 2.

3.2 Experimental materials and methods

Specimen material and preparation and test equipment are similar to the content of Chapter 2, and will not be repeated here. Only the new test procedures are introduced.

3.2.1 *Triaxial creep-fatigue procedure*

Geological conditions such as the general burial depth of the salt cavern storage and testing conditions such as the maximum capacity of the testing machine, were both taken into consideration. Four confining pressure (σ_c) values were considered: 3 MPa, 6 MPa, 9 MPa and 12 MPa. Firstly, 12 salt rock samples were tested under monotonic compressive loading until failure, at different σ_c. Each σ_c level was repeated three

times, and the average triaxial compressive strength (TCS) are given in Table 3.1. The results for uniaxial compressive tests presented in Chapter 2 are repeated here for comparison.

Table 3.1 Compressive strengths of the salt rock samples under various confining pressure.

Confining pressure/MPa	Test No.1	Test No.2	Test No.3	Average TCS/MPa
0	29.5	30.2	30.6	30.1
3	54.3	57.5	61.6	57.8
6	71.1	78.2	73.3	74.2
9	86.8	84.7	90.4	87.3
12	102.5	108.6	100.3	103.8

According to the average TCS for different σ_c, the stress level for triaxial creep–fatigue tests were designed. For each confining pressure, the upper stress $\sigma_{a,max}$ is taken equal to 85% of the peak differential stress, and the lower stress $\sigma_{a,min}$ is set to 3% of the peak differential stress, as given by the following equation:

$$\begin{cases} \sigma_{a,max}=0.85(\sigma_{TCS}-\sigma_c)+\sigma_c \\ \sigma_{a,min}=0.03(\sigma_{TCS}-\sigma_c)+\sigma_c \end{cases} \tag{3.1}$$

The values for upper and lower stresses are presented in Table 3.2. Note that the plateau duration is fixed to 5min in this test series.

Table 3.2 Parameters adopted in the TCFT.

Confining pressure/MPa	Upper stress bound/MPa	Lower stress bound/MPa	Plateau time/min
3	49.2	4.56	5
6	64.1	8.2	5
9	76.2	11.6	5
12	90.5	14.8	5

The tests are defined as triaxial creep–fatigue (TCF)tests. For the TCF tests, the ratio of the upper to lower stress bounds is the same, despite different σ_c. The specific loading and unloading paths are as follows: Initially, using a computer-controlled program, the σ_c is increased to a predetermined level. Subsequently, the axial stress is increased at the loading rate of 2 kN/s up to $\sigma_{a,max}$, where it is also held T-stage. This step is carried out to simulate the rheological condition of the surrounding rock of the salt cavern after the initial injection of air owing to the sustained high-pressure environment, consistent with the purpose of the uniaxial creep fatigue test. This T-stage is then followed by a decrease in stress to $\sigma_{a,min}$ at the same 2 kN/s rate. After, linear

loading and unloading are applied between $\sigma_{a,min}$ and $\sigma_{a,max}$ still at a rate of 2 kN/s, and a high stress plateau of duration Δt= 5min is applied every two cycles, as shown in Fig 3.1. The testing utilized a higher maximum stress level, $\sigma_{a,max}$, and a lower minimum stress level, $\sigma_{a,min}$, than actual operating pressure of the CAES salt cavern (Minimum air pressure 10mpa, Maximum air pressure 25mpa). This was primarily done to minimize the duration of the testing, enabling a full test to be conducted within a single workday.
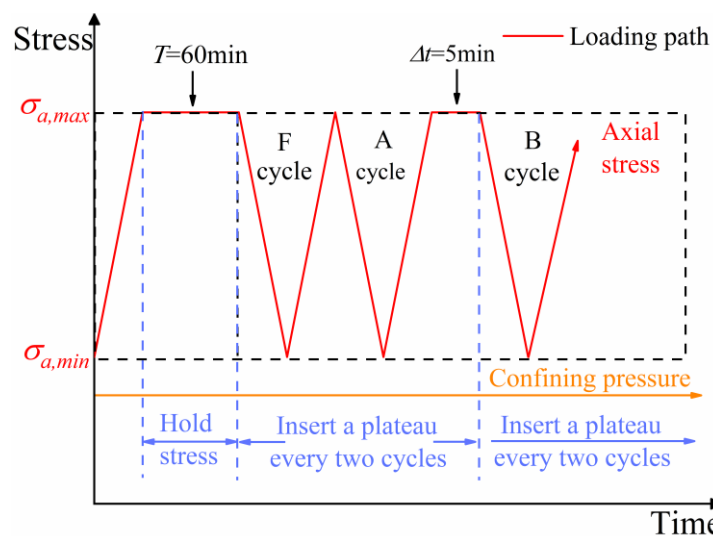
Fig. 3.1 Loading paths during the triaxial creep–fatigue (TCF) tests.

The term "A cycle" refers to the cycle before the high-stress plateaus and "B cycle" to the cycle after the high-stress plateaus. The first cycle (F) belongs to is neither a pre-plateau nor a post-plateau and is called the first cycle. As for uniaxial creep-fatigue tests presented in Chapter 2, the purpose of this setup is to compare and analyze the impacts of two different stress cyclic loadings on the mechanical behaviors of salt rocks in the same samples and to avoid specimen variability.

3.2.2 *Test procedure*

(1) Installation of test pieces, swabbing the end face of the upper and lower pressure head, the test piece is placed between the upper and lower pressure head, so that the center of the three into a straight line; and then the test piece and the sting block set on the heat shrinkable oil-proof sleeve and blowing tightly, with adjustable stainless steel hoop to close the test piece. Lower the triaxial chamber, screw the triaxial chamber

fixing screws and top closing screws.

(2) Start the MTS815 rock mechanics test system and apply 0.1 kN~0.5 kN pressure to fix the specimen. Then open the exhaust valve of the pressure chamber, start the peripheral pressure oil pump, inject oil into the pressure chamber, exhaust the air while injecting oil, and tighten the exhaust valve when the air in the pressure chamber is exhausted.

(3) loading: 0.05 MPa / s loading speed to apply pressure to a predetermined pressure value, in the test process so that this side of the pressure value remains constant, the range of change should not exceed the selected value of ± 2%. Then the computer-controlled program is used to apply a predetermined load until the specimen is destroyed. Subsequently, the pressure is unloaded and the specimen is removed and the damage condition is recorded.

3.3 Test results and analysis

3.3.1 *Stress–strain curve in the triaxial creep-fatigue tests*
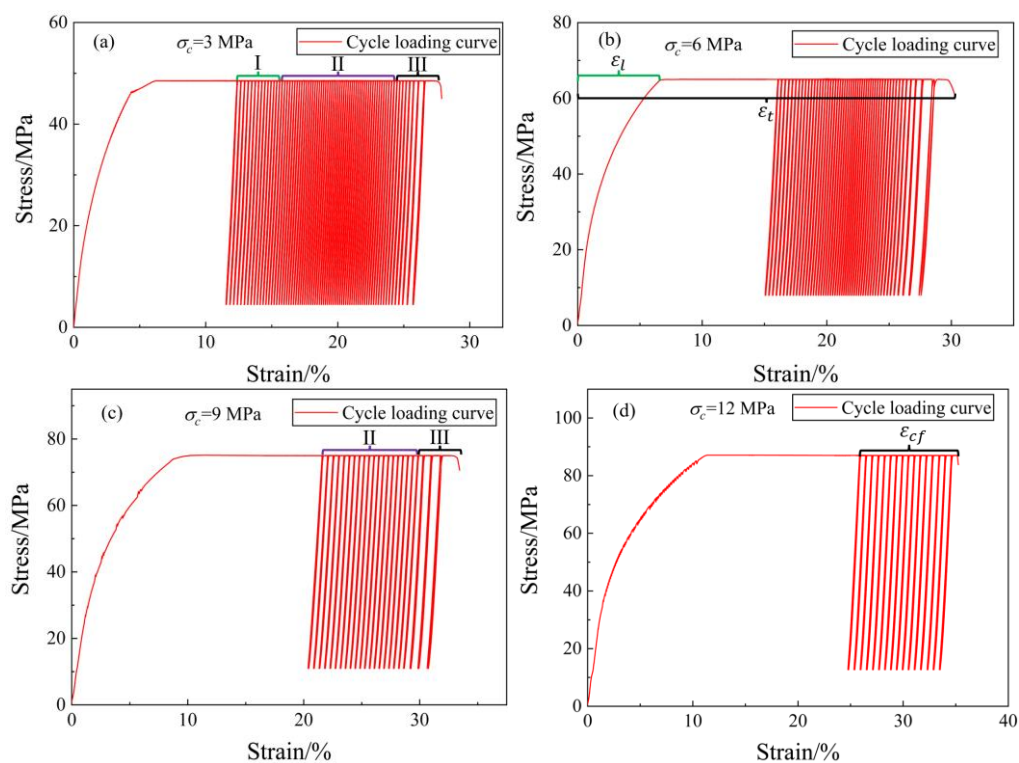
Fig. 3.2 Stress–strain curves for TCF tests with confining pressure values of (a) 3 MPa, (b) 6 MPa, (c) 9 MPa and (d) 12 MPa.

The TCF tests results under various confining pressure σ_c are shown in Fig. 3.2. Taking the result under σ_c = 3 MPa as an example, it is observed that, after initial loading causing a deformation, the high-stress plateau lasting one hour (T-stage) causes significant deformation as well. During the subsequent alternating creep-fatigue stage, the experimental curve exhibits, again, three distinct deformation stages of sparse-dense-sparse, namely the decelerating deformation stage (I), the stable deformation stage (II), and the accelerating deformation stage (III), illustrated in Fig 3.2(a). This indicates that the TCF test follows the characteristics of a conventional fatigue test [245]. This TCFT is also very similar to the pure fatigue test (no upper stress plateau) under triaxial loading (Ren et al., 2013). However, the significant difference is that the proportion of II stage for the stress–strain curve are more obvious of a pure fatigue test under triaxial loading [164]. Stage I of the stress–strain curve is significantly condensed in the TCF test, as it is in the creep–fatigue test with uniaxial loading. Stages II and III are more prominent. These results exhibit the characteristic of three-stage in the TCF test with σ_c changes. Firstly, the deformation of stage I shortens, because the salt rock specimens are compacted and densified during the one-hour high-stress plateau. Secondly, as the σ_c increases, the densification effect of the σ_c leads to the fusion of stage I and stage II of the experimental curve, and the proportion of deformation in Stage II to the total deformation increases. Thirdly, the presence of stage III rather than stage I is more evident during the test with σ_c are 3,6,9MPa, reflecting the change in the high-stress plateau from a compaction/density effect to the force driving the specimen destruction during the final damage phase of the creep–fatigue test. Finally, When the σ_c rises to 12 MPa, the transition from II to the III stage also becomes unclear, the whole stress–strain curve shows the characteristics of only one stage.

To reflect the impact of the σ_c on the creep–fatigue deformation of salt rocks, the total strain of the test specimen is defined as ε_t and the strain of the first loading of the

specimen to the upper stress is defined as ε_l (see Fig 3.2 (b)). The strain after the first loading, $\Delta\varepsilon$, can be calculated as:

$$\Delta\varepsilon = \varepsilon_t - \varepsilon_l \tag{3.2}$$

According to Fig. 3.3, with increasing σ_c, ε_t shows an increasing trend. This is because as σ_c increases, the loose salt rock particles originally damaged by the stress are compacted tightly, the internal fissures are closed more completely, the fissure surfaces that can produce slip are locked, the self-healing effect is enhanced and the structure of the salt rock is more solid [246]. A similar trend is shown for $\Delta\varepsilon$. This reflects that the salt rock behavior gradually changes from brittle–ductile to ductile with the σ_c increase. This increasing plastic deformation capacity, reported extensively for monotonic loading, is also observed here under cyclic loading.
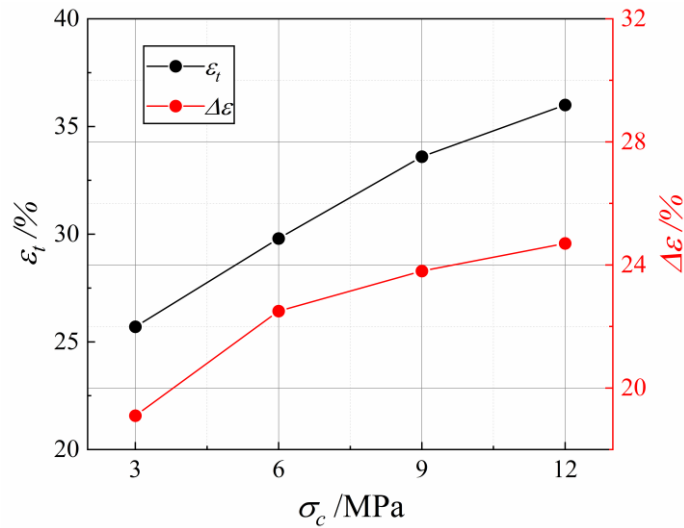
Fig. 3.3 The total strain before failure (ε_t) and strain after first loading ($\Delta\varepsilon$) for TCF tests under different confining pressure values.

The fatigue and creep lifes of salt rock specimens under different σ_c, shown in Fig. 3.4, are found to decrease with confining pressure increasing. This is not exactly consistent with the triaxial pure fatigue test [247]. Our results can be explained by the influence of two types: Firstly, the addition of creep results in a greater deformation during the creep period at higher upper stress limits, causing a reduction in the percentage of plastic deformation generated by fatigue and a decrease in fatigue life.

Secondly, the impact of the one-hour high stress plateaus following the initial loading on the creep deformation of salt rock is non-linear. This leads to a decrease in the proportion of alternating creep-fatigue deformation stages to the total strain in high-confining pressure test samples. The implications of this outcome for the construction of salt cavern reservoirs will be discussed in section 3.4.
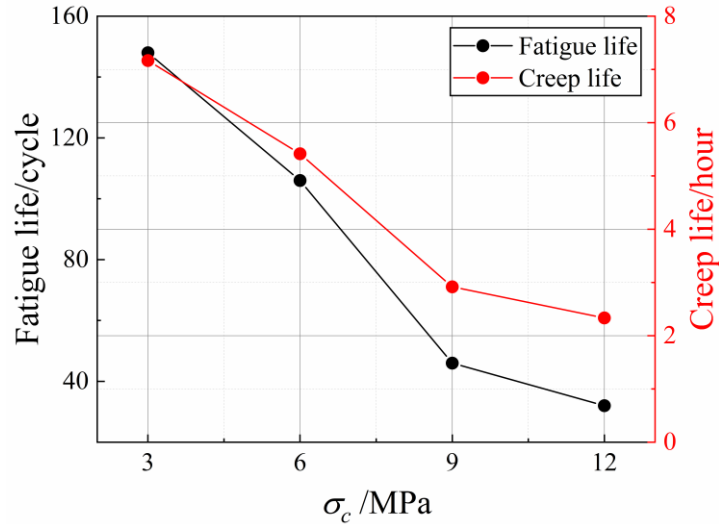
Fig. 3.4 Fatigue life and creep life for TCF tests under different confining pressure values.

3.3.2 *Impact of confining pressure on residual strain in salt rocks during the triaxial creep–fatigue tests*

In order to reveal the effect of confining pressure on the triaxial creep-fatigue test of salt rock, the residual strains of salt rock specimens under four confining pressure values, calculated as in section 2.3.3, are shown in Fig 3.5.
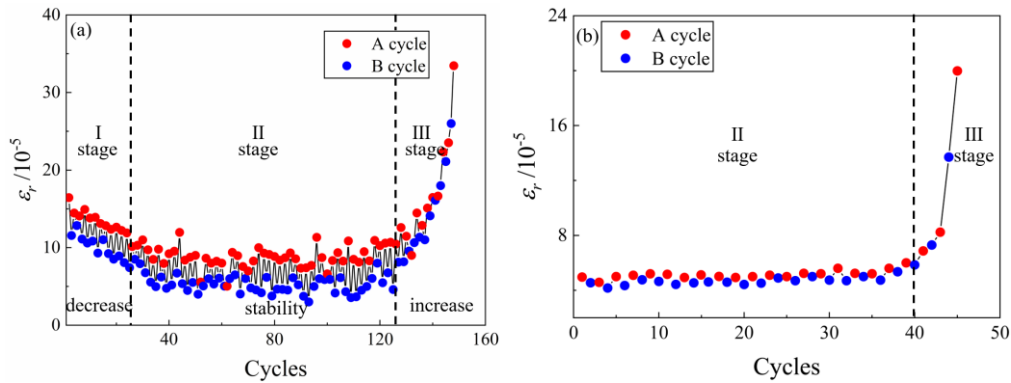
Fig. 3.5 Axial residual strain (ε_r) at each cycle for TCF tests at confining pressure values of (a) 3 MPa and (b) 9 MPa.

The residual strain ε_r of the TCF tests on salt rock under 3 MPa and 9 MPa σ_c were selected for analysis. We find that the ε_r distribution is not the same as for conventional fatigue test. The two confining pressure values present the same characteristics, i.e., larger values of ε_r in cycle A than in cycle B, which is consistent with the conclusion obtained from the uniaxial creep–fatigue tests presented in Chapter 2. The same phenomenon was observed for the confining pressure values of 6 MPa and 12 MPa TCF tests. This indicates that the presence of the σ_c does not change this phenomenon. The reason for this phenomenon is the compaction of the salt rocks crystals under the high-stress plateaus and the accumulation of material filling the internal cracks. It can be assumed that hardening occurs during the creep stage, causing the specimen to resist deformation more. Thus, the compressive strength of the salt rocks is raised.

Comparing the ε_r of the tests at σ_c of 3 MPa and 9 MPa, the apparent difference is that the ε_r of the 3 MPa test still exhibits a clear decelerating deformation stage. In the alternating creep–fatigue phase, stage Ⅰ slowly decreases to the stable Ⅱ stage. The ε_r in the 9 MPa test goes directly to stage Ⅱ, followed by rapid destruction in the accelerating deformation stage. This is similar to the pattern exhibited by the creep–fatigue stress-strain curves of salt rocks, as discussed on the section 3.3.1.

In addition, the difference in ε_r between cycle A and cycle B varies significantly with σ_c. The difference in ε_r for 9 MPa is less important than for 3 MPa. To more accurately compare the effects of different σ_c on ε_r before and after the high-stress plateau, the average residual strain difference between cycle A and cycle B, $\Delta\overline{\varepsilon}_r$, during the stable deformation stage (stage Ⅱ) was computed by Eq (2.6), (2.7), (2.8) defined in section 2.3.3. Figure 3.6 shows the calculated results.
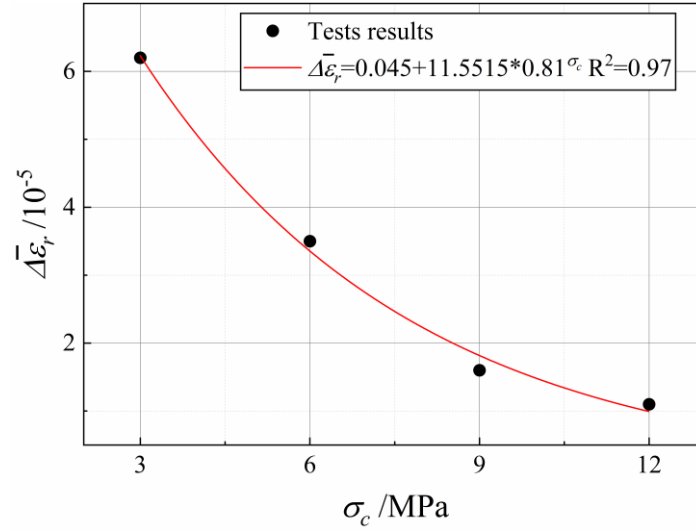
Fig. 3.6 Average residual strain difference between cycles A and B ($\Delta\bar{\varepsilon}_r$) for TCF tests under different confining pressure values.

$\Delta\bar{\varepsilon}_r$ exhibits a declining exponential trend with rising σ_c and the rate of decrease slows. Because as the σ_c rises, the upper stress bound increases with the same stress ratio. The salt rock is compacted more tightly during the creep stage. As the test proceeds, the fractures inside the salt rock will completely close during the high-stress plateau. The initial defects and cracks have difficulty further developing. The hardening effect in the creep stage is no longer obvious, and $\Delta\bar{\varepsilon}_r$ decreases. The decreasing rate indicates that the development and expansion of microcracks are suppressed after the increase in the σ_c reach a certain level. The high σ_c prevents relative slip between the grains of the salt rock. As the increase in the σ_c, it is difficult for damage to evolve, even if the resulting plastic flow produces large deformation [248]. The impact of the σ_c in the creep–fatigue behavior of the salt rocks reaches a threshold.

3.3.3 *Impact of confining pressure on creep deformation in salt rock in the triaxial creep–fatigue tests*

For triaxial creep-fatigue tests, the creep rate and deformation are more important because the brittle-ductile response due to confining pressure is more pronounced for soft rocks. The same equation (2.3) as in section 2.3.2 is used for the calculation of creep rate v_c.
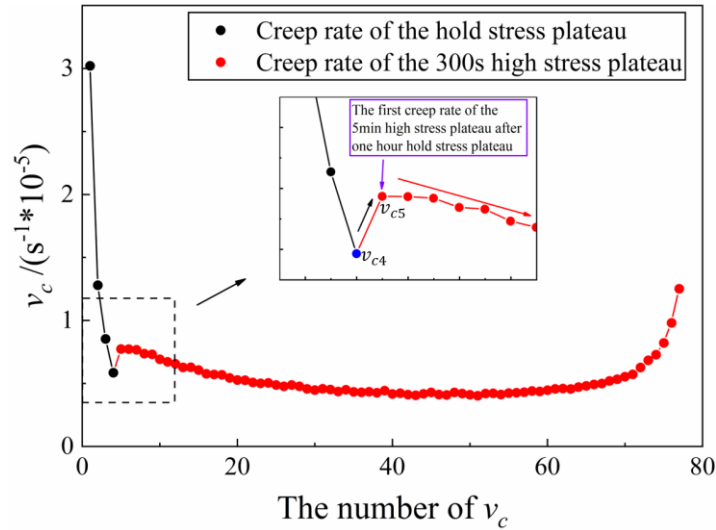
Fig. 3.7 Creep rate (v_c) for TCF test at 3 MPa confining pressure. The black dot is the v_c at the one-hour high-stress plateau, and the red dot is the v_c at the high-stress plateau during the fatigue creep stage.

Taking the TCF test under 3 MPa for analysis, the test results are shown in Fig. 3.7. First, it can be found that the curve is very similar to the curve obtained for uniaxial creep-fatigue test. During the initial T stage, the v_c of the salt rocks show a nearly linear decreasing tendency, but the rate of decrease slows. This indicates that at the higher stress level, the interior structure of the salt rock undergoes rapid adjustment, a large number of fractures are filled and closed, a hardening phenomenon occurs, and the resistance to deformation is enhanced. While entering the creep–fatigue stage, after two cycles of loading, v_c shows a jump, followed by a slow decline into the stable deformation stage. During this stable stage, v_c remains basically unchanged.
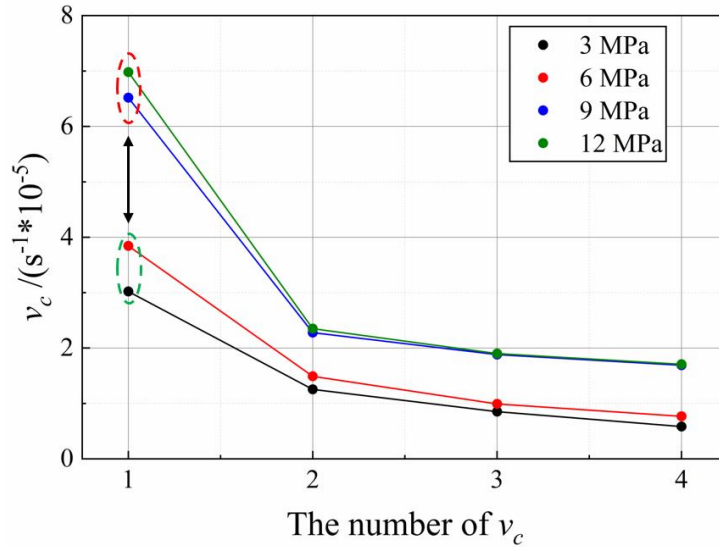
Fig. 3.8 The trends of the first four v_c values during the T stage under different confining pressure.

Figure 3.8 reflects the variation in the creep rate in the initial one-hour high-stress phase of the salt rocks under different σ_c. The creep rate development patterns of the four tests are similar, but the creep rate at larger confining pressure values is much larger than the creep rate at lower confining pressure values. In addition, the distribution of the creep rate also shows obvious zoning characteristics; that is, the creep rates of the samples under σ_c of 12 MPa and 9 MPa (within the red dashed circles) are significantly larger than those of 6 MPa and 3 MPa (within the green circles). The reasons for the above phenomenon are as follow: One reason is that the increase in the upper stress plateau (with the confining pressure) causes the creep rate to increase. Another reason concerns the brittle–ductile transformation for the salt rocks [249]. It has been pointed out that the σ_c has a significant impact in the microfracture and shear expansion of salt rock [250]. The plastic deformation at a low σ_c is dominated by crack extension, while the plastic deformation at a high σ_c is dominated by the dislocation mechanism. With the σ_c increases, the salt rock shows super mobility and significant ductile characteristics [251]. The deformation characteristics of the salt rock are no longer obvious with the change in the σ_c. In this work, we speculated that 6-9 MPa is the critical σ_c for the brittle–ductile transformation of salt rocks, which should be verified by more tests in the future.

The incorporation of fatigue was able to enhance the v_c of the salt rocks during the high-stress plateaus stage, which was demonstrated in all four sets of tests. However,

the effect of different σ_c on the increase in v_c differs. For this purpose, we calculated the ratio of the last v_c datapoint of the first T stage to the first v_c datapoint in the creep–fatigue stage for the salt rock separately and defined it as the growth rate β defined as:

$$\beta = \frac{v_{c5}}{v_{c4}} \tag{3.3}$$

where v_{c5} and v_{c4} indicate the 5th and 4th creep rates in the different TCF tests, respectively, as shown in the detail of Fig 3.7. The statistical result with different σ_c is shown in Fig. 3.9. The growth rate tends to decrease linearly with increasing σ_c. The reason why cyclic loading elevates the creep rate is that the unloading and loading of pressure opens the otherwise closed fracture surfaces and continues to produce slip at the next high-stress plateau. The presence of the σ_c inhibits this behavior, and this constraint becomes more pronounced as the σ_c increases. Similar to the reason for the decrease in residual strain difference, this effect will not change when the confining pressure reaches a threshold. Note that the value of this growth rate is influenced by the choice to split the first T stage into 4 segments. However, it was verified that the growth rate decreases linearly as a function of confining pressure, whatever the chosen number of segments.
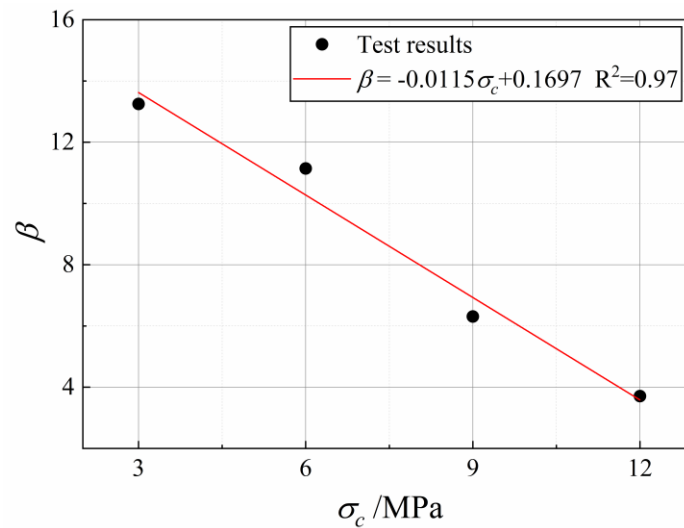
Fig. 3.9 Ratio beta of the last v_c of the first T stage and the first v_c of the creep–fatigue stage in four TCF tests.

To illustrate the impact of different σ_c on creep deformation at a given time, we calculated the average creep strain $\bar{\varepsilon}_c$ of the salt rock during second stage as:

$$\bar{\varepsilon}_c = \frac{\sum_j^k \varepsilon_{ci}}{k-j} \qquad (3.4)$$

where j and k indicate the beginning and end loading cycle numbers of the second stage in every TCFT. The results are plotted in Fig. 3.10.
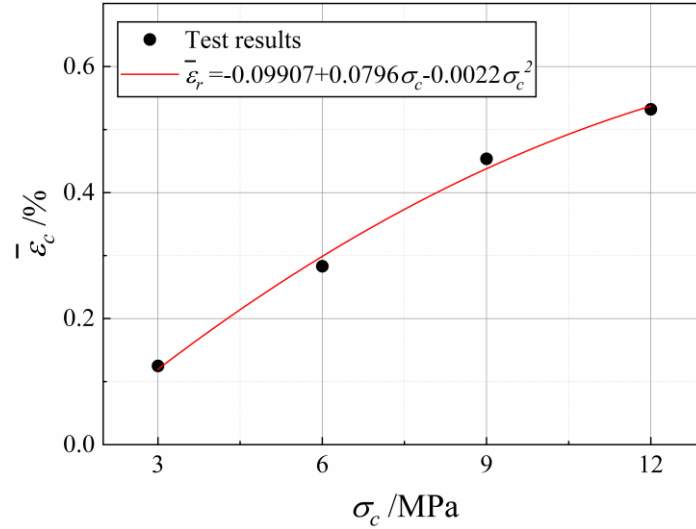
Fig. 3.10 Average creep strain during the high-stress plateau in the stable deformation stage under different confining pressures.

As the σ_c rises, the $\bar{\varepsilon}_c$ of the salt rocks increases significantly in the high-stress plateaus stage. The $\bar{\varepsilon}_c$ of the 12 MPa test is nearly five times higher than that of the 3 MPa test. This is consistent with the evolutionary model on the stress–strain curve in a TCF test.

3.4 Analysis of confining pressure effects on creep-fatigue properties of salt rocks

3.4.1 *Influence of the increase of the confining pressure on the transformation of brittle ductility in salt rocks*

Considering the three-dimensional stress states of underground geotechnical engineering, the research of the mechanical properties of rocks under triaxial stress can reflect the actual loading of underground works more realistically. Researchers have also conducted many triaxial mechanical tests on rocks, and this approach is especially important for salt rock. In contrast to the pure fatigue test on salt rock under triaxial

stress, the introduction of a high stress plateau causes hardening of the salt rocks during the creep phase, resulting in a lower ε_r for the B cycle following the high-stress plateaus than the A cycle before it. At the same time, the introduction of cyclic loading changes the inherent arrangement of salt rock crystals on the high-stress plateaus during unloading and reloading of stress, leading to crystal disorder. As the differences in crystal orientation between crystals increase, the v_c also increases. This is consistent with the reasons for the above phenomena observed in uniaxial creep-fatigue tests. The uniqueness of triaxial testing lies in the fact that with increasing σ_c, both the ε_r difference between the fatigue cycles before and after the high-stress plateaus and the enhancement impact of fatigue on the v_c are reduced. This is because the σ_c inhibits the expansion of fatigue cracks and the slip of salt rock crystals, and this effect becomes more significant with increasing σ_c.

All the rock behavior transforms from a brittle response to a full ductile response with the σ_c increases. However, the transformation pressure of salt rocks (6-9 MPa) is lower than that of other rock materials [244,252]. Under uniaxial compression, salt rocks exhibit certain brittle characteristics, and damage occurs within a small strain range. At this time, the cracks of salt rocks are related to mainly tensile damage, and the cracks will develop along the lower-strength grain boundaries [253]. With increasing axial stress, cracks along the macroscopic cleavage along the direction of the maximum principal stress are formed. At low σ_c (3 MPa for Fig. 3.11(a) and 6 MPa for Fig. 3.11(b)), the plastic zone of the salt rock is extended, and there is a plastic flow phenomenon. Finally, the specimen is sheared along a single oblique plane of damage. However, at σ_c of 9 MPa (Fig. 3.11(c)), the salt rock exhibited stronger flow. On the surface of that damaged specimen, X-shaped conjugate shear zones were observed, but none of them were significantly expanded yet. This indicates that as the increase in the σ_c, the initiation of damage to the specimen is gradually delayed, the accumulated crack volume and the accumulated damage caused by shear cracks increase, and the development of cracks becomes increasingly difficult [254]. We speculate that 6-9 MPa can be regarded as the critical σ_c for the brittle-ductile transformation of salt rocks. When the σ_c continues to rise to 12 MPa (Fig. 3.11(d)), the final damage morphology of the salt rock specimen shows a short, thick cylindrical shape, similar to a drum, with only a few cracks hardly visible.
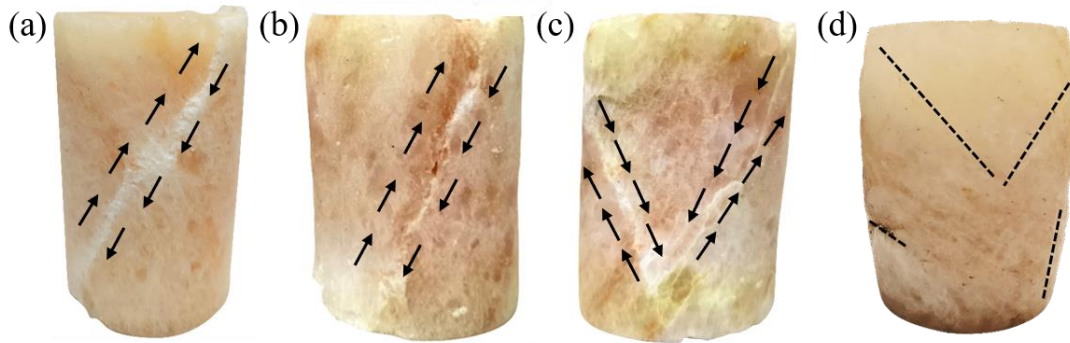
Fig. 3.11 Photos of salt rock specimens after testing under different confining pressure values

(a) 3 MPa, (b) 6 MPa, (c) 9 MPa, (d) 12MPa.

However, there is a lack of quantitative indicators for evaluating and judging the degree and state of the ductile deformation of salt rocks. We surmise that the ratio of creep strain for the first high-stress plateau after two cycles of loading and mean creep strain of the middle 5% of the cycles during the creep–fatigue stage, i.e., the compression density coefficient (α), can be used to illustrate the degree of ductile deformation of the salt rocks in this test. The compression density coefficient results are shown in Fig. 3.12; here α shows a decreasing trend with increasing σ_c and is reduced to approximately 1.07 under 12 MPa of σ_c. We believe that after reaching a certain σ_c, the internal fractures in the salt rock are likely to close completely; thus, the initial defects have difficulty developing. It is difficult for the fatigue cycle load to cause the salt rock fracture surfaces to slip again, and the salt rock specimen truly becomes a uniformly dense rock sample at the macroscopic scale.
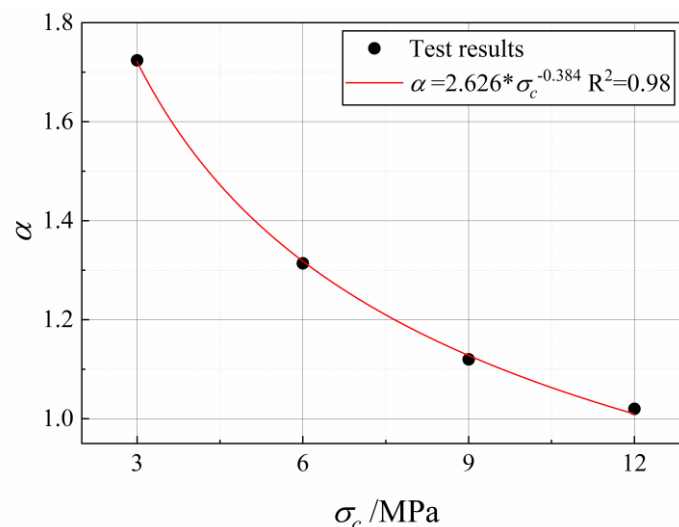
Fig. 3.12 Pressure density factor alpha under different confining pressure values.

Another point of interest is that the total strain ε_t and strain after first loading $\Delta\varepsilon$ of the salt rock indicates an increasing trend as σ_c rises. Nevertheless, the percentage of strain in the creep–fatigue alternating phase (ε_{cf}) to total strain (ε_t), shown in Fig 3.2(d), defined as γ indicates a decreasing trend. As shown in Fig. 3.13, γ under a low σ_c is still above 50%, but γ under 12 MPa of σ_c is only 32.1%. This indicates that the high stress has a greater impact in the deformation for the salt rocks at the T stage under equal stress ratio conditions.
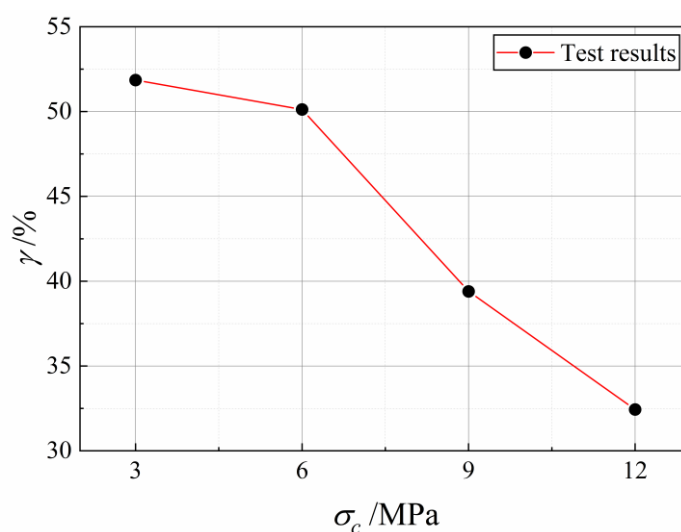
Fig. 3.13 Strain ratio gamma of alternating creep–fatigue stages to all the stress–strain curve stages for different confining pressure values.

The effect of increasing the confining pressure on the one hand increases the ultimate strength of the rock and improves the bearing capacity of the rock; on the other hand, it increases the toughness of the rock, so that some of the rocks, which behave as ordinary hard rocks in the shallow part of the rock, show the characteristics of large deformation of the soft rock in the deep part of the rock. From the results of the compression test, it can be seen that the Young's modulus and deformation capacity of the salt rock become larger with the increase of the confining pressure. Because the confining pressure can limit the generation and expansion of salt rock cracks and prevent the relative slip between salt rock grains, the strength and ductile deformation capacity of salt rock are enhanced. But with the increase of the confining pressure, this effect of the confining pressure is getting smaller and smaller. Therefore, it is possible

to reach a certain confining pressure, salt rock internal cracks completely closed, the original defects are difficult to develop, salt rock specimens really become macroscopically homogeneous and dense rock samples, and the same as found by other researchers, to get Young's modulus has nothing to do with the confining pressure of the conclusion. Because Young's modulus (elastic modulus) as an inherent property of rocks should not vary with the confining pressure. However, due to the presence of natural rock defects, the elastic modulus may show an increasing trend with increasing confining pressure. But when the confining pressure reaches a certain value, the internal primary cracks and defects in the rock will close. The rock then becomes an ideal state, appearing macroscopically as a uniformly dense rock, and at this point, Young's modulus becomes independent of the confining pressure [255].

3.4.2 *Mechanical interpretation of salt rocks affected by confining pressure and the effect of burial depth on the deformation of surrounding rock of the salt cavern*

The brittle fracture evolution is very important for understanding the damage mechanism of rocks, and a large amount of literature has been published to study the fracture process of rocks. The results show that the confining pressure plays an important role in the damage and destruction of brittle rocks. The peak strength, damage evolution and damage pattern of specimens depend on the confining pressure. Moreover, the compressive strength of rocks increases in a nonlinear manner with increasing the confining pressure [256].

The reasons for the deformation affected by confining pressure are explained below in terms of theoretical mechanics. The stress tensor at a point can be decomposed into two parts: the spherical tensor part and the bias tensor part：

$$\begin{bmatrix} \sigma_{11} & \sigma_{12} & \sigma_{13} \\ \sigma_{21} & \sigma_{22} & \sigma_{23} \\ \sigma_{31} & \sigma_{32} & \sigma_{33} \end{bmatrix} = \begin{bmatrix} \sigma_0 & 0 & 0 \\ 0 & \sigma_0 & 0 \\ 0 & 0 & \sigma_0 \end{bmatrix} + \begin{bmatrix} \sigma_{11} - \sigma_0 & \sigma_{12} & \sigma_{13} \\ \sigma_{21} & \sigma_{22} - \sigma_0 & \sigma_{23} \\ \sigma_{31} & \sigma_{32} & \sigma_{33} - \sigma_0 \end{bmatrix} \quad (3.5)$$

In the above equation

$$\sigma_0 = \frac{1}{3}(\sigma_{11} + \sigma_{22} + \sigma_{33}) = \frac{I_1}{3} \quad (3.6)$$

where I_1 is the first invariant of the stress tensor and represents the average stress. Similarly, the strain tensor can be decomposed into the sum of the spherical tensor and the bias tensor:

$$\begin{bmatrix} \varepsilon_{11} & \varepsilon_{12} & \varepsilon_{13} \\ \varepsilon_{21} & \varepsilon_{22} & \varepsilon_{23} \\ \varepsilon_{31} & \varepsilon_{32} & \varepsilon_{33} \end{bmatrix} = \begin{bmatrix} \varepsilon_0 & 0 & 0 \\ 0 & \varepsilon_0 & 0 \\ 0 & 0 & \varepsilon_0 \end{bmatrix} + \begin{bmatrix} \varepsilon_{11} - \varepsilon_0 & \varepsilon_{12} & \varepsilon_{13} \\ \varepsilon_{21} & \varepsilon_{22} - \varepsilon_0 & \varepsilon_{23} \\ \varepsilon_{31} & \varepsilon_{32} & \varepsilon_{33} - \varepsilon_0 \end{bmatrix} \quad (3.7)$$

In the equation，

$$\varepsilon_0 = \frac{1}{3}(\varepsilon_{11} + \varepsilon_{22} + \varepsilon_{33}) = \frac{\theta}{3} \quad (3.8)$$

where θ is the volume strain.

The decomposition of the stress or strain tensors into two parts, the spherical tensor and the bias tensor (or deviatoric tensor), is of profound physical content. The deformation of a point within a rock can be divided into two parts: volume strain and shape change, with the spherical tensor part of the strain tensor representing its volume change and the partial tensor part corresponding to its shape change.

In order to study the change in the volume of the rock, three sets of elastic stress-strain relations are first written out:

$$\begin{aligned} \sigma_{22} &= \lambda\theta + 2\mu\varepsilon_{22} \\ \sigma_{22} &= \lambda\theta + 2\mu\varepsilon_{22} \\ \sigma_{33} &= \lambda\theta + 2\mu\varepsilon_{33} \end{aligned} \quad (3.9)$$

Adding the three equations above and dividing by 3 yields:

$$\begin{bmatrix} \sigma_0 & 0 & 0 \\ 0 & \sigma_0 & 0 \\ 0 & 0 & \sigma_0 \end{bmatrix} = 3k \begin{bmatrix} \varepsilon_0 & 0 & 0 \\ 0 & \varepsilon_0 & 0 \\ 0 & 0 & \varepsilon_0 \end{bmatrix} = k \begin{bmatrix} \theta & 0 & 0 \\ 0 & \theta & 0 \\ 0 & 0 & \theta \end{bmatrix} \quad (3.10)$$

In the equation，

$$k = \frac{2\lambda + 2\mu}{3} \quad (3.11)$$

where k is the volumetric compression modulus of the rock, and from the above equation (3.10) it is clear that the volumetric strain theta of the rock is related to σ_0 and only to σ_0 (this is clearer from the fact that the sum of the main diagonal elements of the bias tensor is always equal to zero)

For intact rocks, fracture is the main form of damage that occurs. Rupture occurs as soon as the pressure σ_1 to which the rock is subjected exceeds its strength. The rupture criterion when the rock is in the stress state of $(\sigma_1, \sigma_2, \sigma_3)$:

$$\sigma_1 = f(\sigma_2, \sigma_3) \quad \sigma_1 \geq \sigma_2 \geq \sigma_3 \quad (3.12)$$

The above equation is the condition under which rupture occurs, at which point σ_1 is also called the strength under the given σ_2, σ_3 conditions. In fact, it is also the relationship between the strength σ_1 and σ_2, σ_3.

If only the simplest case is considered, we usually use the linear Coulomb rupture

criterion. Coulomb's law expressed in terms of positive stresses σ and tangential stresses τ on the rupture surface is

$$|\tau| = S_0 + \mu\sigma \qquad (3.13)$$

where S_0 and μ are material constants related to the rock type. S_0 is called the strength of aggregation, often referred to as cohesion in engineering; μ is called the coefficient of internal friction. Another expression for the Coulomb criterion is obtained when expressed in terms of principal stresses σ_1 and σ_3:

$$\sigma_1 = C_0 + \xi\sigma_3 \qquad (3.14)$$

where C_0 is a constant, for the uniaxial compressive strength of the rock, ξ is the coefficient of the influence of the confining pressure on the strength of the rock, which indicates that when σ_3 increased by a factor of 1, so that the rock rupture the required value of σ_1 needs to be increased by $\xi\sigma_3$ times, the parameters of the S_0, μ and the relationship between C_0 and ξ follows

$$C_0 = 2S_0 \left[(\mu^2 + 1)^{\frac{1}{2}} + \mu \right] \qquad (3.15)$$

$$\xi = \left[(\mu^2 + 1)^{\frac{1}{2}} + \mu \right]^2 \qquad (3.16)$$

For most rocks, $\mu \approx 0.6 - 1.0$, $S_0 = 150 - 360 \text{KPa}$. Thus, an increase in the confining pressure σ_3 greatly increases the rupture strength σ_1. Fig 3.14 shows the difference between the two expressions of strength for rocks, as shown in Eq. (3.13) and (3.14).
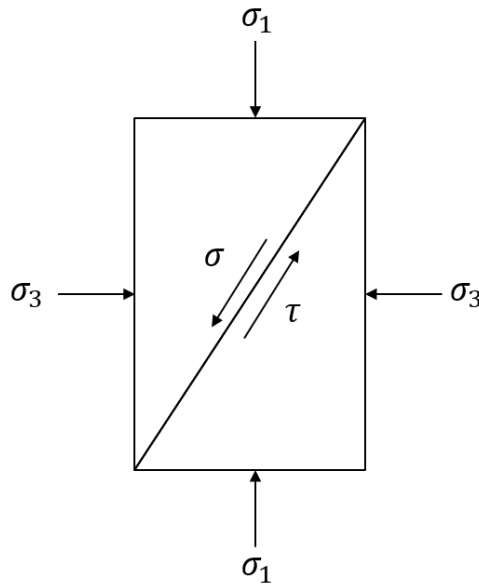
Fig. 3.14 Two kinds of expression for rock rupture criterion

Before summarizing the implications of the test results on the locating, construction,

and operation of a CAES salt caverns, it is necessary to explain the distribution pattern of ground stress. In 1978, E.T. Brown et al. statistically analyzed 120 representative crustal stress (σ_v) measurements collected worldwide and found that the measured values of ground stress are generally compressive stresses and that very few are tensile stresses, and they increase with increasing depth (H) [257]. The linear correlation between stress and depth was strong in the depth range of 2500 m. The vertical stress could be calculated as:

$$\sigma_v = 0.027H \tag{3.17}$$

In addition, the ratio of the average horizontal stress to the vertical stress ranges from 0.5 to 3.5. Considering that the vast majority of salt caverns are within 2000 m of the ground surface, Eq (3.17) can be used to estimate the surrounding rock stresses in salt caverns. According to the above test result, the recommendations are as follow: For a horizontal dissolution cavity (Fig. 3.15(a)), the height (h_4) of the salt cavern in the vertical direction does not varies much. When a CAES plant is operating, the operation plan of the salt cavern can be adjusted according to the depth (h_3). For salt caverns with depths greater than 500 meters, the creep–fatigue alternating load caused by the change in the frequency of peak regulation has less impact on the surrounding rock. The frequency of peaking can be increased appropriately to improve the efficiency of the CAES plant. At shallow depths, the impact of creep–fatigue interaction on the safety operation factor must be considered. Regarding the vertical dissolution cavity (Fig. 3.15(b)), a salt cavern has a large height (h_2) variation in the vertical direction. In addition to the general area of weakness in the surrounding rock–the roof of the salt cavern–we should also pay attention to the differences in the mechanical characteristics of the surrounding rocks due to the variation in depth (h_1). Take the example of the Hutchinson salt mine in Kansas, USA [259]. If h_1 of the salt cavern is 150 meters and h_2 is 200 meters, according to Eq (3.17), the surrounding rocks above (e.g., yellow dashed box) and below (e.g., red dashed line) are under approximately 4 MPa and 9 MPa of σ_c, respectively. The brittle and ductile transformation characteristics of the salt rock should be considered when designing the gas pressure. Otherwise, the salt cavern may not reach its service life and fail.
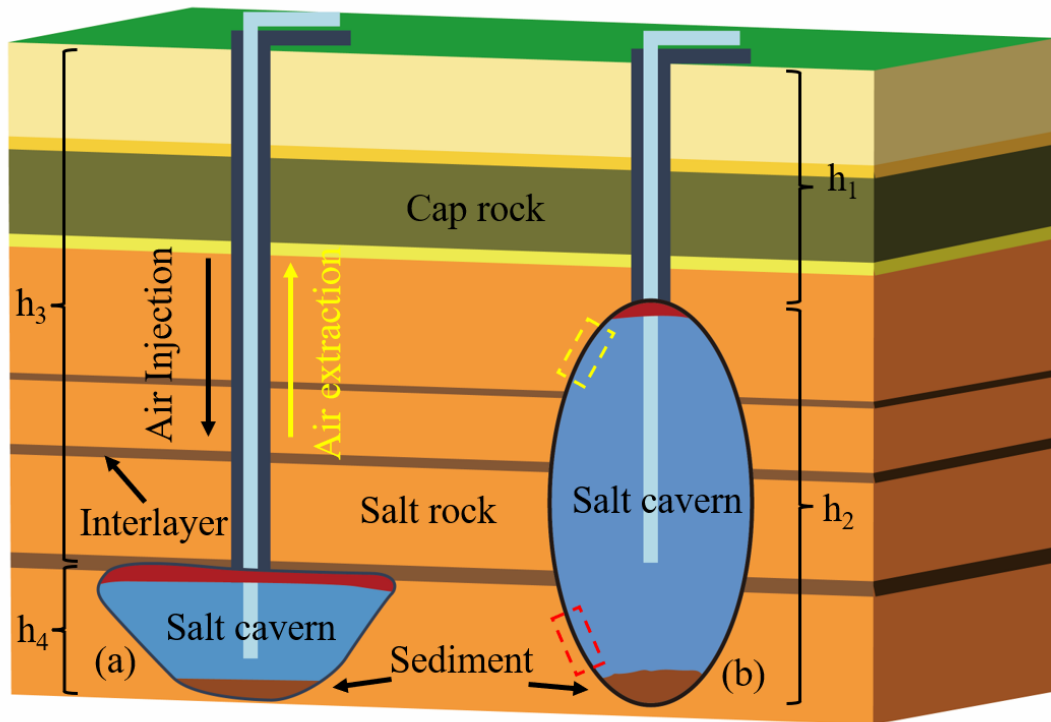
Fig. 3.15 Schematic diagram of two salt cavity shapes: horizontal dissolution cavity (h_1 and h_2 are the depth and height, respectively) (a) and vertical dissolution cavity (h_3 and h_4 are the depth and height, respectively) (b).

Moreover, the effect of the T stage and S_l on salt rock creep–fatigue behavior suggests that we should pay attention to the timing of dissolution cavity construction and the gas pressure and duration of the first gas injection when utilizing and modifying old cavities for the construction of CAES facilities, as these factors are equally important for the stability of the CAES salt cavern.

There are some deviations between experimental design and engineering practice due to the limited experimental conditions, such as load frequency, stress level and temperature condition. The crustal stress conditions in which the corresponding underground works are located are also extremely complex. Despite these limitations, this work can still help engineers evaluate the stability of CAES salt caverns. We will also conduct more tests under different test conditions in the future, such as different T stage durations, different upper stress bounds and higher σ_c to judge the stability of salt rock in the triaxial state more accurately.

3.5 Conclusions

Considering the actual stress state of an underground salt cavern used for a CAES facilities, indoor triaxial creep–fatigue tests were designed for salt rock under different confining pressure and stress level conditions, and the main conclusions are as follows:

(1) The addition of confining pressure not only increases the strength of the salt rocks but also increases the ultimate deformation of the salt rocks. Similar to the stress–strain curves result of uniaxial creep–fatigue tests, the decelerating deformation phase of the triaxial test is also greatly shortened. As the increase in the confining pressure, the salt rocks deformation ultimately reveals only one stage.

(2) The occurrence of a high-stress plateaus significantly influences the fatigue residual strain, causing the residual strain in cycle A before the plateaus to be greater than that in the B cycle after the plateaus. As the confining pressure increases, the residual strain difference between cycles A and B shows a decreasing trend.

(3) The presence of fatigue elevates the creep rate of the salt rocks. However, the increase in the confining pressure suppresses this effect. With increasing confining pressure, the creep strain of the salt rocks during the high-stress plateau indicates an increasing trend at an equal stress ratio.

(4) The brittle–ductile transformation of salt rocks under different confining pressure are responsible for the variation in the creep–fatigue mechanical characteristics of the salt rocks. When designing the gas pressure level of the CAES salt cavern, the impact of depth on the stress state of the surrounding rocks needs to be taken into account. This is particularly important for vertical dissolution caverns.

4 Multi-stage amplitude creep-fatigue mechanical characterization of salt rock with acoustic emission signal analysis

4.1 Introduction

During the operation of a salt cavern CAES power plant, the level of gas injection pressure determines the energy storage capacity of the CAES, and the change of gas injection pressure also affects the damage evolution of the surrounding rocks of the reservoir. Acoustic Emission (AE) technique is an effective tool to study the damage evolution patterns of materials such as metals and rocks. When a material is subjected to external loading, the sudden redistribution of stresses (due to microcracking/deformation) converts mechanical energy into acoustic energy, resulting in the generation of elastic waves [259]. This phenomenon is known as acoustic emission and is a concomitant to stress redistribution in internal structures. Rock research on AE first began in 1941, by Obert rock explosion monitoring in mines [260]. However, the AE signal strength of many materials is very weak (a human ear cannot directly hear it), so there is a need to use sensitive electronic instruments to detect, record, analyze AE signals. In 1950, the German scientist Kaiser [261] took the lead in studying the AE characteristics of engineering materials. With the continuous development of electronic technology, the reliability of AE technology is also improving. Scholars around the world have conducted many studies on the mechanical properties of rocks based on AE monitoring of fatigue, compression, tension and creep. Evaluating the structural stability of rock materials by AE signal parameters (counts, energy, peak frequency, duration, etc.) is a widely used method, which is fast and intuitive. And on the fact that by a refine analysis of AE signals, it is possible to determine the location of microcracks, but distinguish different types of damage (size of cracks) [262,263]. In this Chapter, we will focus on the damage evolution of salt rock under the influence of different confining pressures and stress levels with the help of AE techniques.

4.2 Experimental materials and methods

The specimen preparation and test steps are the same as those in Chapter 2 and 3 and will not be repeated here, but only for the new test principle, equipment and test

program.。

4.2.1 *Acoustic Emission system*

The principle of acoustic emission (AE) monitoring is shown in Fig. 4.1 below. Elastic waves emitted from an AE source (red microcrack) eventually propagate to reach the surface of the material, causing surface waves that can be detected by AE sensors, which convert the mechanical vibrations of the material into electrical signals that are then amplified, processed, and recorded before being analyzed and extrapolated by researchers, The observed AE signals enables to understand the mechanism by which AE is generated by the material.
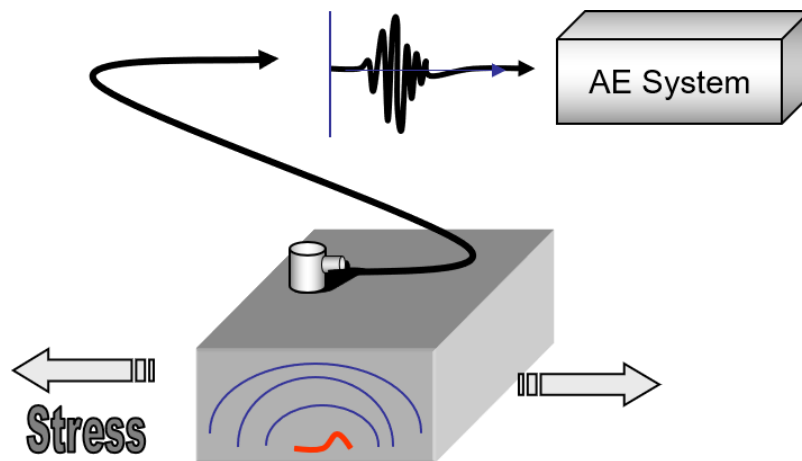
Fig. 4.1 Schematic diagram of the principle of acoustic emission monitoring.

The acoustic emission equipment used in our tests is the PCI-2 acoustic emission monitoring system produced by the U.S. Physical Acoustics Company, as shown in Fig. 4.2 (a). It has a dual-channel detection function, which can simultaneously realize characteristic parameter extraction and waveform processing. The system has 18-bit A/D conversion rate, 1kHZ-3mHZ frequency range. It is a new type of AE research tool for scientific research institutes and universities, with the following main features:

1) Low noise, low power consumption, built-in waveform and HIT processor on the main board, suitable for laboratory research;

2) Built-in 18-bit A/D converter and processor is more suitable for low threshold (17dB) setting;

3) Maximum signal amplitude: 100dB;

4) Dynamic range: >85dB.

5) 4 high pass and 6 low pass filters, selectable via software control;

6) 40MHz, 18-bit A/D converter for real-time analysis of samples and higher signal processing accuracy;

7) The equipment is equipped with AE data flow device, which can continuously store the AE waveforms into the hard disk at a speed of up to 10M/sec;

8) The digital signal processor can meet the requirements of high precision and reliability.
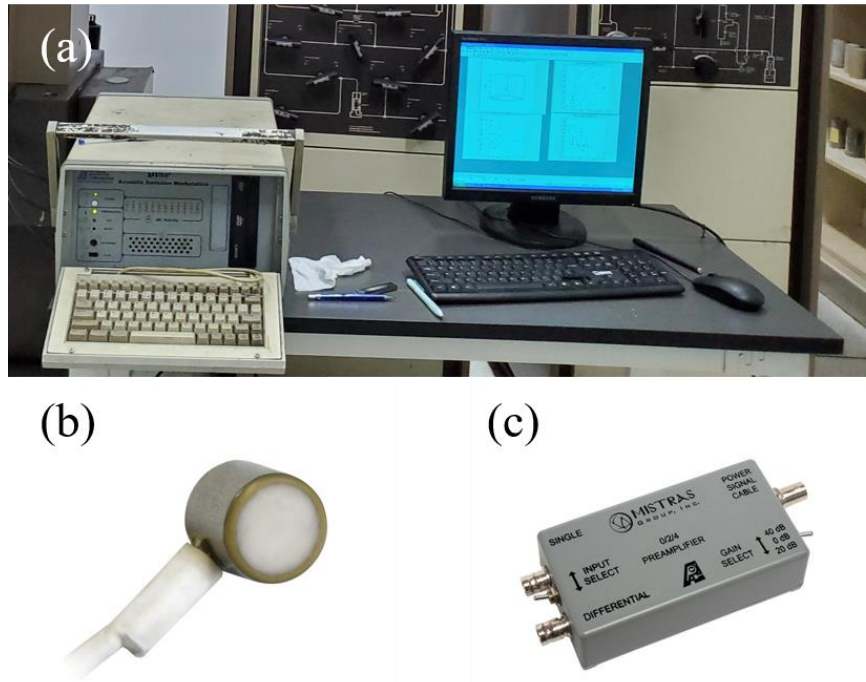
Fig. 4.2 (a) PCI-2 acoustic emission monitoring system, (b) Nano30 miniature AE sensor, and (c) 0/2/4 type advanced universal voltage preamplifier.

The sensor is an important part of the AE detection system, which is an important factor affecting the overall performance of the system. Unreasonable selection of sensors will make the received signal and the actual AE signal have a big difference, which directly affects the realism of the collected data and the data processing results. After comparison and selection, the Nano-30 miniature AE sensor, also from the U.S. Physical Acoustics Corporation, was selected as the AE probe for this test, as shown in Fig. 4.2 (b). This probe has a resonant response at 300Khz and a good frequency response in the range of 125-750kHz, which is suitable for applications in rock mechanics.

Since the voltage signal output from the AE probe is sometimes as low as microvolt

orders of magnitude, the signal-to-noise ratio of such a weak signal, after transmission, is bound to be reduced. A preamplifier is set up close to the transducer to boost the signal to a certain level, which is then transmitted via cable to the processing unit of the PCI-2 mainframe. The main technical specifications of the preamplifier are amplification, passband and input noise voltage. The amplifier used in this experiment is the Model 0/2/4 Advanced General Purpose Voltage Preamplifier manufactured by Physical Acoustics, Inc. as shown in Fig. 4.2 (c). This type of amplifier has switch-selectable gain ranges of 0, 20, and 40 dB. A built-in insertion filter provides the flexibility to optimize transducer selectivity and noise rejection for rock mechanics tests requiring a wide range of gains or frequency bandwidths.

4.2.2 *Data collected by AE*

Typical AE signal parameters include amplitude, ring count, duration, energy, threshold voltage value, arrival time, and impact count rate [264], illustrated in Fig. 4.3.
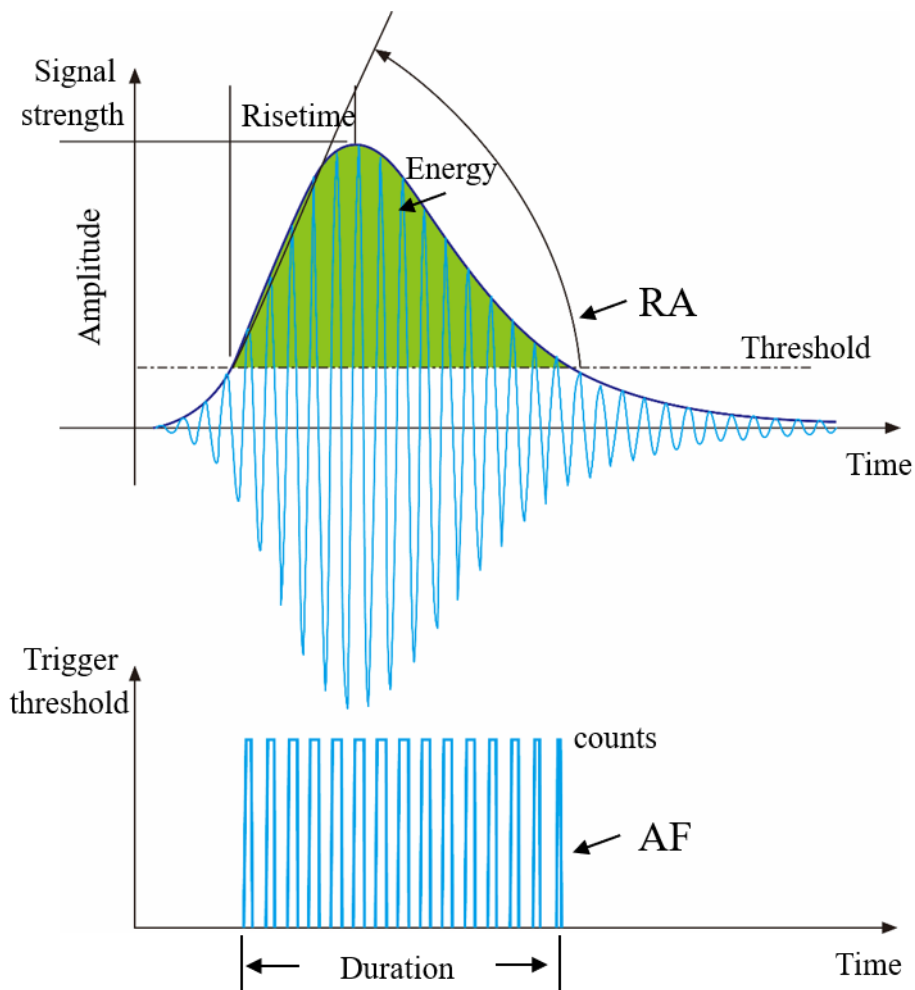
Fig. 4.3 Schematic diagram of typical acoustic emission signal parameters

1) Impact: any signal that exceeds the threshold and causes a channel to acquire data is called an impact. It reflects the total amount and frequency of AE activity and is often used for AE activity evaluation.

2) Count: the same impact is detected by several channels positioned at different location, and the source can therefore be located spatially by analysis of temporal shift.

3) Ring Count: the number of oscillations above the threshold signal, used for AE activity evaluation.

4) Energy: the area under the detection envelope of the signal, reflecting the strength of the signal.

5) Duration: the time interval between the first crossing of the threshold and the final descent of the signal to the threshold.

6) Rise time: the time from the first crossing of the threshold to the maximum amplitude of the signal. The value of RA is calculated by dividing the rise time by the amplitude of the acoustic emission signal, the unit of measurement is $\mu s * V^{-1}$.

7) Average Frequency (AF): AF is calculated by dividing the count of acoustic emission events above the threshold by the duration of acoustic emission impacts and is expressed in kHz.

In this Chapter, representative AE parameters (count, energy, RA, AF and so on) will be selected to analyze the damage evolution of salt rock under different loading conditions

4.2.3 *Mechanical tests series with AE*

The cyclic compressive tests conducted with AE measurements investigated the effect of confining pressure and stress level on the creep-fatigue mechanical properties of salt rock. First, monotonic compression tests were conducted on the salt rock samples at different confining pressures (0 and 3 MPa). Each test was repeated three times, and the average values of the peak stress were computed (see Table 4.1). The results show an average uniaxial compressive strength (UCS) of 30.1 MPa and an average triaxial compressive strength (TCS) under a confining pressure of 3 MPa of 60.2 MPa. Note that the uniaxial compression results presented here are the same as presented in Chapter 2.

Table 4.1 Compressive strength of the salt rock under 0 and 3MPa confining pressure

Confining pressure/MPa	Test no.1/MPa	Test no.2/MPa	Test no.3/MPa	Average/MPa
0	28.9	30.3	31.1	30.1
3	59.5	61.4	59.7	60.2

Then, the uniaxial stepwise creep–fatigue (USCF) test and the triaxial stepwise creep–fatigue (TSCF) test were designed as illustrated in Fig 4.4. These tests were repeated 3 times as well. In the USCF and TSCF tests, the upper and lower stresses were determined based on the compressive strengths of the salt rock under confining pressures of 0 and 3 MPa. The initial upper limit stress was set to 40% peak differential stress of U/TCS defined as stress level (S_l), and the lower limit was set to 3% peak differential stress of U/TCS; an stepwise increase of 10% per S_l was adopted every 20 cycles. Successive S_l values are given in Table 5.2.

Table 5.2 Parameters considered in the USCF and TSCF creep–fatigue tests.

Test scheme	Upper stress limit/MPa	Lower stress limit/MPa	Plateau times/s
USCF	12,15,18,21,24,27,30	0.9	300
TSCF	25.8, 31.5, 37.2,42.9,48.6,54.3,60	4.7	

The purpose of such a stepwise creep–fatigue test is to emulate the realistic rheological state of the salt cavern surrounding rocks owing to the prolonged high-pressure condition when gas is injected inside the salt cavern at different pressure levels.
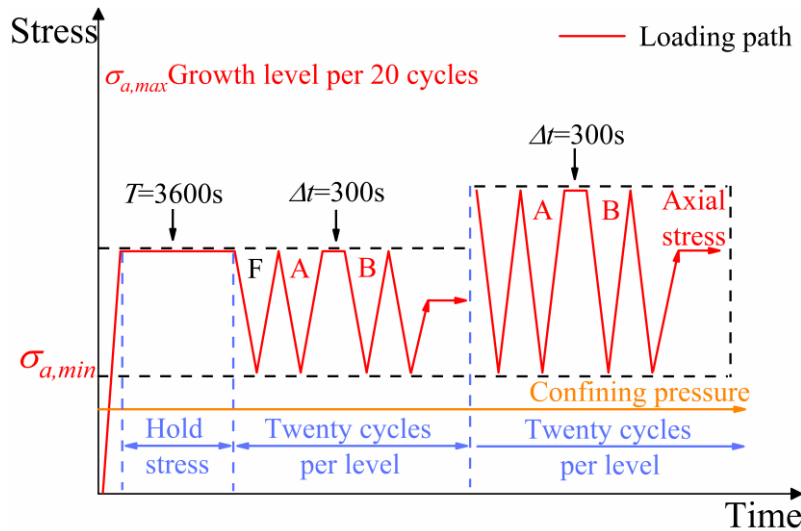
Fig. 4.4 Loading paths for the uniaxial and triaxial stepwise creep–fatigue tests.

First load to initial S_l is hold for one hour before unloading (*T*-stage), and then loading applied to the specimen is a repetitive cyclic loading between the low and high stress, with a high-stress plateau duration of 300 s inserted every two stress cycles. There is a rise in the S_l value after every 20 cycles until specimen's failure. Again, the pre-plateau cycle is defined as cycle A, while the post-plateau cycle is referred to as cycle B. The first cycle in every level is neither a pre-plateau nor post-plateau cycle and is called the first (F) cycle. The test results are shown in Table 4.3.

Table 4.3 USCF and TSCF test results

Test number	Confining pressure/MPa	Final stress level	Fatigue life/cycle
U-1	0	5th	88
U-2	0	5th	94
U-3	0	6th	108
T-1	3	7th	126
T-2	3	6th	112
T-3	3	7th	136

Two Nano 30 AE probes from PAC were installed in symmetrical positions at the middle height of the specimen. A lubricant was applied between the two probes to ensure stable signal acquisition. The AE signals were collected using dual channels throughout the test, from the early occurrence and expansion of microcracks inside the specimen to their coalescence and propagation. The parameters of the AE equipment

were set empirically and are given in Table 4.4.

Table 4.4 Parameters of the PCI-2 acoustic emission equipment.

	Threshold	Peak definition time	Hit definition time	Hit lockout time
Parameters	45dB	35μs	150 μs	300 μs

4.3 Results and analysis of salt rock under multistage creep-fatigue loading

4.3.1 Stress–strain curve of salt rock in the U/TSCF tests

For the following analysis, only representative specimens U-2 and T-3 will be discussed are shown in Fig 4.5. The final failure of the specimens occurred at 0.8 S_l for the USCF test (24 MPa), and 1.0 S_l for the TSCF test (60 MPa). By observing the two stress-strain curves in the USCF and TSCF tests, we can see that there is a significant increasing in the high-stress plateau strain (creep strain) with increasing S_l. However, for a given S_l, the creep strain decreases with the number of cycles, suggesting a stabilization phenomenon. This is valid for all S_l except the last, during which final failure occurs. Indeed, at 0.8 S_l in the USCF test, the creep strain decreases during the first few cycles and increases again during the later cycles, leading to failure. This final increase is a marker that can help to anticipate final failure. Although this phenomenon is not very obvious, the same pattern can be identified at 1.0 S_l in the TSCF test.
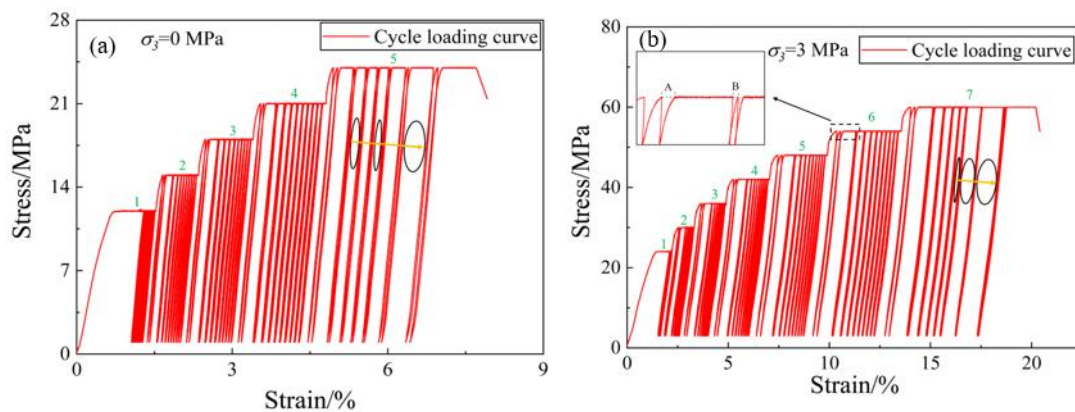
Fig. 4.5 Stress–strain curves from the USCF tests and U-2 (b) and TSCF tests T-3 (d).

To survey the development on the creep strain rate (v_c) during high-stress plateaus, we counted and calculated the v_c for each high-stress plateau in the USCF and TSCF tests using the same equation as in section 2.3.2. The v_c values for the USCF test are

shown in Fig 4.6:
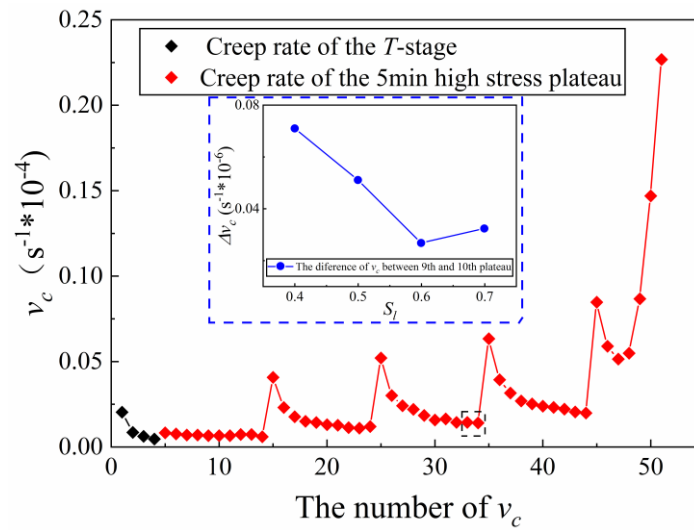
Fig. 4.6 Creep rate during USCF test

The black lozenges in the graph represent the creep rate in the first hour (T stage); the creep rate first decreases before gradually stabilizing (creep state), which is due to the low stress level. Subsequently, due to the additional first cyclic load, there is a sudden increase in the creep rate (first red dot), followed by a steady creep rate.; then when S_l is increased, the creep rate will jump again and stabilize again etc. The creep rates of the first four stages were calculated, and the creep rate difference between the last two high-stress plateau stages (as shown in the black dotted box in Fig 4.6) for each S_l is shown in the blue dashed box in Fig 4.6. The difference in the creep rate is very small, with a ratio of less than 0.1. This indicates that the salt rock enters the steady-state creep stage again after many cycles. At the same time, it can be seen that with the increase in S_l, the creep rate difference, although fluctuating, shows an overall decreasing trend, indicating that the salt rock specimens are in a compacted and dense state before entering the last Sl. The TSCF and USCF tests present similar results.

4.3.2 *Creep fatigue Residual strain of salt rock in U/TSCF test*

106
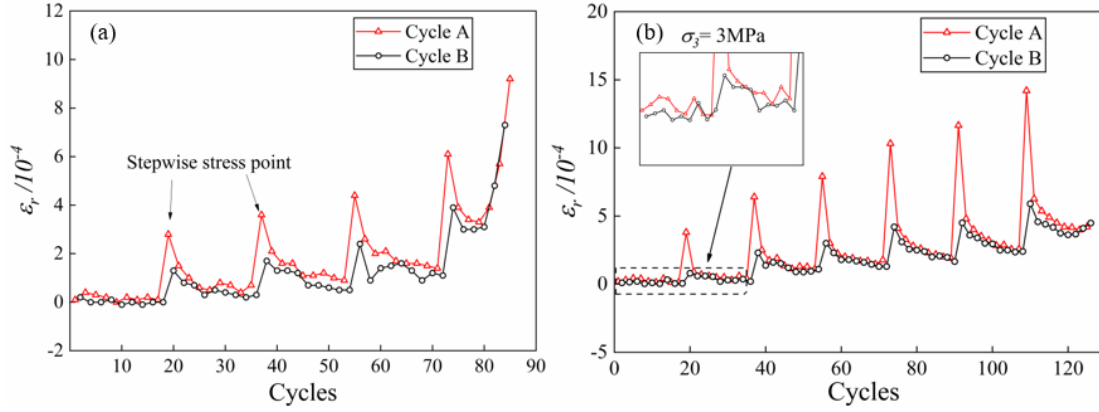
Fig. 4.7 Axial residual strain from each stress cycle during USCF test (a) and TSCF test (b).

The residual strain ε_r evolutions during the USCF and TSCF tests are shown in Fig 4.7. The residual strains before (cycle A) and after (cycle B) high stress plateaus in the aforementioned tests are presented for the USCF tests and TSCF tests. Although this phenomenon is not obvious during the first 20 cycles (at 0.4 S_l), for both the USCF and TSCF tests, differences between cycles A and B begin to appear at the second 20 cycles (at 0.5 S_l). This shows that the high-stress plateaus at lower levels still affect the fatigue cycle ε_r of the rock.

In addition, for each S_l, we computed the difference between the $\varepsilon_{r,A}$ and $\varepsilon_{r,B}$ and its average value ($\Delta\bar{\varepsilon}_r$). Because the last few cycles of the final stress level being on the brink of failure., they were not included in the calculation. The results are shown in Fig 4.8, where the linear regression functions are also proposed.

$$\Delta\bar{\varepsilon}_r = 0.01362S_l - 0.0036 \qquad R^2 = 0.98 \qquad (5.1)$$

$$\Delta\bar{\varepsilon}_r = 0.00675S_l - 0.0013 \qquad R^2 = 0.92 \qquad (5.2)$$

where Eq (5.1) is for the USCF test and Eq (5.2) is for the TSCF test. We find that the $\Delta\bar{\varepsilon}_r$ values in the USCF tests are greater than those in the TSCF tests and that the increasing trend is greater in the USCF test than in the TSCF test.
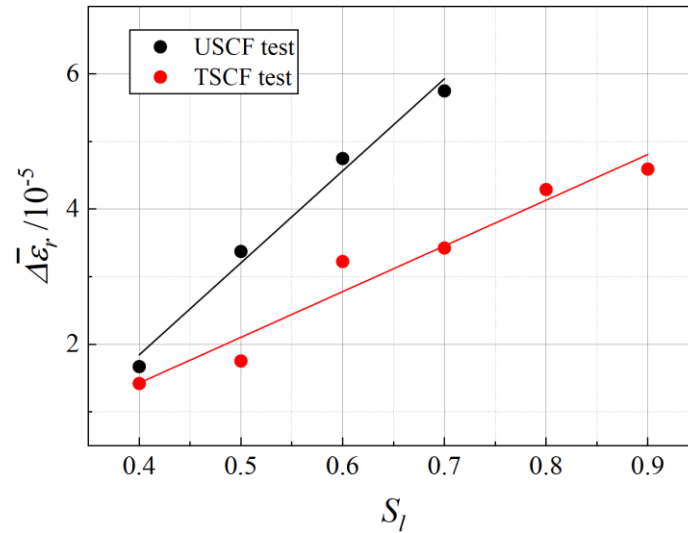
Fig. 4.8 Average residual strain difference between cycles A and B for various increasing stress level S_l, for USCF test and TSCF test.

According to Fig 4.5 and Fig 4.7, it can be seen that the creep strain and residual strain of the salt rock specimens show an overall increasing trend with increasing stress levels. However, the effect of stress levels on creep strain and residual strain is different. For this purpose, the ratio of creep strain to residual strain was calculated for every S_l (excluding the data at the point of abrupt stress elevation) and defined as φ. The results are shown in Fig 4.9.
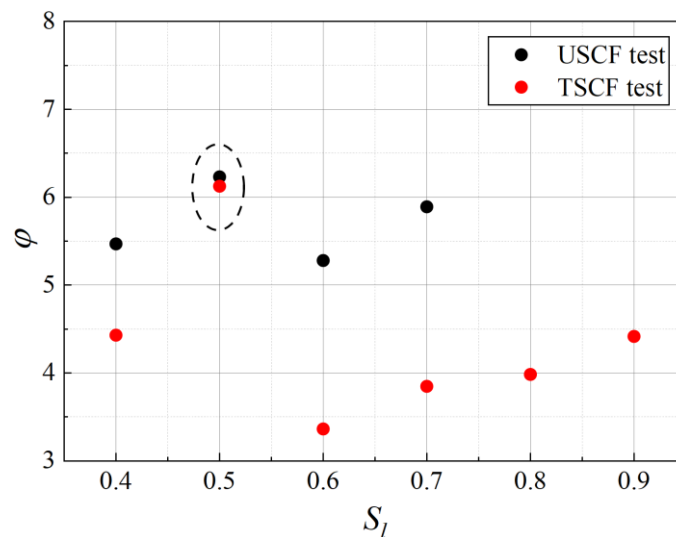
Fig. 4.9 The ratio of creep strain to residual strain φ for every S_l (excluding the data at the point of abrupt stress elevation) for the USCF test and TSCF test.

It can be seen that for the first increase in S_l (0.5 level), there is a sudden jump in the

ratio (as shown in the black circle), followed by a decrease and then an increase. The above phenomenon indicates that the increase in the stress level has more effect on creep than on fatigue. In the second phase, the ratio of creep strain to residual strain peaks. Moreover, it can be observed that the ratio in the TSCF test is consistently lower than that in the USCF test.

4.3.3 *AE counts and energy during creep–fatigue testing of salt rock*

The AE counts (N_{AE}) and AE energy (E_{AE}) both can reflect the development of internal microcracks during loading. Fig 4.10 shows the axial strain, the AE counts N_{AE} and the cumulative E_{AE} during the USCF and TSCF tests.
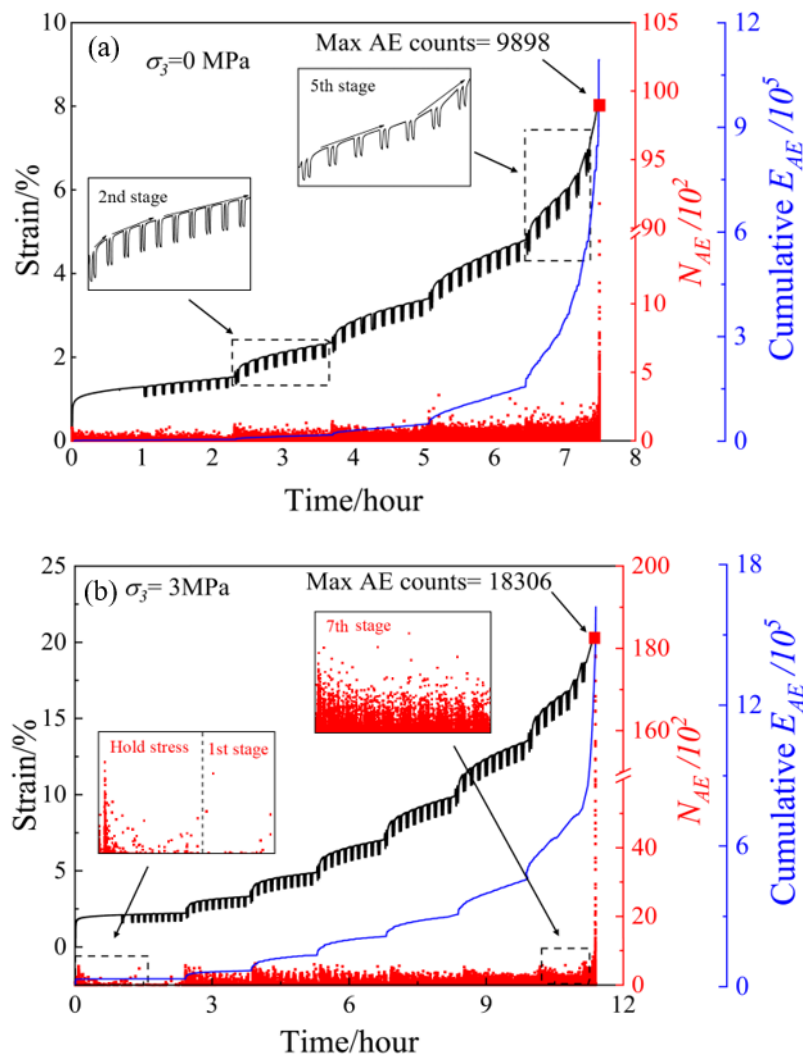
Fig. 4.10 Strain evolution with AE counts and cumulative AE energy for the USCF test (a) and TSCF test (b).

From the overall N_{AE} evolution and cumulative E_{AE}, the damage of the salt rock is consistent with avalanche dynamics damage theory. The N_{AE} in the final rupture stage is extremely large, arising from the mechanical energy released at the moment of damage. Moreover, the extreme value of N_{AE} for the salt rock in the TSCF test (18306 counts) is almost twice larger than the N_{AE} in the USCF test (9898 counts), indicating that the confining pressure provides more strain energy that can be released at final failure [265]. In Fig 4.10(a), for the first creep–fatigue cycle of the USCF test, the N_{AE} values are small, and their variation is insignificant compared to the strain. N_{AE} increases significantly at the beginning of 0.5 S_l. This is due to the increase in S_l, resulting in the fact that initially closed microcracks subjected to more compaction are reopened and that the slipping crystals are creating new cracks. Write a sentence to describe that for every given stress level, the number of AE events is rather regular, with a small increase at each new cycle beginning. During the last cycle before failure (0.8 S_l), peaks of N_{AE} occurs several times before final failure. During this stage, larger cracks develop by the convergence of preexisting cracks and grain-piercing cracks from the fatigue process, and the salt rock loses its internal bearing capacity, leading to final failure.

The N_{AE} counts during the TSCF test, plotted in Fig 4.10(b), shows a similar pattern as the USCF test. In particular, at 1,0 S_l, we find that N_{AE} decreases and increases again, following the stress–strain curve in the same cycle (see section 4.3.1). This observation illustrates the reliability of using N_{AE} to characterize salt rock damage.

4.3.4 *AE peak frequency during the creep-fatigue tests of salt rock*

The AE signal consists of multiple frequency components, with different waveform frequencies and amplitudes for different AE excitation sources. AEs corresponding to different types and scales of cracks have different spectral characteristics, and the peak frequency (PK) is one of the main indicators used to describe the spectral characteristics [266]. Fig 4.11(a) and (b) shows the probability density plots of the frequency distributions for the USCF and TSCF tests, respectively. The PK from AE of salt rock under creep–fatigue cycles are mainly concentrated in three frequency bands: low frequency (0-75 kHz), medium frequency (75-275 kHz), and high frequency (275-400 kHz). When there is no confining pressure, the PK show a rather uniform distribution. The signals firstly appear in the medium-frequency range at low S_l. The low-frequency

and high-frequency signals are rare at the beginning of the test and gradually increase for larger values of S_l. The number of medium-frequency signal is almost constant throughout the test, and the probability density reaches its maximum value at final failure.
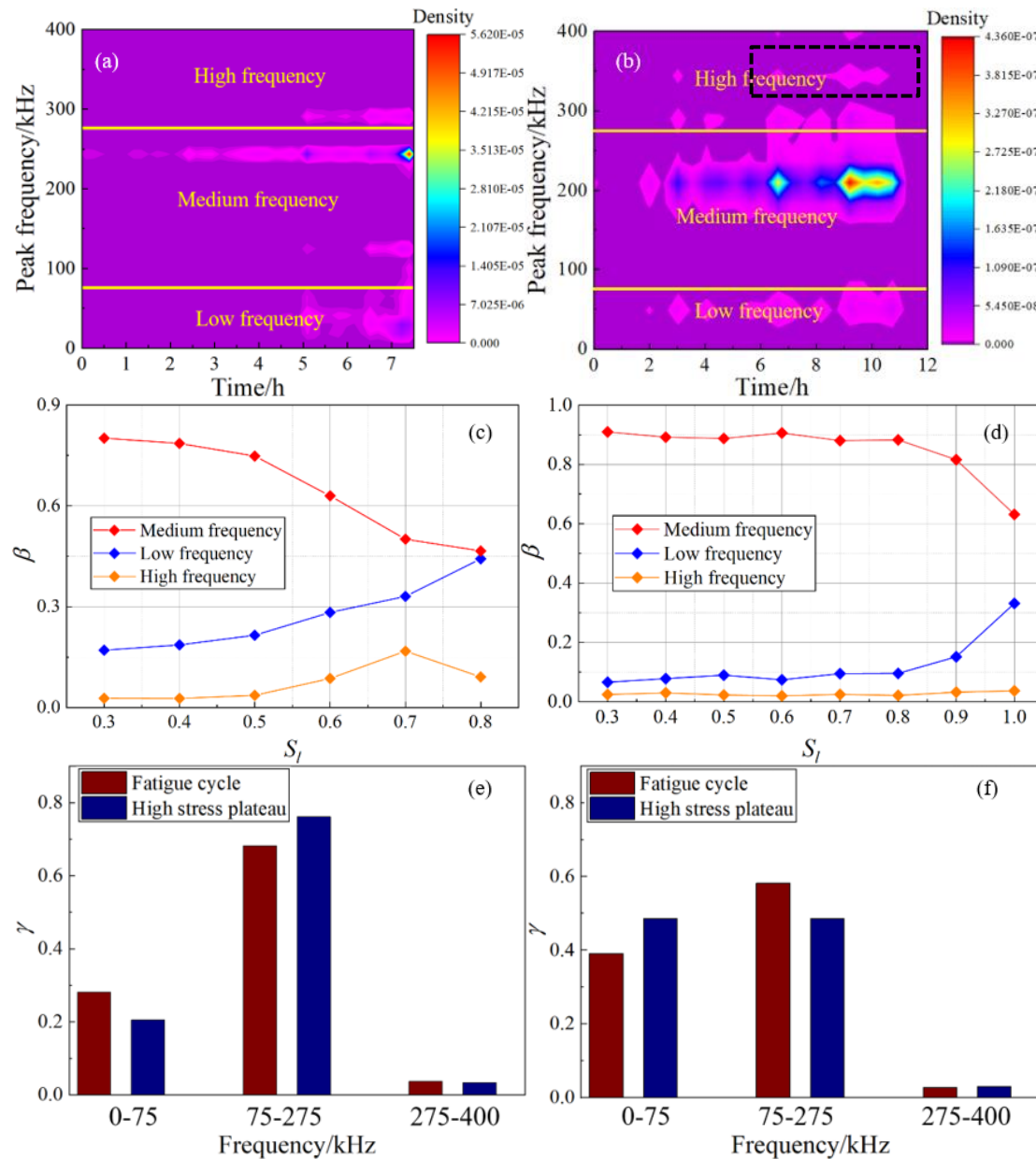
Fig. 4.11 Probability density distribution of peak frequencies and ratio for the three frequency bands for every $S_{l\ levels}$ in the USCF test (a and c) and TSCF test (b and d) (note: 0.3 S_l is the T-stage). Fatigue cycle and high-stress plateau in different frequency bands as a percentage of AE frequency in the USCF test at 0.5 S_l (e) and 0.8 S_l (f).

The frequency distribution in the TSCF test is more distinctly characterized. At the

early stage of loading, only sporadic medium-frequency signal distribution present. only at the early stage of loading. Thereafter, before the start of the cyclic loading phase, the specimen has a very low probability density, which reflects the compression-density effect of the confining pressure on the rock. Until the end of the test, the AE frequency distribution has a high probability density under the medium frequency condition. The USCF test has a wider distribution at lower frequencies, in the range of 5-75 kHz, while the TSCF test has a wider distribution at higher frequencies, with some distribution above 300 kHz.

It has been pointed out that the magnitude of the AE frequency shows an inverse trend with the crack size [267], i.e., high-frequency signals correspond to small cracks, while low-frequency signals correspond to large cracks. Some studies [268,269] also have pointed out that tensile damage produces mainly low-frequency AE signals and that shear damage leads to mainly high-frequency AE signals. To observe the distribution of signals at different frequencies during the test phase (from the beginning of the loading until damage occurs), we define β as the ratio of the distribution of AE frequencies in the three frequency bands. This represents the ratio between the number of frequencies occurring in that band and the total number of frequencies. Fig. 4.11(c) shows the β values corresponding to different stress levels during the USCF test. Throughout the test, the medium-frequency signals have the largest proportion, followed by the low-frequency signals and then the high-frequency signals. As S_l increases, the proportion of high-frequency signals gradually decreases (from 0.801 to 0.465), while that of the low-frequency signals gradually increases. In the last stage (damage stage), the proportions of signals in the two frequency bands (high and low) are almost the same. The proportion of high-frequency signals peaks in the stage before failure and then decreases in the last stage. This variation shows that the proportion of large cracks in salt rock specimens gradually increases with increasing S_l during the test and then reaches a maximum in the final damage stage, forming large macrocracks. The development of microcracks reaches a maximum at 0.7 S_l and then decreases again from 0.8 S_l due to the formation of large cracks by coalescence. Meanwhile, the rupture pattern of a specimen in the USCF test can be assessed based on the distribution ratio of the frequency. These results reflect the joint action of tension and shear. Fig. 4.11(d) shows the corresponding values for the TSCF test. The signal proportion of each frequency band in the TSCF test is similar to that in the USCF test in terms of the overall distribution. In this case, the medium-frequency signals have the highest proportion,

followed by the low-frequency and then the high-frequency signals. The difference, however, is that the medium-frequency signals in the USCF test have a much larger proportion than that in the TSCF test at 0.3-0.8 S_l, indicating that the size of the cracks created during the triaxial test is smaller than that in the uniaxial test. However, a development pattern similar to that of the USCF test was observed in the final stage, i.e., the proportion of low-frequency signals increases rapidly, demonstrating that the cracks gradually transform into large cracks until failure. The above analysis suggests that the change in frequency distribution may be a precursory indicator of failure in salt rock specimens.

To further analyze the differences in the creep–fatigue response of the rock between fatigue and high-stress plateau cycles under different frequency bands, the frequency proportion in two stages of the USCF test (0.5 and 0.8 S_l) was determined and defined as γ. Fig 4.11(e) shows the distribution at 0.5 S_l, where a clear difference between the frequency distribution of fatigue and that of creep can be noticed. There is little difference between the two in the high-frequency range, but the proportions for the low- and medium-frequency ranges are different. In the case of low frequency, the proportion of fatigue cycles is greater than that of creep, while for medium frequency, the proportion of creep is greater than that of fatigue. This indicates that the development of very small cracks is more active during the creep stage, while the opening and closing of large cracks are more predominant during the fatigue stage. The percentage at 0.8 S_l shows a different pattern in Fig 4.11(f). There is still not much difference in the case of the high-frequency signals, while for the low-frequency signals, the proportion of creep is larger than that of fatigue. This indicates that the high stress occurring during the creep stage has been transformed into a force that drives crack expansion and formation, which is consistent with previous data.

4.3.5 *RA and AF metrics of salt rock during U/TSCF tests*
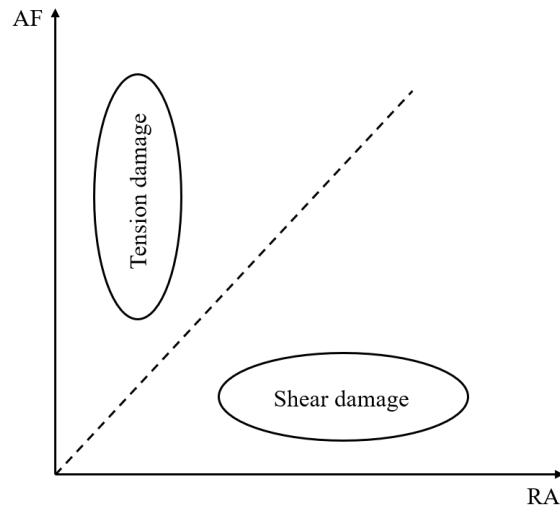
Fig. 4.12 Shear and tensile damage distribution

The risetime/amplitude (RA) and the average frequency (AF) of the AE signal are important parameters that characterize the waveform. These two parameters can be used in the qualitative analysis of the rupture mechanism. Ohno [270] and Nejati et al [271], investigated the distribution of AF and RA values during the damage of different rocks. Existing studies point out that when the AE signal has a large RA value with a small AF value, it corresponds to a shear wave signal. It can be assumed that the AE event corresponding to this signal is caused by shear damage. Conversely, a small RA value with a large AF value corresponds to tensile damage. The AF versus RA measurements are shown in Fig 4.12.
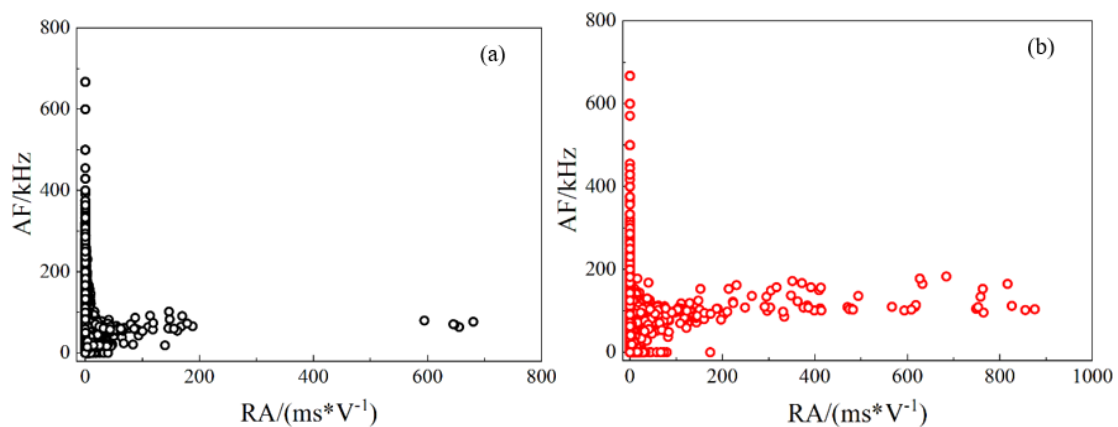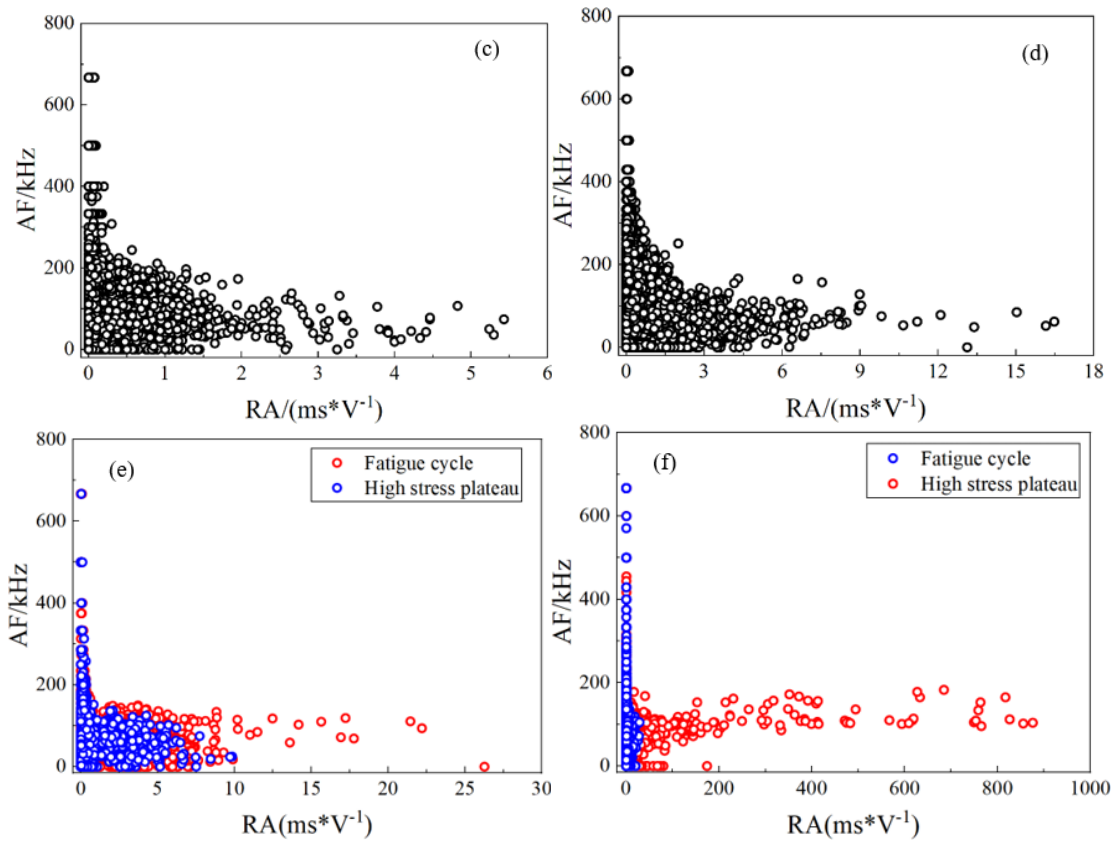
Fig. 4.13 AF versus RA distribution during the USCF test (a) and TSCF test (b) at 0.5 S_l (c) and 0.7 S_l (d) in the USCF test and 0.7 S_l (e) in the TSCF test. The fatigue cycle and high-stress plateau at 0.7 (e) and 1.0 S_l (f) in the TSCF test

Fig 4.13(a) and (b) shows the full-field AF and RA distributions for the USCF and TSCF tests, respectively. The USCF test distributions show a highly concentrated feature, with a continuous distribution in the vertical direction, from (0,0) to (0.25,695), which indicate tensile damage during failure. In the horizontal direction, the distribution is significantly reduced and characterized by an intermittent distribution, with the presence of very few signals with extremely large RA values and small AF values, corresponding to shear cracking, during the specimen rupture. The distribution of TSCF test signals is similar to that of USCF test signals on the whole, but there are significantly more signals distributed horizontally in the case of the TSCF test. In addition, the extreme value of RA in the TSCF test is larger than that of the USCF test, i.e., there are more shear signals with large RA values and small AF values. To observe the effects of different stress levels on RA-AF signals, the RA-AF distributions at 0.5 and 0.7 S_l in the USCF test and 0.7 S_l in the TSCF test were plotted, as shown in Fig 4.13(c), (d) and (e), respectively. Comparing the signal distributions under the two stress levels in the USCF test, it can be found that the overall distribution characteristics

of the signals do not change as S_l increases. However, the RA values corresponding to the shear signals show a clear banding feature. The RA values of the second band are distributed among numbers below 6, while the RA values of the fourth band are distributed among numbers above 6. Considering that the increase in stress will obviously promote the development of cracks, it is assumed that the distribution of RA values may reflect the density or scale of crack development. This will be studied in more detail by conducting microscopic observation tests. The signal distribution at 0.7 S_l in the TSCF test is significantly different from that at 0.7 S_l in the USCF test. Signals with high RA and low AF values are significantly more abundant in the TSCF test. The signals show distinct distribution characteristics along the horizontal direction; the RA extreme values are also significantly larger in the TSCF test than in the USCF test. This reflects a more significant shear damage in the TSCF test. Fig 4.13(e) and (f) shows the characteristics of RA-AF signal distributions for the fatigue and high-stress plateau cycles in the TSCF test. The signal distribution for the high-stress plateau is more compact, while the signal distribution for fatigue is larger. However, during the last stage, the high-stress plateau produces far more signals than the fatigue cycle. In addition, signals with a large RA value and a small AF value are widely distributed.

4.3.6 *Damage variables based on AE counts of salt rock during the U/TSCF tests*

Quantifying the correlation between AE and damage from a micromechanical point of view has been a research focus in various countries [272]. As an effective tool to study rock materials, continuum damage mechanics can be used to analyze the damage mechanism of rocks. Kachanov et al [273]. defined the damage variable as:

$$D = \frac{d}{A} \qquad (4.3)$$

where D is the damage and refers to the deterioration state of the material, d is the area of the defects appearing on the material and A is the area of the initial undamaged material. The Damage variable D can vary from 0 (no area of defect $d = 0$) to 1 (specimen fully broken so $d = A$). Assuming that the initial state of the salt rock specimen has no damage and that the AE counts are N_t when the whole salt rock specimen is damaged, the AE count rate (δ) per unit area of the load-bearing section can be defined as follows:

$$\delta = \frac{N_t}{A} \tag{4.4}$$

This equation shows that when the accumulated damage area on the material bearing section is Z_d, the accumulated AE count can be expressed by the following equation:

$$N = \delta * \mathrm{d} = N_t * \frac{d}{A} \tag{4.5}$$

By associating Eq. (4.4) and Eq (4.5), the relationship between the AE counts N and the damage variable D can be obtained as follows:

$$D = \frac{N}{N_t} \tag{4.6}$$

Eq (4.6) shows that the AE counts can reflect the damage of the material to a certain degree. According to the theory of the Kaiser effect of the appearance of the AE phenomenon, combined with previous studies, the damage variable D_i for the *i-th* cycle is defined as:

$$D_i = \frac{N_i}{N_t} \tag{4.7}$$

The cumulative damage up to the *i-th* cycle can be written as:

$$D_{ti} = \sum_1^i \frac{N_i}{N_t} \tag{4.8}$$

Considering the creep–fatigue test, the test path is slightly different from previous fatigue tests as well as monotonic loading tests. The high-stress plateau also has a large number of AE signals. Therefore, using time as the boundary, the counts in the high-stress plateau stage are counted separately from the N_{AE} in the fatigue phase, and the damage is calculated and then cumulated. The USCF test results are shown in Fig 4.14.
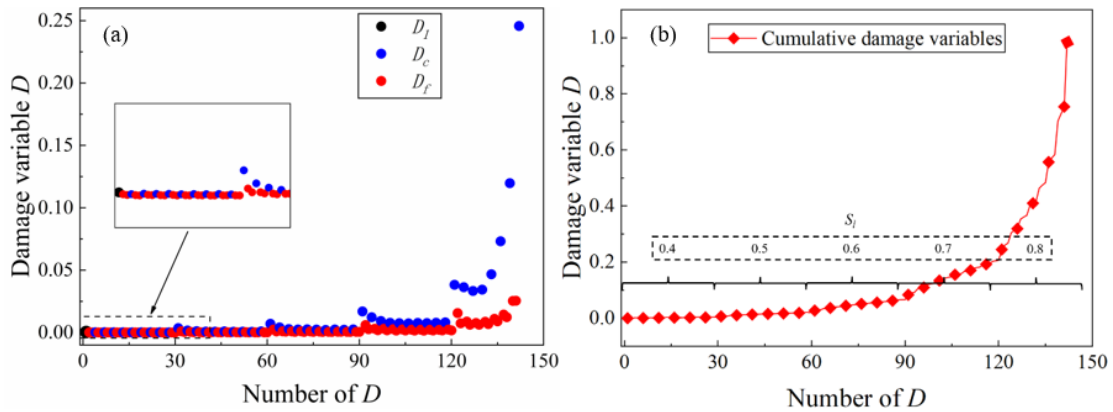
Fig. 4.14 Fatigue cycle and high-stress plateau damage variable development (a) and cumulative damage variable (b) in the USCF test. Damage includes the initial one-hour high-stress plateau (D_l), fatigue cycles (D_f) and high-stress plateau (D_c).

Fig 4.14(a) shows the damage distribution characteristics, where D_l is the damage of the first loading as well as the one-hour stress plateau, D_c is the damage of the high-stress plateau, and D_f is the damage of the fatigue cycle, and Fig 4.14(b) shows the cumulative damage development. At the beginning of the test, the damage in the creep stage was only slightly higher than that in the fatigue cycle, but as the stress increased at 0.7 S_l, the damage in the creep stage was significantly greater than that in the fatigue cycle. In the final stage, the creep stage damage is much larger than that in the fatigue cycle. The cumulative damage shows an almost vertical increase in damage during the final stage. The results for the TSCF test are similar. The test results illustrate that at a lower S_l, the effects in the creep phase and the fatigue cycle are very similar for salt rock; however, as the stress level increases, the creep effect begins to dominate the damage. In addition, the damage difference between the creep stage and the fatigue cycle for each S_l in the USCF and TSCF tests was defined as π.
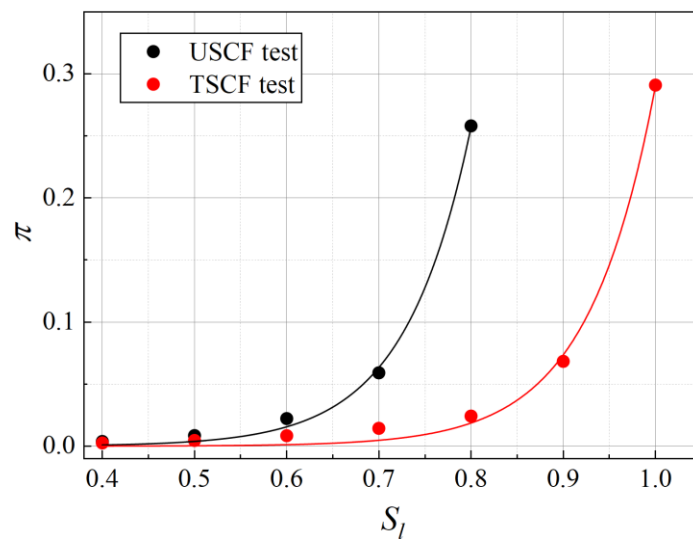
Fig. 4.15 Damage difference π between the creep stage and fatigue cycle for every S_l for the USCF and TSCF tests.

Fig 4.15 shows the development of π in two different tests. It can be seen that π follows a particular trend. At lower stress levels, π is small, and as S_l increases, the difference increases slowly. However, there is a significant increase occurring in the predamage cycle (0.7 S_l and 0.9 S_l). The curves plotted on experimental data have an exponential form. It can also be noticed that the damage difference in the TSCF test is smaller than that in the USCF test for the same S_l.

4.4 Analysis of damage evolution characterization for creep-

fatigue properties of salt rocks

4.4.1 *Discussion of the relationship between residual strain and AE counts of salt rocks during creep-fatigue test*

In this Chapter, the relationship between AE parameters and stress-strain curves was analyzed, and the experimental results showed that AE can well characterize the damage evolution of salt rock specimens, but when analyzing the cumulative counts of AE before and after the fatigue cycles of the intervals in a more thorough way, the feature that the AE counts of the A-cycle are smaller than the AE counts of the B-cycle was found as shown in Fig. 4.16.
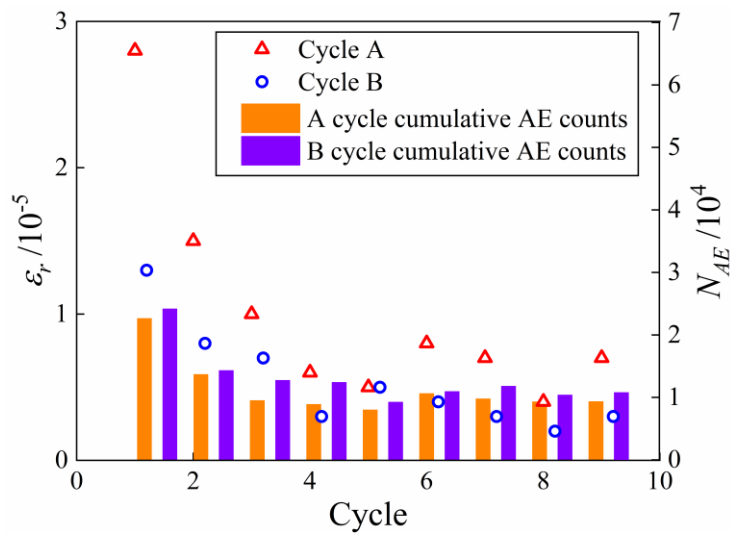
Fig. 4.16 Residual strain and AE counts statistics per cycle in 0.5 S_l from USCF test

In general, AE counts can reflect, the development of internal microcracks during cyclic loading. Previous studies have generally concluded that the larger the plastic deformation produced during cyclic loading, the more pronounced the AE signal of the rock, i.e., the more AE counts [274]. However, there is a difference in the experimental results in this Chapter. The possible reasons for this phenomenon are analyzed as follows.
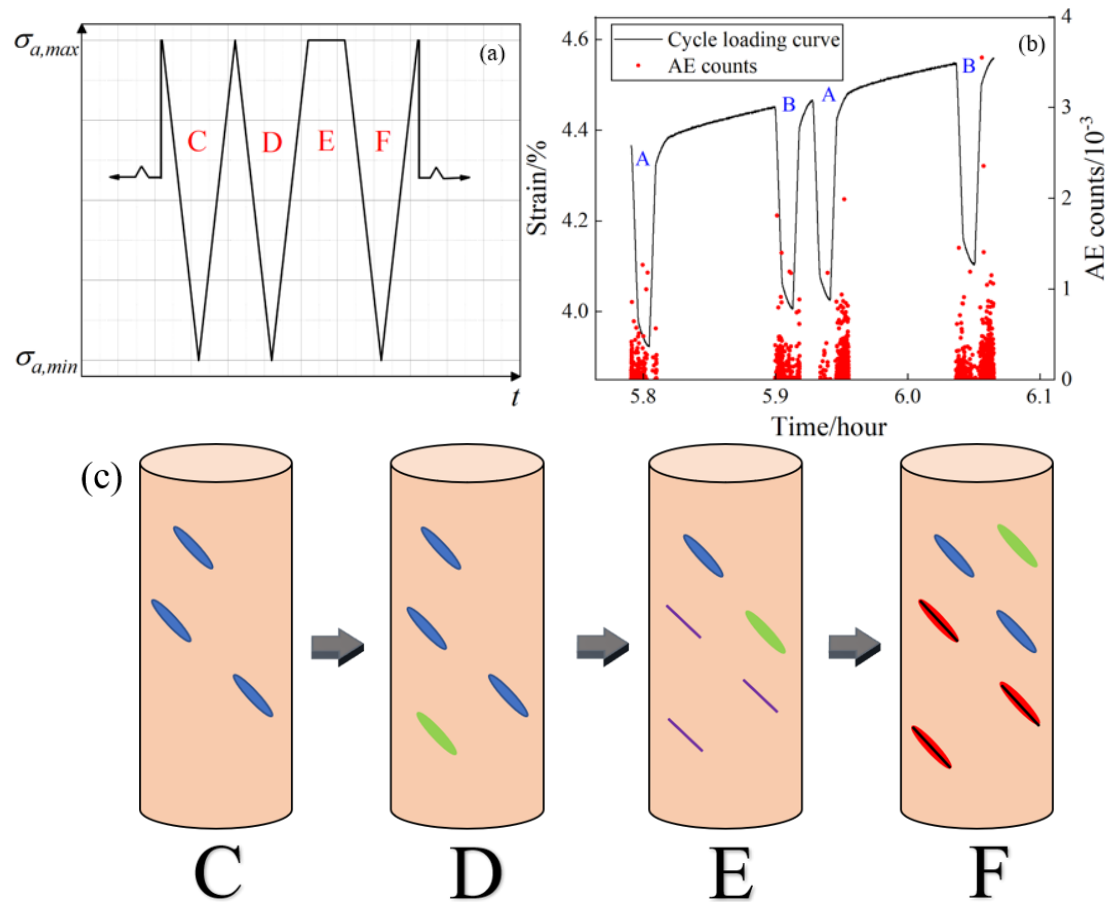
Fig. 4.17 Typical creep fatigue cycle divided into four stages (a); The strain and AE counts for two cycles in 5th level of USCF test(b); Schematic diagram of salt rock crackles development in typical creep fatigue cycle (c)

We can divide a complete creep-fatigue test cycle into 4 stages, as shown in Fig 4.17(a). Stage C - post-previous interval stage, Stage D - pre-current high stress interval cycle load, Stage E - high stress interval period, Stage F - post-high stress interval stage. The evolution of internal fatigue cracks is illustrated in Fig 4.17(c), where blue represents pre-existing cracks, green represents newly generated cracks, purple represents closed cracks, red represents re-opened cracks and black represents re-opened cracks closed again. After a cyclic loading after stage C, new cracks were created inside the salt rock, producing AE signals. After entering the high stress interval E stage, part of the original cracks in the salt rock were closed and the salt rock integrity was enhanced. When entering the F stage after the high stress interval, in addition to the newly generated cracks, the original closed cracks re-open in the unloading section and closed again in the loading section, producing an AE signal greater than that of the

D stage. This is the reason why the number of AE counts is greater after the interval than before. Fig 4.17(b) shows an enlarged view of the strain and AE counts for two cycles of USCF test 5th level and the phenomenon can be clearly seen. In addition, we also found that in the TSCF test, the ratio of AE counts before and after shelving between salt rocks gradually stabilized as the stress level increased as shown in Fig. 4.18. This is due to the fact that as the stress level increases, the salt rock becomes denser and the internal fractures close more tightly under axial stress and confining pressure. The crack re-open in the unloading section of salt rock is reduced. So, the ratio of AE counts before thefailure, which can be used as a criterion for creep fatigue damage of salt rock under the three-way stress state.
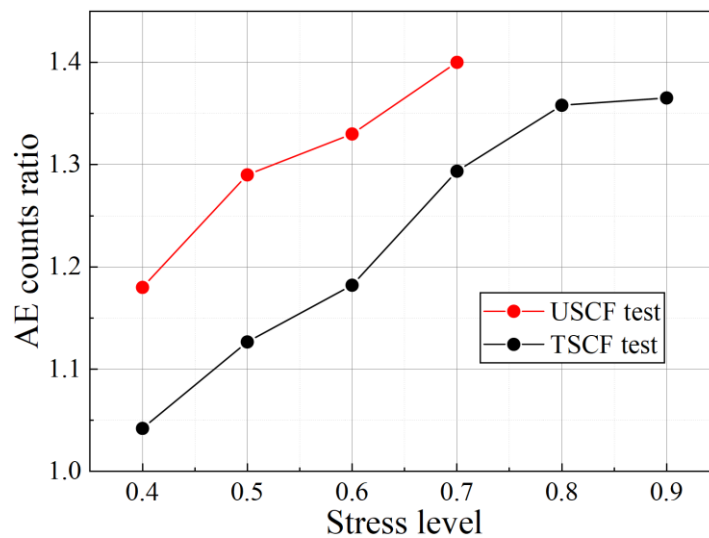
Fig. 4.18 AE count ratio between A and B cycles for various stress levels for USCF and TSCF tests.

4.4.1 *Discussion on rock failure prediction based on RA and AF of salt rocks.*

During the tests, different crack rupture mechanisms were analyzed qualitatively using two parameters, RA and AF. The signals corresponding to tensile damage and shear damage were different. Therefore, a critical value can be defined to serve as a threshold to differentiate tensile cracking and shear cracking. That is, the slope of the split dashed line k given in Eq (11) was used as an indicator to classify shear and tensile ruptures and to quantitatively describe the distribution of shear and tensile cracks.

$$k = {^{AF}}\!/\!_{RA} \qquad (4.9)$$

Many scholars have studied the critical k values of AE to distinguish tension cracking and shear cracking in rocks. Du et al [275]. studied the critical k values of granite, barite, and sandstone based on Brazilian splitting and modified shear tests. The critical k values for granite were also given as 85-95 [276]. However, those authors did not investigate the distribution of k values corresponding to salt rocks. In the future, Brazilian splitting testing on salt rock with AE monitoring could be performed to determine the critical k value of salt rock.

Although there are still very few reports on the k values of salt rocks, some researchers [277] have proposed another simple method to determine the damage of rock specimens using RA and AF values. Some indoor rock mechanics studies have shown that rocks during the unstable stage tend to have more "shear-type" AE signals with larger RA values and smaller AF values. Therefore, parameter θ, as given in Eq (12), can be used as an indicator for rock damage monitoring.

$$\theta = RA/AF \qquad (4.10)$$

An increasing θ value means that the rock is subject to more damage, and extreme values indicate that the rock is in the stage of severe damage.

Fig 4.19(a) shows the distribution of θ values in the USCF test with time. There is no obvious fluctuation in θ in the early stage, and there is only a slight rise and fall when S_l increases. However, there is an obvious upward trend above 0.7 S_l, indicating that the specimen undergoes more damage. The large number of signals with higher θ values at 0.8 S_l suggests that the salt rock specimen will be destabilized and damaged soon. Fig 4.19(b) shows the distribution of θ values with time in the TSCF test. Unlike in the USCF test, in the TSCF test, the θ values undergo obvious changes. There is a clear upward movement with increasing S_l. As S_l increases, the maximum value of θ increases, and the number of signals with large θ values also increases, reaching the maximum at failure. Although the phenomenon in the TSCF test is not as clear as that in the USCF test, it can still be seen that for the creep–fatigue test, this parameter can help make some predictions to a certain extent. It can also be seen that θ values change faster than the mechanical response curve. Future studies will therefore focus on the applicability and reliability of the θ value for salt rock.
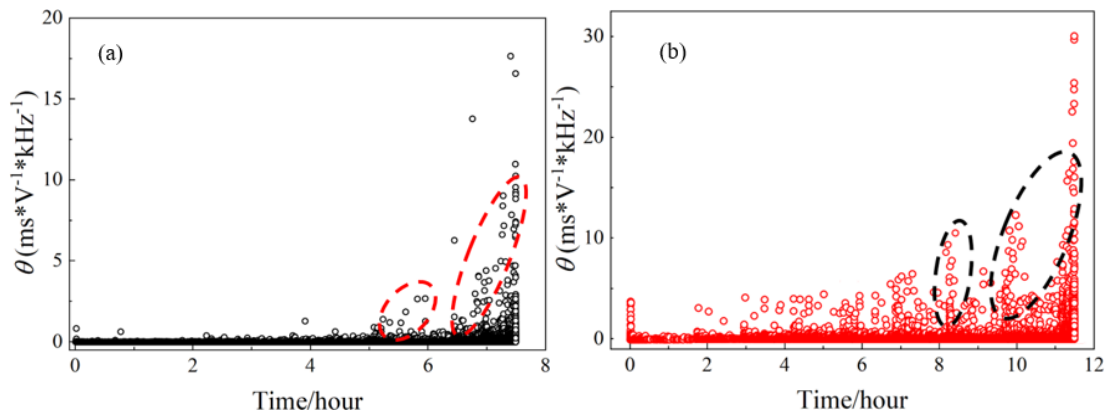
Fig. 4.19 Evolution of θ during USCF test (a) and TSCF test (b).

4.5 Conclusions

Creep–fatigue mechanical tests were designed reflecting realistic operating gas pressure of a CAES plant (cyclic load with or without plateau, various stress level and various confining pressure levels), and the whole damage process of the salt rock during creep–fatigue testing was monitored using acoustic emissions (AE). The following conclusions were obtained:

(1) The creep strain during the high-stress plateau increases with the stress level. Nevertheless, during every level of cycling, the creep strain showed a decreasing trend with increasing number of cycles, suggesting a stabilization phenomenon. Only during the last stage of cycling, the creep strain show a final increase in strain, leading to specimen failure.

(2) At lower stress levels, the high-stress plateaus have an effect on rock: fatigue begins to manifest with a higher residual strain before the plateau than after the plateau. As the stress level increases, the residual strain values before and after the plateau increase. The presence of confining pressure will reduce this growth trend. The hardening effect during creep, which improves the ability of the specimen to resist deformation, is responsible for this phenomenon in salt rock.

(3) The AE peak frequencies have significantly bar distribution characteristics. The difference in the peak frequency distribution reflects the difference in the failure pattern of the specimens. The specimens in the USCF test predominantly exhibit tensile failure, while specimens in the TSCF test predominantly exhibit shear failure.

(4) The AF/RA magnitude of the AE can be used to determine the crack type. Signals with large RA and small AF values in the triaxial tests are significantly more common than those in the uniaxial tests, reflecting the characteristics of increased shear damage

in the TSCF test. Before the failure stage, the signal distribution caused by the high-stress plateau is smaller than that in the fatigue cycle. However, the opposite trend was observed after entering the last stage.

(5) Both the AE parameters and mechanical data show that the plastic strain and damage during the creep stage gradually dominates as the stress level increases. In the final stage, the stress during creep transforms into a force that drives fracture expansion. Therefore, in the design of gas storage, the stress level of the high-stress stabilization stage needs to be considered as an important safety threshold.

5 Long-time creep-fatigue mechanical properties of salt rock

5.1 Introduction

In the preceding three chapters, the influences of multiple factors such as high stress intervals (creep) duration, confining pressure, stress levels, etc., on the mechanical characteristics of salt rock creep-fatigue were systematically investigated. The interactions between creep and fatigue were identified. Based on experimental data and a combination of macroscopic and microscopic observations, an analysis was conducted to understand the diverse responses of internal salt rock structures to creep and fatigue, revealing the reasons behind the variations in creep and fatigue damage. The mutual interaction between creep and fatigue leads to a more intricate evolution of damage within the salt rock specimens, a feature also reflected in the results of acoustic emission monitoring.

However, due to the experimental design, the aforementioned tests were conducted within the timeframe of a single working day. Given that the peak shaving frequency of compressed air energy storage power plants often operates on the scale of days [278], conducting long-duration creep-fatigue tests on salt rock becomes crucial for a precise understanding of the damage evolution in salt cavern reservoirs. Hence, in this chapter, with varying peak shaving frequencies and gas storage pressures, three sets of long-duration salt rock creep-fatigue tests were designed. These tests aim to explore the creep-fatigue mechanical characteristics of salt rock on the operational scale of gas storage facilities, contributing to a comprehensive understanding of the salt cavern reservoir's damage evolution.

5.2 Experimental materials and methods

Specimen preparation, test equipment, and test procedures are consistent with those in chapters 2, 3 and 4, and will not be repeated here. Only the new test program is introduced.

5.2.1 *Long-time creep-fatigue testing*

The loading and unloading path of the test is as follows (see Fig. 5.1): the first stage is the loading stage, the specimen is loaded to the upper limit of stress at a constant stress rate; the second stage is the upper limit of creep stage, keep the upper limit of stress constant and stabilize the pressure to the third stage; the third stage is the unloading stage, with the same constant rate of stress reduced to the lower limit of stress;

the fourth stage is the lower limit of creep stage, keep the lower limit of stress constant and stabilize the pressure to the next first stage. The time of each stage is kept the same, and the four stages are a complete cycle, repeating the above four processes until the specimen is destroyed. Comprehensive consideration of salt cavern gas pressure, CAES power plant frequency, regulation cycle, and testing machine working conditions and other factors, the longest test time is set to 8 days. If the specimen is not damaged after 8 days, the test is manually stop.
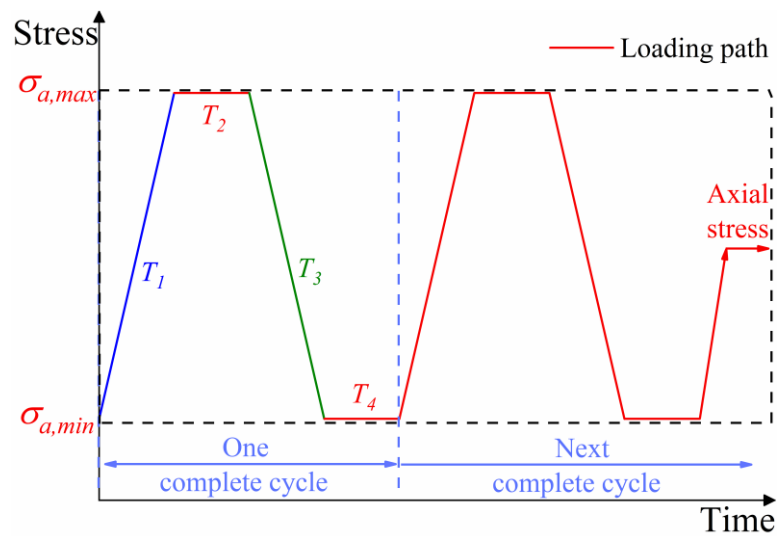
Fig.5.1 Loading path for long-time creep-fatigue (LTCF) tests on salt rocks.

Uniaxial compressive strength (UCS) is taken from experimental data presented in section 2. The lower stress limit of the test was the same as the previous test, set at 3% of UCS, 1 MPa. The upper stress limit of the test was initially set at 85% of the UCS (test L-1), but it was found that the salt rock specimens were damaged within only 3 days, which could not satisfy the preset target of the test (8 days). Therefore, it was decided that the maximum stress limit was finally decreased to 80% of the UCS for the two other tests L-2 and L-3. The specific loading and unloading parameters for the three tests are shown in Table 5.1. Note that we vary the duration T and the stress level, so the resulting loading rate is different for each test.

Table 5.1 Loading and unloading parameters in LTCFT

Test number	T/hour	Upper stress level/MPa	Loading rate/(kN/s)
L-1	24	24	0.00212kN/s
L-2	24	18	0.00157kN/s

| L-3 | 8 | 18 | 0.00472kN/s |

The purpose of this setup is to simulate a salt cavern peaking once or three times a day, and the difference in the upper storage pressure limit can be used to observe the effect of changes in the air injection rate as well.

5.3 Results and analysis of long-time creep-fatigue mechanical properties of salt rock

5.3.1 *Stress-strain curve of salt rock specimen*

Fig. 5.2 shows the stress-strain curves of salt rock specimens under different maximum cyclic stresses and different loading cycles.
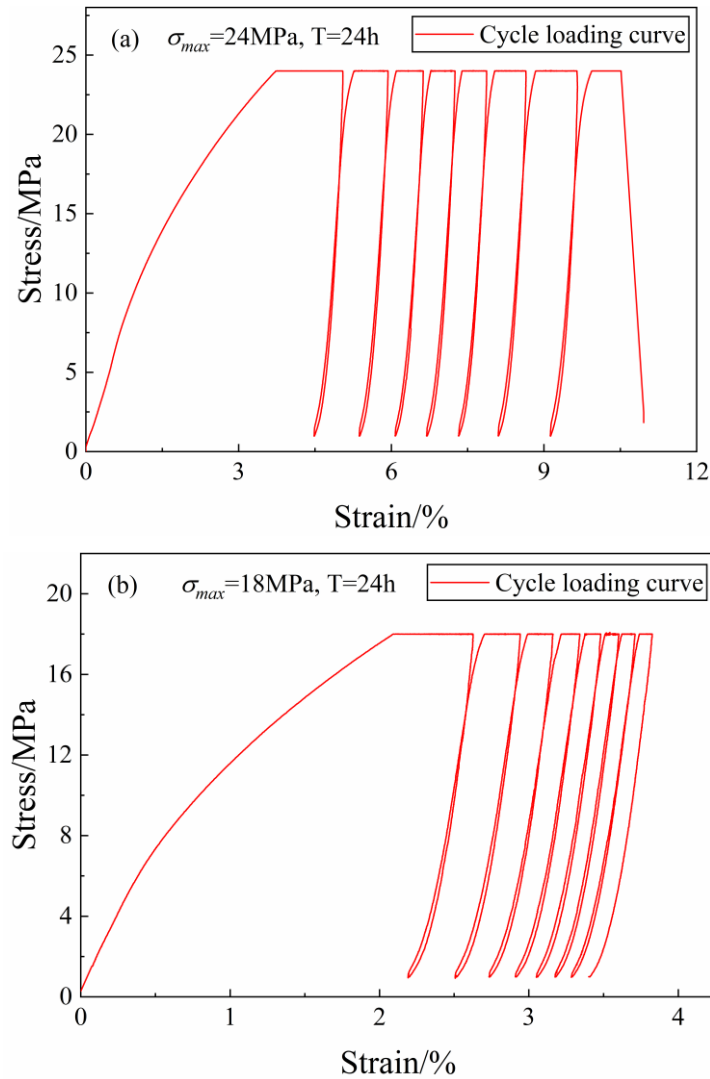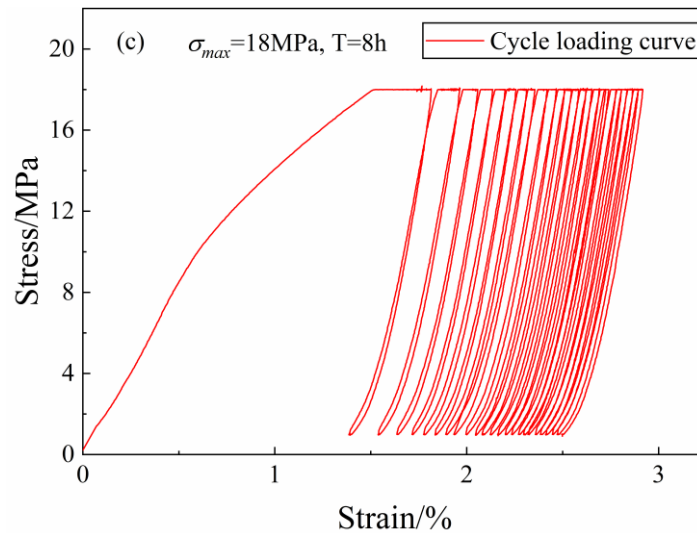
Fig. 5.2 Stress-strain curves for 3 long-time creep-fatigue tests on salt rock.

It can be found that the specimen of L-1 test was damaged after entering the 8th cycle, and the specimen completely passed 3 deformation stages of decelerated deformation, stable deformation and accelerated deformation. For the other two tests L-2 and L-3, due to the lower upper stress limit, the specimens were not damaged after 8 days of complete loading, so the stress-strain curves of the specimens only showed the process of 'sparse' - 'dense'. i.e., it did not stage III and final failure. Since only L-1 test has reached failure, this test will be taken as the main object of analysis, and the long-time creep-fatigue mechanical properties of salt rock will be investigated by comparing the test results of the two other tests. Observing the stress-strain curves of the three tests, it can be found that the increase of the upper stress limit is decisive for the deformation of salt rock compared with the change in loading rate. In the case of constant upper limit stress, the salt rock specimens with frequent peak shifting produced smaller deformation after the same test time.
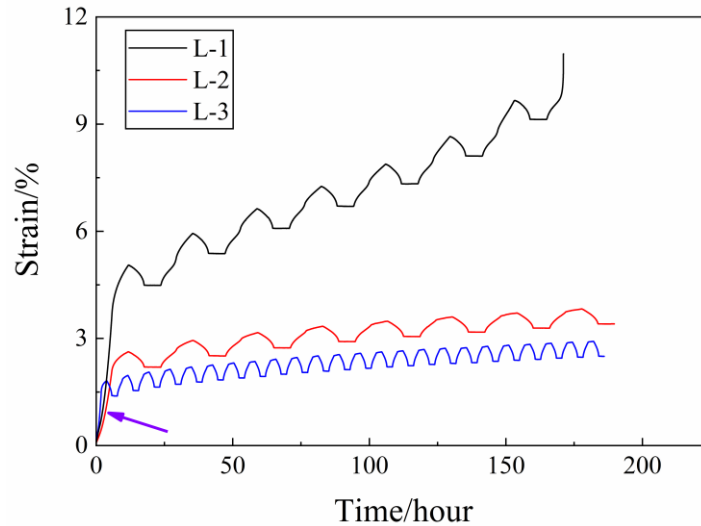
Fig. 5.3 Strain-time curves for three long-time creep-fatigue tests.

Figure 5.3 shows the variation of strain with time for the three tests. The strain curve of the L-1 test shows a rapid rising trend with time, while the second and third tests enter the stage of stable deformation and the strain curves tend to flatten out after a very small number of cycles. Meanwhile, it can be seen that the difference in loading frequency resulted in the strain curves of L-3 tests always lying below the L-2 curves despite the same upper stress limit.

5.3.2 *Strain in salt rock at different loading stages*

In order to clearly show the effect of different loading schemes on the strain development of salt rock specimens, the plastic strains generated at the end of the whole cycle were calculated by taking the beginning and the end of each complete cycle as the boundaries and the results are shown in Figure 5.4,
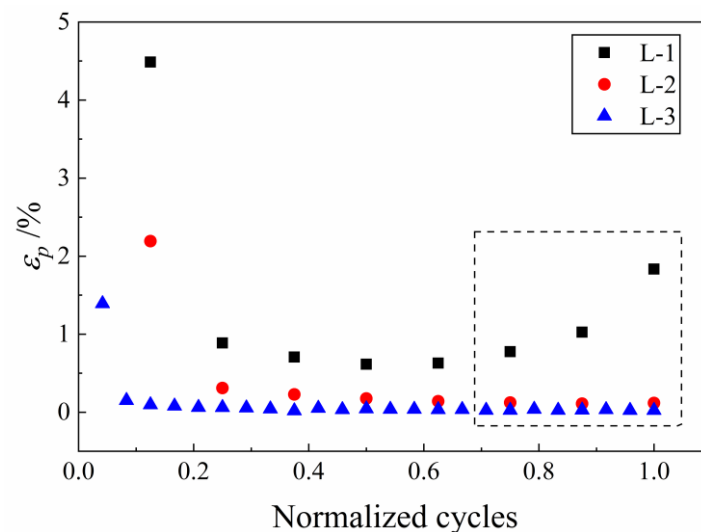
Fig. 5.4 Plastic strain for each complete cycle of the three long-time creep-fatigue tests

It is noted that due to the large number of cycles in the L-3 test, the method of normalizing the number of cycles (cycle number divided by the total number of cycles of the test) is used to put the vertical coordinates of the three groups of tests on a uniform axis for clear comparison. Anyhow, since L-2 and L-3 tests did not reach final failure, the comparison with test L-1 in terms of horizontal axis remain impossible. It can be seen that as the maximum cyclic stress increases, the plastic strain produced in the specimen at the end of each cycle increases; in the L-1 test, when the specimen undergoes damage, in the cyclic stage before the damage, when the cycle is over, the plastic strain produced increases significantly compared with the previous cycle (see the black dotted box in Figure 5.4).
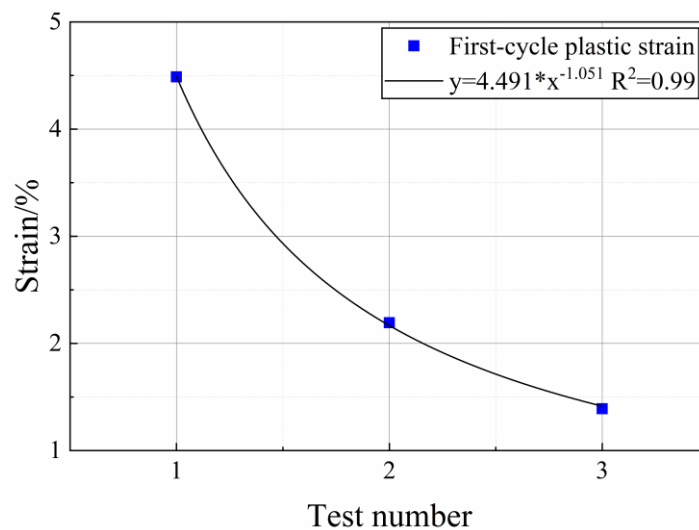
Fig. 5.5 First-cycle strain for three long-time creep-fatigue tests

Considering that the deformation of the initial cycle is much larger than that of other cycles, the cycle of initial loading to the upper stress limit is named as the first cycle, and the results are shown in Fig. 5.5. It can be seen that the strains of the three tests show a linear decreasing trend. Since the upper stress limit of the L-1 test is higher than that of the other two tests, the red squares in the figure are the strains of the salt rock specimens loaded to the same upper stress limit, and it can be found that the strains of the salt rock show a decreasing trend with the increase of the loading rate, which is in line with the existing test conclusions, indicating that in the time scale of the salt cavern CAES operation, the salt rock specimen deformation still satisfies that conclusion.

Since the complete cycle in Figure 5.4 includes both fatigue strains from loading/unloading and creep strains from high/low stress intervals, the strains generated at each stage are calculated separately, and the results are shown in Fig 5.6,
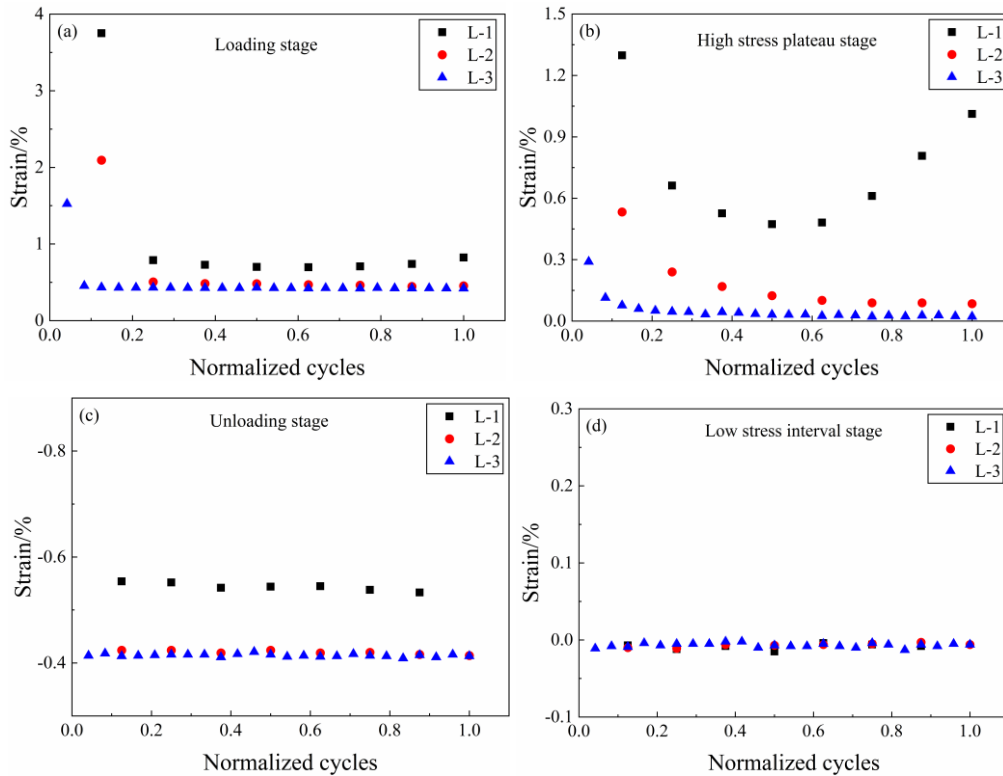
Fig. 5.6 Three long-time creep-fatigue tests: (a) strain during loading, (b) high stress plateau strain, (c) strain during unloading and (d) low stress interval strain.

The most obvious differences between the three sets of tests are in the loading and high stress plateau stage. Firstly, for the complete L-1 test, the deformation in the loading section appeared to be characterized by a distinct second stage and accelerated third deformation stage, where the trend of deformation growth was not obvious for L-2 and L-3 test. In contrast, the development pattern of creep strain is approximately V-shaped, i.e., the strain decreases to a minimum value and does not show a significant stabilizing deformation, which then grows rapidly, and the specimen subsequently undergoes damage. In the L-2 and L-3 tests, which have the same upper stress limit, the loading stage and the high stress plateau stage also appeared to be obviously different, and after the third loading stage, the strain difference between the loading stages of the two groups of tests became very small, which indicates that although the difference in loading rate leads to the difference in the deformation of the salt rock, this effect is weakening as the test proceeds. The speed of the creep strain into the stabilization stage

of the specimens in the L-3 test is significantly faster than that of the specimens in the L-2 test, which reflects that, for the same time span, the higher the number of cycles, the faster the creep strain enters the stable deformation phase. That is, the increase in the frequency of peaking contributes to the stabilization of the creep deformation rate of the surrounding rock in the salt cavern. According to this test phenomenon, when the CAES plant needs to change the operating pressure, the peak frequency can be increased appropriately, in order to make the salt carven surrounding rock enter the stable deformation as soon as possible, and to reduce the influence of pressure change on the salt craven surrounding rock. In the unloading stage, the three tests are the same in that the strain remains basically constant with cycling, and the unloading strain of the higher stress L-1 test is obviously larger than that of the other two groups. In the low-stress interval stage, the strain values of the three groups of tests kept fluctuating around the zero.

5.3.3 *Strain rate and elastic modulus analysis of creep-fatigue curves*

The modulus of elasticity is an important mechanical property parameter of materials. From the macroscopic point of view, the modulus of elasticity is a physical quantity that characterizes the ability of a material to resist deformation under the action of external loading; from the microscopic point of view, the modulus of elasticity is an index that characterizes the bonding strength between ions, atoms, or molecules within a material. Considering that this test is a creep-fatigue test, the loading and unloading also includes a high stress plateau /low stress interval stage, so the elastic modulus is calculated during loading (E_l) and unloading (E_u) phases. The calculations are shown in Eqs 5.1 and 5.2 below. The test results are shown in Fig 5.7.

$$E_l = \frac{\sigma_B - \sigma_A}{\varepsilon_B - \varepsilon_A} \tag{5.1}$$

$$E_u = \frac{\sigma_D - \sigma_C}{\varepsilon_D - \varepsilon_C} \tag{5.2}$$

where E_l is the loading modulus, ε_A and ε_B represent the starting and ending strain values of the approximate linear segment during the loading process, while σ_A and σ_B correspond to the respective stress values. E_u is the unloading modulus, ε_C and ε_D represent the starting and ending strain values of the approximate linear segment during the loading process, while σ_C and σ_D correspond to the respective stress values.
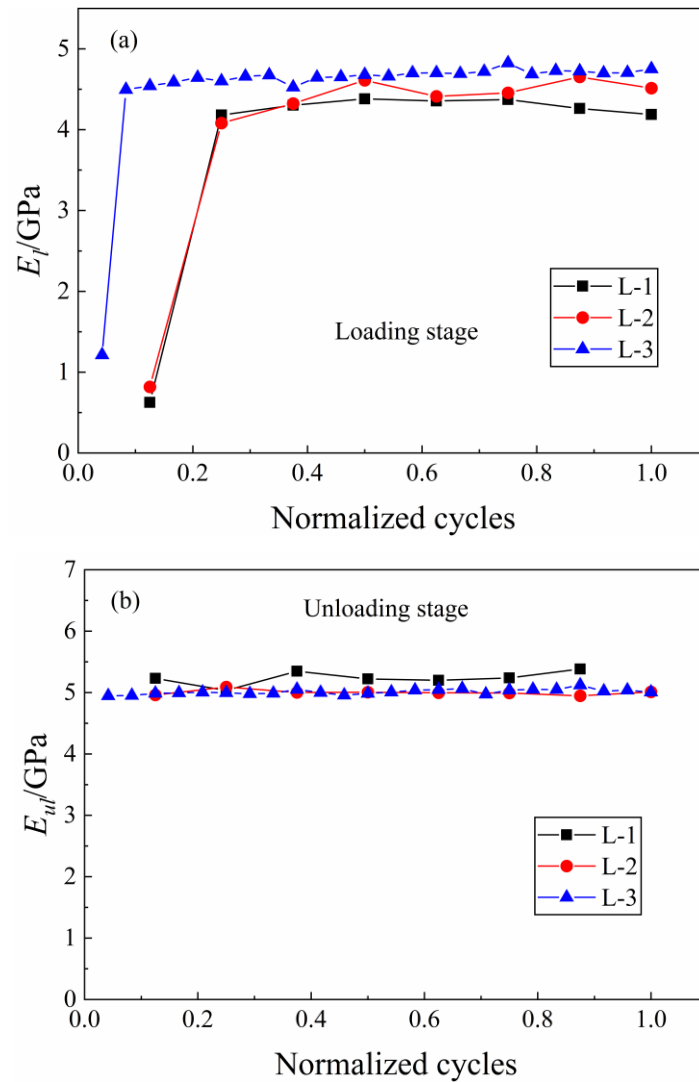
Fig. 5.7 Elastic moduli computed during (a) loading and (b) unloading for three long-time creep-fatigue tests.

Figure 5.7 (a) shows the change of loading elastic modulus. The first cycle modulus is very low, because the salt rock also produces a large amount of creep deformation. Into the second cycle, the loading modulus of the salt rock tends to reach a stable value between 4 and 4.5GPa. Here there is a special phenomenon, that is, the modulus of elasticity of the L-1 test is smaller than that of the L-2 and L-3 test. This may be related to the creep inflection point of the specimen. It has been pointed out that the inflection point of accelerated creep of salt rock occurs at the stress level of 0.6-0.7 during the graded creep experiment of salt rock. For this test, it can be assumed that the strain of the salt rock specimen does not increase linearly in the process of stress growth, so it leads to this phenomenon. It can also be found that the loading modulus of the L-1 test shows a decreasing trend in the later part of the test. The unloaded elasticity reflects the

ability of the specimen to recover from elastic strain. The larger the unloading modulus is, the less elastic strain is recovered and the more damage is produced in the specimen. Among the three groups of tests, the unloaded modulus of the L-1 test is obviously larger than that of the other two groups (Fig. 5.7(b)), in addition, the modulus of the L-2 and L-3 tests shows a slight fluctuation with the progress of the test, and the unloaded modulus of the L-1 test shows a rising trend in the last few cycles. This phenomenon reflects the changes in the internal structure of the salt rock specimens.

Furthermore, another phenomenon can be observed in all three test groups, where the unloading modulus is slightly higher than the loading modulus. This is attributed to the fact that the unloading modulus represents the elastic deformation recovery, exhibiting hysteresis effects and being influenced by the presence of plastic deformation during the loading process. To clearly observe the difference between the loading and unloading moduli in each test group, $\emptyset$ is defined as the average difference between the loading and unloading moduli (excluding the loading modulus of the first cycle) for each test, as shown in Figure 5.8.
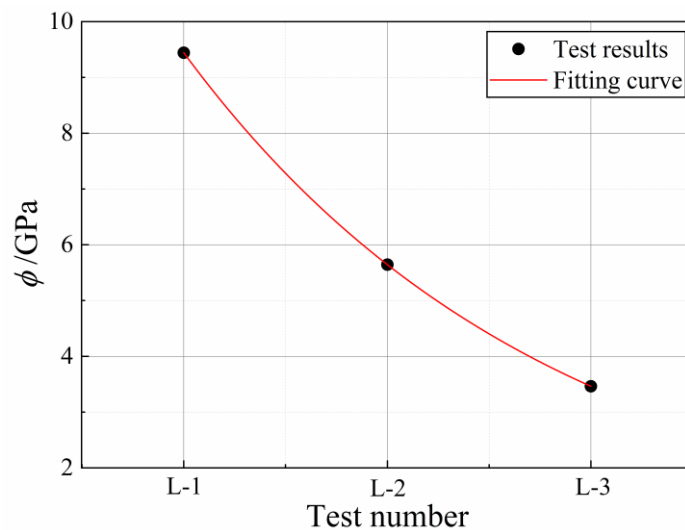
Fig. 5.8 The average of difference between the loaded and unloaded modulus ($\emptyset$) in the three tests.

It can be observed that the stress level has a significant impact on the difference. Due to the fact that salt rock exhibits minimal elastic deformation, higher stress levels result in greater plastic deformation and less elastic recovery, leading to a more noticeable difference between the loading and unloading moduli. Similarly, a faster loading and unloading rate results in less plastic deformation, leading to a smaller difference, indicating a more stable behavior of the salt rock specimen. This phenomenon is closely

related to the natural characteristics of the rock.

Rock is a natural engineering material with a large number of internal microscopic defects (microcracks and micropores, etc.), and the existence of these defects is an important factor affecting the change of the modulus of elasticity of the rock under external loading. Generally speaking, the lower the number of microscopic defects inside the rock, the higher the degree of compactness, the stronger the resistance to deformation, and the higher the modulus of elasticity. Therefore, the change rule of elastic modulus of salt rock specimen with the number of load cycles can be explained from the following aspects: (1) when the number of load cycles is less, the original defects inside the salt rock specimen gradually close under the action of cyclic loading, the internal structure gradually tends to be denser, and the resistance to deformation is enhanced to a certain extent, which macroscopically manifests itself in the gradual increase of elastic modulus with the increase of the number of load cycles; (2) when the number of load cycles is increased to a certain degree, the degree of compactness of the salt rock specimen is close to the maximum value under the upper stress, and after that, it basically does not change with the increase of the number of load cycles; at the same time, the salt rock specimen produces relatively few new cracks in this stage, so the modulus of elasticity basically does not change with the increase of the number of load cycles; (3) when it is close to the destruction, the damage inside the salt rock specimen caused by the microcracks and expansion gradually increases, and the ability to resist deformation gradually increases. (4) Near the damage, the damage caused by microcracks sprouting and expanding inside the salt rock specimen gradually increases, and the ability to resist deformation gradually decreases, which is manifested in the gradual decrease of elastic modulus with the increase of the number of load cycles.

In this test, the deformation rate can be differentiated into the loading and unloading stage and the high stress plateau /low stress interval stage, so in order to describe the development of the deformation rate in a unified way, the calculation method is as follows: for all the three groups of tests, the deformation rate is calculated for one hour with the boundary of every hour, and the results of the two groups of tests of the same time cycle, L-1 and L-2, are chosen for graphical analysis in order to make a clear comparison, and the results are shown in Fig. 5.9.
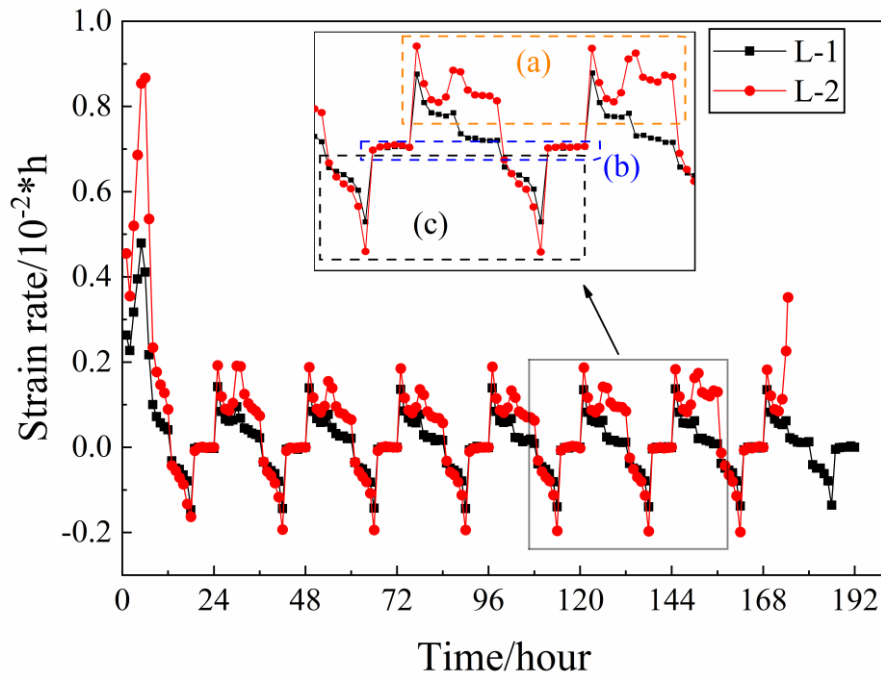
Fig. 5.9 Strain rate versus time for L-1 and L-2 tests.

From Fig. 5.9, it can be found that the development of strain rate changes in the deceleration and stable deformation phases of the two sets of tests is similar, and in the first loading section, the strain rate shows a rapid increase with the application of load, which is attributed to the rapid closure of some primary fissures in the interior of the salt rock at the early stage of loading. However, as the loading continues, the internal structure of the specimen is gradually adjusted in place, and the internal resistance to deformation is enhanced, so the phenomenon of slowing down the rate of increase of strain rate occurs. In the L-1 test, the sixth strain rate of the loading section still shows a rising trend, but it is very close to the fifth strain rate, while in the L-2 test, the last strain rate of the loading section is smaller than the fifth strain rate, which indicates that the deformation rate starts to decrease at this time, which leads to this phenomenon, and the hardening of the specimen is related to the beginning of the phenomenon.

In the high stress plateau, the deformation rate decreases rapidly, but after the specimen passes through the stress adaptation stage, the deformation rate decreasing trend slows down greatly. This pattern is more obvious in the subsequent cycles, indicating that the change of stress state causes a rapid adjustment of the internal structure of the salt rock, but this process will be completed in a relatively short stage of time, and then the salt rock is once again in the process of continuous equilibrium between the internal stress and external load. In the unloading section, the deformation

of the salt rock is mainly driven by the internal stress because the external load is continuously removed and the external force is reduced, so the deformation rate is negative, i.e., it is in the state of recovering deformation, and the strain rate is small at this time. For the two sets of tests, the strain rate in the low stress interval section does not change much, basically fluctuating around the 0 point. Due to the large number of data points and the fact that almost all of the salt rock is in the stable deformation stage when it is operated as a air storage. In order to show more clearly, the two groups of tests under the same loading cycle, the different upper limit stress on the stable deformation and accelerated deformation stage of salt rock. The unloading section and low-stress interval of cycles 5 and 6, and the loading section and high-stress plateau of cycles 6 and 7 of the two sets of tests in Fig. 5.9 were taken and enlarged for cross-comparison. As shown in Fig 5.9. (a) is the strain rate for the loading section and high stress plateau of cycles 6 and 7, (b) is the strain rate for the short low stress interval of cycles 5 and 6, and (c) is the strain rate for the unloading section of cycles 5 and 6.
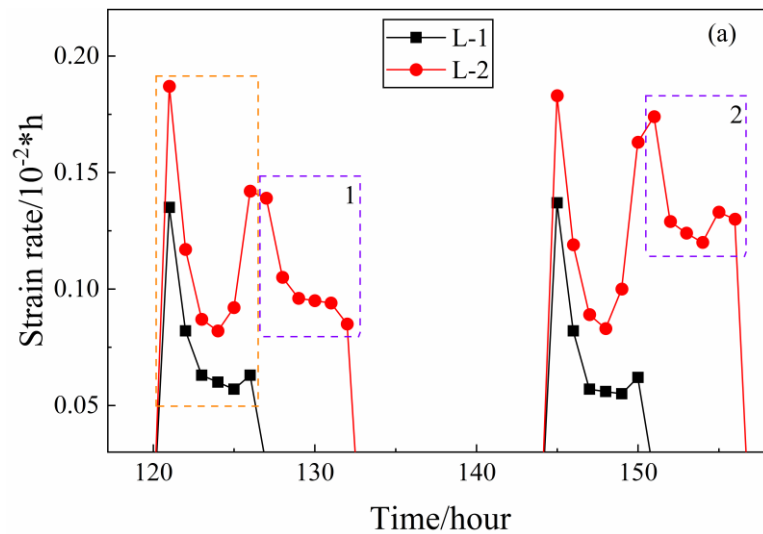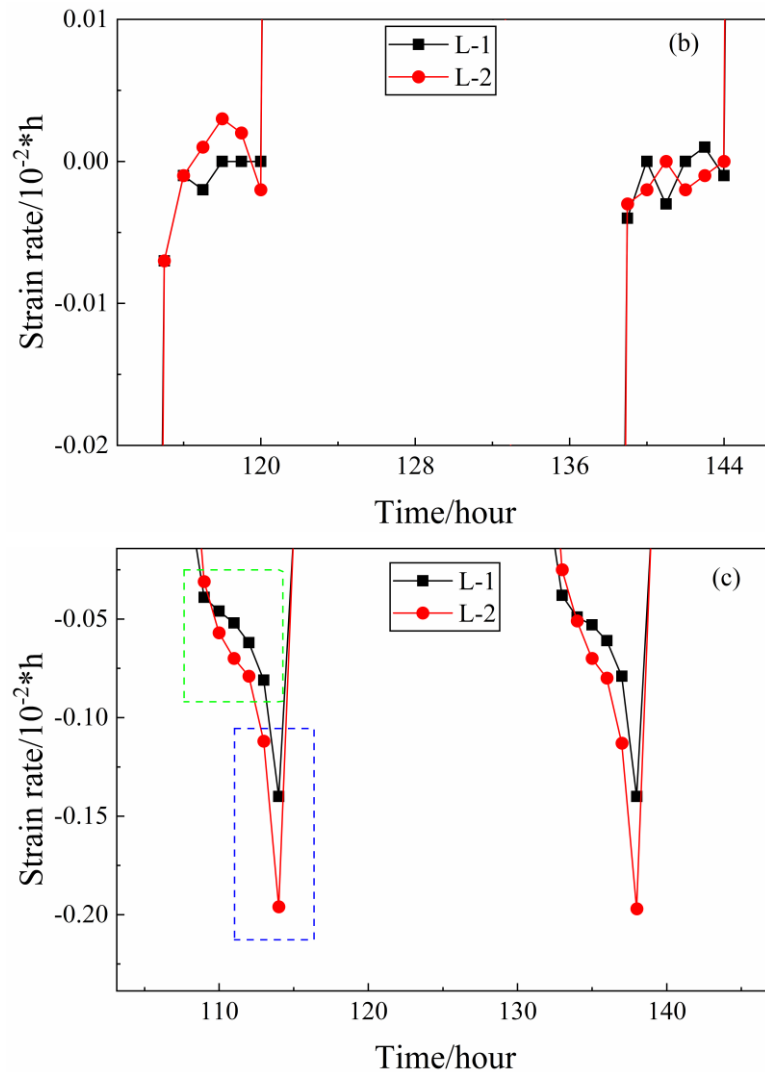
Fig. 5.10 (a) Yellow dashed box of Fig. 5.8, (b) blue dashed box of Fig. 5.8 and (c) black dashed box of Fig. 5.8.

The orange dashed box in Figure 5.10(a) illustrates the variation of deformation rate in the sixth cyclic loading segment for both L-1 and L-2 tests, and it can be noticed that the strain rate increases to a maximum value as the load is applied, and then begins to show a decreasing trend. It is interesting to note that as the stress continues to increase, the fifth strain rate in the loading segment of the L-1 test again shows an increase and the rate of increase is accelerating. Although the increase was small, the last strain rate of the L-2 test still showed an increase. The same phenomenon was observed in the seventh cycle. Similar to what led to the difference in the development of the elastic modulus, this is also related to the inflection point of the stress level for accelerated creep in salt rock. At the fifth strain rate of the L-1 test, where the axial load has been applied for four hours, the stress has grown to more than 60% of the compressive

138

strength of the salt rock, and at the sixth rating it has exceeded 70%, and the stress rating of the L-2 test is also close to 60% of the compressive strength at the sixth strain rate. This is close to the conclusion of existing studies that the inflection point of accelerated creep of salt rock occurs at 60%-70% of the compressive strength, after which the creep rate of salt rock increases rapidly.

Meanwhile, it can be found that in the second cycle of L-1 test, the first strain rate of the loading section and the sixth strain rate are almost the same size, but as the test proceeds the first strain rate of the loading section in each cycle shows only a small decreasing trend, but the sixth strain rate shows a significant decrease, and only in the pre-destruction cycle (i.e., the seventh cycle) does it have a tendency to reappear to grow, which shows that in the process of the experiment, the salt rock This indicates that during the experiment, the hardening effect inside the salt rock increases in the first stage, but maintains the equilibrium state in the second stage, and then shows a weakening trend after entering the third stage, at which time the large cracks inside the salt rock are formed, and the cracks penetrate through the surface, and the salt rock gradually loses its bearing capacity and is destroyed. The purple dashed line box is the deformation rate of the high stress plateau, it can be found that for the sixth cycle (including the second to the fifth cycle), the strain rate of the high stress plateau always shows a decreasing trend, but in the seventh cycle, the strain rate of the high stress plateau shows a trend of decreasing and then increasing, at the same time, the strain rate of the other phases has not yet produced obvious changes, which indicates that in the pre-destruction cycle stage, the high stress of the interval has been transformed into the high stress of the pre-destruction phase. high stress in the interval stage has been transformed into a force driving rock destruction. In addition, the creep rate change during the high stress plateau can be used as an indicator to judge the stability state of the surrounding rock in salt cavern. This is an important guide to ensure the stable operation of the salt cavern CAES plant.

Figure 5.10 (b) reflects the development law of deformation rate during the low stress interval of the fifth and sixth cycles, and it can be found that although slightly different, the difference of test conditions has little effect on the strain rate, and the strain rate of the low stress interval of the two groups of tests has a small difference, with a very small value. Figure 5.10 (c) shows the development law of deformation rate in the unloading section of the fifth and sixth cycles, and it can be found that the difference of strain rate in the green dashed box is very small, which indicates that the

change of the upper stress limit and the loading rate has a small effect on the initial unloading state of the salt rock, but the unloading rate shows a tendency to increase when the external load is unloaded to a certain stress magnitude and the strain rate reaches a maximum when the external load is unloaded to a minimum value. rate reaches the maximum. This is similar for the three sets of test chambers. Moreover, from the second cycle onwards, the development pattern of each cycle is also consistent. The implication of this result is that, as unloading proceeds, the internal structure adjustment of salt rock mainly depends on the differential effects of internal and external stresses, and for the recoverable elastic strain, it basically shows a linear trend according to Hooke's law. When the external force is unloaded to the critical value, the internal stress is greater than the external load, and the deformation rate of the unloaded section of the salt rock grows and grows faster. And it can be noticed that although the L-2 test also showed an increase phenomenon, the final increase value was obviously smaller than that of the L-1 test, which indicates that the difference of the stress state will cause the change of the unloading strain rate. Another feature is that the strain rate in the initial unloading section is smaller compared to the loading section regardless of the test conditions. This provided part of the evidence for the subsequent formulation of the creep-fatigue constitutive equations for salt rocks.

5.4 Mechanistic analysis of salt rock deformation variations due to loading rates

In this chapter, we discovered that different loading rates lead to variations in the deformation rate and deformation magnitude of salt rock specimens, defining this difference as the rate effect of salt rock. From the above test results, a basic law related to the rate effect can be obtained: as the loading rate decreases, the plastic deformation produced by the salt rock in each cycle increases, and the overall fatigue life decreases. Salt rock is a typical sedimentary evaporite-crystalline rock, mainly composed of NaCl crystals. In the crystal, the plastic deformation of the material is mainly formed through the slip of dislocations, and the larger the number of dislocations and the faster the slip of dislocations, the larger the plastic deformation produced. The movement of dislocations in the crystal is affected by the effective stress and temperature, as shown in Eqs. (5.3) and (5.4), respectively.

$$v = B(\sigma *)^{m*} \tag{5.3}$$

$$v = v_c \, exp\left(\frac{-\Delta F^{\neq}}{kT}\right) \tag{5.4}$$

σ^* is the effective stress. m^* is a stress sensitivity factor. k is the Boltzmann constant. T is the absolute temperature. $\Delta F^{\neq}$ is standardized activation energy, denotes the energy required to make the dislocation fully activated. v_c is the dislocation velocity when the standard activation energy is zero, i.e., the speed of sound. The temperature is approximately constant during the test, and it can be assumed that v is only related to the effective stress.
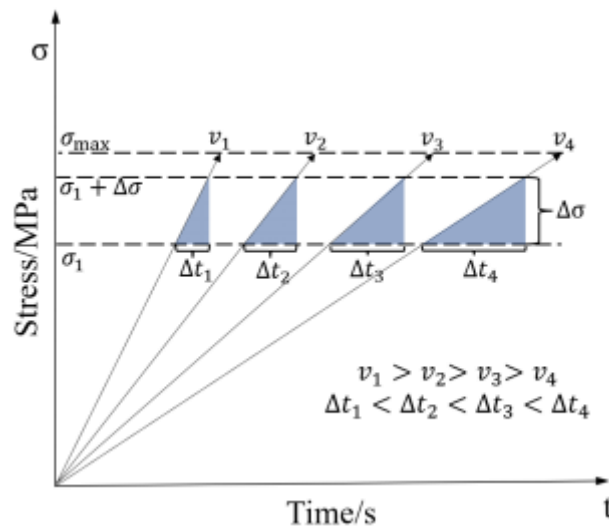
Fig.5.11 Schematic diagram of loading path

The loading and unloading paths of the tests in the paper are identical, only the rates are different, i.e., the time required to reach the same stress value is different. The slower the loading and unloading rate, the longer the time required, as shown in Fig. 5.11, the longer the dislocation slip, the longer the slip displacement, i.e., the larger the resulting plastic deformation (residual deformation). It is known from the fourth strength theory of materials, i.e., the distortion energy theory, that the distortion/plastic deformation is the same when the material undergoes damage under the same conditions. The smaller the loading and unloading rate, the greater the plastic deformation produced per cycle, and the smaller the number of cycles the material undergoes at the time of damage, i.e., the smaller the fatigue life.
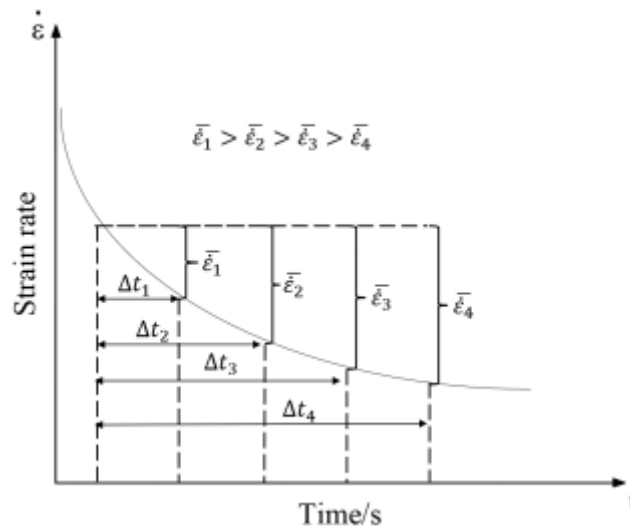
Fig.5.12 Schematic diagram of strain rate change

It should be noted that plastic deformation under the influence of rate effects is not exactly proportional to time or loading and unloading rates. This is due to the fact that during the loading process, the salt rock enters a new stress state from one stress state. Under the new stress state, the salt rock has to gradually proliferate new dislocations to counteract the external force, and the new dislocations are generated to increase the internal force level and reduce the difference between the internal and external forces, so that the dislocations proliferate at a lower rate, and the deformation rate decreases (i.e., deformation stage 1, attenuation deformation stage), until it reaches the balance between the internal and external forces, and enters into the steady-state deformation state. Loading and unloading process stress level actually changes constantly, in a fixed stress level of time is very short, the deformation process is always in the attenuation deformation. As shown in Figure 5.12, the slow loading rate corresponds to a lower average deformation rate, but the cumulative deformation is larger.

5.5 Conclusions

The peaking cycles of salt cavern CAES plants are often designed in terms of days, so conducting long-time creep-fatigue tests on salt rock is crucial for accurately evaluating the stability of salt cavern storage. In this chapter, the long-time creep-fatigue tests of salt rock with different loading and unloading cycles and upper stress limits are carried out against the background of the real gas pressure state during the operation of a CAES plant, and the mechanical properties of salt rock creep-fatigue over a long time span are investigated. The specific conclusions are as follows,

(1) In long-time salt rock creep-fatigue tests, the smaller the loading rate, the lesser the deformation generated during the loading phase. The influence of changes in the stress upper limit on salt rock creep is greater than that of the fatigue loading cycle.

(2) The salt rock specimens in the L-1 test underwent a complete three-stage deformation process. Compared to the loading/unloading and low stress interval stages, the variation of strain during the high stress plateau stage is notably significant in the growth phase, exhibiting an overall V-shaped development pattern.

(3) The loading moduli of the three test groups are relatively small during the initial loading. As the tests progress, the loading moduli of L-2 and L-3 tests gradually stabilize, with the loading modulus of the L-3 test showing a decreasing trend. Additionally, both L-2 and L-3 tests have loading moduli greater than L-1, while the unloading moduli exhibit the opposite trend.

(4) The deformation rates during the loading stage and high stress plateau stage of the L-1 test are almost always higher than the deformation rates at corresponding times in the L-2 test. However, in the unloading stage and low stress interval stage, different patterns are observed. The experiments demonstrate that the stress state significantly alters the deformation rate of the rock, but its impact varies depending on different loading/unloading conditions.

6 New creep-fatigue constitutive modeling of salt rock based on state variables

6.1 Introduction

Through the studies in the previous chapters, the following main conclusions were obtained: with the increase of stress rate, the plastic deformation of salt rock per cycle decreases, and the deformation of salt rock is distinguished into loading deformation which is affected by the stress rate, and creep deformation which is basically unaffected. In the salt rock creep-fatigue research can be found that there is an interaction between creep and fatigue, fatigue can accelerate the creep deformation, and in turn the hardening effect of the creep stage will reduce the residual strain of the salt rock, the final destruction of the salt rock in the creep-fatigue loading is the result of the dual action of creep and fatigue, when the creep-induced grain perforation cracks and fatigue-induced cracks along the grain boundaries of the fracture or grain perforation fractures will meet and converge, will result in the destruction of the salt rock. Changes in the upper stress limit also have a significant effect on the damage of salt rock specimens. The insight given by the above study is that the special features of the creep-fatigue mechanical ontology model for salt rock and other creep and fatigue ontology models should take into account the effects of creep and fracture extension on fatigue as well as the effects of loading and unloading history on creep. In the following, the salt-rock creep-fatigue constitutive model will be derived and validated for this feature based on some of the laws obtained from the tests.

6.2 Constitutive modeling of salt rock considering state variables

6.2.1 *Typical Rock Creep Models.*

(1) Bailey-Norton (Norton) model [279,280]

Bailey-Norton creep model is one of the time-hardening creep models, which is found to be a better description of the initial and steady state phases of rock creep by comparing with a large amount of experimental data and is expressed in the form of creep strain rate:

$$\dot{\varepsilon} = C_1 \sigma^{C_2} t^{C_3} e^{-C_4/T} \qquad (6.1)$$

where $\dot{\varepsilon}$ is the creep strain rate; σ is the equivalent stress; T is the temperature; t is the creep time; C_1、C_2、C_3、C_4 are the parameters of the model respectively.

Since the temperature is constant during the experiment, and hence $e^{-C_4/T}$ is a constant, the above equation can be simplified to the following form:

$$\dot{\varepsilon} = C_1 \sigma^{C_2} t^{C_3} \tag{6.2}$$

The total strain ε can be expressed by the following equation:

$$\varepsilon = \varepsilon_e + \varepsilon_v \tag{6.3}$$

Where ε_e is the elastic strain calculated from Hooke's law. ε_v is the viscous strain given by the creep eigenstructure model of Eq. (6.2). The final form of Eq. (6.3) is:

$$\varepsilon = \frac{\sigma}{E} + \frac{C_1 \sigma^{C_2} t^{C_3+1}}{C_3+1} \tag{6.4}$$

E is the modulus of elasticity of the rock

(2) Burgers model [281,282]

Burgers model can better reflect the transient elastic deformation, viscoelastic deformation, and viscous flow deformation that occurs during the creep process of rock. Burgers model is the classical element model is made of Maxwell and Kelvin bodies in series, and the total strain can be expressed in the following form:

$$\varepsilon = \varepsilon_1(t) + \varepsilon_2(t) \tag{6.5}$$

Where ε is the total strain; $\varepsilon_1(t))$ is the strain expressed in Kelvin body; and $\varepsilon_2(t)$ is the strain expressed in Maxwell body. The expansion is shown below:

$$\varepsilon = \frac{\sigma}{E_1} + \frac{\sigma}{\eta_1} + \frac{\sigma}{E_2}\left[1 - exp\left(-\frac{E_2}{\eta_2}t\right)\right] \tag{6.6}$$

η_1、η_2 are the coefficients of viscosity of the rock, respectively.

(3) Nishihara model [283,284]

The Nishihara model is commonly used to describe the deformation of soft rocks, and is also an elemental model with a structure formed by Hooker, Kelvin, and Bingham bodies in series, and the total strain can be expressed in the following form:

$$\varepsilon = \varepsilon_e + \varepsilon_{ve} + \varepsilon_{vp} \tag{6.7}$$

Where ε_e、ε_{ve}、ε_{vp} denote the strains of the Hooker body, viscoelastic body, and viscoplastic body, respectively. The expansion is shown below:

$$\varepsilon = \frac{\sigma}{E} + \frac{\sigma}{E_3}\left[1 - exp\left(-\frac{E_1}{\eta_1}t\right)\right] \qquad \sigma > \sigma_s \tag{6.8}$$

$$\varepsilon = \frac{\sigma}{E} + \frac{\sigma}{E_3}\left[1 - exp\left(-\frac{E_1}{\eta_1}t\right)\right] + \frac{\sigma-\sigma_s}{\eta_2}t \qquad \sigma < \sigma_s \tag{6.9}$$

σ_s is the yield stress.

Salt rock has good creep deformation characteristics, and can maintain high strength within a certain range of deformation, which is conducive to the stable operation of the gas storage reservoir [285]. The typical creep curve is divided into three parts: transient creep, steady state creep and accelerated creep, and the operation time of salt cavern storage reservoirs is generally up to 30-50 years [286]. Compared with the entire service life, the transient creep time of salt rock is very short, therefore, in the actual engineering generally only consider the damage in the steady state creep stage and the accelerated creep stage, when the damage or creep develops to a certain stage, the creep enters the accelerated stage [287,288]. Compared with other models Bailey-Norton model has been used a lot in describing the steady state creep rate of salt rock due to fewer parameters, which are easy to be obtained from experiments, and the model has been widely used in many numerical calculations and engineering evaluations. The present salt-rock creep-fatigue model is derived based on the Norton model, which also creates conditions for future numerical embedding.

The Norton model [289] is mainly used to describe the relationship between stress and strain in the steady-state creep phase of rock-like materials：

$$\dot{\varepsilon} = a\sigma^n \tag{6.10}$$

where $\dot{\varepsilon}$ denotes the strain rate, i.e., the first-order derivative of strain with respect to time, σ denotes the stress, a denotes the material coefficient, and n is the stress coefficient. Although the Norton model is able to make good predictions for the phase characteristics of deformation, there are several problems such as：

(1) The model mainly focuses on the first and second stages of deformation, i.e., the deceleration deformation stage and the stabilization deformation stage. The prediction error is large for the last stage of deformation (third stage), i.e., the accelerated deformation stage before final failure.

(2) The model mainly considers the loading process, and does not fully consider for the unloading process. The result is that the loading and unloading produce exactly the same viscoplastic deformation, which is not consistent with the experimental observations.

(3) The model does not consider the influence of historical loading and unloading stress paths on viscoplastic behavior, i.e., historical cumulative damage or cumulative hardening/softening characteristics are not taken into account in the model.

For these reasons, a new creep intrinsic model is developed to describe the creep-

fatigue stress-strain relationship of salt rocks affected by unloading stress paths, taking into account the physical and mechanical properties of salt rocks.

6.2.2 *Definition of plasticity factor (state variable)*

Component models tend to have a more explicit physical meaning [290,291]. A general viscoelastic-plastic model, as shown in Fig 6.1, consists of a spring component, a friction component, and a damping component, where the spring component (E) characterizes the stress-strain relationship of elasticity, the friction component (σ_{s1}), characterizing loading plasticity, the friction component (σ_{s0}) characterizes the plastic behavior of the material, and the damping component (η_2) usually characterizes the viscous nature of the strain rate proportional to the rate.
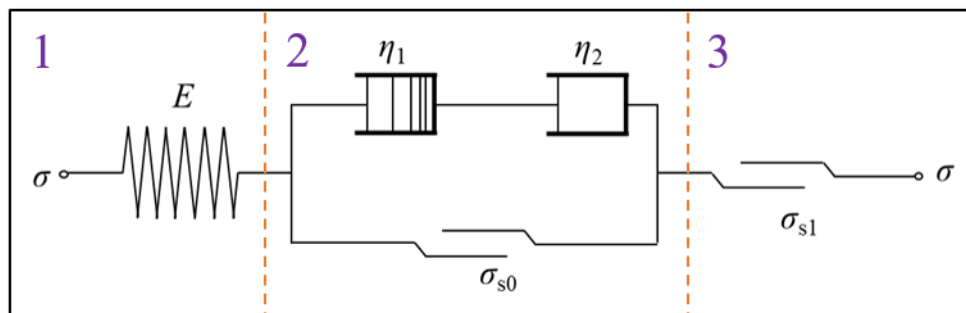
Fig. 6.1 Creep-fatigue rheological model.

Damping component (η_2) represents the variable-rate creep process of the salt rock, specifically the first stage of deformation, where the specimen is undergoing continuous hardening, resulting in a gradual decrease in deformation capacity, indicating the decelerated deformation stage. Once the specimen enters the steady-state stage, the decelerated creep disappears, indicating a correlation between state changes and time. When stress undergoes further changes, the material requires a certain time to enter a new steady-state stage, suggesting a correlation with stress as well. Here, the concept of state variable is introduced.

During loading and deformation of rocks occurs a process of continuous loss of elastic deformation capacity, i.e., the process of increasing plastic deformation, so a plasticity factor is the state variable in the process of loading of rocks, and this state variable characterizes the elastic recovery capacity of rocks, which can be understood as the unloading elastic modulus of standard rock specimens.

(1) Effect of loading

Salt rock is a sedimentary rock formed by evaporation as a polycrystal of sodium

chloride, and its deformability is related to the density of internal dislocations. Dislocations determine the magnitude of creep deformation; dislocation density is related to the magnitude of the internal force in the deformation zone (i.e., the region where dislocation distortion is produced) within the salt rock [292,293]. When the external force is larger than the internal force in the deformation zone, the crystal proliferates and produces more dislocations, while the internal force is elevated and the deformation rate gradually slows down, i.e., the deceleration creep phase. When the external force is balanced with the internal force, the dislocation proliferation and slip tend to stabilize, and the deformation rate reaches a stable stage, i.e., the steady-state stage. The state variable σ^* is defined here to characterize the degree of plastic deformation related to the dislocation density within the salt rock. The state variable can be written in the following functional form：

$$\sigma^* = \frac{\sigma}{1+c\sigma^m t^k} \tag{6.11}$$

where c, m, and k are material coefficients; t is the testing time. The above formula can be transformed into the following formula:

$$\frac{\sigma^*}{\sigma} = \frac{1}{1+c\sigma^m t^k} \tag{6.12}$$

Observing Eq. (6.12), it can be found that if the stress is constant, the state variable will approach the external force σ toward infinite time. When the stress changes (here, only the loading process is considered for the time being), the equation is no longer applicable. The effect of the accumulated plastic deformation needs to be considered. Assuming that the state variable before the new stress action is σ_0^*, then the following equation can be obtained：

$$\sigma_0^* = \frac{\sigma}{1+c\sigma^m (t_0)^k} \tag{6.13}$$

$$1 + c\sigma^m (t_0)^k = \frac{\sigma}{\sigma_0^*} \tag{6.14}$$

$$c\sigma^m (t_0)^k = \frac{\sigma-\sigma_0^*}{\sigma_0^*} \tag{6.15}$$

$$(t_0)^k = \frac{\sigma-\sigma_0^*}{c\sigma^m \sigma_0^*} \tag{6.16}$$

$$t_0 = \left(\frac{\sigma-\sigma_0^*}{c\sigma^m \sigma_0^*}\right)^{1/k} \tag{6.17}$$

where t_0 is the time corresponding to the state variable σ_0^*. Then after a period of time the new state deformation can be expressed as：

$$\sigma^* = \frac{\sigma}{1+c\sigma^m (t+t_0)^k} + \sigma_0^* \tag{6.18}$$

According to the above study, the plasticity factor is a state variable characterized by stress and time, and the effect of creep-fatigue interaction on the deformation of salt rock is achieved by changing the value of the state variable, and the intrinsic model established on this basis considers the influence of the loading and unloading path and time on the deformation.

The deformation in the first stage, i.e., the deceleration deformation stage, is mainly influenced by the rapidly generated dislocations, i.e., the plasticity factor, which can be expressed by drawing on the steady-state creep stress-strain relationship of Norton's model as:

$$\varepsilon = b \frac{\sigma^*}{\sigma} \sigma^n \tag{6.19}$$

where b is the material coefficient. In the second stage of stable deformation, the creep rate is almost constant and the Norton model can be used directly , the strain given in Eq. (6.10) at this time can be expressed as:

$$\varepsilon = \dot{\varepsilon} t = at\sigma^n \tag{6.20}$$

The joint Eq. (6.19) and (6.20) give both the stress-strain relationship between the deceleration deformation phase and the stabilization deformation phase:

$$\varepsilon = \sigma^n \left(at + \frac{\sigma^*}{\sigma} b \right) \tag{6.21}$$

The above equation can be rewritten as:

$$\varepsilon = \sigma^n (at + \frac{b}{1+c\sigma^m t^k}) \tag{6.22}$$

The relationship between the strain rate and the stress and state variables can be obtained by finding the first order derivative of time for Eq. (6.22):

$$\frac{\partial \varepsilon}{\partial t} = \dot{\varepsilon} = \sigma^n \{ a - \frac{bck\sigma^m (t+t_0)^{k-1}}{[1+c\sigma^m (t+t_0)^k]^2} \} \tag{6.23}$$

The relationship between the state variable rate and stress can be obtained by finding the first order derivative of time for Eq. (6.18):

$$\frac{\partial \sigma^*}{\partial t} = \dot{\sigma}^* = - \frac{ck\sigma^{m+1}(t+t_0)^{k-1}}{[1+c\sigma^m(t+t_0)^k]^2} \tag{6.24}$$

From the above Eq. (6.23) and (6.24), it can be seen that the strain rate changes accordingly when the stress changes. During loading, if the stress loading rate is v, the stress at time t can be expressed as:

$$\sigma = vt + \sigma_0 \tag{6.25}$$

where σ_0 is the initial stress.Then the state variables can be obtained by integrating

the following equation:

$$\sigma^* = ck \int \frac{(\sigma_0+vt)^{m+1}(t+t_0)^{k-1}}{[1+c(\sigma_0+vt)^m(t+t_0)^k]^2} \, dt + \sigma_0^* \tag{6.26}$$

Then the strain during loading can be obtained by integrating the following equation：

$$\varepsilon = \int (\sigma_0 + vt)^n \{ a - \frac{bck(\sigma_0+vt)^m(t+t_0)^{k-1}}{[1+c(\sigma_0+vt)^m(t+t_0)^k]^2} \} dt + \varepsilon_0 \tag{6.27}$$

where ε_0 is the initial strain. The above equation can be simplified to obtain：

$$\varepsilon = \int (\sigma_0 + vt)^n (a + \frac{b\dot{\sigma}^*}{\sigma_0+vt}) dt + \varepsilon_0 \tag{6.28}$$

(2) Effect of unloading stage.

In the unloading state, there may be a situation where the external force is less than the state variable, when the material is in the "over-hard" state internally, the dislocation occurs in reverse motion, and the local dislocation density gradually decreases, which is the state variable of：

$$\sigma^* = \frac{\sigma}{1-c\sigma^m(t+t_0)^k} \tag{6.29}$$

Considering that when unloading, the external force is withdrawn, the internal structure of the salt rock is adjusted completely by internal force, and the adjustment rate is slow, introduce the variable speed creep unloading factor (state variable unloading factor) U_1, find the first order derivative of time, and get the new state variable rate as：

$$\dot{\sigma}^* = U_1 \frac{ck\sigma^{m+1}(t+t_0)^{k-1}}{[1-c\sigma^m(t+t_0)^k]^2} \tag{6.30}$$

$$t_0 = \left(\frac{\sigma_0^*-\sigma}{c\sigma^m\sigma_0^*} \right)^{1/k} \tag{6.31}$$

The deformation rate of stable creep is also affected by the introduction of a stable creep unloading factor U_2, and the strain integral form can be rewritten as：

$$\varepsilon = \int (\sigma_0 + vt)^n \{ aU_2 + \frac{U_1 bck(\sigma_0+vt)^m(t+\sigma_0^{-*})^{k-1}}{[1-c(\sigma_0+vt)^m(t+\sigma_0^{-*})^k]^2} \} dt + \varepsilon_0 \tag{6.32}$$

(3) Stress-strain relationships in the accelerated creep phase

Before considering the third stage, i.e., the accelerated creep stage, we need to first explain the damage of the rock. The concept of damage to materials was originally proposed by Kachanov in 1958 and refers to the structural changes in materials under the action of temperature, load, environment, time and other factors that cause defects, resulting in the deterioration of the mechanical properties of the material and eventually the formation of macroscopic material damage [294]. From the point of view of fine

physics, damage is the result of the formation and development of defects such as dislocations, slips, microporosity and cracks experienced by the material [295]. Macroscopically, the loss of load-bearing capacity of a part of the material is considered damage, as defined here：

$$D = \frac{d}{A} \qquad (6.33)$$

D is the material damage, d is the area without load-bearing capacity material, that is, the damage area, A is the initial area of the material. Assuming that the initial porosity of the material is f, at this time the material, in addition to the pores, are the initial loadable area, it can be considered that the damage is：

$$D = \frac{f}{A} \qquad (6.34)$$

Due to the special geological structure of salt rocks, their microscopic spatial structure is extremely dense and the porosity is almost zero, so the initial damage can be considered as zero. The main mechanism of crystal plastic deformation is dislocation slip. During dislocation slip, the corresponding material part does not produce significant damage loss of energy. Here the formation of cracks, holes and other defects that make the material lose its load-bearing capacity is mainly considered as damage, and dislocations are considered as the development of damage, not actual damage. And crack formation is mainly generated by the accumulation of dislocations, a large number of dislocations plugging the stress field generated and the superposition of the external stress field formed by the strength factor to reach the fracture toughness, that is, the generation of fractures (or called fracture nucleation) [296,297]. The fracture nucleation has not been observed directly from rock experiments and is tentatively considered to be a rapid and instantaneous process. It is assumed that the initial cleavage shaped nucleus has a length of d_0 and is formed instantaneously. The moment of its formation is related to the externally applied stress and accumulated plastic deformation. At this point the damage can be defined as：

$$D = \frac{d_0}{A} \qquad (6.35)$$

Assuming that the material produces a plastic deformation rate of $\dot{\varepsilon}$, the rate of change of damage area $\dot{d}$ can be expressed as:

$$\dot{d} = A\dot{D} = \mu_d \dot{\varepsilon} \qquad (6.36)$$

where $\dot{D}$ is the damage rate, μ_d is the crack expansion factor, i.e. the actual crack

coefficient due to plastic deformation, with the same magnitude as the area. Then the crack extension area d can be calculated by the following formula:

$$d = \mu_d \int \dot{\varepsilon} dt + d_0 \tag{6.37}$$

After the damage, the bearing area of the material decreases and the corresponding stress changes, i.e., the effective stress σ_{eff}^n can be found by the following equation:

$$\sigma_{eff}^n (1 - D) + \lambda D \sigma = \sigma \tag{6.38}$$

Where λ is the coefficient of dynamic friction of the fracture surface, i.e. the sum of the product of the effective stress and undamaged and the product of the fracture that has produced damage and the coefficient of dynamic friction and the actual stress is the actual stress.

Eq. (6.38) can be rewritten as,

$$\sigma_{eff}^n = \frac{1 - \lambda D}{1 - D} \sigma \tag{6.39}$$

After sorting, it gives the following equation:

$$\sigma_{eff}^n = \frac{A - \lambda d}{A - d} \sigma \tag{6.40}$$

Bringing in the effective stress, the fracture expansion can be expressed as:

$$d = \mu_d \int \sigma_{eff}^n \{a - \frac{bck\sigma_{eff}^m (t + \sigma_0^{-*})^{k-1}}{[1 + c\sigma_{eff}^m (t + \sigma_0^{-*})^k]^2}\} dt + d_0 \tag{6.41}$$

In summary, considering the formation of fissures, the deformation of salt rock in the third stage can be calculated by the following equation:

$$\varepsilon = \int \sigma_{eff}^n \{a - \frac{bck\sigma_{eff}^m (t + \sigma_0^{-*})^{k-1}}{[1 + c\sigma_{eff}^m (t + \sigma_0^{-*})^k]^2}\} dt + \varepsilon_0 \tag{6.42}$$

(4) Three-dimensional form

The potential function is usually used to characterize the direction of plastic flow in plastic constitutive models [298]. If the potential function is similar to the yield function, it is called the correlation criterion. If it is different, it is called the noncorrelation criterion. In most cases, the flow direction measured in the experiment does not have a strong relationship with the yield function. Therefore, the non-associaed criterion is used here.

$$\varepsilon_{ij} = \gamma < F > \frac{\partial Q}{\partial \sigma_{ij}} \tag{6.43}$$

where F is the yield function, the starting condition for creeping, Q is the plastic potential function, and its partial derivative with respect to time represents the plastic

flow direction, γ is the relationship between creep deformation and stress, which can be calculated with Eq. (6.33). Theoretically, this model has a particular proportional relationship between the plastic deformations in each direction. However, most experimental results do not reflect this relationship. The accumulation of NaCl polycrystalline particles forms salt rock, and its deformation is mainly dominated by dislocation generation and slip. Therefore, the direction of the slip is related to that of plastic flow.

When the salt rock is in steady-state creep, the internal dislocation and external forces reach a dynamic equilibrium. The generation, slip and removal of dislocations occur within an orderly and stable state. The dislocation mainly slips along the direction of the system that most easily slips, which is the direction of the maximum shear stress, and the resulting plastic deformation is similar in all directions. In the first stage, the external force is obviously more significant than the internal force, and the dislocation multiplies and slips rapidly. In the rapid generation and slip process, the "supersaturation" state of dislocations may occur, resulting in the emergence of new slip systems, such as climbing and other behaviours, thus causing changes in the proportions of plastic deformation in all directions. Therefore, a "double potential function" constitutive model of the plastic potentials of the two stages was established in this paper.

$$\varepsilon_{ij} = \gamma_1 < F > \frac{\partial Q_1}{\partial \sigma_{ij}} + \gamma_2 < F > \frac{\partial Q_2}{\partial \sigma_{ij}} \tag{6.44}$$

The viscoelastic–plastic constitutive equation is

$$\varepsilon_{ij} = \gamma_1 < F > \frac{\partial Q_1}{\partial \sigma_{ij}} + \frac{\Delta\sigma}{E} + \gamma_2 < F > \frac{\partial Q_2}{\partial \sigma_{ij}} + \frac{\Delta\sigma}{E} \tag{6.45}$$

where γ_1 and γ_2 are the motion functions of the first and second stages, respectively, Q_1 and Q_2 are the plastic potential functions of the first and second stages, respectively. F is the start condition shared by the first two stages, and E is the elastic modulus. Here, a form similar to the Drucker–Prager (D-P) criterion was adopted by the plastic potential function.

$$Q = \sqrt{J_2} - \alpha I_1 \tag{6.46}$$

The derived creep-fatigue model for salt rock uses only eight parameters, which is

not only able to consider the interaction between creep and fatigue, but also greatly reduces the parameters compared with other models. In the following, the derived salt rock creep-fatigue constitutive model will be used to validate the experimental data and analyze the applicability of the model.

6.3 Validation of the creep-fatigue constitutive model for salt rock in creep, fatigue and creep-fatigue test

6.3.1 Validation of the creep-fatigue constitutive model in pure creep test for salt rock

(1) The creep deformation and fitting results under single stress.

The test specimens, the specimen environment, and the test apparatus are the same as the previous test, the constant stress level creep test program is as follows: 1 kN / s rate of uniform loading to the design stress level, the stress level of 4 MPa, 8 MPa, 12 MPa, 16 MPa and 20 MPa, respectively, loading and unloading path shown in Fig 6.2.
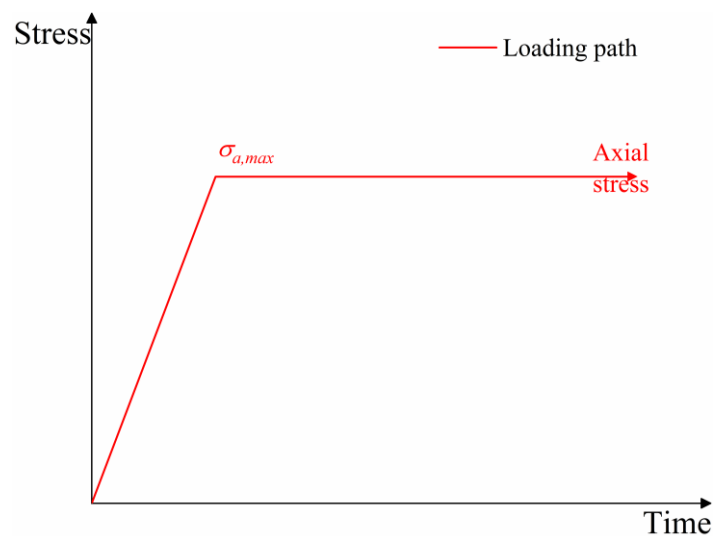
Fig. 6.2 Loading path for single stress level creep test on salt rock.

The creep test curves were parametrically fitted by the creep-fatigue model, and compared with the Bailey-Norton model and the Burgers model, and the results are shown in Fig. 6.3.
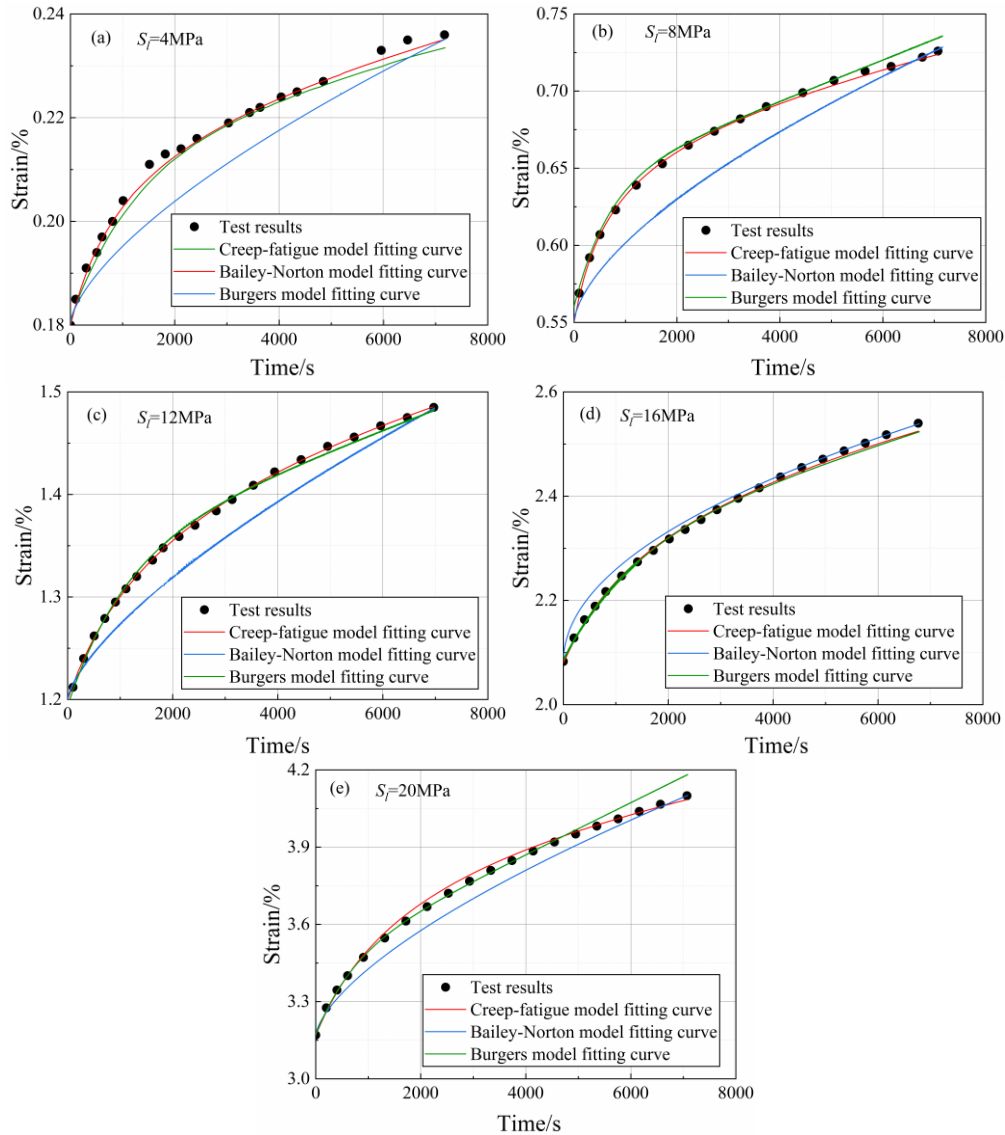
Fig. 6.3 Strain versus time for different model and experimental data, for creep tests with stress levels: (a) 4 MPa, (b) 8 MPa, (c) 12 MPa, (d) 16 MPa, and (e) 20 MPa on salt rock.

In order to show the creep deformation process more clearly, Fig. 6.3 does not show the loading stage. The values of the vertical axis within the dashed circles represent the corresponding strain values when loading is completed. From the fitting results, compared with the Bailey-Norton model and Burgers model fitting results, the model can better fit the creep deformation under different stresses, including the decelerated creep stage and steady state creep stage. The five sets of fitted curves under different stress levels and different initial state variable levels all have a good fit with the experimental data and a small error, indicating that the model can better describe the creep characteristics of salt rock under different loads and has good applicability. The model parameters of the creep-fatigue model under different stresses are shown in Table

6.1. It can be found that the model parameters obtained change with the change of stress level, however, the regularity of the change is not obvious, which is similar to the disordered parameters obtained when fitting other models with different stress levels. This is mainly due to the fact that the multi-parameter model, in order to achieve the effect of the highest fit, ignores the overall optimal solution for some single parameters.

Table 6.1 Parameters of creep-fatigue constitutive model.

Stress/MPa	a	b	c	n	m	k	R^2
4	11	1.25	200	1.95	1	-0.72	0.99
8	11.5	1.05	42	2.13	0.7	-0.68	0.99
12	6.9	1.68	45	2.1	1	-0.61	0.99
16	6.9	1.4	45	2.1	1.2	-0.64	0.99
20	6.5	2	52	2.2	0.9	-0.7	0.99

(2) The creep deformation and fitting results under increasing/ decreasing stress.

In order to verify the fitting effect of the creep-fatigue model on the creep deformation of salt rock under different loading and unloading paths and the same stress level, two sets of creep experiments of salt rock with elevated stress were carried out respectively. In the elevated stress experiments, the specimen was loaded to 4 MPa according to the loading rate of 1 kN/s and kept constant for 2 h. Subsequently, the elevated stress creep tests were conducted according to the same rate, kept for the same time, and increased by 4 MPa at each level until the specimen was damaged. The results of the increasing stress level creep test showed that the salt rock specimens were damaged after the last step of 24 MPa, which was kept for 40 min only. Based on this, in the stress reduction experiment, the same loading rate was used to first load the salt rock specimen to 20 MPa, i.e., the pre-destruction stress level of the ascending stress creep, and kept for 2 h, with same rate used to reduce it to 0 step by step, with gradient of each step still 4 MPa. The loading and unloading paths are shown in the following Fig. 6.4.
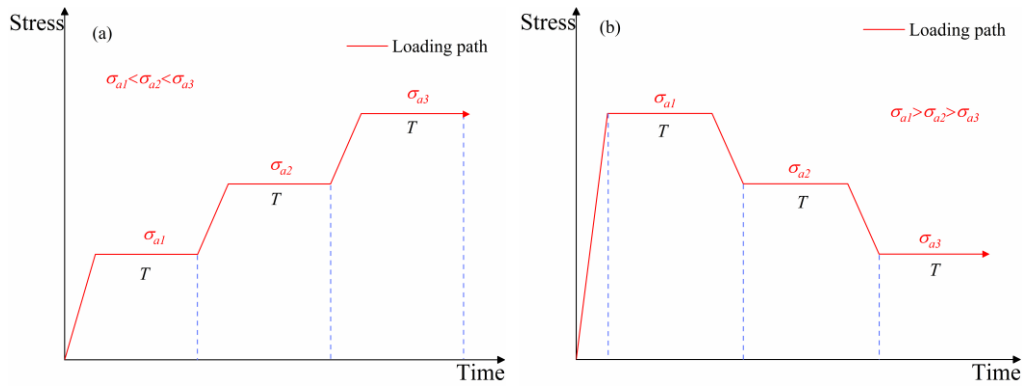
Fig. 6.4 Loading paths for (a) increasing stress level creep test and (b) decreasing stress level creep test.

The creep strain and creep rate at different stress levels of the increasing stress level creep test and the decreasing stress level creep test were compared and the results are shown in Table 6.2.

Table 6.3 Comparison of test results

Stress/MPa	Increasing stress level creep test		decreasing stress level creep test	
	Creep strain/%	Creep rate/h	Creep strain/%	Creep rate/h
4	0.057	0.0258	-0.012	-0.006
8	0.180	0.090	-0.002	-0.001
12	0.304	0.152	-0.003	-0.0015
16	0.460	0.230	0.029	0.0145
20	0.930	0.465	1.202	0.601

As can be seen from Table 6.2, the creep rate and the amount of creep of salt rock increase with stress levels in the increasing stress level creep tests. This phenomenon is similar to the results obtained in many literatures [299]. In the decreasing stress level creep test, both the creep rate and the creep amount of the salt rock gradually decrease with the decrease of the stress level. However, when the load was less than 16 MPa, the phenomenon of 'negative creep' appeared, which did not occur in the conventional ascending gradient loading. Comparing the creep tests of increasing stress level creep and decreasing stress level creep, the creep deformation rate of salt rocks in decreasing stress level creep test is much smaller than that of increasing stress level creep test at the same stress level, except for the 20 MPa level. This is mainly due to the fact that the internal structure of the salt rock in the increasing stress level creep test is gradually hardened under the action of the gradual increase of the external load (the degree of

hardening and dislocation density are closely related, and will not be discussed again here); whereas, the 20 MPa in the decreasing stress level creep test is directly loaded to the corresponding level, and does not undergo the long-term hardening similar to that in the increasing stress level creep test, which results in the creep deformation rate under the maximum stress level in the decreasing stress level creep test is greater than that in the ascending gradient creep deformation rate. rate. In the decreasing stress level creep test, after the hardening effect of high stress, the creep deformation rate under the subsequent stress level is much smaller than that in the increasing stress level creep test, which is due to the fact that the hardening effect under the action of high stress is much larger than that produced by low stress.

The experimental results show that the stress loading path has a significant effect on the creep properties of salt rock. The experimental results in the increasing stress level creep test were validated using the creep-fatigue model, and the obtained fits and experimental results are shown in Fig 6.5(a).
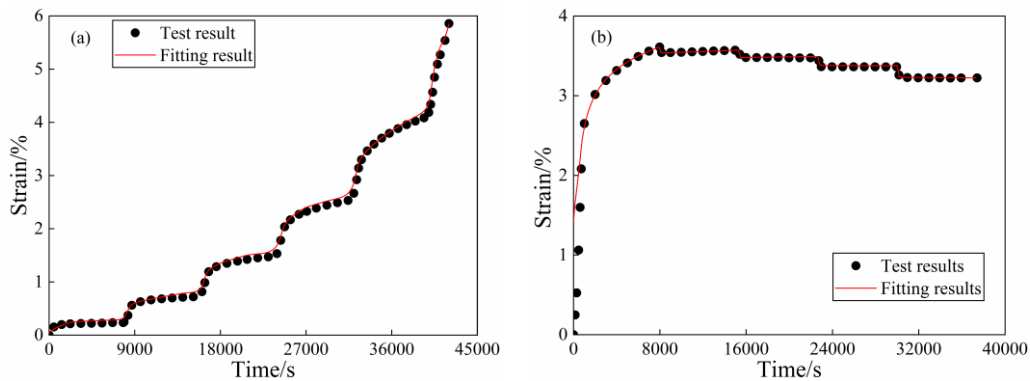
Fig. 6.5 Comparison of creep test results and creep-fatigue model fitting results for stress-leveling creep under (a) increasing stress and (b) decreasing stress.

The model fully considers the effects of time, load and state (loading stage and creep stage) on the creep characteristics, from the fitting results, it can be a better fit for both the creep stage and the loading stage, the 1st, 4th and 5th steps of the loading stage and the creep stage of the test curves and the fitted curves of the fit curve is higher, the 2nd and 3rd steps of the loading stage and the creep stage of the test curves and the fitted curves are basically the same. Although there is some error in the fitted curves, the change trends of the fitted curves and the test curves are basically the same. When the load was increased from 20 MPa to 24 MPa, the salt rock showed an accelerated creep

stage, and the specimen was destabilized and damaged, and the model showed good results for the simulation of the three stages.

For the decreasing stress level creep test of salt rock, the creep-fatigue model was validated against the experimental results of reduced gradient, and a comparison of the fitted situation and the test results obtained is shown in Fig. 6.5(b). The salt rock specimens were subjected to graded creep with a falling gradient, and the strains under all levels of stress levels produced both variable-rate creep strains and steady-state creep strains.

The model can not only fit the creep deformation law of the first stress level (20 MPa) well, but also can fit the creep deformation that occurs at each stress level after the reduction of the stress level, especially the phenomenon of 'negative creep' also has a good effect. 4 unloading stage and creep stage of the test curves and the fitted curves of the fit curve are high, and the error is very small. In particular, the first and fourth two stages of the test results and fitting results completely overlap, while the second and third stage of the test results and fitting results, show a small error of 2% only, indicating that through the introduction of state variables and variable-speed creep and steady-state creep unloading factor of the improved model and the degradation of decreasing stress level creep test data with a high degree of agreement.

Overall, the creep-fatigue model is able to well predict the development of creep deformation of salt rock under different lifting gradient stress paths. Compared with the traditional creep constitutive model, the model parameters change when the stress occurs, and the applicability of the model is greatly reduced, which brings a lot of constraints to engineering applications. The model only uses a set of parameters to completely describe the behavior of creep properties under different stress paths, and most of these parameters are only related to the material properties, which provides a convenient engineering stability assessment and application.

6.3.2 Validation of the creep-fatigue constitutive model in pure fatigue test for salt rock

(1) The fatigue deformation and fitting results with pure fatigue test.

The data used in the test come from the salt rock pure fatigue test completed by our group in 2017 [300]. The loading and unloading scheme of the salt rock uniaxial fatigue test is as follows: the upper and lower limits of the test set stress level are 90% and 20% of the uniaxial compressive strength of the salt rock, respectively. The loading and

unloading rate are set to 2kN/s. The stress path is shown in Fig. 6.6(a). According to the experimental results, the stress-strain curve is obtained as shown in Fig. 6.6(b).
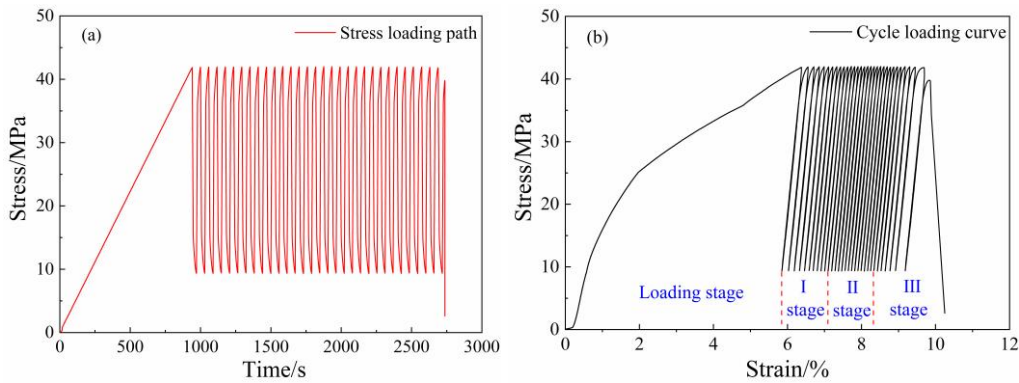
Fig. 6.6 Salt rock fatigue test: (a) stress path and (b) stress-strain curve.

The fatigue deformation of salt rock and the approximation of rock rheology under static force are divided into three phases, which are the initial will phase, the isokinetic phase, and the accelerated phase. The loading phase represents the process of increasing stresses applied before the start of the cycle. In Fig. 6.6(b), the hysteresis loops show a sparse-dense-sparse distribution with different phases, corresponding to the three stages of fatigue deformation, respectively, and the hysteresis loops are decreasing in interval in the initial phase, the interval in the isokinetic phase is basically the same, and the accelerated phase increases until the specimen is damaged.
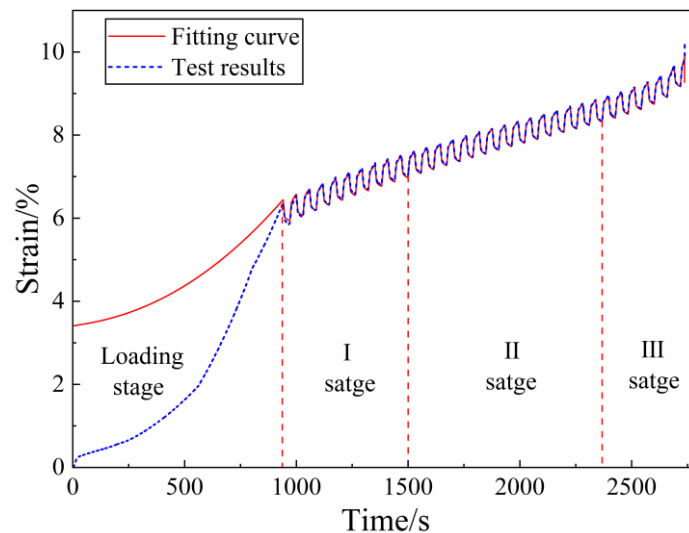
Fig. 6.7 Comparison between experimental results and fitted results, obtained from stress upper limit of 90% and lower limit of 20%

Using the creep-fatigue model proposed in this paper to fit the fatigue test data, the

results are shown in Fig 6.7, and it can be seen that the overall prediction curve of the model and the experimental results are very close to each other, which indicates that the prediction accuracy of the model is high. However, the fitting results in the loading stage differ greatly from the experimental data, and the reasons for this are analyzed as follows: the loading stage in the experimental process gradually increases from zero load, and under the influence of the compression and density of the primary fracture of the specimen, the specimen produces a large deformation, but due to the fact that in the operation of the air storage, the storage enclosing rock has often already gone through the initial loading stage, and thus the creep-fatigue model used is mainly to describe the deformation of the specimen after going through the loading stage. The model is mainly used to describe the deformation after the loading stage into the deceleration deformation or stable deformation stage, so the fitting effect for the initial loading stage is not good. For comparison, the prediction curves were shifted upward to coincide with the start of unloading in the first cycle (discussed later).
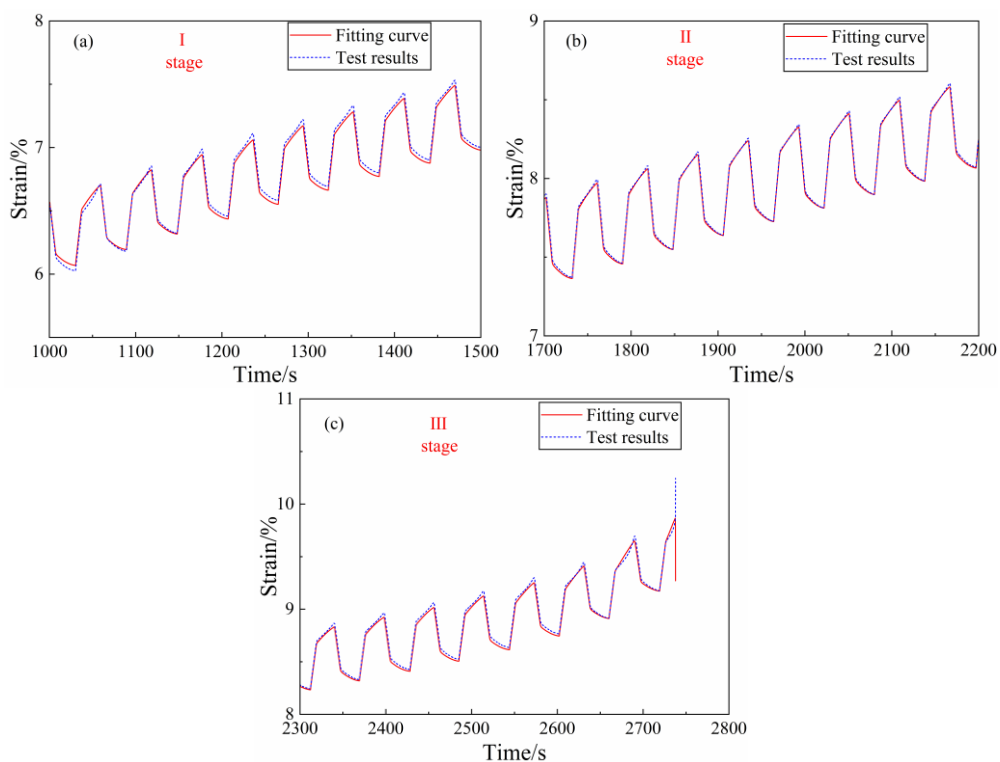
Fig. 6.8 Curve presented in Fig. 6.7 close-up on: (a) decelerating deformation stage, (b) steady deformation stage, and (c) accelerating deformation stage.

The test results of the time-strain relationship are also divided into three stages, as shown in Fig 6.8. According to the comparison between the model prediction results

and the experimental results, it can be found that the strain rate calculated by the model in the high stress part of the initial and accelerated phases is relatively low, and in the isotropic phase, the model calculation results are in good agreement with the experimental results. On the whole, the model can fully consider the effects of time, load and state on the fatigue deformation, and can well reflect the three stages of uniaxial compression cyclic loading and deformation of salt rock, with good applicability. In the three stages, the model prediction curves and the experimental curves almost completely coincide.

It should be pointed out that, in the last cycle of destruction, the specimen in the model can continue to carry the load, showing that the strain decreases with rebound in the process of stress decrease, which is mainly due to the fact that the actual testing machine is not a rigid testing machine, and the accumulated elastic energy of the testing machine is quickly released when the specimen is about to be destroyed, resulting in the rapid development of the cracks in the specimen, and thus the destruction. As a result, the experimental strain of the last cycle and the strain development trend predicted by the model differed greatly.

In order to verify the fitting effect of the creep-fatigue model on the fatigue deformation of salt rock under different stress ratios, cyclic loading and unloading fatigue experiments were carried out on the salt rock, with different lower and upper stress limits set. Divided into two groups of experiments, the first group, set the upper stress limit to 90%, the lower limit is set to 30%; the second group, set the lower stress limit to 20%, the upper stress limit is set to 95%. The obtained experimental results and fitting results are compared to those shown in Figs. 6.9(a), 6.9(b), and the model parameters are obtained as shown in Table 6.4.
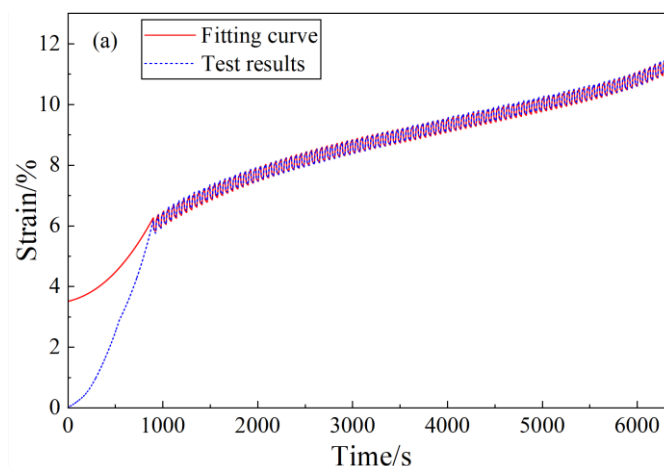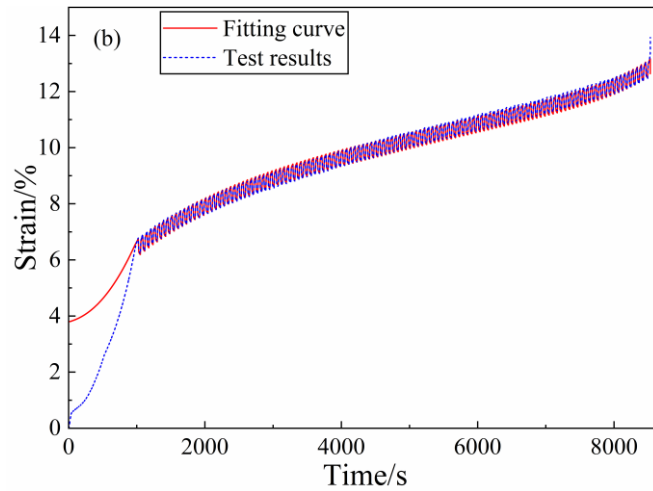
Fig. 6.9 Comparison graphs of test results and fitting results, (a) with stress upper limit at 90% and stress lower limit at 30%, and (b) with stress upper limit at 95% and stress lower limit at 20%.

According to the test data, when the stress ratio of uniaxial cyclic loading and unloading experiments is different, the fatigue life of salt rock and also corresponds to different, and the fatigue life increases with the increase of the lower or upper limit stress ratio. From the fitting results, it can be seen that the model is able to predict the different stages of uniaxial cyclic loading compressive fatigue deformation of the results better, whether it is different upper limit stress ratios or lower limit stress ratios, and the prediction results are able to follow the stage characteristics better (i.e., higher degree of overlap). Similarly, the error in the first cycle loading stage comes from the compression-tightening effect of the first loading process; the deviation of the displacement trend in the final cycle is mainly due to the non-ideal rigidity of the rigid testing machine.

Table 6.4 Parameters of fatigue test model

Upper limit	Lower limit	a	b	c	d_0	μ_d
90%	30%	0.24	37	265	0.039	0.000015
95%	20%	0.30	37	340	0.034	0.00001

Overall, the model reflects the three stages of salt rock fatigue deformation well. The model considers the effects of time, load and state on salt rock fatigue, and the prediction/fitting results show that the simulation can fit the three stages under salt rock

loading better. It shows that the model can describe the fatigue deformation of salt rock better and can reflect the three stages of fatigue deformation of salt rock well.

(2) The fatigue deformation and fitting results with low-stress interval fatigue test.

Again, the creep-fatigue model is validated upon the low-stress interval fatigue test of salt rock. The data used in the test come from the low-stress interval test completed earlier by this group (ref), and the specific loading and unloading paths are shown in Fig 6.10.
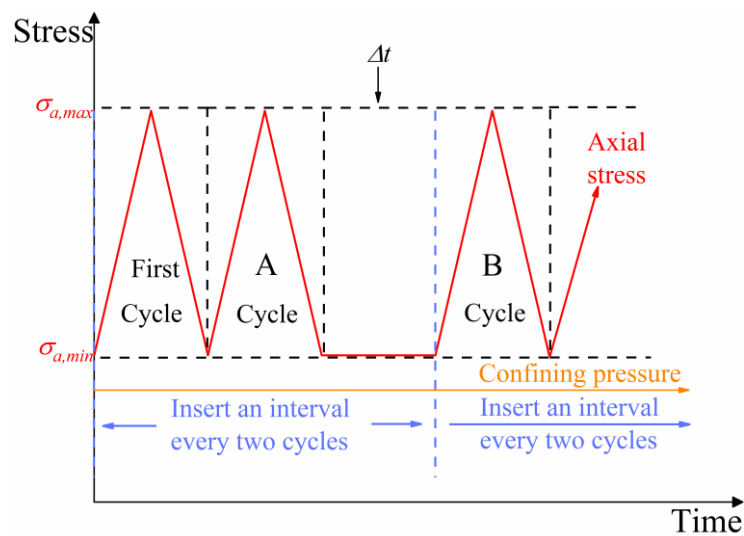
Fig. 6.10 Low stress interval fatigue test loading path.

The loading and unloading scheme for the uniaxial low-stress interval fatigue test of salt rock is as follows: the upper limit of the stress level is set to 35 MPa, the lower limit is 1 MPa, the loading and unloading rate is 2 kN/s, and after two cycles of loading and unloading, there is a stage of time of low-stress interval, and the set intervals are 5 and 15 min, respectively. For the sake of presenting a clear presentation, the graphs only show the test results of the first few stress cycles and the comparative graphs of the fitted results. The comparative graphs of the test results and model results are shown in Fig. 6.11, and the model parameters are obtained as shown in Table 6.5.
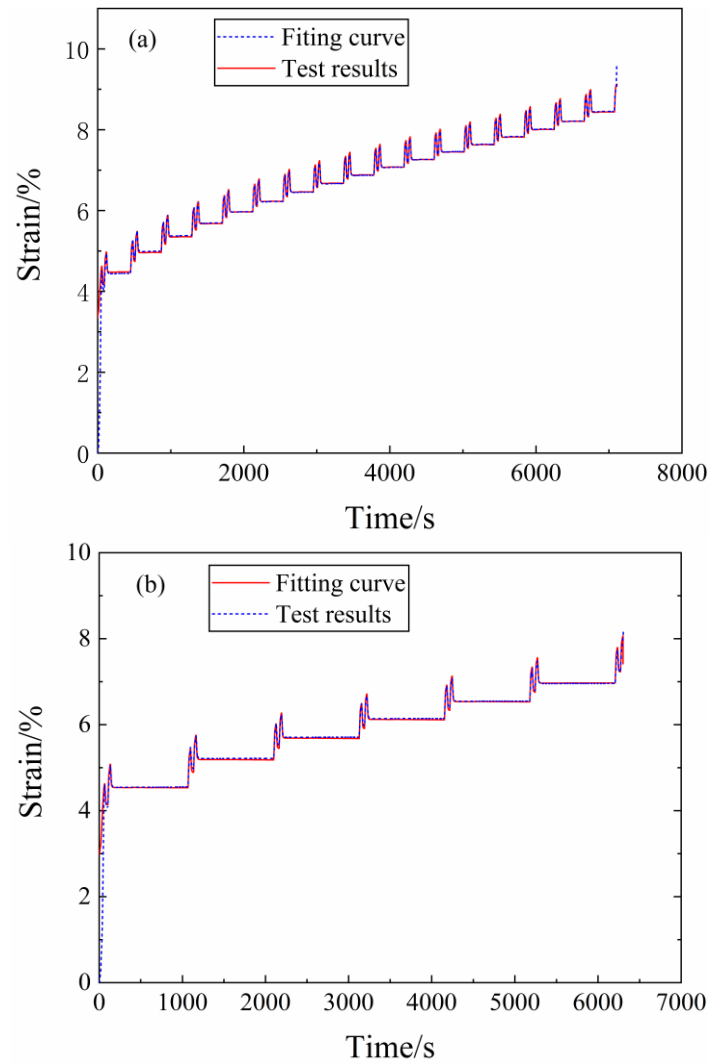
Fig. 6.11 Comparison of test results and fitted results, (a) low stress interval of 5 minutes, (b) low stress interval of 15 minutes.

From the comparison between the model results and the test results in Fig 5.21, the model can better predict the deformation process of unloaded salt rock at the lower limit interval. Selecting a cycle for comparison, it is found that the strain is increasing in two consecutive cycles of loading and unloading test results, and there is no obvious change in the strain of salt rock when it is in static stress, which is presumed to be due to the smaller constant force load (1MPa) and shorter time, and the deformation generated is almost negligible.

Overall, the model has high consistency in the overall prediction of cyclic loading and unloading at different lower stress intervals. The model is able to reflect the mutual influence of creep fatigue deformation in the deformation process. From the model prediction results, it is seen that the model can fit the deformation under the creep-fatigue interaction of salt rock better, indicating that the model has good applicability.

Table 6.5 Parameters of creep-fatigue model

Time/min	a	b	c	n	m	k
5	36	15.6	345	1.1	1.1	-0.72
15	25	15.0	280	0.9	0.92	-0.72

6.3.3 Validation of the creep-fatigue constitutive model in creep-fatigue test for salt rock

(1) Firstly, the creep-fatigue model is verified on the creep-fatigue test completed in this thesis (Chapter 2,3and 4), and the comparison are shown in Fig 6.12.
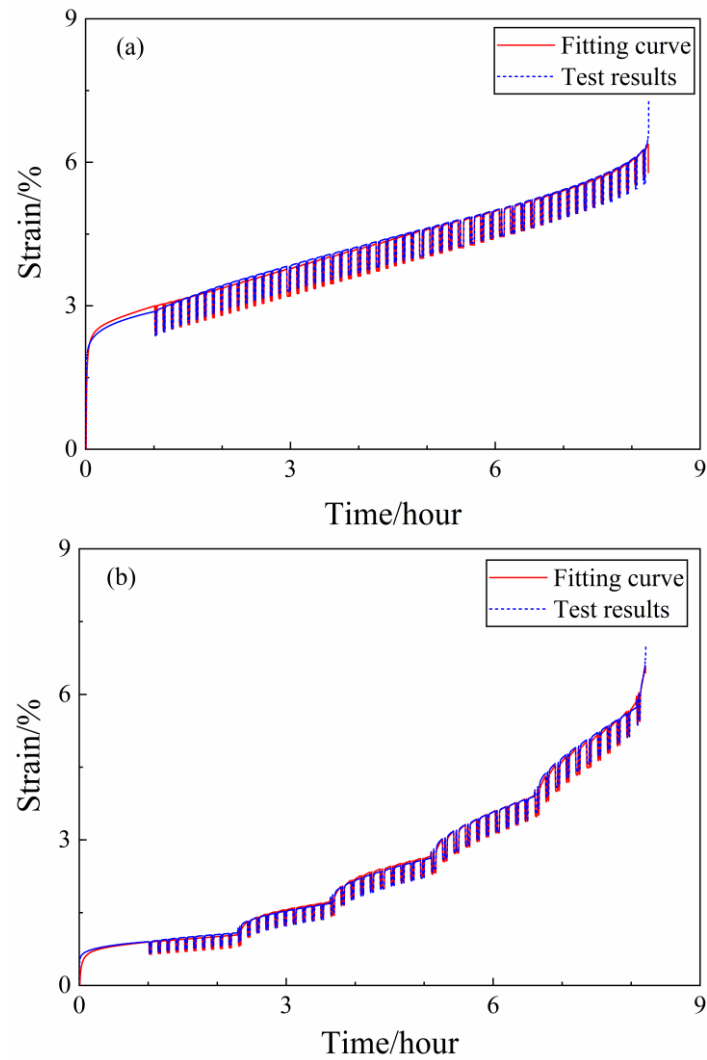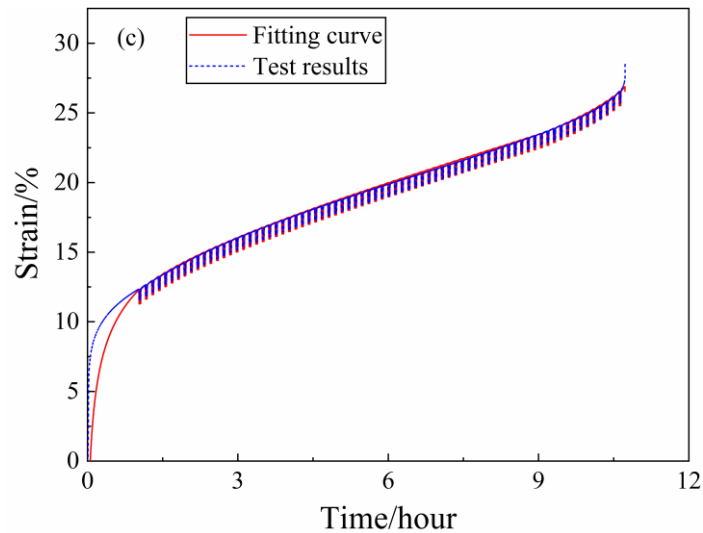
Fig. 6.12 Comparison graphs of test results and fitting results, (a) uniaxial 5-minute high-stress plateau creep-fatigue test (CCFT), (b) uniaxial 5-minute graded high-stress plateau creep-fatigue (USCF) test, and (c) triaxial creep-fatigue test (TCFT) at a confining pressure of 3 MPa.

Figure 6.12 shows the results of the three sets of creep-fatigue tests and the fitting results of the intrinsic model. Overall, the creep-fatigue model fits the results of the uniaxial, graded and triaxial creep-fatigue tests of salt rock with high accuracy, which reflects that the proposed model has a good general applicability. Especially for the initial loading section, the fitting effect is also significantly improved compared with the pure fatigue test, which may be attributed to the following reasons: firstly, the modeling is based on the consideration of the interaction between fatigue cyclic load and constant stress creep load, so the fitting effect is naturally better for the creep-fatigue test, and secondly, the initial high stress plateau is added to the creep-fatigue test, which makes the test already in creep condition when it enters into cyclic load state, and this is the reason for the good fitting results of both graded and triaxial salt-rock tests. Secondly, the initial high stress plateau is added to the creep-fatigue test, so that the test is already in the creep state when entering the cyclic loading state, which is also closer to the actual state of the salt cavern surrounding rock, i.e., before the construction of the CAES plant, the salt carven surrounding rock has been subjected to a longer stage of bias stress load, and it has been in the process of rheology. For the graded creep-fatigue test, the proposed creep-fatigue model realizes that the characteristics of the creep-fatigue strain curves of salt rock under different stress paths can be perfectly fitted using one set of parameters, which provides a convenient way to assess the stability of

the salt cavern CAES plant under different operating conditions during its operation.

(2) Secondly, the creep-fatigue model is verified on the long term creep-fatigue test completed in this thesis (Chapter 5), and the comparison are shown in Fig 6.13.
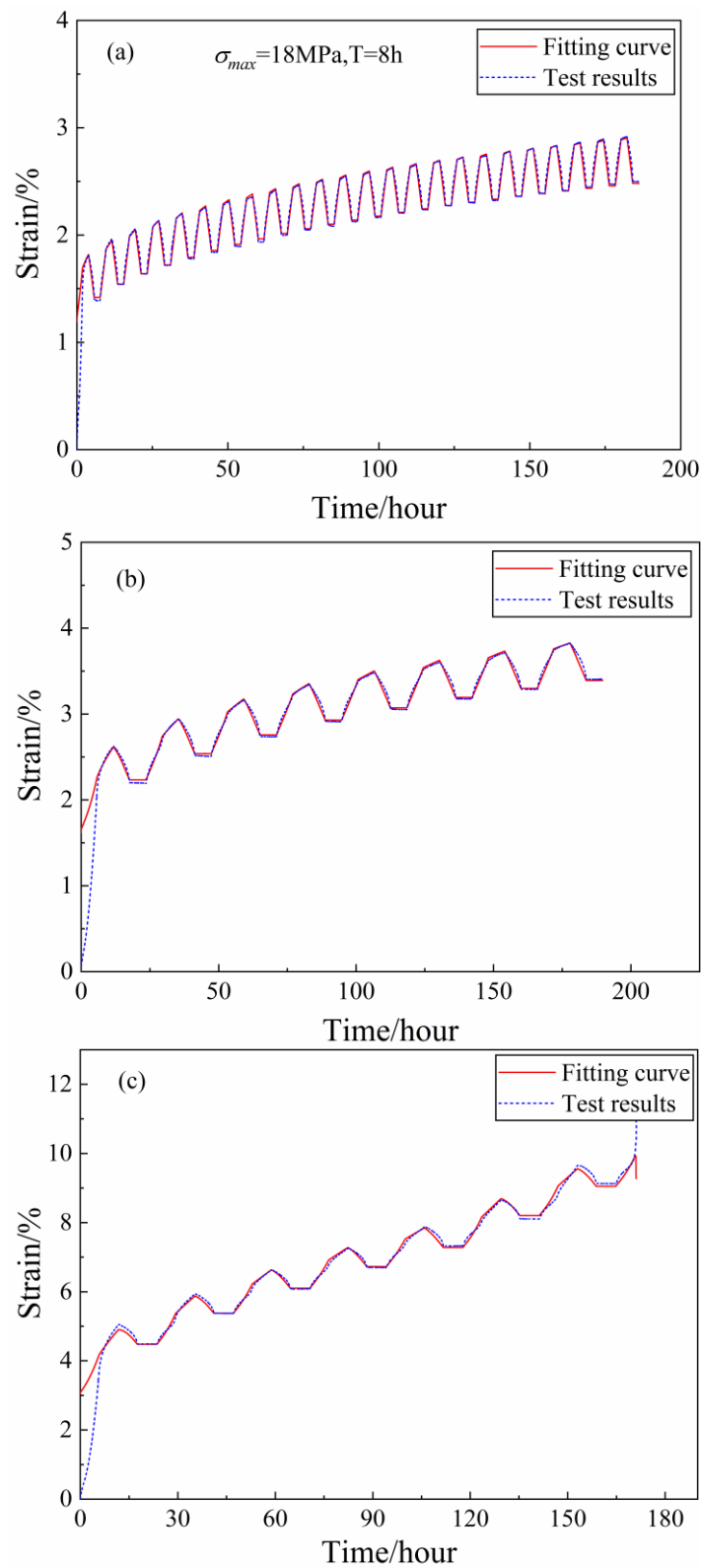
Fig. 6.13 Comparison graphs of test results and fitting results, (a) long-term creep-fatigue test with a stress upper limit of 18MPa and a cycle duration of 8 hours, (b) long-term creep-

fatigue test with a stress upper limit of 18MPa and a cycle duration of 24 hours, and (c) long-term creep-fatigue test with a stress upper limit of 24MPa and a cycle duration of 24 hours

Figure 6.13 shows the experimental and constitutive model fitting results for three sets of salt rock long-time creep-fatigue tests. Similarly, on the whole, the creep-fatigue constitutive model has better fitting results for the salt rock long-time creep-fatigue tests with different loading cycles and different stress ceilings, and the fitting accuracy is high, which reflects that the proposed model has good applicability for the long-time tests close to the operating frequency of CAES plants, and verifies the prospect of the model in engineering applications. From Fig. 6.13 (a) cycle 8-hour stress upper limit 18MPa long-time creep-fatigue test and (b) cycle 24-hour stress upper limit 18MPa long-time creep-fatigue test, the two sets of tests. The creep-fatigue constitutive model can simulate the first two phases of the test better, even at very low loading and unloading stress rates. For the complete experience of three deformation stages of the cycle of 24 hours stress upper limit 24MPa long-time creep-fatigue test, creep-fatigue model for the accelerated deformation stage of the fit is also very good. It fully demonstrates that the model can be used to predict and evaluate the deformation and stability of the surrounding rocks of the salt cavern.

6.4 Analysis of the influence of model parameters in creep and fatigue tests for salt rock

6.4.1 Analysis of the influence of model parameters in creep tests for salt rock

Comparison of model predictions and experimental results obtained from different stress ceilings as well as ascending and descending stress creep tests, it can be found that the established creep-fatigue damage ontological model is able to predict/describe the creep deformation behavior of salt rock under complex paths in a better way. The parameters involved in the model include a, b, c, n, m, k, d_0 and μ_d. In this part, the same stress path will be used, and the four parameters of c, n, m, and k, which have high influence in the creep test, will be selected to analyze and discuss their roles in the overall model.

(1) Analysis of the influence of k index on the model.

Figure 6.14 shows the creep deformation-time diagram when the rest of the

parameters are unchanged and k takes different values. As can be seen from the figure, when the k value is taken as -0.2 and -0.4, the salt rock creep process does not appear obvious non-stationary stage; when the k value continues to decrease, the creep curve will appear variable speed stage. And as the k value decreases, the faster the variable speed stage appears. k value is smaller, the same moment the creep strain is larger, at the same time, the variable speed creep stage of the creep curve radius of curvature is smaller, the earlier into the steady state creep. It can be seen that the change of k value has a greater impact on the salt rock creep model, and the size of k value directly affects the morphology of the creep curve of the salt rock, and the non-steady stage occurs when the k value <-0.4.
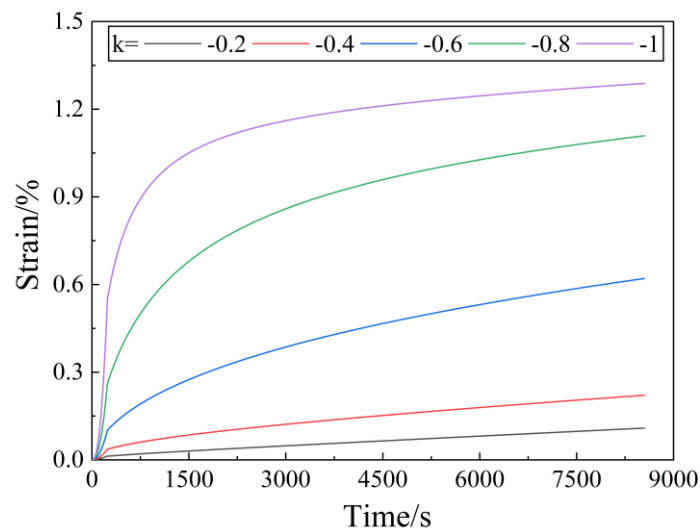
Fig.6.14 Creep-fatigue curves under pure creep for different *k* values.

The *k* metric affects the change in the creep curve by affecting the state variables in the model. Figure 6.15 shows a plot of the change in state variables when only the value of *k* in the model is changed. The creep curve plot and the state variable change plot have similar trends. As the value of k decreases, the curve gradually appears the stage of variable speed, the smaller the value of k, the faster the stage of variable speed appears, the larger the change of state variable, the earlier it tends to be stabilized; the larger the value of the state variable at the same moment, the higher the degree of hardening of the rock.
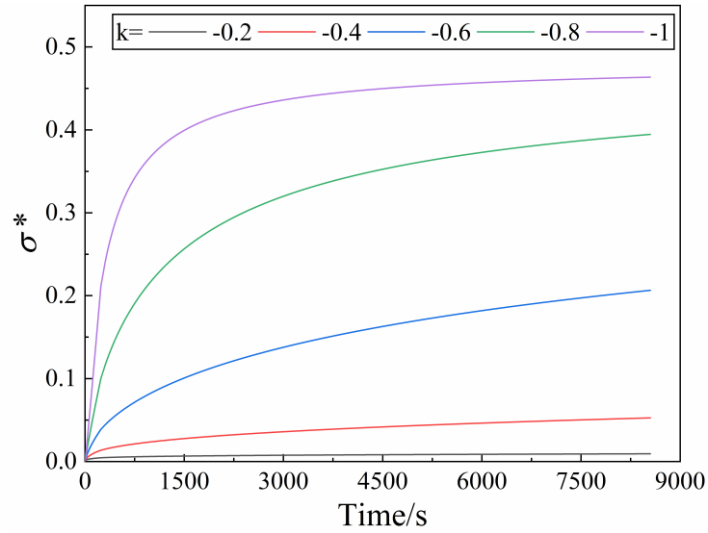
Fig.6.15 The state-variable diagram of the model under different k values

(2) Analysis of the effect of the *m* index on the model

When the stress and the rest of the parameters are the same, only change the value of m in the model. From Figure 6.16, it can be seen that the larger the value of *m*, the larger the value of creep strain at the same moment, at the same time, the smaller the radius of curvature of the creep curve at the stage of variable-speed creep, and the earlier it enters the steady state creep. It can be seen that the size of the m value mainly affects the size of the creep strain and the length of the steady state creep stage.
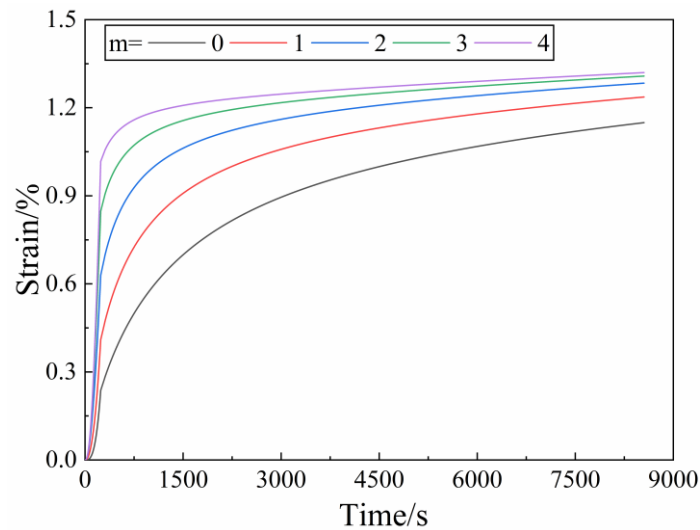
Fig.6.16 Model creep curves under different m values

Figure 6.17 shows the graph of state variables when changing the value of m in the model. The creep curve graph and the state variable change graph have a similar trend,

the larger the value of m, the earlier the state variable value tends to stabilize; the larger the state variable value at the same moment, the higher the degree of rock hardening.
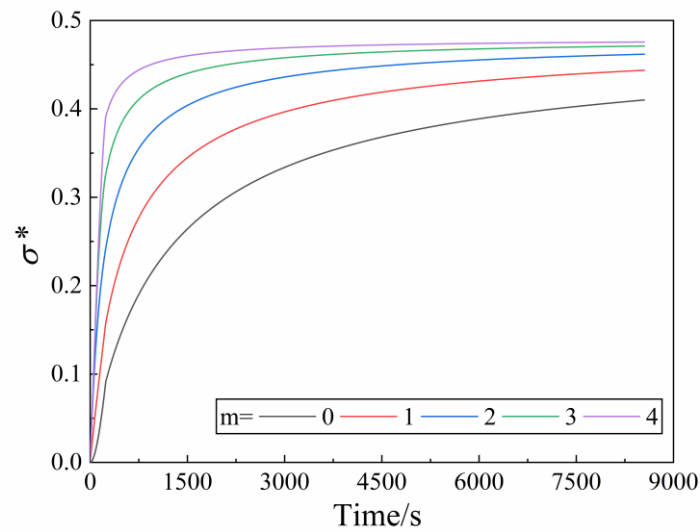
Fig.6.17 The state variable diagram of the model under different m values

(3) Analysis of the effect of *n* index on the model

As can be seen in Fig 6.18, when the value of *n* in the model is changed, the creep deformation decreases, and at the same time, the radius of curvature of the curve in the variable-speed creep stage becomes smaller, and the rate of change of the curve becomes slower and slower. It can be seen that the size of the n value mainly affects the size of the overall creep deformation amount and creep rate of the salt rock.
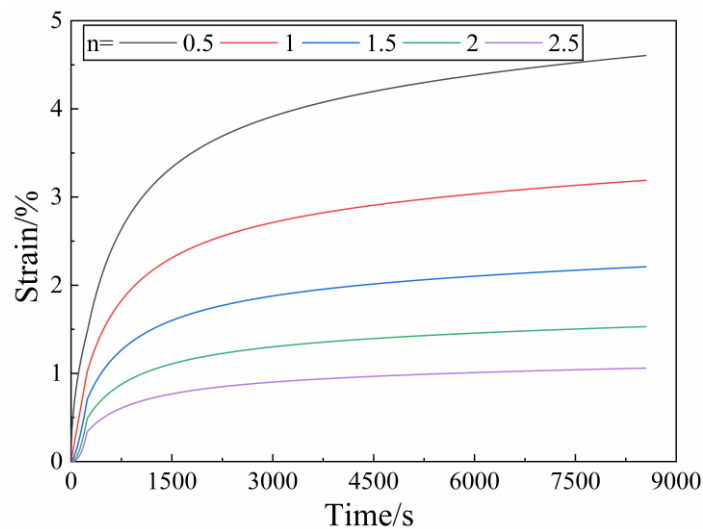
Fig.6.18 Model creep curves under different n values

Since the accelerated creep phase is equally controlled by the two parameters d_0 and μ_d, and since the penetration and expansion of the cleavage surfaces are mainly generated during the loading and unloading process (especially in the third stage of the test). Therefore, for these two parameters will be discussed in the fatigue session. Therefore, the effects of model parameters on the decelerated creep and isokinetic creep stages are mainly analyzed here. n indicator affects both the change of decelerated creep strain in the model, characterizing the sensitivity of creep deformation to stress, as shown in Fig. 6.19 (a). It also affects the change in steady-state creep strain in the model, as shown in Fig. 6.19 (b). n values are larger, the smaller the values of both variable-velocity creep strain and isokinetic creep strain at the same moment. As the value of n increases, the variable-speed creep deformation is smaller and smaller, the radius of curvature of the curve is smaller and smaller, the creep rate change is slower and slower, and the creep rate is smaller and smaller; the larger the value of n, the smaller the isokinetic creep deformation is, and the smaller the creep rate is.
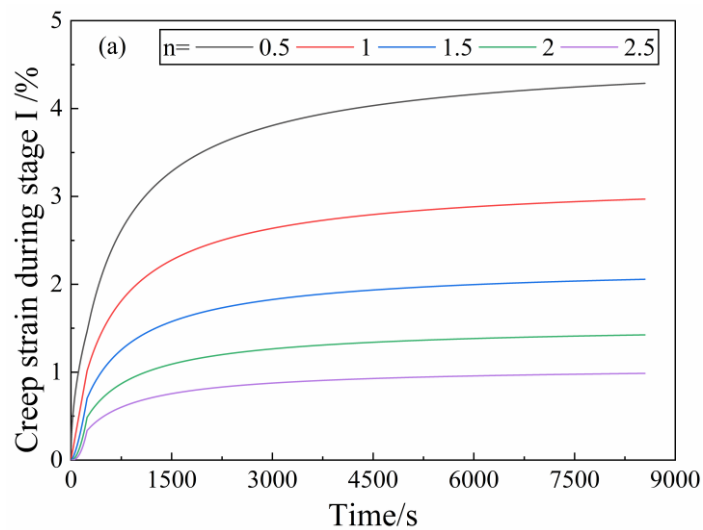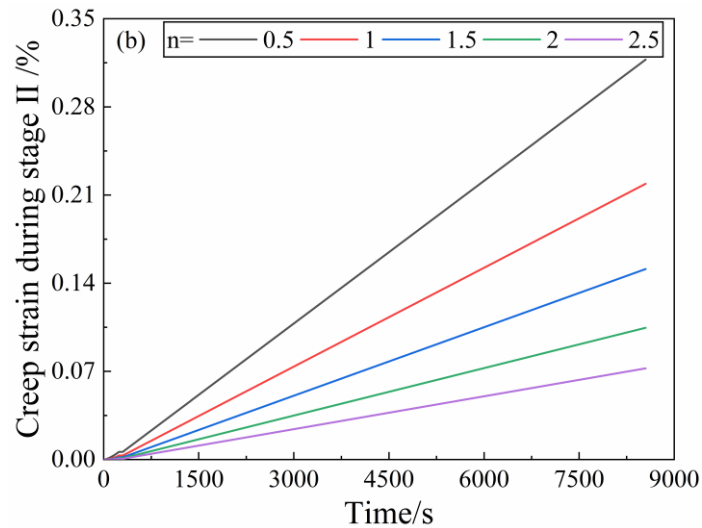
Fig.6.19 (a) Model variable speed creep curves under different n values and (b) The constant velocity creep curve of the model under different n values

(4) c parameter of the influence of indicators on the model

Parameter a in the model is the overall coefficient of the model, which affects the overall creep deformation and rate; parameter b is the overall coefficient of the damping element 2, which affects the deformation and rate of deceleration creep. The significance of the more explicit, in the part of the creep test is not discussed for the time being. Keep the rest of the parameters unchanged and only change the value of c in the model. From Figure 6.20, it can be seen that the smaller the value of c, the larger the value of creep strain at the same moment, and at the same time, the smaller the radius of curvature of the creep curve in the stage of variable-speed creep, the earlier the salt rock enters the steady state stage.
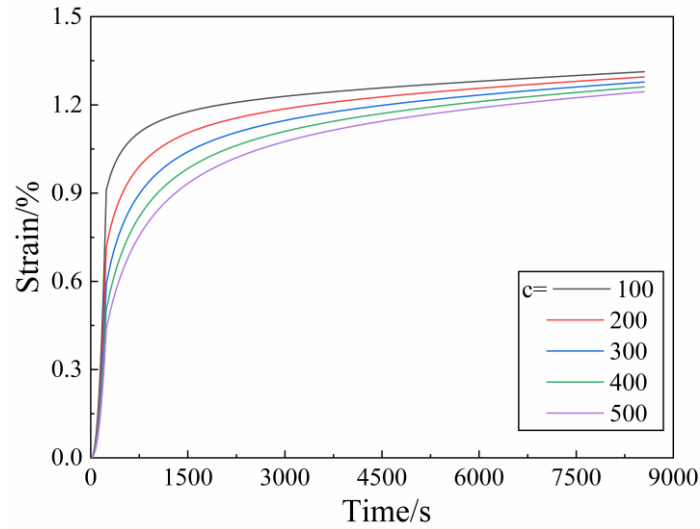
Fig.6.20 Model creep curves under different c values

The *c* parameter affects the change of the creep curve by influencing the state variables in the model, as shown in Figure 6.21. The creep curve graph and the state variable change graph have a similar trend. the smaller the c value, the faster the relative state variable changes in the variable speed creep stage, the sooner the state variable stabilizes; the larger the state variable value at the same moment, the faster the rock hardening rate and the higher the degree of hardening.
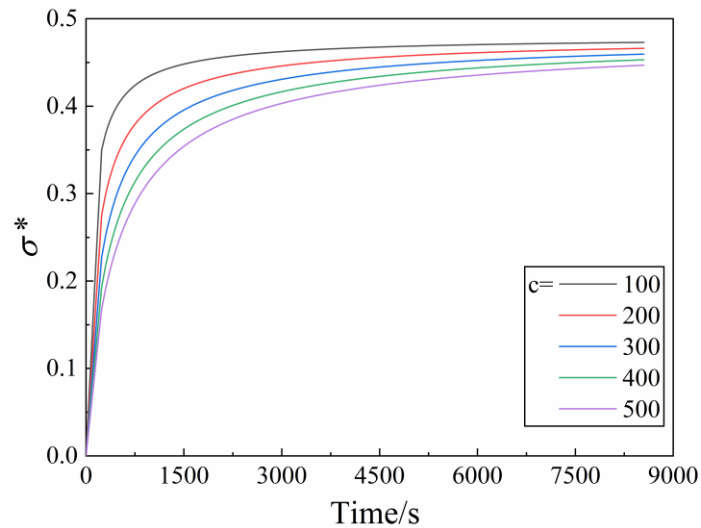
Fig.6.21 The state variable diagram of the model under different c values

6.4.2 Analysis of the influence of model parameters in fatigue tests for

salt rock

By changing different stress ratios to get the comparison of model prediction and experimental results, it can be found that the established creep-fatigue damage ontology model can better predict/describe the fatigue deformation behavior of salt rock under complex paths. In this part, the same stress path will be used, and the four parameters a, b, d_0, and μ_d, which have high influence on in the fatigue test, will be selected to act in the overall model to be analyzed and discussed.

Rocks under uniaxial cyclic compression are divided into three stages, each of which is related to the loads applied to the rock. The deformation of salt rock is the sum of plastic and elastic deformation, and the elastic deformation is only related to the state of force, shown that the parameter change does not affect the elastic deformation change, and will not be described in the subsequent analysis. The stress path of the fatigue test is shown in Fig. 6.22 below.
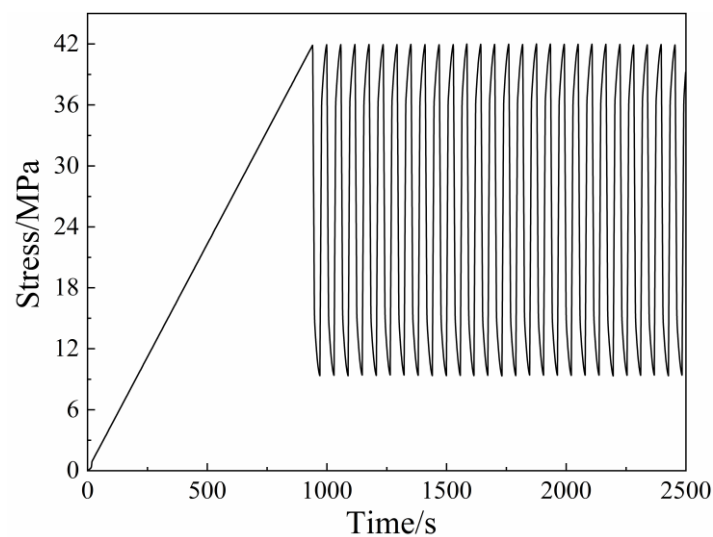
Fig.6.22 Loading path in fatigue testing of salt rocks

(1) Influences on the steady state deformation phase (influence of a)
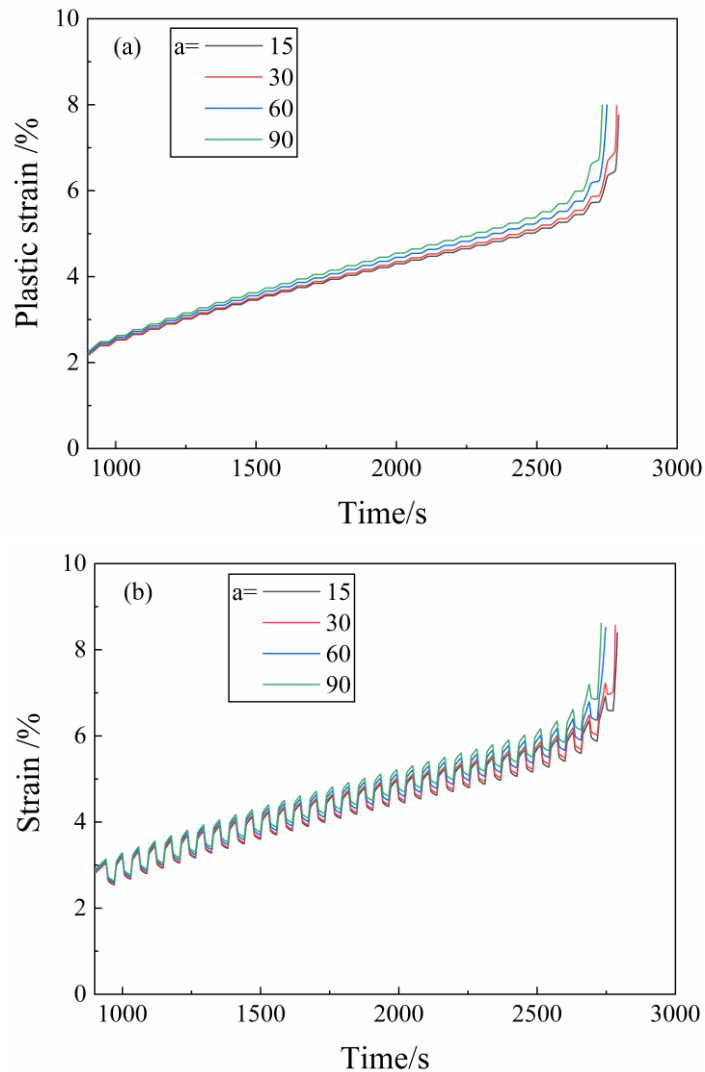
Fig.6.23 Model deformation curves corresponding to different values of a (a) plastic strain

and (b) total strain

Only change the value of parameter *a* in the model, the rest of the parameters are kept unchanged, to get different fatigue curves as shown in Fig 6.23. When *a* = 0, according to the formula can be seen, the steady state deformation rate of the material is also 0, there is no practical significance, but also the salt rock deformation is growing, so the value of *a* must be a positive number; as can be seen from Fig. 6.23, the first stage of deformation regardless of the size of *a*, basically overlap with each other, meaning that the value of a is almost independent of the decelerating strain of the first stage. The second stage of steady state (uniform) deformation stage, the mutual difference is larger, the overall slope of the curve in this stage with the increase in the value of *a*. The larger the value of *a*, the greater the rate of viscoelastic deformation of the rock; in terms of cyclic loading, the larger the value of a fatigue strain of a single

177

cycle of the beginning and end of the difference between the value of *a* (i.e., residual strain) is also the greater, and therefore the greater the slope of the curve growth. As shown in Fig 6.23(b), fatigue deformation exhibits a similar pattern when elastic deformation is considered.

(2) Factors affecting the initial deceleration phase (effect of *b*)
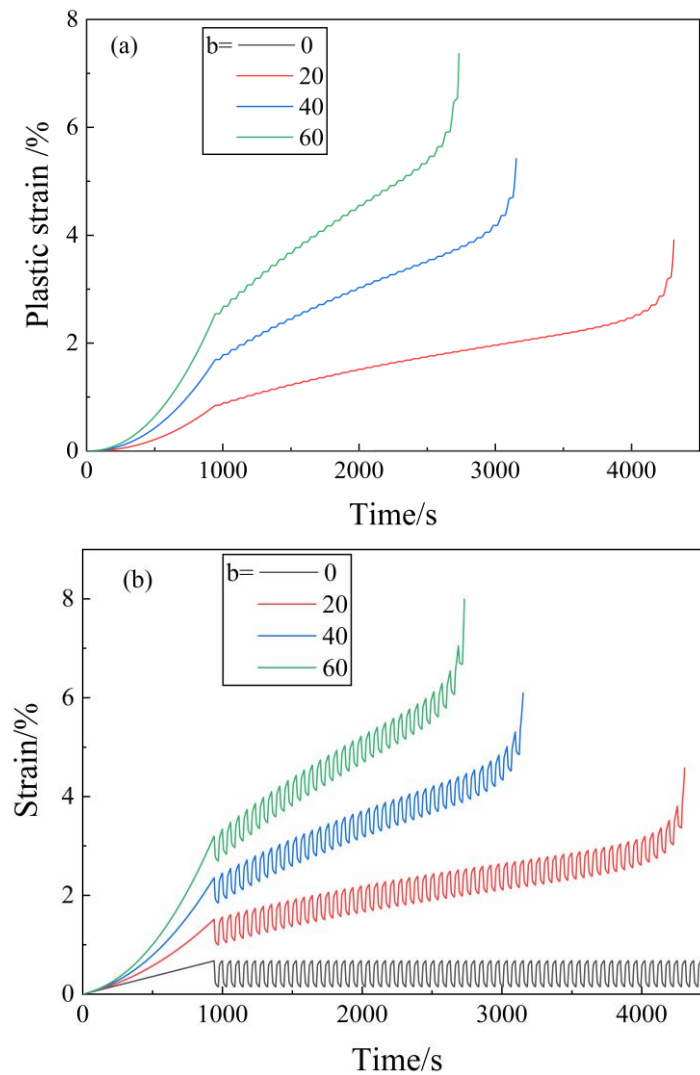
Fig.6.24 Model deformation curves corresponding to different values of *b* (a) plastic strain and (b) total strain

When the other parameter values are kept constant, varying the size of the *b*-value, different fatigue strain component curves are obtained, as shown in Fig. 6.24. The relative differences between the fatigue curves with different b values are more significant, and the gap is more obvious from the initial stage to the steady state stage. It can be found that when the *b*-value is small, the curve quickly enters the steady state

178

deformation stage, and the overall development trend is almost linear; with the increase of the *b*-value, the curvature of the front development trend of the fatigue deformation curve increases, and the overall first stage (initial deceleration deformation stage) becomes longer, i.e., the duration increases. Therefore, the change of *b*-value only affects the variable speed strain part of the model prediction curve. As shown in Fig. 6.24 (a) and (b), as the value of *b* increases, and the corresponding radius of curvature at the beginning of the cyclic loading and unloading corresponds to a larger radius of curvature at the beginning of the cyclic loading and unloading, the corresponding deformation at the end of the loading phase increases with the value of *b*, thus affecting the overall rate of change of the model-predicted curves.

Overall, the parameter *b* mainly affects the variable-rate strain part of the fatigue deformation of the rock, which is mainly manifested in the radius of curvature at the beginning of the loading stage, and the size of the strain at the beginning of the initial stage, the larger the value of *b* is, the larger the radius of curvature is, and the larger the initial strain is, which in turn affects the overall slope of the fatigue curve predicted by the model.

(3) Influences of deformation in the accelerated phase (effects of d_0 and μ_d)
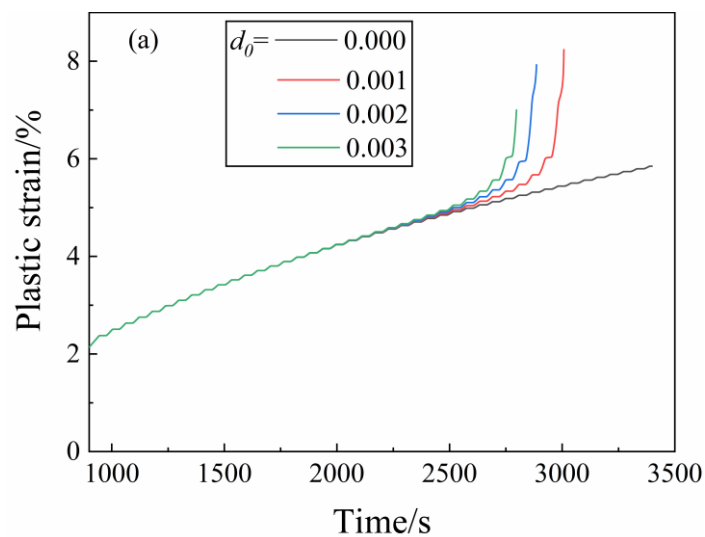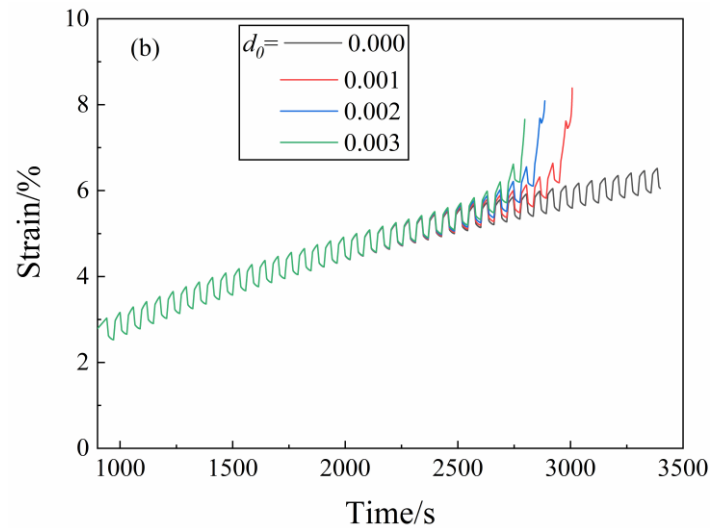
Fig.6.25 Model deformation curves corresponding to different values of d_0 (a) plastic strain and (b) total strain

When other parameters are unchanged, only the values of d_0 and μ_d in the model parameters are changed, and different fatigue strain component curves are obtained, as shown in Fig. 6.25 and Fig. 6.26. From the figure, it can be seen that the parameters d_0 and μ_d change, the initial stage of fatigue deformation of the rock and isotropic stage has almost no effect, different values of the corresponding curves almost completely overlap, only in the accelerated stage of the effect exists. d_0 increases, the curve in the accelerated stage of the increasing strain rate, combined with the model can be seen, near the destruction of the strain slope with the increase in the value of d_0 and gradually become larger. When μ_d increases, the strain rate of the curve in the accelerated stage is increasing, combined with the model, it can be seen that when the value of μ_d is 0~0.00008, the deformation in the stage of proximity to destruction increases slowly with the increase of the value of μ_d, and the overall change is very small, but when the value of μ_d is 0.00012, the strain is suddenly increased.
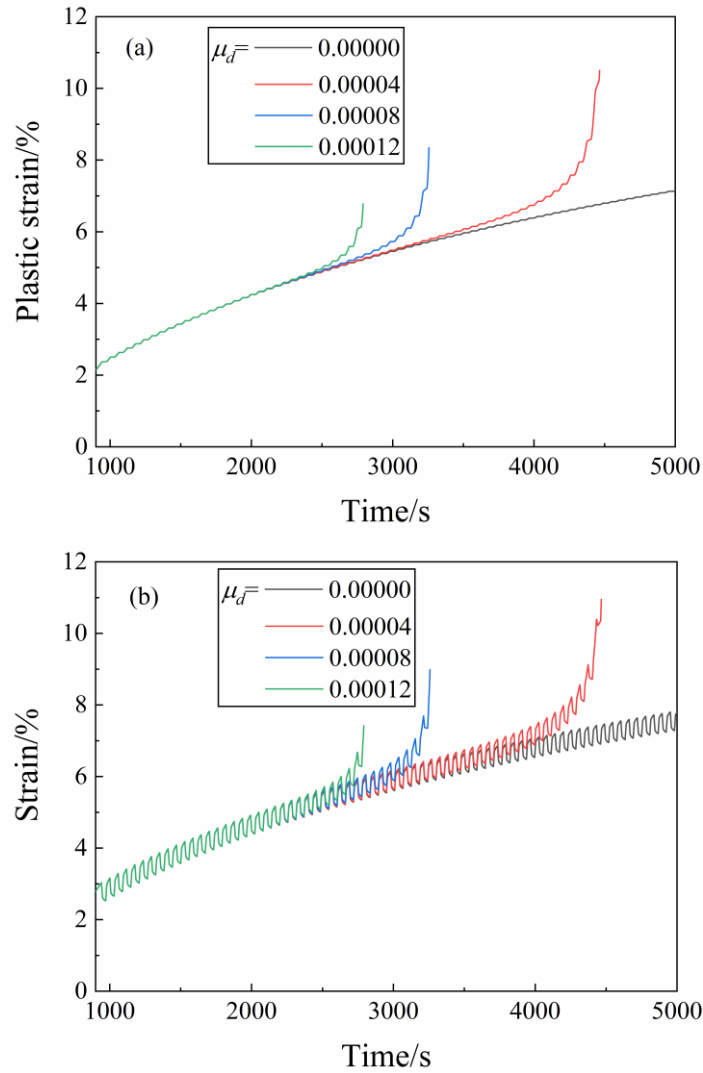
Fig.6.26 Model deformation curves corresponding to different values of μ_d (a) plastic strain and (b) total strain

Overall, the parameters d_0 and μ_d together affect the variable-velocity strain and isochronous strain of the fatigue deformation, and mainly affect the accelerated strain phase in the model prediction curve.

6.5 Conclusions

In this chapter, based on a detailed analysis of the inadequacy of previous salt-rock creep models, the creep-fatigue intrinsic model of salt rock, which can consider the creep-fatigue interaction, was established by defining state variables and introducing unloading factor and fracture factor. Based on the mechanical test results of salt rock under three different stress paths of creep, fatigue and creep-fatigue, data analysis and

model prediction are carried out to compare and analyze the accuracy of the model and the related parameter characteristics. The specific conclusions are as follows,

(1) A new creep-fatigue intrinsic model of salt rock considering creep-fatigue interaction is established by introducing the state variable characterizing the hardening degree of the rock on the basis of the Norton creep model. Based on the proposed creep-fatigue ontological model, the deformation of salt rock is divided into two parts: creep deformation (time-dependent deformation) and loading deformation (time-independent deformation).

(2) Four different loading paths, namely, constant stress creep test, cyclic loading and unloading fatigue test, uni/triaxial creep-fatigue test and long-time creep-fatigue test, are used to verify the creep-fatigue model. Comparison between the fitted curves of the four unused stress paths and the experimental curves shows that the agreement between the two is better, which means that the model can well describe the creep-fatigue model under different stress paths by taking into account the effects of time, loading and state on the creep and fatigue of the salt rock. characterize the creep-fatigue plastic deformation of salt rock under different stress paths.

(3) Through the analysis of the influence of different indexes on the model, the influence of different indexes on the creep and fatigue of salt rock is obtained. Parameter k mainly affects the decay rate of creep with time, which is the time-sensitive factor of creep rate decay; parameter m mainly affects the creep deformation amount and the length of the steady-state creep stage through stress, which is the stress-sensitive factor of creep rate decay; parameter n mainly affects the creep deformation amount and the size of creep rate through stress, which is the stress-sensitive factor of the model; parameter c mainly affects the size of creep deformation amount and the size of steady-state creep stage of the salt rock; parameter c mainly affects the creep deformation amount and the size of steady-state creep stage of the salt rock; parameter d mainly affects the creep deformation amount and the size of steady-state creep stage of the salt rock. Parameter c mainly affects the size of the amount of creep deformation and the length of the steady state creep phase, for the model of the overall strain rate decay sensitivity factor. Parameter a mainly affects the isotropic stage of the creep-fatigue damage model, and the isotropic strain rate increases with the increase of the value of a. Parameter b mainly affects the initial stage of the creep-fatigue damage model, and the decelerating strain rate increases with the increase of the value of b, while the isotropic strain rate is almost unaffected by the value of b. The parameter c is the overall

strain rate decay sensitive factor of the model. Parameters d_0 and μ_d, on the other hand, jointly affect the acceleration stage of the fatigue damage model.

7 Conclusion

7.1 Main conclusions

In order to meet the requirements of the United Nations Framework Convention on Climate Change, specifically the Paris Agreement, countries worldwide have developed action plans to achieve carbon peaking and carbon neutrality. The use of renewable energy is promoted to meet these goals. Due to its excellent rheological properties, low porosity, low permeability, and self-healing characteristics, utilizing salt caverns for compressed air energy storage (CAES) is an effective approach to enhance the efficiency of renewable energy utilization. Considering the practical operating conditions of CAES power plants, the surrounding rock of salt caverns needs to withstand discontinuous cyclic loads with varying injection frequencies and pressures, involving creep-fatigue interaction. This study adopted a combination of survey analysis, experimental research, and theoretical derivation to investigate the creep-fatigue characteristics of salt rock under different plateaus times and confining pressures. A total of 11 type tests were conducted, each lasting between 1 and 8 hours. Additionally, acoustic emission monitoring was utilized during some of the creep-fatigue tests to analyze the influence of stress level on damage evolution in salt rock. Moreover, to better reproduce actual operating loading conditions of CAES power plants, long-term (several days) creep-fatigue tests were conducted on salt rock. The microstructural reasons and patterns of creep and fatigue interaction under different conditions were analyzed using scanning electron microscopy. Considering the creep-fatigue interaction in salt rock, a state variable-based creep-fatigue constitutive model for salt rock was proposed and calibrated, with its validity verified. The main research conclusions are as follows:

(1) Considering the need for peak shaving in compressed air energy storage (CAES) power plants, there is a certain time interval between the fluctuation of gas pressure, resulting in creep-fatigue loading conditions on the surrounding rock of salt caverns. Uniaxial creep-fatigue tests were conducted to study the creep-fatigue interaction in salt rock by setting different high-stress plateau times. The study revealed that the creep-fatigue mechanical characteristic curve of salt rock exhibits three deformation stages similar to traditional fatigue tests. The application of cyclic loading promotes creep deformation, but this promoting effect diminishes gradually with an increase in high

stress plateau time. The presence of a high-stress plateau leads to larger residual strains before the interval cycles than after. As the high-stress plateau duration increases, the fatigue life of the salt rock specimens decreases, while the creep life increases. There is an interaction between creep and fatigue, and the different responses of the internal structure of salt rock to fatigue and creep are the reasons for this phenomenon, detailed in conclusion (3).

(2) Considering that the salt cavern used in the compressed air energy storage (CAES) power plant is located underground, the surrounding rock of the storage cavern is subjected to triaxial stress states. Creep-fatigue tests were conducted under different confining pressure values to study the influence of confining pressure on the creep-fatigue mechanical characteristics of salt rock. The study revealed that increasing the confining pressure not only enhances the strength of the salt rock but also increases its ultimate deformation. With the increase of confining pressure, the deformation of salt rock ultimately shows only one stage, similar to uniaxial creep-fatigue tests. Fatigue also promotes creep, and the pattern of residual strain shows consistent trends. However, with the increase of confining pressure, this difference tends to decrease. The brittle-ductile transition of salt rock under different confining pressure values is the reason for the variation in creep-fatigue mechanical characteristics of salt rock. When designing the operating gas pressure levels of the salt cavern CAES power plant, the influence of depth on the surrounding rock stress state needs to be taken into account.

(3) Acoustic emission (AE) technology can be used to monitor the internal damage evolution of rocks. With the aid of AE equipment, the influence of different stress levels on the creep-fatigue mechanical characteristics of salt rock was monitored under uniaxial and triaxial conditions. The study revealed that creep strain increases with the increase of stress levels. However, within each cycle, creep strain shows a decreasing trend with the increase of cycle number. Only in the final stages of the cycles, creep strain exhibits a final increase. Even at lower stress levels, high-stress intervals still affect the fatigue cycles, and the residual strain values before and after the plateau increase with the increase of stress levels. The presence of confining pressure reduces this growth trend. The AE signals also reflect different failure modes, with shear failure being more severe in the triaxial creep-fatigue tests compared to uniaxial tests. Both AE parameters and mechanical data indicate that with the increase of stress levels, plastic deformation and damage gradually become dominant during the creep stage.

(4) Considering the actual frequency of peak shaving in the compressed air energy

storage power station, long-term creep-fatigue tests on salt rock were conducted. By designing different loading-unloading cycles and stress limits, the creep-fatigue mechanical characteristics of salt rock over extended time spans were studied. The research showed that in the long-term creep-fatigue tests, the smaller the loading stress rate, the greater the deformation generated in salt rock. The variation in stress level has a greater impact on creep than fatigue loading cycles (stress loading rate). The change in stress state significantly affects the deformation rate of salt rock.

(5) Based on the test conclusions of this study, a new creep-fatigue constitutive model for salt rock was developed by introducing state variables to characterize the degree of rock hardening. This model incorporates the unloading factor (U_1) and fissure factor (μ_d), and considers the interaction between creep and fatigue. It is built upon the Norton creep model and contains 6 parameters. Once calibrated, this model accurately describes the viscoplastic mechanical behavior of salt rock during creep, fatigue, CCF,, TCF, USCF, LTCF tests. The proposed creep-fatigue constitutive model was then validated using mechanical test data from four different stress paths on salt rock (long-term…give tests names). A comparison between the fitted curves from the model and the experimental curves demonstrated good agreement, indicating that the model effectively predicts the effects of time, loading, and state on salt rock's creep-fatigue behavior. This model can effectively describe the creep-fatigue plastic deformation characteristics of salt rock under different stress paths.

.

7.2 Main innovations

The innovative research work carried out in this paper is mainly reflected in the following two aspects:

(1) The creep-fatigue test of salt rock under different test conditions and influencing factors was carried out, and it was clarified that there is an interaction between creep and fatigue of salt rock, and the micro-mechanism of the interaction between creep and fatigue was analyzed in detail, and it was found that the change of the state of stress affects the deformation characteristics of salt rock. A theoretical basis is established for the proposal of the creep-fatigue constitutive equation of salt rock.

(2) A new creep-fatigue constitutive model of salt rock considering creep-fatigue interaction is established by introducing a state variable characterizing the hardening degree of the rock. Based on the proposed creep-fatigue ontological model, the

deformation of salt rock is divided into two parts: creep deformation (time-dependent deformation) and loading deformation (time-independent deformation). The new model can well characterize the creep-fatigue plastic deformation of salt rock under different stress paths.

Reference

[1] Leon Hermanson, Smith Doug, Seabrook Melissa, et al. WMO global annual to decadal climate update: A prediction for 2021 – 25[J]. Bulletin of the American Meteorological Society, 2022, 103(4): E1117-E1129.

[2] Michael-F Wehner, Reed Kevin-A. Operational extreme weather event attribution can quantify climate change loss and damages[J]. PLOS Climate, 2022, 1(2): e13.

[3] Rebecca Lindsey. Climate change: Global sea level[J]. Available online: Climate. gov (accessed on 14 August 2020), 2021.

[4] Piers-M Forster, Smith Christopher-J, Walsh Tristram, et al. Indicators of Global Climate Change 2022: annual update of large-scale indicators of the state of the climate system and human influence[J]. Earth System Science Data, 2023, 15(6): 2295-2327.

[5] Cara-A Horowitz. Paris agreement[J]. International Legal Materials, 2016, 55(4): 740-755.

[6] Carl-Friedrich Schleussner, Rogelj Joeri, Schaeffer Michiel, et al. Science and policy characteristics of the Paris Agreement temperature goal[J]. Nature Climate Change, 2016, 6(9): 827-835.

[7] John McCormick. The origins of the world conservation strategy[J]. Environmental Review, 1986, 10(3): 177-187.

[8] John Pezzey. Sustainable development concepts[J]. World, 1992, 1(1): 45.

[9] Gro-Harlem Brundtland. What is sustainable development[J]. Our common future, 1987, 8(9).

[10] Glen-P Peters, Andrew Robbie-M, Canadell Josep-G, et al. Key indicators to track current progress and future ambition of the Paris Agreement[J]. Nature Climate Change, 2017, 7(2): 118-122.

[11] Spencer Dale. BP statistical review of world energy[J]. BP Plc: London, UK, 2021, 14-16.

[12] Dolf Gielen, Gorini Ricardo, Wagner Nicholas, et al. Global energy transformation: a roadmap to 2050[J]. 2019.

[13] Elisa Asmelash, Prakash Gayathri, Gorini Ricardo, et al. Role of IRENA for global transition to 100% renewable energy[J]. Accelerating the transition to a 100% renewable energy era, 2020, 51-71.

[14] Dahai Zhang, JiaqiWang, Yonggang Lin, et al. Present situation and future prospect of renewable energy in China[J]. Renewable and Sustainable Energy Reviews, 2017, 76865-871.

[15] Zongze Li, Zhenyu Yang, JinYang Fan, et al. Fatigue mechanical properties of salt rocks under high stress plateaus: the interaction between creep and fatigue[J]. Rock Mechanics and Rock Engineering, 2022, 55(11): 6627-6642.

[16] Wei Liu, Zhixin Zhang, Jie Chen, et al. Feasibility evaluation of large-scale underground hydrogen

storage in bedded salt rocks of China: A case study in Jiangsu province[J]. Energy, 2020, 198117348.

[17] JinYang Fan, Heping Xie, Jie Chen, et al. Preliminary feasibility analysis of a hybrid pumped-hydro energy storage system using abandoned coal mine goafs[J]. Applied Energy, 2020, 258114007.

[18] Ning Zhang, Lu Xi, McElroy Michael-B, et al. Reducing curtailment of wind electricity in China by employing electric boilers for heat and pumped hydro for energy storage[J]. Applied energy, 2016, 184987-994.

[19] Mengye Zhu, Qi Ye, Belis David, et al. The China wind paradox: the role of state-owned enterprises in wind power investment versus wind curtailment[J]. Energy Policy, 2019, 127200-212.

[20] Xiaowei Ma, Zhiren Zhang, Hewen Bai, et al. A Mid/Long-Term Optimization Model of Power System Considering Cross-Regional Power Trade and Renewable Energy Absorption Interval[J]. Energies, 2022, 15(10): 3594.

[21] Jin Xiao, Guohao Li, Xie Ling, et al. Decarbonizing China's power sector by 2030 with consideration of technological progress and cross-regional power transmission[J]. Energy Policy, 2021, 150112150.

[22] Xu Peng, Guangle Gao, Gaoge Hu, et al. Research on inter-regional renewable energy accommodation assessment method based on time series production simulation[A]//IEEE, 2019: 2031-2036.

[23] Amit-Kumar Rohit, Devi Ksh-Priyalakshmi, Rangnekar Saroj. An overview of energy storage and its importance in Indian renewable energy sector: Part I – Technologies and Comparison[J]. Journal of Energy Storage, 2017, 1310-23.

[24] John-P Barton, Infield David-G. Energy storage and its use with intermittent renewable energy[J]. IEEE transactions on energy conversion, 2004, 19(2): 441-448.

[25] S-Ould Amrouche, Rekioua Djamila, Rekioua Toufik, et al. Overview of energy storage in renewable energy systems[J]. International journal of hydrogen energy, 2016, 41(45): 20914-20927.

[26] A-G Olabi. Renewable energy and energy storage systems. Elsevier, 2017: 1-6.

[27] Lei Zhang, Tianshu Zhou, Yongxia Zhao, et al. Research on Electricity Cost Changes of Consumer from Developing Renewable Energy during the 14th Five-Year Plan Period — Case Studies of Ningxia Power Grid[J]. Theory & Practice, 2022, (04): 102-105.

[28] Weihe Huang, Jingkuan Han, YushengWang, et al. Strategies and Countermeasures for Ensuring Energy Security in China[J]. Strategic Study of CAE, 2021, 23(1): 112-117.

[29] Mathew Aneke,Wang Meihong. Energy storage technologies and real life applications – A state of the art review[J]. Applied Energy, 2016, 179350-377.

[30] TMI Mahlia, Saktisahdan T-J, Jannifar A, et al. A review of available methods and development on energy storage; technology update[J]. Renewable and sustainable energy reviews, 2014, 33532-545.

[31] Md-Mustafizur Rahman, Oni Abayomi-Olufemi, Gemechu Eskinder, et al. Assessment of energy storage technologies: A review[J]. Energy Conversion and Management, 2020, 223113295.

[32] K-C Divya, Østergaard Jacob. Battery energy storage technology for power systems—An overview[J]. Electric power systems research, 2009, 79(4): 511-520.

[33] Yury Gogotsi. Energy storage wrapped up[J]. Nature, 2014, 509(7502): 568-569.

[34] WeilongWang, Guo Shaopeng, Li Hailong, et al. Experimental study on the direct/indirect contact energy storage container in mobilized thermal energy system (M-TES)[J]. Applied energy, 2014, 119181-189.

[35] Venkata-Suresh Vulusala G, Madichetty Sreedhar. Application of superconducting magnetic energy storage in electrical power and energy systems: a review[J]. International Journal of Energy Research, 2018, 42(2): 358-368.

[36] SD-Gamini Jayasinghe, Vilathgamuwa D-Mahinda, Madawala Udaya-K. Direct integration of battery energy storage systems in distributed power generation[J]. IEEE Transactions on Energy Conversion, 2011, 26(2): 677-685.

[37] John-B Goodenough. Electrochemical energy storage in a sustainable modern society[J]. Energy & Environmental Science, 2014, 7(1): 14-18.

[38] Kun Zhang, Bo Peng, Jiaojiao Guo, et al. Application Status and Prospective Analysis of Chemical Energy Storage Technology in Large-scale Energy Storage Field[J]. Power Capacitor & Reactive Power Compensation, 2016, 37(2): 54-59, 66.

[39] Cong Ding, Huamin Zhang, Xianfeng Li, et al. Vanadium flow battery for energy storage: prospects and challenges[J]. The journal of physical chemistry letters, 2013, 4(8): 1281-1294.

[40] KangliWang, Kai Jiang, Chung Brice, et al. Lithium – antimony – lead liquid metal battery for grid-level energy storage[J]. Nature, 2014, 514(7522): 348-350.

[41] Montaser Mahmoud, Ramadan Mohamad, Olabi Abdul-Ghani, et al. A review of mechanical energy storage systems combined with wind and solar applications[J]. Energy Conversion and Management, 2020, 210112670.

[42] Mustafa-E Amiryar, Pullen Keith-R. A review of flywheel energy storage system technologies and their applications[J]. Applied Sciences, 2017, 7(3): 286.

[43] JinYang Fan, Wei Liu, Deyi Jiang, et al. Thermodynamic and applicability analysis of a hybrid

CAES system using abandoned coal mine in China[J]. Energy, 2018, 15731-44.

[44] Deyi Jiang, Shao Chen, Wenhao Liu, et al. Underground hydro-pumped energy storage using coal mine Goafs: system performance analysis and a case study for China[J]. Frontiers in Earth Science, 2021, 9947.

[45] Ahmad Arabkoohsar. Chapter Eight - Conclusion. Academic Press, 2021: 177-188.

[46] Mike McWilliams. 6.08 - Pumped Storage Hydropower. Oxford: Elsevier, 2022: 147-175.

[47] Ryan Wiser, Bolinger Mark, Hoen Ben, et al. Land-based wind market report: 2022 edition. Lawrence Berkeley National Lab.(LBNL), Berkeley, CA (United States), 2022.

[48] Alessandro Tallini, Vallati Andrea, Cedola Luca. Applications of micro-CAES systems: energy and economic analysis[J]. Energy Procedia, 2015, 82797-804.

[49] Hussein Ibrahim, Younès Rafic, Ilinca Adrian, et al. Study and design of a hybrid wind－diesel-compressed air energy storage system for remote areas[J]. Applied Energy, 2010, 87(5): 1749-1762.

[50] Rui Li, Laijun Chen, Tiejiang Yuan, et al. Optimal dispatch of zero-carbon-emission micro Energy Internet integrated with non-supplementary fired compressed air energy storage system[J]. Journal of Modern Power Systems and Clean Energy, 2016, 4(4): 566-580.

[51] Qian Zhou, Du Dongmei, Lu Chang, et al. A review of thermal energy storage in compressed air energy storage system[J]. Energy, 2019, 188115993.

[52] Elaheh Bazdar, Sameti Mohammad, Nasiri Fuzhan, et al. Compressed air energy storage in integrated energy systems: A review[J]. Renewable and Sustainable Energy Reviews, 2022, 167112701.

[53] Jie Chen, Song Ren, Chunhe Yang, et al. Self-healing characteristics of damaged rock salt under different healing conditions[J]. Materials, 2013, 6(8): 3438-3450.

[54] Mengsu Hu, Steefel Carl-I, Rutqvist Jonny, et al. Microscale THMC Modeling of Pressure Solution in Salt Rock: Impacts of Geometry and Temperature[J]. Rock Mechanics and Rock Engineering, 2022, 1-19.

[55] A Mortazavi, Nasab H. Analysis of the behavior of large underground oil storage caverns in salt rock[J]. International Journal for Numerical and Analytical Methods in Geomechanics, 2017, 41(4): 602-624.

[56] Janos-L Urai, Spiers Christopher-J, Zwart Hendrik-J, et al. Weakening of rock salt by water during long-term creep[J]. Nature, 1986, 324(6097): 554-557.

[57] Dilara-Gulcin Caglayan, Weber Nikolaus, Heinrichs Heidi-U, et al. Technical potential of salt caverns for hydrogen storage in Europe[J]. International Journal of Hydrogen Energy, 2020, 45(11): 6793-6805.

[58] Fritz Crotogino. Traditional bulk energy storage－Coal and underground natural gas and oil

storage. Elsevier, 2022: 633-649.

[59] Katarzyna Cyran. Insight into a shape of salt storage caverns[J]. Archives of Mining Sciences, 2020, 65(2).

[60] P Renoux. Geological and Geophysical Study of an Hydrocarbon Storage in Salt Caverns in Manosque (France)[A]//European Association of Geoscientists & Engineers, 2013: 348.

[61] Paula-D Weber, Gutierrez Karen-A, Lord David-L, et al. Analysis of SPR salt cavern remedial leach program 2013. Sandia National Lab.(SNL-NM), Albuquerque, NM (United States); GRAM, Inc ···, 2013.

[62] Ioan Iordache, Schitea Dorin, Gheorghe Adrian-V, et al. Hydrogen underground storage in Romania, potential directions of development, stakeholders and general aspects[J]. international journal of hydrogen energy, 2014, 39(21): 11071-11081.

[63] M Langer. Use of solution-mined caverns in salt for oil and gas storage and toxic waste disposal in Germany[J]. Engineering geology, 1993, 35(3-4): 183-190.

[64] P Vidal-Nunes, Da Gama C-Dinis. Underground gas storage in Portuguese salt caverns[A]//ISRM, 2014: ISRM-EUROCK.

[65] Mandhapati Raju, Khaitan Siddhartha-Kumar. Modeling and simulation of compressed air storage in caverns: a case study of the Huntorf plant[J]. Applied energy, 2012, 89(1): 474-481.

[66] Xinjing Zhang, Li Yang, Gao Ziyu, et al. Overview of dynamic operation strategies for advanced compressed air energy storage[J]. Journal of Energy Storage, 2023, 66107408.

[67] Xilin Shi, Xinxing Wei, Chunhe Yang, et al. Problems and Countermeasures for Construction of China's Salt Cavern Type Strategic Oil Storage[J]. Bulletin of Chinese Academy of Sciences, 2023, 38(1): 99-111.

[68] Chunhe Yang, Tao He,Wang Tongtao. Research and development progress of oil and gas storage construction technology in bedded salt rock formation[J]. Oil & Gas Storage and Transportation, 2022, 41(6): 614-624.

[69] Chun-he Yang, LIANG Wei-guo, WEI Dong-hou, et al. Investigation on possibility of energy storage in salt rock in China[J]. Chinese Journal of Rock Mechanics and Engineering, 2005, 24(24): 4409-4417.

[70]Guangkuo Li,Wang Guohua, XUE Xiaodai, et al. Design and Analysis of Condenser Mode for Jintan Salt Cavern Compressed Air Energy Storage Plant of China[J]. Automation of Electric Power Systems, 2021, 45(19): 91-99.

[71]Chen Jie, Jiang Deyi, Liu Wei, et al. Research Progress of Solution Mining and Comprehensive Utilization of Salt Cavern[J]. Bulletin of National Natural Science Foundation of China, 2021, 35(6): 911-916.

[72] Chunhe Yang,Wang Tongtao. Advance in deep underground energy storage[J]. Chinese Journal of Rock Mechanics and Engineering, 2022, 41(9): 1729-1759.

[73] Guimin Zhang, Zhenshuo Wang, Yuxuan Liu, et al. Research on stability of the key roof above horizontal salt cavern for compressed air energy storage[J]. Rock and soil mechanics, 2021, 42(3): 800-812.

[74] M Langer. Use of solution-mined caverns in salt for oil and gas storage and toxic waste disposal in Germany[J]. Engineering geology, 1993, 35(3-4): 183-190.

[75] Xilin Shi, Qinglin Chen, Hongling Ma, et al. Geomechanical investigation for abandoned salt caverns used for solid waste disposal[J]. Bulletin of Engineering Geology and the Environment, 2021, 801205-1218.

[76] Jie Yang, Zhengyou Liu, Chunhe Yang, et al. Mechanical and microstructural properties of alkali wastes as filling materials for abandoned salt caverns[J]. Waste and biomass valorization, 2021, 121581-1590.

[77] Glenn-M Duyvestyn, Davidson Brett-C, Dusseault Maurice-B. Salt solution caverns for petroleum industry toxic granular solid waste disposal[A]//SPE, 1998: 47250.

[78] Glenn-M Duyvestyn, Davidson Brett-C, Dusseault Maurice-B. Salt solution caverns for petroleum industry toxic granular solid waste disposal[A]//SPE, 1998: 47250.

[79] Yiwei Ren, Yuan Qiang, Kang Yanfei, et al. Experimental Determination of Polycrystalline Salt Rock Thermal Conductivity, Diffusivity and Specific Heat From 20 to 240° C[J]. Frontiers in Earth Science, 2022, 10835974.

[80] Hafssa Tounsi, Lerche Svetlana, Wolters Ralf, et al. Impact of the compaction behavior of crushed salt on the thermo-hydro-mechanical response of a generic salt repository for heat-generating nuclear waste[J]. Engineering Geology, 2023, 107217.

[81] Hafssa Tounsi, Rutqvist Jonny, Hu Mengsu, et al. Long-term sinking of nuclear waste canisters in salt formations by low-stress creep at high temperature[J]. Acta Geotechnica, 2023, 1-16.

[82] Pedro-ALP Firme, Roehl Deane, Romanel Celso. Salt caverns history and geomechanics towards future natural gas strategic storage in Brazil[J]. Journal of Natural Gas Science and Engineering, 2019, 72103006.

[83] Peng Li, Li Yinping, Shi Xilin, et al. Stability analysis of U-shaped horizontal salt cavern for underground natural gas storage[J]. Journal of Energy Storage, 2021, 38102541.

[84] JinYang Fan, Wei Liu, Deyi Jiang, et al. Time interval effect in triaxial discontinuous cyclic compression tests and simulations for the residual stress in rock salt[J]. Rock Mechanics and Rock Engineering, 2020, 534061-4076.

[85] J Lemaitre, Plumtree A. Application of damage concepts to predict creep-fatigue failures[J]. 1979.

[86] Xiao-Cheng Zhang, Gong Jian-Guo, Xuan Fu-Zhen. A deep learning based life prediction method for components under creep, fatigue and creep-fatigue conditions[J]. International Journal of Fatigue, 2021, 148106236.

[87] Jinlong Li, Chunhe Yang, Xilin Shi, et al. Construction modeling and shape prediction of horizontal salt caverns for gas/oil storage in bedded salt[J]. Journal of Petroleum Science and Engineering, 2020, 190107058.

[88] Zhaofei Chu, Zhijun Wu, ZhiYangWang, et al. Micro-mechanism of brittle creep in saturated sandstone and its mechanical behavior after creep damage[J]. International Journal of Rock Mechanics and Mining Sciences, 2022, 149104994.

[89] Lei Zhang, Hongwei Zhou, XiangyuWang, et al. A triaxial creep model for deep coal considering temperature effect based on fractional derivative[J]. Acta Geotechnica, 2022, 1-13.

[90] Qiang Zhang, Zhanping Song, JunbaoWang, et al. Creep properties and constitutive model of salt rock[J]. Advances in Civil Engineering, 2021, 20211-29.

[91] N Erarslan, Williams D-J. Mechanism of rock fatigue damage in terms of fracturing modes[J]. International Journal of Fatigue, 2012, 4376-89.

[92] P-B Attewell, Farmer I-W. Fatigue behaviour of rock[A]//Elsevier, 1973: 1-9.

[93] V-V Adushkin, Spivak A-A, Kharlamov V-A. Effects of lunar-solar tides in the variations of geophysical fields at the boundary between the Earth's crust and the atmosphere[J]. Izvestiya, Physics of the Solid Earth, 2012, 48104-116.

[94] FINN Surlyk, Noe-Nygaard NANNA. Sand remobilisation and intrusion in the Upper Jurassic Hareelv Formation of East Greenland[J]. Bulletin of the Geological Society of Denmark, 2001, 48169-188.

[95] Chuang Liu, Huamin Li, Mitri Hani. Effect of strata conditions on shield pressure and surface subsidence at a longwall top coal caving working face[J]. Rock Mechanics and Rock Engineering, 2019, 521523-1537.

[96] Yi Liu, Feng Dai. A review of experimental and theoretical research on the deformation and failure behavior of rocks subjected to cyclic loading[J]. Journal of Rock Mechanics and Geotechnical Engineering, 2021, 13(5): 1203-1230.

[97] Xiurun Ge, Yu Jiang, Yunde Lu, et al. Testing study on fatigue deformation law of rock under cyclic loading [J]. Chinese Journal of Rock Mechanics and Engineering, 2003, 22(10): 1581-1585.

[98] Yintong Guo, Kelie Zhao, Guanhua Sun, et al. Experimental study of fatigue deformation and damage characteristics of salt rock under cyclic loading[J]. Rock and soil mechanics, 2011, 32(5): 1353-1359.

[99] Linjian Ma, Xinyu Liu, Hongfa Xu, et al. Experimental study on triaxial deformation and strength

characteristics of salt rock under cyclic loads [J]. Chinese Journal of Rock Mechanics and Engineering, 2013, 32(4): 849-856.

[100] Yunfeng Zhao, Ren Song, Jiang Deyi, et al. Influence of wetting-drying cycles on the pore structure and mechanical properties of mudstone from Simian Mountain[J]. Construction and Building Materials, 2018, 191923-931.

[101] Yanbo Zhu, Xing Huang, Jie Guo, et al. Experimental study of fatigue characteristics of gypsum rock under cyclic loading[J]. Chinese Journal of Rock Mechanics and Engineering, 2017, 36(4): 940-952.

[102] Shuhong Wang, Zihe Wang, Kaiyi Wang, et al. Evolution Law of Elastic Modulus of Sandstone with Double Fissures Under Cyclic Loading[J]. Journal of Northeastern University(Natural Science), 2020, 41(2): 282-286.

[103] ming Gao Lu, Yuanhui Li. Influence of confining pressure on fatigue deformation properties of yellow sandstone[J]. Rock and soil mechanics, 2016, 37(7): 1847-1856.

[104] Yue Han, Hongling Ma, Chunhe Yang, et al. A modified creep model for cyclic characterization of rock salt considering the effects of the mean stress, half-amplitude and cycle period[J]. Rock Mechanics and Rock Engineering, 2020, 533223-3236.

[105] JinYang Fan, Jie Chen, Deyi Jiang, et al. Discontinuous cyclic loading tests of salt with acoustic emission monitoring[J]. International Journal of Fatigue, 2017, 94140-144.

[106] JinYang Fan, Deyi Jiang, Wei Liu, et al. Discontinuous fatigue of salt rock with low-stress intervals[J]. International Journal of Rock Mechanics and Mining Sciences, 2019, 11577-86.

[107] Deyi Jiang, Fan JinYang, Jie Chen, et al. A mechanism of fatigue in salt under discontinuous cycle loading[J]. International Journal of Rock Mechanics and Mining Sciences, 2016, 86255-260.

[108] Feng Chen, Chunhe Yang, Shiwei Bai. Investigation on optimized gas recovery velocity of natural gas storage in salt rock layer by numerical simulation[J]. Rock and soil mechanics, 2007, 28(1): 57-62.

[109] Hongwei Zhou, Jinming He, Zhide Wu. Permeability properties of interbedded saline rocks and their fine structure characterization [J]. Chinese Journal of Rock Mechanics and Engineering, 2009, 28(10): 2068-2073.

[110] Hongbo Gao, Weiguo Liang, Suguo Xu, et al. Study on the response of mechanical properties of salt rock under cyclic loads [J]. Chinese Journal of Rock Mechanics and Engineering, 2011, (Z1).

[111] Feng He, Song Yang. Study on the viscoelastic-plastic fractional creep model of sandstone in uniaxial compression[J]. Chinese Journal of Applied Mechanics, 2022, 1-8.

[112] Ming Huang, Xinrong Liu, Yunhua Zhu, et al. A study of behaviors of generalized Kelvin-Voigt model under low frequency cyclic load[J]. Rock and soil mechanics, 2009, 30(8): 2300-2304.

[113] Qiangguo Jian. Study on the Criterion of Rock Salt Based on Energy Principles and its Application in Engineering[D]. Chongqing university, 2014.

[114] Benjamin Cerfontaine, Charlier Robert, Collin Frédéric, et al. Validation of a new elastoplastic constitutive model dedicated to the cyclic behaviour of brittle rock materials[J]. Rock Mechanics and Rock Engineering, 2017, 502677-2694.

[115] Qiang Zhang, Junbao Wang, Zhanping Song, et al. Microstructure variation and empirical fatigue model of salt rock under cyclic loading[J]. Rock and soil mechanics, 2022, 43(4): 995-1008.

[116] Yongjie Yang Yang, Song, Jun Chu. Experimental study on strength and deformation characteristics of coal rock under cyclic loading effects [J]. Chinese Journal of Rock Mechanics and Engineering, 2007, 26(1): 201-205.

[117] Yi Liu, Dai Feng. A damage constitutive model for intermittent jointed rocks under cyclic uniaxial compression[J]. International Journal of Rock Mechanics and Mining Sciences, 2018, 103289-301.

[118] Shu chun Li, JiangXu, Yunqi Tao, et al. Low cycle fatigue damage model and damage variable expression of rock[J]. Rock and soil mechanics, 2009, 30(6): 1611-1614, 1619.

[119] C-H Scholz. Mechanism of creep in brittle rock[J]. Journal of Geophysical Research, 1968, 73(10): 3295-3302.

[120] Q-YWang, Zhu W-C, Xu T, et al. Numerical simulation of rock creep behavior with a damage-based constitutive law[J]. International Journal of Geomechanics, 2017, 17(1): 4016044.

[121] E Maranini, Brignoli M. Creep behaviour of a weak rock: experimental characterization[J]. International Journal of Rock Mechanics and Mining Sciences, 1999, 36(1): 127-138.

[122] Nicolae Cristescu, Hunsche Udo. Time effects in rock mechanics[M]. Wiley New York, 1998.

[123] H Ito, Sasajima S. A ten year creep experiment on small rock specimens[A]//Elsevier, 1987: 113-121.

[124] David Griggs. Creep of rocks[J]. The Journal of Geology, 1939, 47(3): 225-251.

[125] Dehong Li, Mingyuan Yu, Dapeng Tian, et al. Study on Creep Law and Nonlinear Creep Model of Serpentine Marble[J]. Chinese Journal of Underground Space and Engineering, 2023, 19(2): 420-427.

[126] Xunjian Hu, Kang Bian, Jian Liu, et al. Discrete element simulation study on the influence of microstructure heterogeneity on the creep characteristics of granite[J]. Chinese Journal of Rock Mechanics and Engineering, 2019, 38(10): 2069-2083.

[127] Changbing Zhou, Zhijun Wan, Yuan Zhang, et al. Creep characteristics and constitutive model of gas coal mass under high temperature and triaxial stress[J]. Journal of China Coal Society, 2012, 37(12): 2020-2025.

[128] Yuan Zhang, YalingWang, Jin Yu, et al. Creep behavior and its nonlinear creep model of deep

gypsum mudstone[J]. Rock and soil mechanics, 2018, (s1).

[129] Sana Zafar, Hedayat Ahmadreza, Moradian Omid. Micromechanics of fracture propagation during multistage stress relaxation and creep in brittle rocks[J]. Rock Mechanics and Rock Engineering, 2022, 55(12): 7611-7627.

[130] C-J Spiers, Peach C-J, Brzesowsky R-H, et al. Long-term rheological and transport properties of dry and wet salt rocks. Commission of the European Communities, 1988.

[131] Diansen Yang, Chen Weizhong, Yang Jianping, et al. Application of digital image correlation technique in experimental study of the creep behavior and time dependent damage of natural rock salt[J]. Journal of Testing and Evaluation, 2012, 40(2): 220-226.

[132] Yue Ma, Mian Chen, Chunhe Yang. Study on the effect of gypsum content on the creep rate of salt paste layer [J]. Chinese Journal of Rock Mechanics and Engineering, 2013, (z2): 3238-3244.

[133] Lance-A Roberts, Buchholz Stuart-A, Mellegard Kirby-D, et al. Cyclic loading effects on the creep and dilation of salt rock[J]. Rock Mechanics and Rock Engineering, 2015, 482581-2590.

[134] Wenjing Li, Han Yanhui,Wang Tao, et al. DEM micromechanical modeling and laboratory experiment on creep behavior of salt rock[J]. Journal of Natural Gas Science and Engineering, 2017, 4638-46.

[135] Amornrat Luangthip, Wilalak Naphaphat, Thongprapha Thanittha, et al. Effects of carnallite content on mechanical properties of Maha Sarakham rock salt[J]. Arabian Journal of Geosciences, 2017, 101-14.

[136] M Hamami. Experimental and numerical studies of rock salt strain hardening[J]. Geotechnical & Geological Engineering, 2006, 241271-1292.

[137] Jianqing He, Mengyuan Lin, Liguo Chen, et al. Empirical creep model for K0 consolidation of lacustrine soft clay considering confining pressure[J]. Journal of Natural Disasters, 2022, 31(1): 147-156.

[138] Baodi Wang, Liping Su, Yang Liu. Improved Nishihara creep model research and secondary development calculation[J]. Journal of Safety Science and Technology, 2022, 18(8): 128-134.

[139] Juntao Yang, Yanqi Song, Hongfa Ma, et al. A creep constitutive model of salt rock considering hardening and damage effects[J]. Rock and soil mechanics, 2023, (10): 1-14.

[140] Lixin Wu, JinzhuangWang. A preliminary study of the rheological properties of coal rocks and their microscopic influence characteristics [J]. Chinese Journal of Rock Mechanics and Engineering, 1996, 4(4).

[141] JingYang Ding, Hongwei Zhou, Chao Li, et al. Fractional order creep intrinsic modeling of salt rock based on Weibull distribution [J]. Chinese Journal of Solid Mechanics, 2013, 34(5): 8.

[142] Xiangdong Zhang, Qiang Fu. Study on triaxial creep test of mudstone[J]. Chinese Journal of

Applied Mechanics, 2012, 29(2): 154-158.

[143] You Wang, Xiaoyu Wang, Yaqian Li. Studies on the Improved Generalized Kelvin Rock Creep Model[J]. Journal of Hebei University of Engineering(Natural Science Edition), 2020, 37(4): 47-51.

[144] Yang Han, Yuehu Tan, Erbing Li, et al. Nonconstant Burgers creep model for rocks and its parameter identification [J]. Engineering Mechanics, 2018, 35(3): 210-217.

[145] Qianfeng Yin, Haifeng Lu, Fengchun Zhao. A Plasticity - based Improved Maxwall Model of Rock Creep[J]. Journal of Tangshan University, 2017, 30(03): 55-57.

[146] Haifei Jiang, Dongyan Liu, Wei Huang, et al. Creep properties of rock under high confining pressure and different pore water pressures and a modified Nishihara model[J]. Chinese Journal of Geotechnical Engineering2014, 36(03): 443-451.

[147] Qinghui Jiang, Yajing Qi, ZhijianWang, et al. An extended Nishihara model for the description of three stages of sandstone creep[J]. Geophysical Journal International, 2013, 193(2): 841-854.

[148] Anrun Li, Deng Hui, Zhang Haojie, et al. Developing a two-step improved damage creep constitutive model based on soft rock saturation-loss cycle triaxial creep test[J]. Natural Hazards, 2021, 108(2): 2265-2281.

[149] Ehsan Haghighat, Rassouli Fatemeh-S, Zoback Mark-D, et al. A viscoplastic model of creep in shale[J]. Geophysics, 2020, 85(3): MR155-MR166.

[150] Linjian Ma,Wang MingYang, Zhang Ning, et al. A variable-parameter creep damage model incorporating the effects of loading frequency for rock salt and its application in a bedded storage cavern[J]. Rock Mechanics and Rock Engineering, 2017, 502495-2509.

[151] Aditya Singh, Kumar Chandan, Kannan L-Gopi, et al. Engineering properties of rock salt and simplified closed-form deformation solution for circular opening in rock salt under the true triaxial stress state[J]. Engineering Geology, 2018, 243218-230.

[152] Kui Wu, Shao Zhushan, Sharifzadeh Mostafa, et al. Analytical approach to estimating the influence of shotcrete hardening property on tunnel response[J]. Journal of Engineering Mechanics, 2022, 148(1): 4021127.

[153] Rongbin Hou, Kai Zhang, Jing Tao, et al. A nonlinear creep damage coupled model for rock considering the effect of initial damage[J]. Rock Mechanics and Rock Engineering, 2019, 521275-1285.

[154] Hao Cheng, YuChen Zhang, Xiaoping Zhou. Nonlinear creep model for rocks considering damage evolution based on the modified Nishihara model[J]. International Journal of Geomechanics, 2021, 21(8): 4021137.

[155] HongWei Zhou, ChunPing Wang, ZhiQiang Duan, et al. Time-based fractional derivative approach

to creep constitutive model of salt rock[J]. SCIENTIA SINICA Physica,Mechanica & Astronomica, 2012, 42(3): 310-318.

[156] XingangWang, Yin Yueping,Wang Jiading, et al. A nonstationary parameter model for the sandstone creep tests[J]. Landslides, 2018, 151377-1389.

[157] Yibin Zhang, Yihai Zhang, Haitao Ma, et al. Study on nonlinear viscoelasto-plastic damage creep model of rock and its parameter identification[J]. Journal of Safety Science and Technology, 2023, 19(6): 13-19.

[158] Bingbing Yu, Qing Li, Tongde Zhao, et al. Full-time nonlinear creep damage model of fractured rock mass based on stress-time double threshold[J]. Chinese Journal of Rock Mechanics and Engineering, 2023, 1-17.

[159] H-W Zhou, C-PWang, B-B Han, et al. A creep constitutive model for salt rock based on fractional derivatives[J]. International Journal of Rock Mechanics and Mining Sciences, 2011, 48(1): 116-121.

[160] Youliang Chen, Qijian Chen, Yungui Pan, et al. A Chemical Damage Creep Model of Rock Considering the Influence of Triaxial Stress[J]. Materials, 2022, 15(21): 7590.

[161] Dashnor Hoxha, Homand Françoise, Auvray Christophe. Deformation of natural gypsum rock: Mechanisms and questions[J]. Engineering Geology, 2006, 86(1): 1-17.

[162] Xiaozhao Li, Qishuo Zhang, Fucong Chai, et al. Modeling of static creep fracture of brittle rock after dynamic damage [J]. Chinese Journal of Theoretical and Applied Mechanics, 2023, 55(04): 903-914.

[163] Xiulei Li, Qiwei Li, Qian Li. A study of the creep model of rock considering fractures and thermal damage[J]. Hydrogeology and Engineering Geology, 2019, 46(6): 46-56.

[164] Zongze Li, Zhenyu Yang, JinYang Fan, et al. Fatigue mechanical properties of salt rocks under high stress plateaus: the interaction between creep and fatigue[J]. Rock Mechanics and Rock Engineering, 2022, 55(11): 6627-6642.

[165] Sunggi Baik, Raj R. Mechanisms of creep-fatigue interaction[J]. Metallurgical Transactions A, 1982, 131215-1221.

[166] Jean Lemaitre, Desmorat Rodrigue. Engineering damage mechanics: ductile, creep, fatigue and brittle failures[M]. Springer Science & Business Media, 2006.

[167] Hongyin Mao, Mahadevan Sankaran. Reliability analysis of creep–fatigue failure[J]. International journal of fatigue, 2000, 22(9): 789-797.

[168] P Rodriguez, Rao K-Bhanu-Sankara. Nucleation and growth of cracks and cavities under creep-fatigue interaction[J]. Progress in materials science, 1993, 37(5): 403-480.

[169] M Sauzay, Mottot M, Allais L, et al. Creep-fatigue behaviour of an AISI stainless steel at 550 C[J].

Nuclear Engineering and Design, 2004, 232(3): 219-236.

[170] R-P Skelton, Gandy D. Creep–fatigue damage accumulation and interaction diagram based on metallographic interpretation of mechanisms[J]. Materials at High Temperatures, 2008, 25(1): 27-54.

[171] Yasuhide Asada, Dozaki Koji, Ueta Masahiro, et al. Exploratory research on creep and fatigue properties of 9Cr-steels for the steam generator of an FBR[J]. Nuclear engineering and design, 1993, 139(3): 269-275.

[172] ZhenWang, Wu WenWang, Liang Jiecun, et al. Creep–fatigue interaction behavior of nickel-based single crystal superalloy at high temperature by in-situ SEM observation[J]. International Journal of Fatigue, 2020, 141105879.

[173] Sunil Goyal, Mariappan K, Shankar Vani, et al. Studies on creep-fatigue interaction behaviour of Alloy 617M[J]. Materials Science and Engineering: A, 2018, 73016-23.

[174] Hongzhou Zhu, Heng Yan, Boming Tang. Damage Model of Interaction Between Fatigue and Creep for Asphalt Mixture[J]. China Journal of Highway and Transport, 2011, 24(04): 15-20.

[175] Jiali Qi. Research on cumulative deformation of saturated soft clay considering the creep effect under long-term cyclic loading [D]. Tianjin University, 2016.

[176] Xiaxing Zhou, Dagang Li. Fracture Mechanism of Plastic-wood Floors under Fatigue and Creep Interaction[J]. FORESTRY MACHINERY & WOODWORKING EQUIPMENT, 2009, 37(03): 21-23.

[177] M-M Sain, Balatinecz J, Law S. Creep fatigue in engineered wood fiber and plastic compositions[J]. Journal of Applied Polymer Science, 2000, 77(2): 260-268.

[178] Deyi Jiang, Zhenyu Yang, JinYang Fan. et al. Experimental study of load rate effect of salt rock during loading and unloading[J]. Rock and soil mechanics, 2023, 44(2): 403-414.

[179] Junbao Wang, Xinrong Liu, Ming Huang. et al. Analysis of axial creep properties of salt rock under low frequency cyclic loading using Burgers model[J]. Rock and soil mechanics, 2014, (4): 933-942.

[180] Sheng-jun Miao, Pengjin Yang, Hui Wang, et al. Fatigue rheological damage modeling of siltstone under cyclic loads [J]. Engineering Mechanics, 2022, 39(7): 70-80.

[181] Hongfa Xu, Liangliang Qi, Bin Liu, et al. Poyhting-Thomson model of rock salt under cyclic loading[J]. Journal of vibration and shock, 2018, 37(13): 203-209.

[182] Zong-ze Li, Deyi Jiang, JinYang Fan, et al. Experimental study of triaxial interval fatigue of salt rock[J]. Rock and soil mechanics, 2020, 41(4): 1305-1312, 1322.

[183] Deyi Jiang, JinYang Fan, Jie Chen, et al. Influence of interval fatigue tests on fatigue characteristics of salt rock[J]. 岩土工程学报, 2016, 38(7): 1181-1186.

[184] Yao Cui, Deyi Jiang, Fengbin DU, et al. Experimental study on character of acoustic emission caused by interval fatigue of salt rock[J]. Journal of Central South University（Science and Technology), 2017, 48(7): 1875-1882.

[185] Deyi Jiang, Wenhao Liu, Jie Chen, et al. Fatigue performance of ordinary concrete subjected to stepwise discontinuous cyclic loading[J]. Journal of Southeast University(Natural Science Edition), 2019, 49(4): 631-637.

[186] JuWang, Jiangteng Li, Zhanming Shi. Deformation damage and acoustic emission characteristics of red sandstone under fatigue – creep interaction[J]. Theoretical and Applied Fracture Mechanics, 2022, 117103192.

[187] Zhanming Shi, Jiangteng Li, JuWang. Effect of creep load on fatigue behavior and acoustic emission characteristics of sandstone containing pre-existing crack during fatigue loading[J]. Theoretical and Applied Fracture Mechanics, 2022, 119103296.

[188] Linjian Ma, YunxiaoWang, MingYang,Wang et al. Mechanical properties of rock salt under combined creep and fatigue[J]. International Journal of Rock Mechanics and Mining Sciences, 2021, 141104654.

[189] Kai Zhao, Ma Hongling, Xiaopeng Liang, et al. Damage evaluation of rock salt under multilevel cyclic loading with constant stress intervals using AE monitoring and CT scanning[J]. Journal of Petroleum Science and Engineering, 2022, 208109517.

[190] Oliver SChenk, Urai Janos-L. Microstructural evolution and grain boundary structure during static recrystallization in synthetic polycrystals of sodium chloride containing saturated brine[J]. Contributions to Mineralogy and Petrology, 2004, 146671-682.

[191] Syed-Asim Hussain, Han Feng-Qing, Ma Zhe, et al. Unraveling sources and climate conditions prevailing during the deposition of neoproterozoic evaporites using coupled chemistry and boron isotope compositions (δ 11B): the example of the salt range, Punjab, Pakistan[J]. Minerals, 2021, 11(2): 161.

[192] C-E Fairhurst, Hudson John-A. Draft ISRM suggested method for the complete stress-strain curve for intact rock in uniaxial compression[J]. International journal of rock mechanics and mining sciences (1997), 1999, 36(3): 279-289.

[193] Zongze Li, Jinjie Suo, JinYang Fan , et al. Damage evolution of rock salt under multilevel amplitude creep – fatigue loading with acoustic emission monitoring[J]. International Journal of Rock Mechanics and Mining Sciences, 2023, 164105346.

[194] JinYang Fan, Jie Chen, Deyi Jiang, et al. Fatigue properties of rock salt subjected to interval cyclic pressure[J]. International Journal of Fatigue, 2016, 90109-115.

[195] Zengliang Gao, Yuxuan Song, Zhouxin Pan, et al. Nanoindentation investigation on the creep

behavior of P92 steel weld joint after creep-fatigue loading[J]. International Journal of Fatigue, 2020, 134105506.

[196] Stefan Holmström, Auerkari Pertti. A robust model for creep-fatigue life assessment[J]. Materials Science and Engineering: A, 2013, 559333-335.

[197] I Salam, Tauqir A, Khan A-Q. Creep-fatigue failure of an aero engine turbine blades[J]. Engineering failure analysis, 2002, 9(3): 335-347.

[198] Bara-Wasfi Al-Mistarehi, Khadaywi Taisir-S, Hussein Ahlam-Khaled. Investigating the effects on creep and fatigue behavior of asphalt mixtures with recycled materials as fillers[J]. Journal of King Saud University-Engineering Sciences, 2021, 33(5): 355-363.

[199] Hongfu Liu, Xinyu Yang, Lijun Jiang, et al. Fatigue-creep damage interaction model of asphalt mixture under the semi-sine cycle loading[J]. Construction and Building Materials, 2020, 251119070.

[200] RJH Thompson, Bonfield P-W, Dinwoodie J-M, et al. Fatigue and creep in chipboard: Part 3. The effect of frequency[J]. Wood science and technology, 1996, 30(5): 293-305.

[201] Jie Zhang, Qiuhua Rao, Wei Yi. A New Creep–Fatigue Interaction Model for Predicting Deformation of Coarse-Grained Soil[J]. Materials, 2022, 15(11): 3904.

[202] JunbaoWang, Qiang Zhang, Zhanping Song, et al. Microstructural variations and damage evolvement of salt rock under cyclic loading[J]. International Journal of Rock Mechanics and Mining Sciences, 2022, 152105078.

[203] Anne-ES Forbes, Blake Steven, Tuffen Hugh. Entablature: fracture types and mechanisms[J]. Bulletin of Volcanology, 2014, 761-13.

[204] Xiaohui Ni, Zhende Zhu, Xiaojuan Li, et al. Quantitative test study of meso-damage of rock under cyclic load[J]. Rock and soil mechanics, 2011, 32(7): 1991-1995.

[205] Shangzhi Zhou, Jun Li, Ying Liu. Rock fatigue crack propagation mechanism based on far field cyclic compression[J]. Journal of Changsha University of Technology (Natural Science Edition), 2009, 6(1): 19-23.

[206] Erik Rybacki, Niu Lu, Evans B. Semi–brittle deformation of Carrara marble: Hardening and twinning induced plasticity[J]. Journal of Geophysical Research: Solid Earth, 2021, 126(12): e2021JB022573.

[207] Rashid-Geranmayeh Vaneghi, Thoeni Klaus, Dyskin Arcady-V, et al. Fatigue damage response of typical crystalline and granular rocks to uniaxial cyclic compression[J]. International Journal of Fatigue, 2020, 138105667.

[208] J-Y Huang, JC E, Huang J-W, et al. Dynamic deformation and fracture of single crystal silicon: fracture modes, damage laws, and anisotropy[J]. Acta Materialia, 2016, 114136-145.

[209] Taoying Liu, Cui Mengyuan, Li Qing, et al. Fracture and Damage Evolution of Multiple-Fractured Rock-like Material Subjected to Compression[J]. Materials, 2022, 15(12): 4326.

[210] Xiaoping Zhou, Xiaokang Pan, Berto Filippo. A state‑of‑the‑art review on creep damage mechanics of rocks[J]. Fatigue & Fracture of Engineering Materials & Structures, 2022, 45(3): 627-652.

[211] Dongxu Chen, LaiguiWang, Chuang Sun, et al. Particle flow study on the microscale effects and damage evolution of sandstone creep[J]. Computers and Geotechnics, 2023, 161105606.

[212] BinxuWang, Tingchun Li, Qingwen Zhu, et al. Study on the creep properties and crack propagation behavior of single-fissure sandstone based on the damage bond model[J]. Theoretical and Applied Fracture Mechanics, 2023, 124103805.

[213] Junbao Wang, Xinrong Liu, Zhanping Song, et al. A whole process creeping model of salt rock under uniaxial compression based on inverse S function[J]. Chinese Journal of Rock Mechanics and Engineering, 2018, 37(11): 2446-2459.

[214] Shuang-Shuang Yuan, Qi-Zhi Zhu, Lun-Yang Zhao, et al. Micromechanical modelling of short- and long-term behavior of saturated quasi-brittle rocks[J]. Mechanics of Materials, 2020, 142103298.

[215] Hongwen Jing, Qian Yin, Shengqi Yang, et al. Micro-mesoscopic creep damage evolution and failure mechanism of sandy mudstone[J]. International Journal of Geomechanics, 2021, 21(3): 4021010.

[216] R-D Campbell. Creep/fatigue interaction correlation for 304 stainless steel subjected to strain-controlled cycling with hold times at peak strain[J]. ASME J. Eng. Ind, 1971, 93887-892.

[217] K Gurumurthy, Srinivasan Balaji, Krishna Penchala-Sai, et al. Creep-fatigue design studies for process reactor components subjected to elevated temperature service as per ASME-NH[J]. Procedia Engineering, 2014, 86327-334.

[218] Yukio Takahashi, Dogan Bilal, Gandy David. Systematic evaluation of creep-fatigue life prediction methods for various alloys[J]. Journal of Pressure Vessel Technology, 2013, 135(6): 61204.

[219] L-K Severud, Winkel B-V. Elastic creep-fatigue evaluation for ASME code[A]//1987: 123-131.

[220] Joseph Oldham, Abou-Hanna Jeries. A numerical investigation of creep-fatigue life prediction utilizing hysteresis energy as a damage parameter[J]. International journal of pressure vessels and piping, 2011, 88(4): 149-157.

[221] Jill-K Wright, Carroll Laura-J, Sham T-L, et al. Determination of the creep-fatigue interaction diagram for Alloy 617[A]//American Society of Mechanical Engineers, 2016: V005T12A004.

[222] R Lagneborg, Attermo RJMT. The effect of combined low-cycle fatigue and creep on the life of austenitic stainless steels[J]. Metallurgical Transactions, 1971, 21821-1827.

[223] Hongfu Liu, Xinyu Yang, Lijun Jiang, et al. Fatigue-creep damage interaction model of asphalt mixture under the semi-sine cycle loading[J]. Construction and Building Materials, 2020, 251119070.

[224] JunbaoWang, Qiang Zhang, Zhanping Song, et al. Experimental study on creep properties of salt rock under long-period cyclic loading[J]. International Journal of Fatigue, 2021, 143106009.

[225] Deyi Jiang, Yao Cui, JinYang Fan, et al. Experimental study of mechanical characteristics of salt rock under discontinuous cyclic loading[J]. Rock and soil mechanics, 2017, 38(5): 1327-1334.

[226] J-L Urai, Spiers C-J. The effect of grain boundary water on deformation mechanisms and rheology of rocksalt during long-term deformation. CRC Press, 2017: 149-158.

[227] Guillaume Desbois, Urai Janos-L, de Bresser Johannes-HP. Fluid distribution in grain boundaries of natural fine-grained rock salt deformed at low differential stress (Qom Kuh salt fountain, central Iran): Implications for rheology and transport properties[J]. Journal of structural geology, 2012, 43128-143.

[228] Tingting Xu, Arson Chloé. Self-consistent approach for modeling coupled elastic and visco-plastic processes induced by dislocation and pressure solution[J]. International Journal of Solids and Structures, 2022, 238111376.

[229] C-J Spiers, Schutjens PMTM. Intergranular pressure solution in NaCl: Grain-to-grain contact experiments under the optical microscope[J]. Oil & Gas Science and Technology, 1999, 54(6): 729-750.

[230] J-H Ter Heege, De Bresser JHP, Spiers C-J. Rheological behaviour of synthetic rocksalt: the interplay between water, dynamic recrystallization and deformation mechanisms[J]. Journal of Structural Geology, 2005, 27(6): 948-963.

[231] JH-D Ter Heege, De Bresser JHP, Spiers C-J. Dynamic recrystallization of wet synthetic polycrystalline halite: dependence of grain size distribution on flow stress, temperature and strain[J]. Tectonophysics, 2005, 396(1-2): 35-57.

[232] Hugh-C Heard. Steady-state flow in polycrystalline halite at pressure of 2 kilobars[J]. Geophysical monograph series, 1972, 16191-209.

[233] G-M Pennock, Drury M-R. Low‑angle subgrain misorientations in deformed NaCl[J]. Journal of microscopy, 2005, 217(2): 130-137.

[234] G-M Pennock, Drury M-R, Peach C-J, et al. The influence of water on deformation microstructures and textures in synthetic NaCl measured using EBSD[J]. Journal of structural geology, 2006, 28(4): 588-601.

[235] Jaroslav Pokluda, Černý Miroslav, Šandera Pavel, et al. Calculations of theoretical strength: State of the art and history[J]. Journal of computer-aided materials design, 2004, 111-28.

[236] Stephen Horseman, Passaris Evan. Creep tests for storage cavity closure prediction[A]//1981: 119-157.

[237] Xinrong Liu, Xin Yang, JunbaoWang. A nonlinear creep model of rock salt and its numerical implement in FLAC 3D[J]. Advances in Materials Science and Engineering, 2015, 2015.

[238] Yujie Wei, Bower Allan-F, Gao Huajian. Recoverable creep deformation and transient local stress concentration due to heterogeneous grain-boundary diffusion and sliding in polycrystalline solids[J]. Journal of the Mechanics and Physics of Solids, 2008, 56(4): 1460-1483.

[239] Michel Aubertin, Julien Michel-R, Servant Stéphane, et al. A rate-dependent model for the ductile behavior of salt rocks[J]. Canadian Geotechnical Journal, 1999, 36(4): 660-674.

[240] P-D Portella, Rie K-T. Low cycle fatigue and elasto-plastic behaviour of materials[M]. Elsevier, 1998.

[241] Yanfei Kang, JinYang Fan , Deyi Jiang, et al. Influence of geological and environmental factors on the reconsolidation behavior of fine granular salt[J]. Natural Resources Research, 2021, 30805-826.

[242] D Grgic, Al Sahyouni F, Golfier F, et al. Evolution of gas permeability of rock salt under different loading conditions and implications on the underground hydrogen storage in salt caverns[J]. Rock Mechanics and Rock Engineering, 2022, 1-24.

[243] Linjian Ma, Xinyu Liu,Wang Ming-Yang, et al. Experimental investigation of the mechanical properties of rock salt under triaxial cyclic loading[J]. International Journal of Rock Mechanics and Mining Sciences, 2013, 6234-41.

[244] John Handin, Hager Jr Rex-V. Experimental deformation of sedimentary rocks under confining pressure: tests at high temperature[J]. AAPG Bulletin, 1958, 42(12): 2892-2934.

[245] Ren Song, Yueming Bai, JingPeng Zhang, et al. Experimental investigation of the fatigue properties of salt rock[J]. International Journal of Rock Mechanics and Mining Sciences, 2013, 6468-72.

[246] Jie Chen. Catastrophic Mechanism induced by Damaged Surrounding Rock and Mitigation Principle During bedded salt Cavern Construction Period[D]. Chongqing university, 2012.

[247] Mingming He, Ning Li, Caihui Zhu, et al. Experimental investigation and damage modeling of salt rock subjected to fatigue loading[J]. International Journal of Rock Mechanics and Mining Sciences, 2019, 11417-23.

[248] Aditya Singh, Kumar Chandan, Kannan L-Gopi, et al. Engineering properties of rock salt and simplified closed-form deformation solution for circular opening in rock salt under the true triaxial stress state[J]. Engineering Geology, 2018, 243218-230.

[249] Weiguo Liang, Chunhe Yang, Yangsheng Zhao, et al. Experimental investigation of mechanical

properties of bedded salt rock[J]. International Journal of Rock Mechanics and Mining Sciences, 2007, 44(3): 400-411.

[250] G Walton. A new perspective on the brittle – ductile transition of rocks[J]. Rock Mechanics and Rock Engineering, 2021, 54(12): 5993-6006.

[251] Shih-Che Yuan, Harrison J-P. An empirical dilatancy index for the dilatant deformation of rock[J]. International Journal of Rock Mechanics and Mining Sciences, 2004, 41(4): 679-686.

[252] Wolfgang-R Wawersik. Determination of steady state creep rates and activation parameters for rock salt[M]. ASTM International, 1985.

[253] H Alkan, Cinar Y, Pusch G. Rock salt dilatancy boundary from combined acoustic emission and triaxial compression tests[J]. International Journal of Rock Mechanics and Mining Sciences, 2007, 44(1): 108-119.

[254] H Horii, Nemat-Nasser Siavouche. Brittle failure in compression: splitting faulting and brittle-ductile transition[J]. Philosophical Transactions of the Royal Society of London. Series A, Mathematical and Physical Sciences, 1986, 319(1549): 337-374.

[255] Mingqing You. Effect of circumferential pressure on the strength of rock specimens and discretization [J]. Chinese Journal of Rock Mechanics and Engineering, 2014, (5): 929-937.

[256] Melvin Friedman. Fracture in rock[J]. Reviews of Geophysics, 1975, 13(3): 352-358.

[257] E-T Brown, Hoek E. Trends in relationships between measured in-situ stresses and depth[A]//Pergamon, 1978: 211-215.

[258] Pierre Bérest, Réveillère Arnaud, Evans David, et al. Review and analysis of historical leakages from storage salt caverns wells[J]. Oil & Gas Science and Technology – Revue d'IFP Energies nouvelles, 2019, 7427.

[259] Md-Yeasin Bhuiyan, Lin Bin, Giurgiutiu Victor. Acoustic emission sensor effect and waveform evolution during fatigue crack growth in thin metallic plate[J]. Journal of Intelligent Material Systems and Structures, 2018, 29(7): 1275-1284.

[260] Leonard Obert. The microseismic method: discovery and early history[A]//1977: 11-12.

[261] David-J Holcomb. General theory of the Kaiser effect[A]//Elsevier, 1993: 929-935.

[262] Patricia Rodríguez, Celestino Tarcisio-B. Application of acoustic emission monitoring and signal analysis to the qualitative and quantitative characterization of the fracturing process in rocks[J]. Engineering Fracture Mechanics, 2019, 21054-69.

[263] V-L Shkuratnik, KravChenko O-S, Filimonov Yu-L. Acoustic emission of rock salt at different uniaxial strain rates and under temperature[J]. Journal of Applied Mechanics and Technical Physics, 2020, 61479-485.

[264] DEW Stone, Dingwall P-F. Acoustic emission parameters and their interpretation[J]. NDT

international, 1977, 10(2): 51-62.

[265] Z-H Chen, Tham L-G, Yeung M-R, et al. Confinement effects for damage and failure of brittle rocks[J]. International Journal of Rock Mechanics and Mining Sciences, 2006, 43(8): 1262-1269.

[266] Mitiyasu Ohnaka, Mogi Kiyoo. Frequency characteristics of acoustic emission in rocks under uniaxial compression and its relation to the fracturing process to failure[J]. Journal of geophysical research: Solid Earth, 1982, 87(B5): 3873-3884.

[267] YWang, JQ Han, CH Li. Acoustic emission and CT investigation on fracture evolution of granite containing two flaws subjected to freeze–thaw and cyclic uniaxial increasing-amplitude loading conditions[J]. Construction and Building Materials, 2020, 260119769.

[268] Jie Huang, Qianting Hu, ChaoZhong Qin, et al. Pre-peak acoustic emission characteristics of tight sandstone failure under true triaxial stress[J]. Journal of Natural Gas Science and Engineering, 2022, 102104576.

[269] LR Li, JH Deng, L Zheng, et al. Dominant frequency characteristics of acoustic emissions in white marble during direct tensile tests[J]. Rock Mechanics and Rock Engineering, 2017, 501337-1346.

[270] Kentaro Ohno, Ohtsu Masayasu. Crack classification in concrete based on acoustic emission[J]. Construction and Building Materials, 2010, 24(12): 2339-2346.

[271] Hamid-Reza Nejati, Nazerigivi Amin, Sayadi Ahmad-Reza. Physical and mechanical phenomena associated with rock failure in Brazilian Disc Specimens[J]. International Journal of Geological and Environmental Engineering, 2018, 12(1): 35-39.

[272] Chengsheng OuYang, Landis Eric, Shah Surendra-P. Damage assessment in concrete using quantitative acoustic emission[J]. Journal of Engineering Mechanics, 1991, 117(11): 2681-2698.

[273] Lasar Kachanov. Introduction to continuum damage mechanics[M]. Springer Science & Business Media, 1986.

[274] W Swindlehurst. Acoustic emission-1 introduction[J]. Non-destructive testing, 1973, 6(3): 152-158.

[275] Kun Du, Li Xuefeng, Tao Ming, et al. Experimental study on acoustic emission (AE) characteristics and crack classification during rock fracture in several basic lab tests[J]. International Journal of Rock Mechanics and Mining Sciences, 2020, 133104411.

[276] Yixiong Gan, Shunchuan Wu, Yi Ren, et al. Evaluation indexes of granite splitting failure based on RA and AF of AE parameters[J]. Rock and soil mechanics, 2020, 41(07): 2324-2332.

[277] Haocong Hu, Juanhong Liu, JinAn Wang. Toughness test and acoustic emission characteristics analysis of fiber reinforced concrete[J]. Journal of China Coal Society, 2023, 48(3): 1209-1219.

[278] Henrik Lund, Salgi Georges. The role of compressed air energy storage (CAES) in future sustainable energy systems[J]. Energy conversion and management, 2009, 50(5): 1172-1179.

[279] Zhen Yang, WanCheng Zhu, Kai Guan, et al. Influence of dynamic disturbance on rock creep from time, space and energy aspects[J]. Geomatics, Natural Hazards and Risk, 2022, 13(1): 1065-1086.

[280] HaiYang Yi, Lele Lu, Wei Cao, et al. Parameters identification and comparative analysis of typical creep models of impurity salt rock[J]. Journal of North China Institute of Science and Technology, 2020, 17(2): 77-81.

[281] TongBin Zhao, YuBao Zhang, QianQing Zhang, et al. Analysis on the creep response of bolted rock using bolted burgers model[J]. Geomechanics & engineering, 2018, 14(2): 141-149.

[282] Shuquan Peng, Peiyu Wang, Ling Fan, et al. Research on elasto-plastic viscous fatigue constitutive model of jointed rock[J]. Rock and soil mechanics, 2021, 42(02): 379-389.

[283] Liu Yang, Li Zhi-da. Nonlinear variation parameters creep model of rock and parametric inversion[J]. Geotechnical and Geological Engineering, 2018, 362985-2993.

[284] Yonghui Li, Shaoyun Pu, Junying Rao, et al. Study on a modified Nishihara fatigue model for rock with cyclic loading[J]. Water Resources and Hydropower Engineering, 2017, 48(7): 129-135.

[285] JingYang Ding, Hongwei Zhou, Qiong Chen, et al. Characters of rheological damage and constitutive model of salt rock[J]. Rock and soil mechanics, 2015, 36(3): 769-776.

[286] Deyi Jiang, Wang Yifan, Wei Liu, et al. Construction simulation of large-spacing-two-well salt cavern with gas blanket and stability evaluation of cavern for gas storage[J]. Journal of Energy Storage, 2022, 48103932.

[287] Yanlin Zhao, Ping Cao, Youdao Wen, et al. Elasto-viscoplastic rheological tests and nonlinear rheological modeling of rocks [J]. Chinese Journal of Rock Mechanics and Engineering, 2008, 27(3): 477-486.

[288] Kaiyun Liu, Yongtao Xue, Hui Zhou. A nonlinear viscoelastic plastic creep model of soft rock with unsteady parameters[J]. Journal of China University of Mining and Technology, 2018, 47(04): 921-928.

[289] YifanWang, Xiong Zhang, Deyi Jiang, et al. Study on stability and economic evaluation of two-well-vertical salt cavern energy storage[J]. Journal of Energy Storage, 2022, 56106164.

[290] JunbaoWang, Xinrong Liu, Jianqiang Guo, et al. Creep properties of salt rock and its nonlinear constitutive model[J]. Journal of China Coal Society, 2014, 39(03): 445-451.

[291] Fei Wu, Heping Xie, Jianfeng Liu, et al. Experimental study of fractional order viscoelastic-plastic creep modeling [J]. Chinese Journal of Rock Mechanics and Engineering, 2014, (5): 964-970.

[292] Ruidong Peng, Zhide Wu, Hongwei Zhou, et al. A fine-scale experimental study of crack extension patterns in layered salt rocks [J]. Chinese Journal of Rock Mechanics and Engineering, 2011, (S2): 3953-3959.

[293] Deyi Jiang, JinYang Fan , Jie Chen, et al. Compression-shear fatigue characterization and

dislocation damage study of salt rocks [J]. Chinese Journal of Rock Mechanics and Engineering, 2015, (5): 895-906.

[294] Masoud-K Darabi, Al-Rub Rashid-K-Abu, Little Dallas-N. A continuum damage mechanics framework for modeling micro-damage healing[J]. International Journal of Solids and Structures, 2012, 49(3-4): 492-513.

[295] Lazar-M Kachanov. Rupture time under creep conditions[J]. International journal of fracture, 1999, 97(1-4): 11-18.

[296] Qiang Liu, Yanlin Zhao, Liming Tang, et al. Mechanical characteristics of single cracked limestone in compression-shear fracture under hydro-mechanical coupling[J]. Theoretical and Applied Fracture Mechanics, 2022, 119103371.

[297] A-G Evans. The role of inclusions in the fracture of ceramic materials[J]. Journal of Materials Science, 1974, 91145-1152.

[298] Kavan Khaledi, Mahmoudi Elham, Datcheva Maria, et al. Stability and serviceability of underground energy storage caverns in rock salt subjected to mechanical cyclic loading[J]. International journal of rock mechanics and mining sciences, 2016, 86115-131.

[299] Jie Chen, Chen He, Wu Fei, et al. Creep Properties of Mudstone Interlayer in Bedded Salt Rock Energy Storage Based on Multistage Creep Test: A Case Study of Huai'an Salt Mine, Jiangsu Province[J]. Geofluids, 2022, 2022.

[300] Jinyang Fan. Fatigue damage and dilatancy properties for salt rock under discontinuous cyclic loading[D]. Chongqing university, 2017.

List of publications

[1] **Li, Zongze**, Kang Yanfei, Fan Jinyang, Fourmeau Marion, Jiang Deyi, Nelias Daniel. Creep–Fatigue Mechanical Characteristics of Salt Rocks under Triaxial Loading: An Experimental Study [J]. *Engineering Geology* 2023,107175.

[2] **Li, Zongze**, Suo Jinjie, Fan Jinyang, Fourmeau Marion, Jiang Deyi, Nelias Daniel. Damage Evolution of Rock Salt under Multilevel Amplitude Creep–Fatigue Loading with Acoustic Emission Monitoring [J]. *International Journal of Rock Mechanics and Mining Sciences* 2023, 164:105346.

[3] **Li, Zongze**, Yang Zhenyu, Fan Jinyang, Fourmeau Marion, Jiang Deyi, Nelias Daniel. Fatigue Mechanical Properties of Salt Rocks under High Stress Plateaus: The Interaction between Creep and Fatigue [J]. *Rock Mechanics and Rock Engineering* 2022, 55(11):6627–42.

[4] **Li, Zongze**, Yang Fan, Fan Jinyang, Jiang Deyi, Ambre Julien. Fatigue Effects of Discontinuous Cyclic Loading on the Mechanical Characteristics of Sandstone [J]. *Bulletin of Engineering Geology and the Environment* 2022, 81(8):336.

[5] **Li Zongze,** Jiang Deyi, Fan Jinyang, Chen Jie, Liu Wei, Wu Fei, et al. Experimental study of triaxial interval fatigue of salt rock. *Rock and Soil Mechanics* (in Chinese), 2020, 41(4), 1305-+.

[6] Ren, Yiwei, Yuan Qiang, Kang Yanfei, Wei Like, **Li Zongze**, Jiang Deyi, He Huayong, Xu Hong. Experimental Determination of Polycrystalline Salt Rock Thermal Conductivity, Diffusivity and Specific Heat From 20 to 240 Degrees C. *Frontiers in Earth Science* 2022, 10.

[7] Kang, Yanfei, Fan Jinyang, Jiang Deyi, **Li Zongze**. Influence of Geological and Environmental Factors on the Reconsolidation Behavior of Fine Granular Salt. *Natural Resources Research* 2021, 30(1):805–26.

[8] Jiang, Deyi, Chen Shao, Liu Wenhao, Ren Yiwei, Guo Pengyv, **Li Zongze**. Underground Hydro-Pumped Energy Storage Using Coal Mine Goafs: System Performance Analysis and a Case Study for China. *Frontiers in Earth Science* 2021, 9.

[9] Peng, Huihua, Fan Jinyang, Zhang Xiong, Chen Jie, **Li Zongze**, Jiang Deyi, Liu Chun. Computed Tomography Analysis on Cyclic Fatigue and Damage Properties of Rock Salt under Gas Pressure. *International Journal of Fatigue* 2020, 134, 105523.

[10] Chen, Bo, **Li Zongze**, Liu Chun, Du Chao, Jiang Deyi. Study on Creep Characteristics of Salt Rock under Unloading Conditions. *International Journal of Geomate* 2020, 19(75):215–24.

[11] Jiang Deyi, Yang Zhenyu, Fan Jinyang, **Li Zongze**, Suo Jinjie, Chen Jie. Experimental study of load rate effect on fatigue characteristics of salt rock. *Rock and Soil Mechanics* (in Chinese),

2023,44(02):403-414.

[12] Kang Yanfei, Chen Jie, Jiang Deyi, **Li Zongze**, Du chao, Chen Jie. Mesoscopic characteristics and mechanisms of microcracks healing in impurity-containing rock salt. *Rock and Soil Mechanics* (in Chinese), 2020,41(S2):1-10

FOLIO ADMINISTRATIF

THESE DE L'INSA LYON, MEMBRE DE L'UNIVERSITE DE LYON

NOM : LI   DATE de SOUTENANCE :
(avec précision du nom de jeune fille, le cas échéant)

Prénoms : Zongze

TITRE : Study on Creep Fatigue Mechanical Characteristics and Constitutive Model of Salt Rock

NATURE : Doctorat   Numéro d'ordre :   2023INSALXXXX

Ecole doctorale : Ecole Doctorale N° 162 Mécanique, Energétique, Génie civil, Acoustique

Spécialité : Génie Mécanique

RESUME : To meet the requirements of the United Nations Framework Convention on Climate Change, i.e., the Paris Agreement, countries around the world have developed carbon-peaking and carbon-neutral action programs. The use of renewable energy sources is an effective means of meeting this requirement. Because salt rock has good rheology, low porosity, low permeability and damage self-healing characteristics, compressed air energy storage using salt caverns is an effective way to enhance the efficiency of renewable energy use. Considering the operational requirements for load balancing in compressed air energy storage plants, the surrounding rock of salt cavern reservoirs is subjected to discontinuous cyclic loading with varying gas injection rates and pressures i.e. alternating creep-fatigue loading. Through a combination of theoretical analysis, laboratory experiments, and model studies, this research investigated the creep-fatigue mechanical characteristics of salt rocks with varying high-stress interval times, and the creep-fatigue mechanical characteristics of salt rocks under different confining pressures. Additionally, the impact of different stress levels on the creep-fatigue damage evolution of salt rocks was monitored and analyzed using acoustic emission devices. Long-term creep-fatigue tests on salt rocks under different loading rate and level were conducted based on the actual frequency of load balancing in compressed air energy storage plants. The reasons and patterns of the salt rock's interaction between creep and fatigue under different conditions were analyzed. Based on the consideration of the creep-fatigue interaction in salt rocks, a state variable-based creep-fatigue constitutive model for salt rocks was proposed and established, and its validity was verified. The research findings provide important guidance for ensuring the stability of salt cavern reservoirs.

MOTS-CLÉS : Salt rock, Creep-fatigue, Confining pressure, Acoustic emission, State variables, Constitutive model.

Laboratoire (s) de recherche : Laboratoire de Mécanique des Contacts et des Structures (LAMCOS), INSA-Lyon

Directeur de thèse: Daniel NELIAS, Deyi JIANG

Président de jury : Christophe PETIT

Composition du jury : Christophe PETIT, Yang JU, Daniel DIAS, Daniel NELIAS, Deyi JIANG, Marion FOURMEAU